MODELLING OF SINGLE COMPONENT AND BICOMPONENT EXTRUSION FLOWS

By

ARISTOTELIS KARAGIANNIS, Dipl. Chem. Eng.

A Thesis

Submitted to the School of Graduate Studies

in Partial Fulfillment of the Requirements

for the Degree

Doctor of Philosophy

McMaster University

June 1989

MODELLING OF SINGLE COMPONENT AND BICOMPONENT EXTRUSION FLOWS

To my wife, Petroula

DOCTOR OF PHILOSOPHY (1989)
(Chemical Engineering)

McMASTER UNIVERSITY
Hamilton, Ontario

TITLE: Modelling of Single Component and Bicomponent Extrusion Flows

AUTHOR: Aristotelis Karagiannis,
Dipl. Chem. Eng. (Aristotle University of Thessaloniki, Greece)

SUPERVISORS: Drs. A.N. Hrymak and J. Vlachopoulos

NUMBER OF PAGES: xxviii, 304

ABSTRACT

Flow phenomena associated with die extrusion and coextrusion have a significant impact on the final product shape and layer uniformity. The present work is concerned with the mathematical modelling and numerical simulation of three dimensional single-component and stratified multi-component extrusion. The objective is to provide an understanding of the flow phenomena involved and investigate their impact on the shape and interface configuration of the extruded article.

A three dimensional non-isothermal study of viscous free-surface flows with exponential dependence of viscosity on temperature is presented. The effects of non-isothermal conditions and/or geometry on the extrudate shape are investigated with a fully three dimensional finite element/Galerkin formulation. Special free surface update schemes (pathline, spine and hybrid spine/pathline methods) are presented and enable the study of the extrudate swelling out of very complicated 3-D geometric shapes. Apart from the well known thermally induced extrudate swelling phenomenon, bending and distortion of the extrudate may occur because of temperature differences and/or geometric asymmetries. A temperature difference across the die can be imposed by heating or cooling the die walls, but can also arise because of asymmetric viscous heat generation due to the die geometry. Temperature differences affect velocity profiles because of the temperature dependence of viscosity and lead to extrudate bending and distortion. It is also shown numerically and confirmed experimentally that the die geometry can induce extrudate bending even in the case of isothermal Newtonian flows.

A powerful finite element algorithm for the 3-D numerical simulation of bicomponent stratified free surface flows is described. The presence of multiple free surfaces (interface, external free surfaces) is tackled with advanced free surface update schemes. The

pressure and viscous stress discontinuity at the interface occurring because of the viscosity mismatch is handled with both a double node (u-v-w-P_1-P_2-h_1-h_2) formulation and a penalty function (u-v-w-P-h_1-h_2) formulation.

The interface shape development and extrudate swelling behaviour of stratified flows in a sheath- core configuration is examined. The viscosity mismatch has an effect on both the interface and the external free surface shapes. The flowrate ratio, die geometry and layer configuration are also shown to affect the areas of flow of the individual layers and the extrudate swelling behaviour of the bicomponent system.

The experimentally observed tendency of the less viscous layer to encapsulate the more viscous layer in stratified bicomponent flows of a side-by-side configuration is established with the aid of both a fully 3-D analysis and a 1-D optimization analysis, in agreement with experimental evidence. It is shown that the direction and degree of encapsulation depend directly on the viscosity ratio. For shear thinning fluids exhibiting a viscosity crossover point, interface curvature reversal may occur if the shearing level is such that the crossover point is exceeded. The effects of the length of flow and slip at the wall on the degree of encapsulation are investigated. The effect of initial conditions and design of the layer merging part on the interface shape development downstream is also examined and potential sources of instabilities are identified. The extrudate bending and distortion of the bicomponent system because of the viscosity mismatch is also shown.

ACKNOWLEDGMENTS

I would first like to express my sincere appreciation to my supervisors, Professors J. Vlachopoulos and A.N. Hrymak for their constant encouragement, guidance, interest and enthusiasm throughout the course of this work, and for providing a stimulating and outstanding environment for learning.

I am especially grateful to Henk Pool, Gert Berendsen and Thomas McCullough of the Dow Chemicals Company for making available the experimental results on coextrusion and for providing their much needed industrial experience and innumerable discussions and suggestions.

I am deeply grateful to my wife Petroula for her constant confidence, patience and encouragement during the years of this work.

I would also like to thank my colleagues for many helpful discussions and for providing a stimulating environment. In particular I wish to thank Harry Mavridis, Costas Tzoganakis, John Perdikoulias and Jiri Vlcek.

I would like to acknowledge the financial support of the Department of Chemical Engineering and the School of Graduate Studies at McMaster University, the Natural Sciences and Engineering Research Council of Canada, the Ontario Ministry of Colleges and Universities and Shell Canada Limited.

Finally, I would like to thank the staff of the Engineering Word Processing Centre of McMaster University for their excellent work and patience during the preparation of this thesis.

TABLE OF CONTENTS

TABLE OF CONTENTS (continued)

TABLE OF CONTENTS (continued)

TABLE OF CONTENTS (continued)

TABLE OF CONTENTS (continued)

LIST OF FIGURES

LIST OF FIGURES (continued)

LIST OF FIGURES (continued)

LIST OF FIGURES (continued)

LIST OF FIGURES (continued)

LIST OF FIGURES (continued)

LIST OF FIGURES (continued)

LIST OF FIGURES (continued)

LIST OF FIGURES (continued)

LIST OF TABLES

NOMENCLATURE

a,b,c,d	: coefficients of polynomials
A,A'	: Contact point
A_I	: Interfacial Area
b_{jk}	: Inner product, Eqn. B.21
BR	: Broyden's method
BR-N	: Broyden's method interchanged with Newton-Raphson
BR-P	: Broyden's method interchanged with Picard
C	: Specific heat capacity
$\underline{\underline{d}}$	: Tensor defined in eqn. 5.22
$\underline{d}$	: Search direction
DE-1	: One dominant eigenvalue
DE-2	: Two dominant eigenvalues
$\underline{e}^i$	: Unit vector for i-th spine
$\underline{f}$	: Vector of functions
$\underline{F}$	: Load vector
H	: Height, mean curvature of the interface
$\underline{\underline{H}}$	: Approximation to the inverse of the Jacobian matrix
h	: Heat transfer coefficient
$\underline{h}$	: Vector of h-parameters
h_e	: Degree of encapsulation
h^i	: Free surface parameter for the i-th spine
$h_1{}^i$	: Interface parameter for the i-th spine
$h_2{}^i$	: External free surface parameter for the i-th spine

$\underline{\underline{I}}$: unit tensor

$II_{\dot{\gamma}}$: Second invariant of rate-of-strain tensor

$\underline{\underline{J}}$: Jacobian matrix

$\underline{\underline{J}}^*$: Jacobian matrix

$\underline{\underline{K}}$: "Stiffness" matrix

k : Thermal conductivity

k : Material constant of power law model

L : Characteristic length

m : number of dependent variables

$\underline{m}$: tangent vector

N^i : Quadratic basis function of the i-th node

N^i_x : $\partial N^i/\partial x$

N^i_y : $\partial N^i/\partial y$

N^i_z : $\partial N^i/\partial z$

N^i_ξ : $\partial N^i/\partial \xi$

N^i_η : $\partial N^i/\partial \eta$

$N^i\zeta$: $\partial N^i/\partial \zeta$

N^i_p : Linear basis function of the i-th node

NR : Newton-Raphson

n : Power-law index, number of unknowns

n_c : Number of nodal points on a 2-D (y – z) grid

n_h : number of unknown interface parameters

n_a : number of available equations

$\underline{n}$: Normal vector

n_1, n_2, n_3 : Components of the normal vector

P	: Dimensionless (scaled) pressure
P'	: Dimensional pressure
PI	: Picard
P_i, p^i	: Nodal pressure for i-th node
p_i, p_j	: used in Broyden's algorithm
Q	: Flowrate
Q_1, Q_I	: Flowrate of fluid 1 or I
Q_2, Q_{II}	: Flowrate of fluid 2 or II
q	: Flowrate ratio (Q_1/Q_2)
$\underline{q}$	: Vector used in Broyden's algorithm
R	: Radius
$\underline{R}$	: Vector of residuals
R_x, R_y, R_z	: x-, y- and z- momentum residuals
R_{mB}	: Momentum residual boundary integral
R_c	: continuity residual
R_T	: Energy equation residual
R_k	: Kinematic condition residual
$R_{z,s}$	: z-momentum residual contribution of slip velocity
$\underline{r}$	: Free surface definition in Eqn. 5.25
$\underline{r}$	: Vector used in Broyden's algorithm
s	: Line search variable, Eqn. B.14
T	: Dimensionless (scaled) Temperature
T'	: Dimensional Temperature
T^i	: Nodal temperature for i-th node
T'_w	: Temperature at the die wall

T_∞ : Temperature of the ambient air

T_x : $\partial T/\partial x$

T_y : $\partial T/\partial y$

T_z : $\partial T/\partial z$

T_ξ : $\partial T/\partial \xi$

T_η : $\partial T/\partial \eta$

T_ζ : $\partial T/\partial \zeta$

$\underline{t}, \underline{t}_1, \underline{t}_2$: Tangential vectors at the interface

U : Characteristic velocity

u : x- velocity component

$\underline{u}^{ip}$: Predicted solution in DE method, Eqn. B.17

u_x : $\partial u/\partial x$

u_y : $\partial u/\partial y$

u_z : $\partial u/\partial z$

u_ξ : $\partial u/\partial \xi$

u_η : $\partial u/\partial \eta$

u_ζ : $\partial u/\partial \zeta$

v : y-velocity component

v^i : Nodal velocity for i-th node

$\underline{v}$: velocity vector

v_s : slip velocity

v_x : $\partial v/\partial x$

v_y : $\partial v/\partial y$

v_z : $\partial v/\partial z$

v_ξ : $\partial v/\partial \xi$

v_η : $\partial v/\partial \eta$

v_ζ : $\partial v/\partial \zeta$

w : z- velocity component

w_x : $\partial w/\partial x$

w_y : $\partial w/\partial y$

w_z : $\partial w/\partial z$

w_ξ : $\partial w/\partial \xi$

w_η : $\partial w/\partial \eta$

w_ζ : $\partial w/\partial \zeta$

$\underline{X}$: Vector of unknowns

x : x-coordinate direction

$\underline{x}$: position vector

$\underline{x}_p$: Vector of free surface coordinates. Pathline method.

x_ξ : $\partial x/\partial \xi$

x_η : $\partial x/\partial \eta$

x_ζ : $\partial x/\partial \zeta$

$\underline{Y}$: Set of dependent variables

y : y-coordinate direction

y_ξ : $\partial y/\partial \xi$

y_η : $\partial y/\partial \eta$

y_ζ : $\partial y/\partial \zeta$

$\underline{Z}$: Set of independent variables

z : z-coordinate direction

z_ξ : $\partial z/\partial \xi$

z_η : $\partial z/\partial \eta$

z_ζ : $\partial z/\partial \zeta$

Greek symbols

a : Exponential factor in the viscosity-temperature relation

a : Weighting factor, Eqn. B.8

β : Slip coefficient

β : Damping factor, Eqn. B.12

Γ : Boundary of flow domain

$\dot{\gamma}$: Shear rate

$\underline{\underline{\dot{\gamma}}}$: Rate-of-strain tensor

γ : surface tension

$\underline{\delta}$: Vector used in Broyden's algorithm

ε : Tolerance

ζ : Local coordinate in the parent element

η : Local coordinate in the parent element

λ : Time constant in Carreau model (Eqn. 2.35)

λ : Penalty parameter (Eqn. 5.14)

λ : Underrelaxation factor (Eqn. 6.2)

μ : Dimensionless (scaled) viscosity, dominant eigenvalue

μ'_w : Viscosity at the die wall temperature

μ'_c : Characteristic viscosity

μ'_0 : Zero-shear viscosity

ν : Number of dominant eigenvalues

ξ : Local coordinate in the parent element

ρ : Density

$\underline{\underline{\sigma}}$: Total stress tensor

$\underline{\underline{\tau}}$: Dimensionless (scaled) deviatoric stress tensor

τ' : Deviatoric stress tensor

τ_w : Wall shear stress

Ω : Flow domain

Ω_1 : Flow domain of fluid 1

Ω_2 : Flow domain of fluid 2

Dimensionless Groups

B : Dimensionless measure of slip, $\beta \mu/L$

Br : Brinkman Number, $\mu'_w U^2/k(T'_w-T'_\infty)$

Ca : Capillary number, $\mu U/\gamma$

Nu : Nusselt Number, hL/k

Pe : Peclet Number, $\rho CUL/k$

Superscripts

(e) : of the element level

i : index

j : index

k : index

(k) : iteration number

T : Transpose

Subscripts

0	: Base point
F	: Free surface
I	: Interface
w	: Wall

Symbols

$<\cdot,\cdot>$	: inner product
$\|\cdot\|$	: norm
$\times$	: vector product

Underlines

$\underline{\ }$	: vector
$\underline{\underline{\ }}$	: tensor

CHAPTER 1

INTRODUCTION

1.1 EXTRUSION AND MULTICOMPONENT EXTRUSION OF POLYMER MELTS

Extrusion is a major polymer processing operation that involves the conversion of polymeric materials whose initial form may be a solid, into finished products of desired shape and/or thermal/mechanical properties. The process is continuous and encompasses the melting, transportation and final shaping of the polymers. The shaping is achieved by extruding the molten polymers through dies of the appropriate shape before the extrudate is cooled and solidification takes place. Depending on the application, a winding mechanism may be used to wind and optionally draw the product following its exit from the die.

Multicomponent extrusion (coextrusion) is the simultaneous extrusion from a single die, not necessarily a single orifice, of two or more homogeneous fluids which form a laminar structure. In recent years coextrusion has gained wide recognition as an approach to achieving unique product performance (by combining the properties of different materials) and lower costs. Figure 1.1 summarizes various geometric shapes and layer configurations that are used in the polymer processing industry. The cylindrical dies are mainly used in the production of conjugate and sheath-core fibers, the slit dies in coextruded film and sheet, and the annular dies in the coextruded wire and cable or blown film industry.

The unique feature of the coextrusion process is the stratified nature of the multiphase flow where the different materials are separated by continuous internal free surfaces (interfaces).

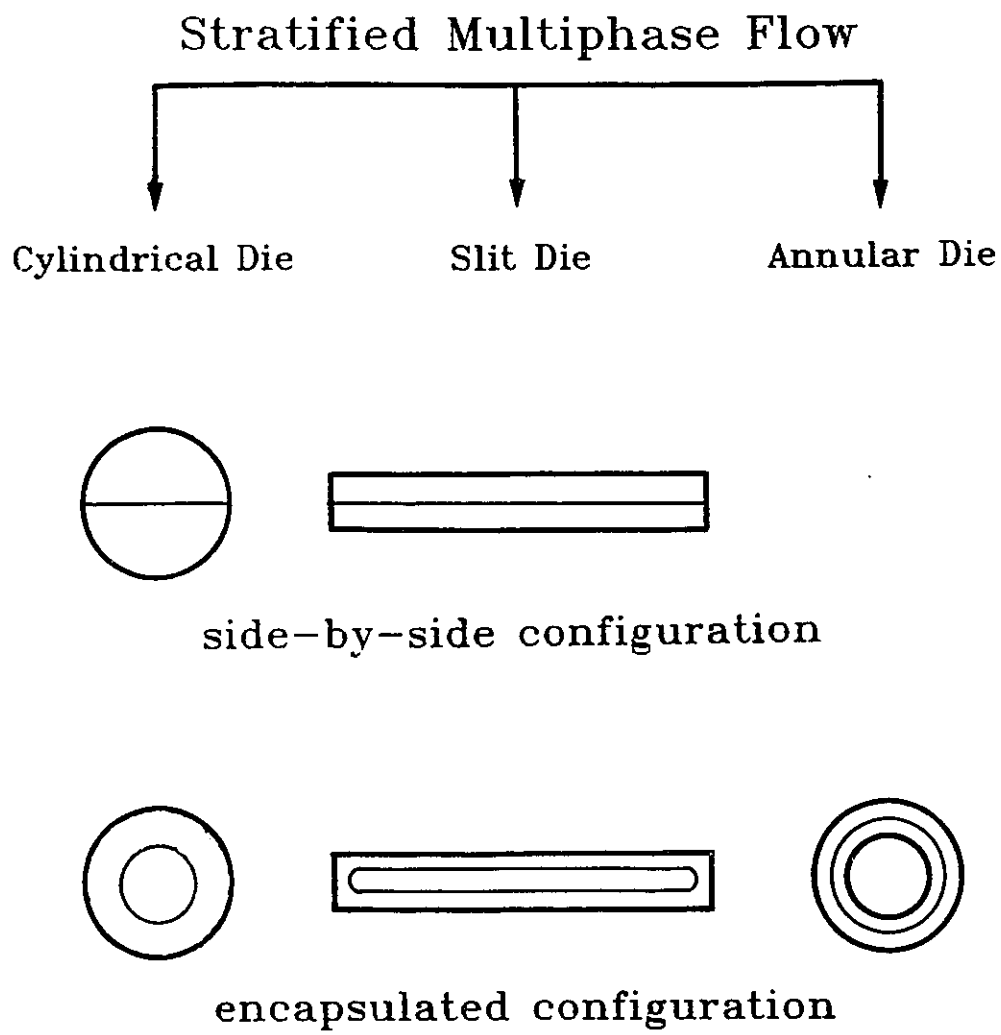

Figure 1.1 Schematic of typical geometric shapes and layer configurations used in bicomponent extrusion.

The polymer processing step is very close to the final user and so quality and economic considerations are very important. Part quality and production efficiency are extremely important since there is global competition for producing articles. Figure 1.2 shows the tight relationship between polymer feedstock, processing conditions and final properties. There are many ways to process a material and there are many materials that could be processed and/or combined to give a set of desired ultimate properties. The usual procedure is to process a material (or system of materials in coextrusion), obtain a structure and evaluate the product properties. A catalogue of such properties allows the selection of the proper material/process combination for a needed article.

The advantage of computer analysis tools would be to help avoid expensive design-test-redesign cycles on a component of the machinery to produce a specified article by offering an understanding of the process characteristics and the relationships between the factors involved.

The modelling and simulation of polymer melt extrusion flows requires simultaneous consideration of the mass, momentum and energy conservation principles. The geometry of the flow domain enters through boundary conditions and appropriate constitutive equations must be employed to relate stresses to velocity gradients. The complexity of process die geometries and the non- linear polymer melt properties result in a mathematical problem that must be solved numerically. Today's availability of powerful numerical techniques and high speed vector processing computers with large memory resources, renders such an analysis economical and attractive. However, there are a number of complications that arise from the nature of die extrusion flows.

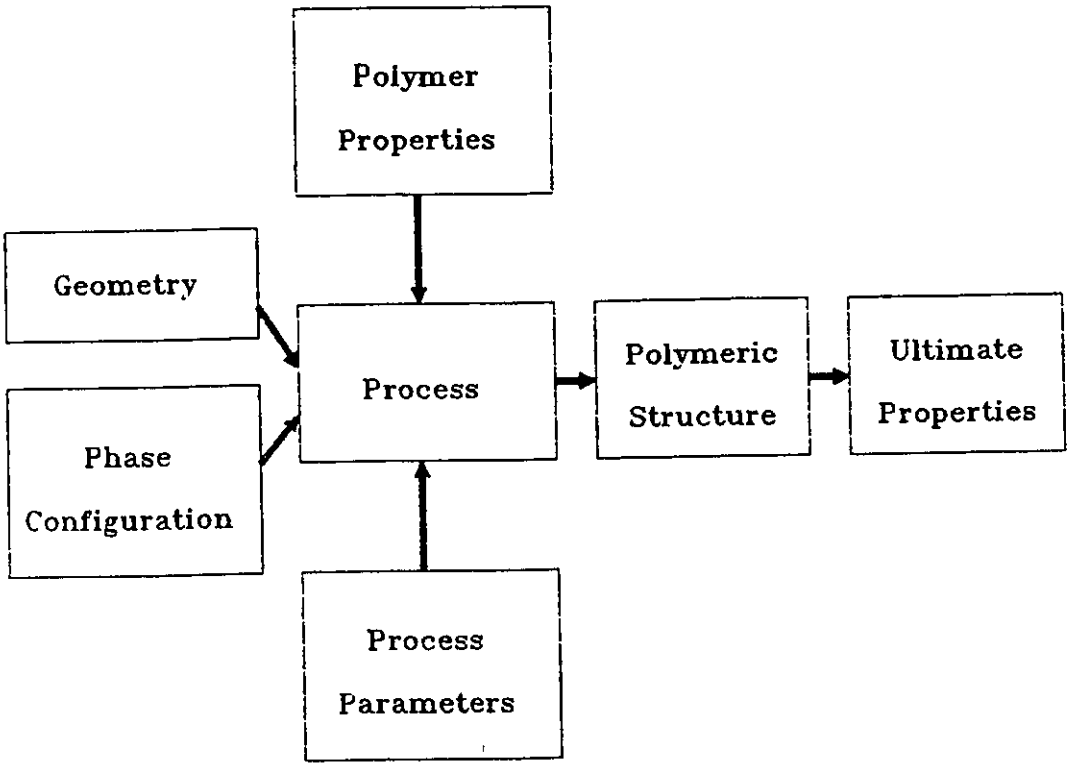

Figure 1.2 Processing, structure and ultimate property relationship.

Extrusion flows involve the presence of external free surfaces (melt/air interfaces) and internal free surfaces (melt/melt interfaces) the shape and location of wnich are unknown. The mathematical problem becomes nonlinear because part of the integration domain boundary of the partial differential equations is not known a priori and must be included in the calculation.

A variety of boundary types exist in this type of flow, since solid walls, external and internal free surfaces and three phase contact lines (solid/melt/air at the die exit or solid/melt/melt at the interface/wall contact lines) are present. Contact lines introduce mathematical singularities whose nature, especially with no significant surface tension effects present, is still poorly understood.

Experimental studies of the extrusion of two-phase polymer melts have shown that the interface between the two melt phases changes in shape during the course of the flow through slit and round dies when the two melts possess different viscous and/or elastic properties (Southern and Ballman, 1975; Everage, 1975; Han, 1981). There is a tendency of the less viscous fluid to encapsulate the more viscous fluid and it has been shown that viscosity differences generally dominate over elasticity differences. Near the die walls the movement of the interface is a purely three dimensional (3-D) effect which accepts no 1-D or 2-D simplifications. The initial configuration, die geometry and processing conditions affect the interface shape and further complicate the modelling.

The three dimensional modelling, necessary to study the 3-D extrudate swelling and the interface shape change in bicomponent flows, gives rise to large systems of equations and requires vast computer power and resources. Also, the handling of the three dimensional free surface is not trivial and may become very intricate when complicated geometries such as those of actual production dies are involved.

Further modelling difficulties arise due to the non-Newtonian character of polymeric materials. The rheological properties of polymer melts depend on the temperature of the melt, the degree of shearing and extension as well as on the deformation history that the material has experienced. Typical polymer processing operations involve flow out of short dies at high shear and extension rates. Under such conditions, the viscoelastic character of polymer melts may become important and produce a quite different flow behaviour as compared to that of Newtonian fluids. Heat transfer and viscously generated heat affect the rheological properties of the fluids and their effect may also be crucial.

The modelling of extrusion and multicomponent flows, in three dimensions, poses a theoretical challenge since so far intuition and experimental trial- and-error have been the major contributors in the explanation of the associated phenomena. Coupled with experiments and theory, analysis may lead to better process design and operation. The development of a numerical tool for the analysis of single and multi-layer extrusion flows would offer insight into the flow mechanisms, and help in the understanding and assessment of the phenomena involved.

1.2 LITERATURE REVIEW

A brief survey of previous experimental and theoretical work in the areas of single layer extrudate swelling and stratified bicomponent flows is given.

1.2.1 Single Layer Extrudate Swelling

The extrusion of single components is one of the major operations in polymer processing. The complex rheology of polymer melts and the interaction of various parameters such as the material properties, stress field, thermal conditions and die geometry compose a problem of enormous fundamental and practical interest. The swelling behaviour of the

extruded molten polymer comprises one aspect of this problem. Polymer melts, upon emerging from the die exhibit an increase of the area of flow relative to that inside the die, a phenomenon that is known as "extrudate swelling" (Han, 1981; Tanner, 1985). In operating polymer processes, it is often observed that the shape of the final product can be quite different from that at the die exit (Han, 1971; 1981; White and Huang, 1981; Tadmor and Gogos, 1979). Extrudate swell has motivated numerous investigations because of the impact that the swelling behaviour has on the final product shape.

After the numerical study of viscous free surface flows by Nickell et al. (1974) appeared, the simulation of the extrudate swelling phenomenon has been an area of intense research. Of the numerical methods that have been used, the finite element method has become the most popular, mainly because of its ability to handle complicated geometric boundaries and the matrix structure of the resulting system of equations.

Two dimensional or axisymmetric problems have been studied (Crochet et al, 1984; Tanner, 1985; Crochet and Keunings, 1982; Caswell and Viriyayuthakorn, 1983; Mitsoulis, 1984; Keunings; 1987) and little work has been done on the three dimensional simulation of extrudate swelling. The first three dimensional studies were those by Bush and Phan-Thien (1985) and Tran-Cong and Phan-Thien (1988a,b,c) who used a boundary element approach to study the extrudate swell out of square and triangular geometries. Shiojima and Shimazaki (1987) presented the first finite element approach, where they examine the flow out of rectangular geometries for Newtonian and Maxwell fluids. Attempts and discussions towards 3-D solutions were also presented by Tanner (1986), Menges at al. (1985), and Schwenzer and Menges (1987).

Non-isothermal conditions occur in a number of polymer processing operations such as film and pipe extrusion, fiber spinning, profile extrusion, etc. The temperature inside the die affects the flow field and the swelling behaviour, through the viscosity-temperature

functional relationship. Phuoc and Tanner (1980) were the first to display the effects of non-isothermal conditions on the extrudate swelling for generalized Newtonian fluids. They demonstrated that the swelling ratio is a function of the material temperature, and the higher the temperature in the core of the material compared to the walls, the higher the swelling ratio. This phenomenon is known as the thermally induced extrudate swelling and is based on a purely viscous mechanism. Ben Sabar and Caswell(1981) and Huynh(1983) have also studied the phenomenon and Finlayson and McClelland (1985, 1988), Sugeng et al. (1987), Milthorpe and Tanner (1987) and Vlcek and Vlachopoulos (1989) have studied the coupling between temperature-induced and stress-induced swelling. All of the cited non- isothermal work has concentrated on the 2-D non-isothermal extrudate swelling and its interactions with the stress field.

In this thesis, a general 3-D finite element approach is formulated to study isothermal and non-isothermal flows inside and out of geometries of high complexity. Chapter 2 presents the numerical method and Chapter 3 studies of isothermal and non-isothermal extrusion out of several different die shapes. Significant 3-D effects such as gross movement of the extrudate in space (bending) and extrudate distortion are displayed, resulting from thermal and/or geometric asymmetries.

The finite element method was chosen as the numerical tool in this thesis. The finite element method allows the incorporation of additional effects such as non-isothermal conditions, slip at the wall and surface tension. Furthermore, this thesis is oriented toward the study of stratified flows. Finite element formulations of two dimensional stratified flows have been successfully undertaken (Mitsoulis, 1986; Mavridis, 1987; Dheur and Crochet, 1987) and form a solid basis for the extension to 3-D which is presented in this thesis. No boundary element formulation of stratified flows has been presented thus far. Vectorization of the

FORTRAN codes leads to favorable performance and low CPU times on CRAY and other vector computers and renders the use of finite elements attractive and economical.

1.2.2 Multi-Layer Flows

Stratified two-phase flow in a cylindrical tube has been a subject of considerable interest in the late 1950's and early 1960's in the transportation of heavy viscous crude oil through long pipelines. The addition of a small amount of water to the crude oil flowing through the pipeline reduced the pressure gradient considerably, resulting in a reduction in pumping cost. This observation stimulated both theoretical (Russell and Charles, 1959; Charles and Redberger, 1962; Gemmell and Epstein, 1962; Charles and Lilleleht, 1965; Yu and Sparrow, 1967; Hasson and Nir, 1970; Bentwich, 1964) and experimental (Russel et al., 1959; Charles et al., 1961; Yu and Sparrow, 1969; Hasson et al., 1970) studies dealing with the stratified flow of oil-water mixtures in a cylindrical tube.

In the polymer processing area, investigations on stratified two-phase flow of molten polymers were undertaken by a number of researchers. The main phenomenon of interest is the observed interface shape change during the course of flow of the bicomponent system inside the process dies (Han, 1981; Southern and Ballman, 1973; Everage, 1975) which may result in layer non- uniformity and increased operating cost. Also, of major interest is the wave- like and incipient interfacial instabilities that cause a rugged interface (Han, 1981; Schrenk et al, 1978) which impacts the product appearance and value. The objective of these studies was to study the flow mechanisms that cause the interface shape change and the interfacial instabilities.

Viscosity differences were shown to cause interface shape change (Southern and Ballman, 1973; 1975; Everage, 1973; 1975; Han, 1981; Lee and White, 1974; 1975) with the less viscous fluid always tending to encapsulate the more viscous fluid. The effect of normal

stress differences on the interface shape was studied by White et al (1972) who suggested that apart from viscosity differences, second normal stress differences influence the interface shape. In the experimental investigation by Lee and White (1974) it was shown that in bicomponent stratified flow in tubes, the less viscous melt encapsulated the more viscous melt irrespective of the relative values of the first and second normal stress differences thereby establishing that the factor dominating the interface shape is the viscosity mismatch. Southern and Ballman (1975) and Khan and Han (1976) have also suggested that viscosity differences predominate over the elasticity ratio in determining the interface shape.

Southern and Ballman (1973,1975), using two polystyrenes which exhibit a viscosity curve crossover, showed that for shear thinning materials the level of shearing is critical for the flow configuration. There is an inversion of the interface curvature when the viscosity crossover point is exceeded so that the less viscous melt was always concave and tended to encapsulate the more viscous melt. Lee and White (1974), and Han and Kim (1976) have also observed the interface curvature reversal when viscosity ratio reversal occurred.

The effect of the viscosity ratio on the degree of encapsulation was investigated by Lee and White (1974) and Minagawa and White (1975) and an increase in encapsulation was observed with increasing viscosity ratio.

The swelling behaviour of bicomponent systems upon leaving the die has also been studied. Southern and Ballman (1973, 1975) were the first to report that the extrudate axis of a stratified structure in a side-by-side configuration deviates from that of the tube and forms an "extrudate exit angle". The observed extrudate bending occurs because of flow rearrangement in the extrudate due to the viscosity mismatch. Everage (1975) showed the dependence of the exit angle of a nylon/nylon system flowing in a tube on the interface shape. He displayed that extrudate bending occurs when the bicomponent stratified system is in a side-by-side configuration when it emerges from the die, the exit angle decreases as

encapsulation progresses and no extrudate bending occurs when the flow is in a side-by-side configuration.

Everage (1975) also studied the effect of the length of flow on the degree of encapsulation. He displayed that encapsulation is a very slow phenomenon and a very long die (L/D=120) is required for complete encapsulation to occur in the very viscous bicomponent polymeric system. Lee and White (1974), and Southern and Ballman (1975) have also studied the effect of the length of flow and they concluded that encapsulation increases with the residence time of the bicomponent system inside the die.

In his theoretical analysis Everage (1973, 1975) makes use of the "principle of minimum viscous dissipation" to prove that the encapsulated configuration with the more viscous fluid at the core is energetically preferred. The "principle" states that the interface shape and flow configuration must be such that the energy dissipation is minimized. The same idea was also used by MacLean (1973) and Williams (1975) in their theoretical analyses. No rigorous mathematical proof was presented but the experimentally observed occurrence of the sheath-core configuration seems to at least partly agree with the "principle". In Chapter 4 of this thesis, these ideas are used to show that encapsulation occurs when a viscosity mismatch is present in stratified flow through very long dies. A theoretical work by White and Lee (1975) based on Reynolds' lubrication theory predicts a small curvature of the interface but is far from predicting encapsulation.

Multilayer flat film extrusion with 3 and 5 layers was considered by Han and Shetty (1976) and reduction of the pressure gradient when the less viscous fluid was wetting the walls was observed. Han and Rao (1976) studied the wire coating process and observed the onset of interfacial instability when the shear stress and the viscosity ratio of the two components at the interface exceeded certain critical values. Schrenk et al (1978) and Schrenk and Alfrey (1978) reached similar conclusions for film flow. It seems (Han, 1981; Southern and Ballman,

1975) that the elasticity ratio plays an important role in the formation of rugged interface shapes in this type of instability.

Non-isothermal studies of stratified flows were also undertaken. Chin et al. (1984) presented a study of a two-layer flat film coextrusion process. The effects of the non-isothermal conditions on the interface position and the temperature profile were investigated but no encapsulation effects were considered. Sornberger et al. (1986, 1987) studied the non-isothermal stratified flow between parallel plates and through a flat die, a fish-tail die and a coat-hanger die. The results of their theoretical study are in good agreement with the experimental trends but encapsulation is ignored. Uhland (1977) numerically investigated the non-isothermal stratified bicomponent flow in circular dies and Basu (1981) the non-isothermal flow in wire coating coextrusion dies.

It can be seen that although experimental work has been done, very little work has been undertaken to study the purely 3-D interface shape change and the occurrence of the encapsulation phenomenon. The theoretical and numerical studies presented so far deal with 2-D flows and there is a vacuum in modelling the 3-D effects. This fact motivates the approach followed in this thesis which studied, in a fully 3-D manner, the flow mechanisms that lead to encapsulation.

Many attempts to shed light on the phenomena involved in coextrusion have been made through studying the stability of the stratified flow of two fluids. The most significant studies include those of Yih (1967) and Hickox (1971) who showed that in simple shear flows, viscosity differences alone are sufficient to cause instability of the stratified flow. Hooper and Boyd (1983) found that the effect of surface tension is always stabilizing which is not the case with density differences. Khan and Han (1977) considered the Poiseuille flow of two superposed viscoelastic fluids and found that the viscosity difference has a more dominant

effect than the elasticity difference. Waters (1983) showed that the stability of plane Couette flow of two superposed power-law fluids depends on the ratio of the power-law parameters.

Joseph et al. (1984) studied the bicomponent stratified pipe flow. Based on their linear stability analysis results, they concluded that the configuration with the more viscous fluid encapsulated by the less viscous fluid is not always stable. It seems that when the encapsulated more viscous fluid occupies most of the pipe the flow is stable while it is not stable when there is more of the less viscous fluid. The same flow configuration was studied by Wong and Jeng (1987) who found that the steady state flow can be unstable, depending on certain combinations of the values of physical parameters, to infinitesimal axisymmetric disturbances of large wavelengths, for any Reynolds number however small. Than et al (1987) studied the stability of plane Poiseuille flow of two immiscible liquids flowing in three layers with one of the fluids centrally located. They found that the flow with the high viscosity fluid centrally located was always stable while centrally located layers of less viscous fluid were always unstable.

Experimental evidence however (Southern and Ballman, 1973, 1975; Everage, 1975; also see Chapter 7), shows that steady-state conditions exist when the more viscous layer is located at the core and even when the less viscous layer is located at the core, provided that absolute symmetry exists (Han, 1981). This fact, combined with the potential error that may be introduced by the linearized stability analysis, justifies the steady-state analysis presented in Chapters 4 to 7 of this thesis.

The existence of the interface in stratified flows is a very complex feature for the mathematical modeling and simulation of the process. Using the Finite Element method, researchers were only recently able to account for the discontinuity of pressure and material properties across the interface. Mavridis et al. (1987), Mitsoulis (1986) and Mitsoulis and Heng (1987) used a continuous pressure approximation approach within each of the two phases and

accounted for the discontinuity across the interface by introducing double nodes at the interface (i.e. each pair of double nodes is assigned the same spatial coordinates and velocities but each node possesses different pressure). Dheur and Crochet (1987), Binding et al. (1987) used a discontinuous pressure representation where the pressure within each element is given by a first order degree polynomial and is discontinuous across interelement boundaries. Both approaches were used to simulate 2-dimensional flows successfully and provide a solid basis for the extension to the 3-D simulation of the interface evolution and die swell in stratified flows through dies with complex shapes. Recently Mitsoulis (1988) employed the lubrication approximation theory to study 2-D multilayer sheet flows but the method can only provide gross effects such as pressure or the general interface shape with no 3-D development.

The 3-D finite element method presented in Chapters 5 to 7 is capable of studying both encapsulated and side-by-side stratified flows and establishes the effects of viscosity ratio, flowrate ratio and geometric shape on the interface shape.

1.3 OBJECTIVES

The purpose of this thesis is to develop the mathematical and computational tools that enable the numerical study of three dimensional free surface extrusion and multilayer extrusion flows. The objective is to contribute to the fundamental understanding of both the microscale phenomena (visualization of the velocity field, calculation of the variation of polymer properties) and the macroscale phenomena (position and shape of the external and internal free surfaces, pressure profile) associated with the single or multilayer extrusion. This thesis also provides a numerical tool that could lead to improved process simulation, design and operation.

The finite element method is used because of its superb ability to handle complex geometric shapes and different material properties. Efficient finite element techniques are

presented that allow simulation of three dimensional free surface flows of Newtonian and shear thinning fluids. Advanced free surface handling techniques are introduced that treat the complex three dimensional free surface problem.

The effects of the three dimensional geometry, material properties, flow configuration, processing conditions and thermal policy are examined and modelling results are compared to available experimental data. In die extrusion flows, extrudate shape distortions and pronounced swelling are shown to result from geometric and thermal asymmetries. In bicomponent extrusion flows, the tendency of the less viscous fluid to encapsulate the more viscous fluid is established. The extrudate bending phenomenon in side-by-side flows is shown and the shape of the internal and external free surfaces are studied.

1.4 THESIS OUTLINE

Chapter 2: This chapter gives the mathematical background with the governing equations and boundary conditions. The finite element formulation and methodology for the simulation of three dimensional non- isothermal free surface flows is described in detail. The implications of the free surface update schemes and the related non-linear update strategies are also presented.

Chapter 3: The Isothermal and non-Isothermal flow and extrudate swelling behaviour of Newtonian fluids flowing through several typical three dimensional geometries is presented. The effect of geometry, processing conditions and thermal policy on the extrudate shape is demonstrated. The distortion and bending of the extrudate that results from asymmetric temperature or velocity profiles is displayed and explained.

Chapter 4: An optimization/finite element method combination to study bicomponent stratified flows in long dies is presented. The minimum viscous dissipation principle is employed to formulate the mathematical problem. The occurrence of encapsulation of the more viscous fluid by the less viscous fluid is demonstrated and the interface shape as determined by the viscosity ratio, flowrate ratio and geometric shape is studied. Break-up of the inner layer in dies of complex geometric shape is shown.

Chapter 5: The three dimensional analysis of bicomponent stratified flows in a sheath-core configuration is presented. The effects of viscosity and flowrate ratios, die geometry, initial conditions and layer configuration on the interface shape are examined. The complex extrudate swelling behaviour of the bicomponent system is studied and the effect of the above mentioned parameters on both the free surface and interface shapes is demonstrated.

Chapter 6: The three dimensional analysis of bicomponent stratified flows in a side-by-side configuration is presented. The tendency of the less viscous fluid to encapsulate the more viscous fluid is numerically established. The interface shape dependence on the viscous properties and processing conditions is examined for Carreau type fluids exhibiting viscosity function crossover. Extrudate bending and distortion is shown to occur depending on the viscous properties of the fluids and the die geometry.

Chapter 7: An experimental investigation of the interface shape evolution during the side-by-side flow in a square die is presented. A simulation of the experimental conditions is undertaken and the degree of qualitative and quantitative agreement between simulation and experiment is assessed and discussed.

Chapter 8: The most important results of this thesis are summarized in this chapter. Conclusions and recommendations for future work are presented.

CHAPTER 2

MATHEMATICAL MODELLING OF THREE DIMENSIONAL VISCOUS FREE SURFACE FLOWS

2.1 INTRODUCTION

The Galerkin/finite element method, the numerical tool used in this thesis to study the steady, viscous, three dimensional free surface flows, is presented in this chapter. The finite element method as an engineering tool has historically been in use in structural analysis long before the first study of free surface flows (Nickell et al, 1974) appeared. A number of standard texts provide the background and applications-oriented portraits of the method (Zienkiewicz, 1977; Huebner and Thornton, 1982; Dhatt and Touzot 1984; Crochet et al, 1984).

Since this thesis is oriented towards the study of three dimensional effects, the Galerkin/finite element formulation in the primitive variables (u-v-w-p-h-T) developed to study three dimensional, non-isothermal, free surface flows of Newtonian fluids is summarized in this chapter. The formulation for the more complex bicomponent flow studies is presented later in the corresponding chapters.

2.2 GOVERNING EQUATIONS AND BOUNDARY CONDITIONS

Polymer processes are generally modelled in the steady state using the assumptions that the flow is creeping, incompressible and with no body forces. The governing equations are the momentum, continuity and energy equations which in their dimensionless form are respectively:

$$\nabla \cdot \underline{\underline{\tau}} - \nabla P = \underline{0} \tag{2.1}$$

$$\nabla \cdot \underline{v} = 0 \tag{2.2}$$

$$Pe\, \underline{v} \cdot \nabla T = \nabla^2 T + Br\, \underline{\underline{\tau}} : \nabla \underline{v} \tag{2.3}$$

where $\underline{v}$ is the velocity vector.

The Newtonian constitutive relation for the extra stress tensor is:

$$\tau_{ij} = \mu\left(\frac{\partial v_i}{\partial x_j} + \frac{\partial v_j}{\partial x_i}\right) \tag{2.4}$$

and the Newtonian viscosity is of the form

$$\mu = \mu_w \exp(-\alpha T) \tag{2.5}$$

The dimensionless variables and groups are :

$$\begin{array}{lll} \underline{x} = \underline{x}'/L & \underline{v} = \underline{v}'/U & T = (T'-T'_w)/(T'_w-T'_\infty) \\ p = p'L/\mu'_w U & \underline{\underline{\tau}} = \underline{\underline{\tau}}'L/\mu'_w U & \\ \mu = \mu'/\mu'_w & \alpha = \alpha'(T'_w-T'_\infty) & \\ Pe = \rho CUL/k & Br = \mu'_w U^2/k(T'_w-T'_\infty) & Nu = hL/k \end{array} \tag{2.6}$$

and C, k, ρ, h are respectively the specific heat capacity, thermal conductivity, density of the melt and heat transfer coefficient between the extrudate and the ambient air. The scaling factors L (characteristic length), U (average velocity), μ_w (viscosity at T_w) are defined in each of the cases studied, T_w is the die wall temperature and T_∞ is the ambient temperature given in degrees Celsius. Pe, Br and Nu are the Peclet, Brinkman and Nusselt dimensionless numbers.

The exit flow problem described by equations (2.1-2.3) is an elliptic problem and becomes complete with the specification of boundary conditions. Figure 2.1 shows a schematic of a non-isothermal three dimensional free surface flow and the associated boundary conditions.

At solid boundaries the no-slip hypothesis is employed and temperature is also assigned at the die walls (planes AEHD, DHGC, Figure 2.1).

At the inflow planes (plane ABCD, Figure 2.1) the velocity and temperature profiles of a viscously heated fluid are assumed fully developed and assigned as boundary conditions. To obtain these fully developed profiles for a general three-dimensional geometry, the corresponding fully developed flow non-isothermal problem has to be solved numerically, since analytical expressions exist only for very simple geometric shapes (tubes, rectangles with uniform wall temperatures). For a general complex two-dimensional (in y-z) inlet die geometry (Figure 2.1) the following 2-D equations are solved:

$$\frac{\partial u}{\partial y}\left(\mu \frac{\partial u}{\partial y}\right) + \frac{\partial u}{\partial z}\left(\mu \frac{\partial u}{\partial z}\right) - \frac{\partial P}{\partial x} = 0 \tag{2.7}$$

and

$$\frac{\partial^2 T}{\partial y^2} + \frac{\partial^2 T}{\partial z^2} + Br\left[\left(\frac{\partial u}{\partial y}\right)^2 + \left(\frac{\partial u}{\partial z}\right)^2\right] = 0 \tag{2.8}$$

where u is the velocity component along the main flow direction (x-coordinate).

For polymer flows, because of the magnitude of the viscous effects, surface tension effects are negligible and the free surface (areas EILH and HLKG, Figure 2.1) is then considered a force-free surface

$$\underline{n} \cdot \underline{\underline{\sigma}} = 0 \tag{2.9}$$

where the velocity component normal to the free surface vanishes (kinematic condition)

$$\underline{n} \cdot \underline{v} = 0 \tag{2.10}$$

and the convection boundary condition is given as

$$\nabla T \cdot \underline{n} = -\frac{h}{k}(T - T_\infty) \tag{2.11}$$

where $\underline{\underline{\sigma}} = \underline{\underline{\tau}} - p\underline{\underline{I}}$ is the total stress tensor and $\underline{n}$ is the direction of the outward normal vector.

Far downstream (Plane IJKL, Figure 2.1) we impose zero traction, zero cross flows $v = w = 0$ and we impose the thermal boundary condition $\partial T/\partial x = 0$.

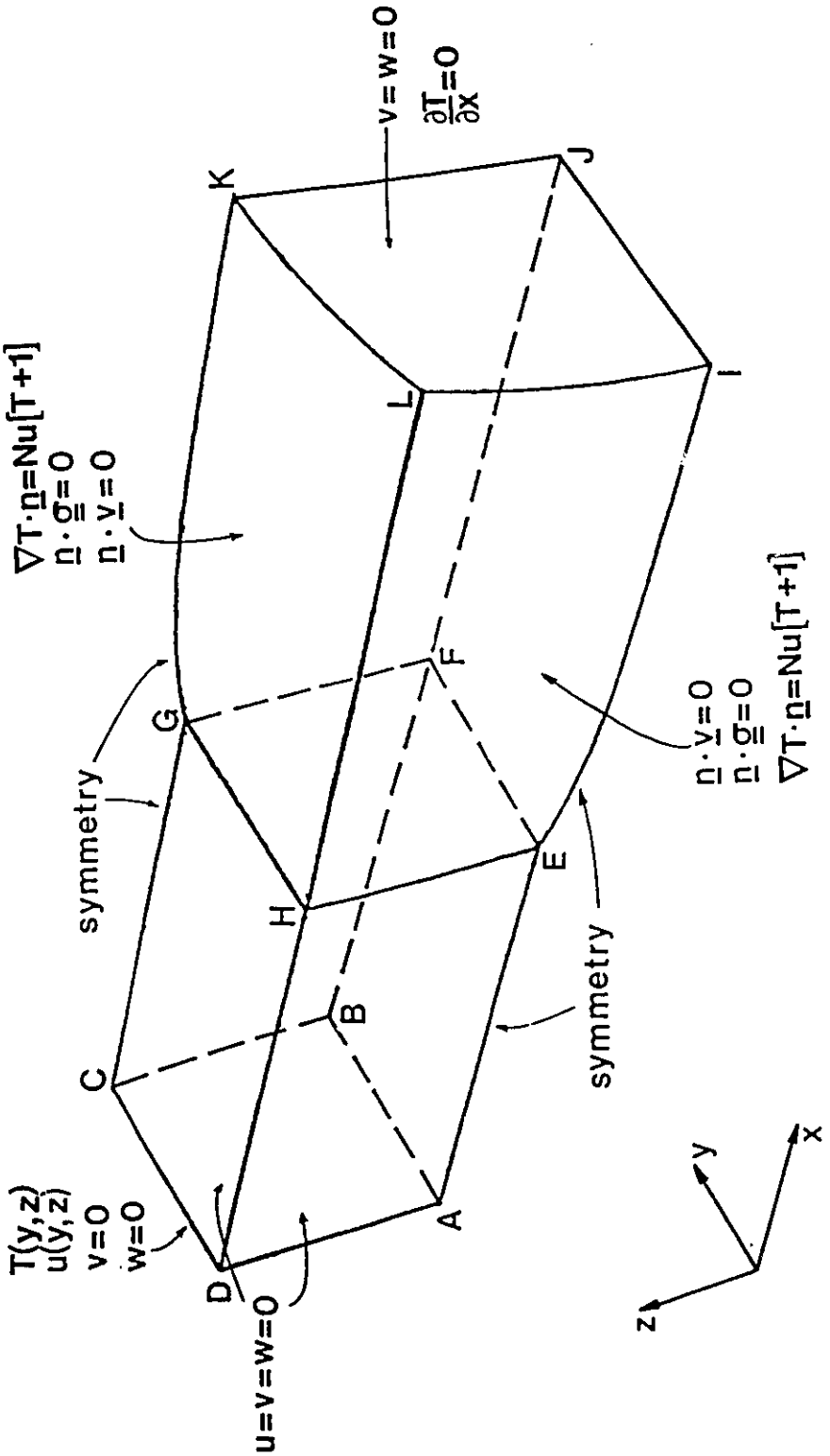

Figure 2.1 Schematic of three dimensional non-isothermal free surface flow and boundary conditions.

Symmetry conditions are imposed, where possible, to reduce the size of the three dimensional problem (planes AEIJFB and BFJKGC, Figure 2.1).

2.3 FINITE ELEMENT METHOD

2.3.1 Preliminaries

The finite element method divides the flow domain into a number of subdomains or finite elements as Figure 2.2 shows, and the field variables (velocities, pressures) as well as the spatial coordinates are then approximated with low order polynomials within each finite element.

Two types of three dimensional elements are used in this thesis for the discretization of the flow domain into finite elements (Figure 2.2), the 27-node brick and the 18-node triangular prism element (Figure 2.3), both belonging in the Lagrangian family. Within each element, velocity, pressure and temperature are approximated by:

$$v_j^{(e)} = \sum_i N^i(\xi, \eta, \zeta)\, v_j^i, \qquad j = 1, 2, 3 \tag{2.12}$$

$$p^{(e)} = \sum_i N_p^i(\xi, \eta, \zeta)\, p^i, \tag{2.13}$$

$$T^{(e)} = \sum_i N^i(\xi, \eta, \zeta)\, T^i \tag{2.14}$$

where v^i_j, p^i, T^i are nodal values and N^i, N^i_p are quadratic and linear interpolation (basis) functions respectively. The basis functions are defined within each element with respect to the local (ξ,η,ζ) coordinate system (Figure 2.3).

In order to get an accurate finite element solution, it has been found that pressure basis functions must be an order lower than the velocity and temperature approximation (Taylor and Hood, 1973; Huyakorn et al, 1978). In this chapter, linear basis functions (C^0–P^1) are used for the pressure approximation while quadratic basis functions (C^0–P^2) are used for

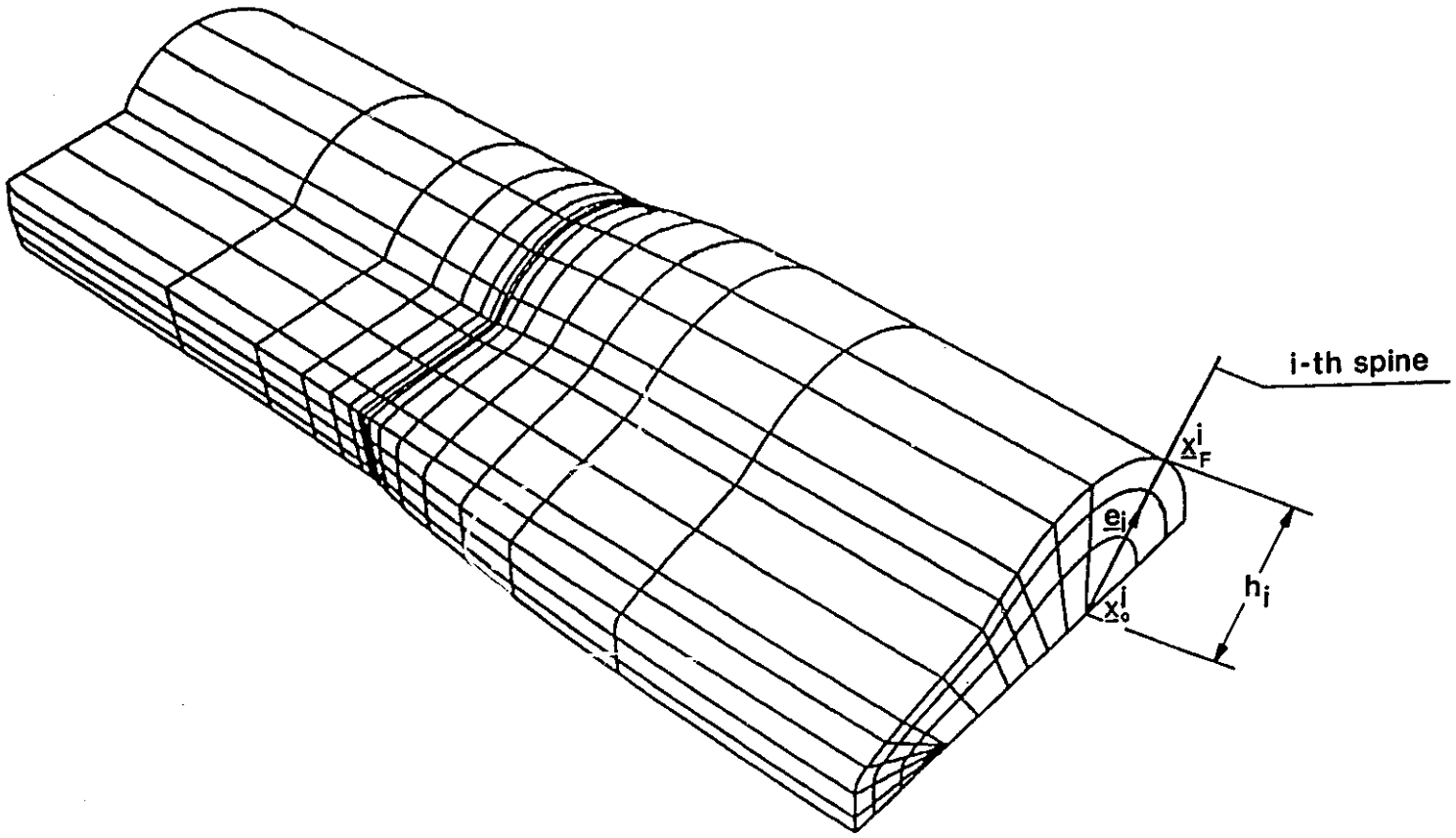

Figure 2.2 Perspective view of a three dimensional finite element grid; free surface parametrization with spines.

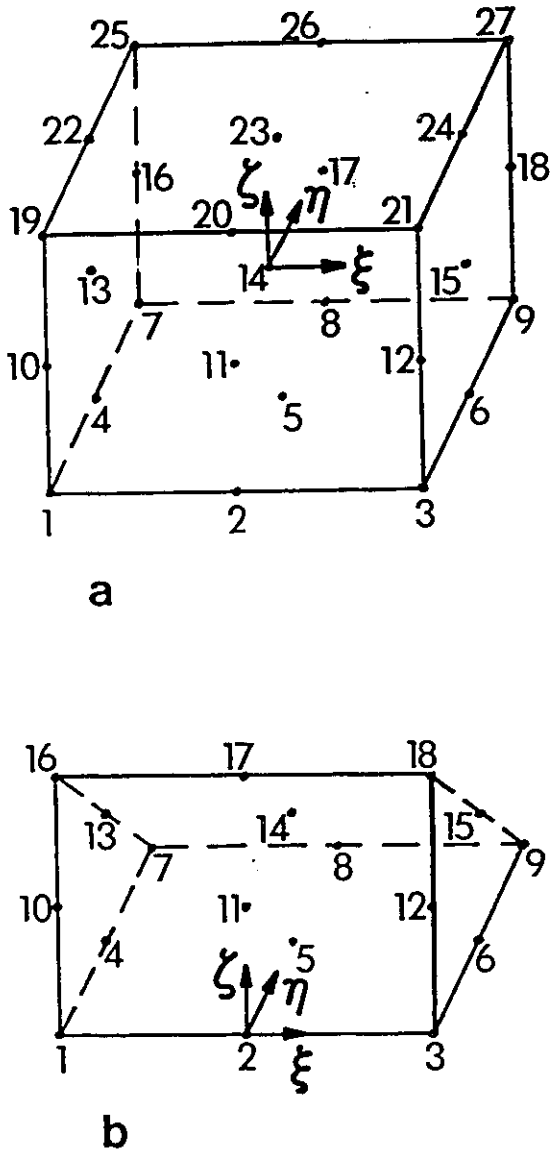

Figure 2.3 Parent three dimensional finite elements; a) 27-node brick and b) 18-node triangular prism.

velocity and temperature approximation. The shape functions for these elements are presented in Appendix A.

Complex geometries are handled through an isoparametric mapping of the deformed element onto the corresponding parent element of Figure 2.3. The Cartesian nodal coordinates $\underline{x}$ are approximated within each element as:

$$x_j^{(e)} = \sum_i N^i(\xi, \eta, \zeta)\, x_j^i, \qquad j = 1, 2, 3 \tag{2.15}$$

In the (u-v-w-p-h-T) formulation, the free surface parametrization, entering through the "h" parameters, is based on the idea of spines (see also paragraph 2.5.2) which are predefined straight lines in space (Kistler, 1984; Kistler and Scriven, 1983). The free surface node $\underline{x}^i_F$ is parametrized as the distance h^i along the i-th spine, Figures 2.2, 2.4a. Each spine is defined by a base point $\underline{x}^i_o$ and a unit vector $\underline{e}^i$.

The free surface nodes are then defined as

$$\underline{x}^i_F = \underline{x}^i_o + h^i \underline{e}^i \tag{2.16}$$

while other nodes along the same spine move in constant proportions. Throughout this thesis, spines are allowed to move on a y-z plane only (Figures 2.1 and 2.2)

If $\underline{x}^i_F$, $i = 1,2,3,\ldots,9$ are the nine nodes that define a part of the free surface as the face of a 27-node brick, the free surface is

$$\underline{x} = \sum_j \underline{x}^j_F N^j(\xi, \eta = 1, \zeta) \tag{2.17}$$

where the 27-node element is mapped isoparametrically onto the parent ξ, η, ζ cube by the triquadratic basis functions $N_i(\xi, \eta, \zeta)$ and $\eta = 1$ is the face of the parent element that corresponds to the free surface.

The two types of elements are used simultaneously to simplify the grid generation and the free surface parametrization in complex geometric shapes. With respect to Figure 2.2, where curved boundaries or corners are present many spines originate radially from a single point toward the boundary and the 18-node elements are employed to form the first layer of

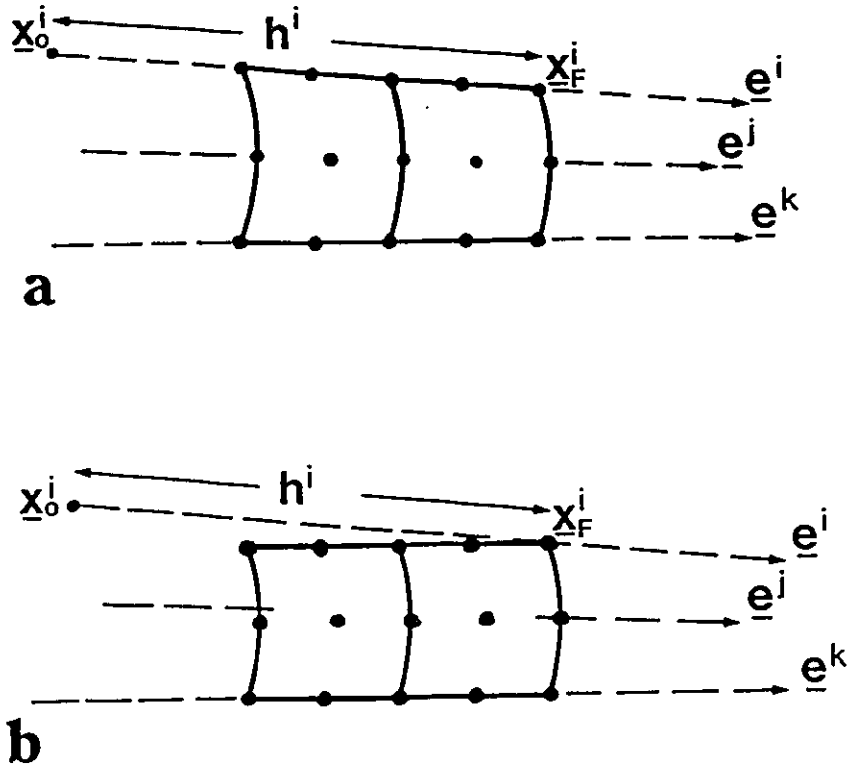

Figure 2.4 Definition of spines; a) spines form the element sides, b) only the free surface node moves on the spine direction.

elements to which layers of 27-node bricks are connected. Simple boundary shapes require only 27-node bricks. The density of the grid along the downstream direction has an impact on the accuracy of the calculated swelling ratio and also poses a limit on the size of the problem.

2.3.2 Galerkin/Finite Element Formulation

The system of governing equations 2.1-2.3 together with the proper boundary conditions is solved by the Galerkin/finite element method. The presence of free surfaces, the locations of which are not known a priori, renders the system non-linear and an iterative procedure is required.

The set of equations 2.1-2.3 are discretized and application of the standard Galerkin procedure (Huebner and Thornton, 1982) yields

$$\int_{V^{(e)}} \{\nabla \cdot \underline{\underline{g}}\} N^i \, dV = 0 \tag{2.18}$$

$$\int_{V^{(e)}} \{\nabla \cdot \underline{v}\} N_p^i \, dV = 0 \tag{2.19}$$

$$\int_{V^{(e)}} \{Pe(\underline{v} \cdot \nabla T) - \nabla^2 T - Br \, \underline{\underline{\tau}} : \nabla \underline{v}\} N^i \, dV = 0 \tag{2.20}$$

where $\underline{\underline{g}} = \underline{\underline{\tau}} - p\underline{\underline{I}}$ is the total stress tensor.

After the divergence theorem is applied and the velocity components are introduced, the weighted residual equations with no surface traction can be finally written in the discretized form as:

$$R_x^i = \int_{-1}^{1}\int_{-1}^{1}\int_{-1}^{1} \{(-P + 2\mu u_x)N_x^i + \mu(u_y + v_x)N_y^i + \mu(u_z + w_x)N_z^i\}|J| \, d\xi d\eta d\zeta \tag{2.21}$$

$$R_y^i = \int_{-1}^{1}\int_{-1}^{1}\int_{-1}^{1} \{\mu(u_y + v_x)N_x^i + (-P + 2\mu v_y)N_y^i + \mu(v_z + w_y)N_z^i\}|J| \, d\xi d\eta d\zeta \tag{2.22}$$

$$R_z^i = \int_{-1}^{1}\int_{-1}^{1}\int_{-1}^{1} \{\mu(u_z + w_x)N_x^i + \mu(v_z + w_y)N_y^i + (-P + 2\mu w_z)N_z^i\}|J|\, d\xi d\eta d\zeta \tag{2.23}$$

$$R_c^i = \int_{-1}^{1}\int_{-1}^{1}\int_{-1}^{1} \{u_x + v_y + w_z\}N_p^i |J|\, d\xi d\eta d\zeta \tag{2.24}$$

$$R_T^i = \int_{-1}^{1}\int_{-1}^{1}\int_{-1}^{1} \Big\{ Pe(u T_x + v T_y + w T_z) + (T_x N_x^i + T_y N_y^i + T_z N_z^i)$$

$$- 2Br\mu(u_x^2 + v_y^2 + w_z^2) - Br\mu[(u_y + v_x)^2 + (u_z + w_x)^2 + (v_z + w_y)^2] \Big\}$$

$$\cdot N^i |J|\, d\xi d\eta d\zeta - \int_{-1}^{1}\int_{-1}^{1} Nu(T+1)N^i |J^*|\, d\xi d\zeta, \quad \eta = 1 \tag{2.25}$$

The weighted residual of the kinematic condition applying at the free surface (eqn 2.10) becomes

$$R_k^i = \int_{-1}^{1}\int_{-1}^{1} \{\underline{n} \cdot \underline{v}\}N^i |J^*|\, d\xi d\zeta, \quad \eta = 1 \tag{2.26}$$

The surface integral of equation (2.25) expresses the convection boundary condition and $|J|,|J^*|$ are the Jacobian of the isoparametric transformation (x,y,z)–(ξ,η,ζ) for the volume and surface integrals respectively, where

$$J = \begin{Bmatrix} x_\xi & y_\xi & z_\xi \\ x_\eta & y_\eta & z_\eta \\ x_\zeta & y_\zeta & z_\zeta \end{Bmatrix} \tag{2.27}$$

The vector $\underline{n}$ is the outward normal to the free surface and in the three dimensional frame can be found (Zienkiewicz, 1977) as a vector product of any two vectors tangent to the free surface (at $\eta = 1$). Thus

$$\underline{n} = \begin{Bmatrix} x_\xi \\ y_\xi \\ z_\xi \end{Bmatrix} \times \begin{Bmatrix} x_\zeta \\ y_\zeta \\ z_\zeta \end{Bmatrix} = \begin{Bmatrix} y_\xi z_\zeta - y_\zeta z_\xi \\ x_\zeta z_\xi - x_\xi z_\zeta \\ x_\xi y_\zeta - x_\zeta y_\xi \end{Bmatrix} \tag{2.28}$$

and

$$|J^*| = (n_1^2 + n_2^2 + n_3^2)^{1/2} \tag{2.29}$$

The Galerkin/finite element procedure finally reduces the set of differential equations into a set of algebraic equations:

$$\underline{R}(\underline{X}) = \underline{0} \tag{2.30}$$

where $\underline{R}$ is the vector of residuals

$$\underline{R}^T = [\underline{R}^T_x, \underline{R}^T_y, \underline{R}^T_z, \underline{R}^T_c, \underline{R}^T_k, \underline{R}^T_T] \tag{2.31}$$

and $\underline{X}$ the vector of unknowns

$$\underline{X} = [\underline{v}^T, \underline{P}^T, \underline{h}^T, \underline{T}^T]. \tag{2.32}$$

The spine approach offers the advantage that the solution of eqn. (2.30) yields the velocity, pressure, temperature and the free surface location simultaneously.

The Newton-Raphson iteration is used to solve $\underline{R}(X) = 0$ as:

$$\underline{X}^{(k+1)} = \underline{X}^{(k)} + \Delta\underline{X}^{(k)} \tag{2.33}$$

$$\underline{\underline{J}}(\underline{X}^{(k)})\, \Delta\underline{X}^{(k)} = -\underline{R}(\underline{X}^{(k)}) \tag{2.34}$$

where $\underline{\underline{J}} = \partial\underline{R}/\partial\underline{X}$ is the Jacobian matrix of the algebraic system (2.30). Detailed derivations of the finite element equations and the analytic Jacobian matrix are given in Appendix A. Typically, the Newton-Raphson iteration exhibits quadratic convergence. Insisting on quadratic convergence, by imposing a strict convergence criterion, proved to be a good test of the correctness of the Jacobian matrix. The Jacobian is very complicated due to the presence of the free surface derivatives and a central finite difference scheme was used (Mavridis, 1988) to check the Jacobian entries.

The implications of the free surface handling scheme and the non-linear iteration strategies that it requires are discussed in detail in section 2.5.

2.4 SHEAR-THINNING CONSTITUTIVE RELATION

The viscosity of polymer melts is generally non-Newtonian, exhibiting a shear-thinning character. An empirical equation that is quite successful on its non-Newtonian viscosity predictions is the Carreau viscosity model (Carreau, 1968)

$$\mu(\dot{\gamma}) = (\mu_0-\mu_\infty)\,[1+(\lambda\,\dot{\gamma})^2]^{(n-1)/2} \tag{2.35}$$

where n, μ_0, μ_∞, λ are material properties of the fluid and $\dot{\gamma}$ is the square root of one half the second invariant of the rate of strain tensor

$$\dot{\gamma}=\sqrt{1/2II_{\dot{\gamma}}} \tag{2.36}$$

If viscosity is made dimensionless with respect to the zero shear viscosity $\mu=\mu'/\mu_0$, then the viscous stress terms in the momentum residuals (equations 2.21-2.23) are simply multiplied by μ. There are additional terms multiplying the Newtonian viscous stress terms entering in the Jacobian matrix because of the dependency of μ on v,u,w and h.

The derivatives of viscosity with respect to u,v,w and h are easily evaluated using the chain rule and the isoparametric map and they yield:

$$\frac{\partial\mu}{\partial u^j} = \frac{\partial\mu}{\partial\dot{\gamma}}\frac{\partial\dot{\gamma}}{\partial u^j} = (\mu_o-\mu_\infty)(n-1)\lambda^2\,\dot{\gamma}[1-(\lambda\dot{\gamma})^2)^{(n-3)/2}\,\frac{\partial\dot{\gamma}}{\partial u^j} \tag{2.37}$$

$$\frac{\partial\mu}{\partial v^j} = \frac{\partial\mu}{\partial\dot{\gamma}}\frac{\partial\dot{\gamma}}{\partial v^j} = (\mu_o-\mu_\infty)(n-1)\lambda^2\,\dot{\gamma}[1-(\lambda\dot{\gamma})^2)^{(n-3)/2}\,\frac{\partial\dot{\gamma}}{\partial v^j} \tag{2.38}$$

$$\frac{\partial\mu}{\partial w^j} = \frac{\partial\mu}{\partial\dot{\gamma}}\frac{\partial\dot{\gamma}}{\partial w^j} = (\mu_o-\mu_\infty)(n-1)\lambda^2\,\dot{\gamma}[1-(\lambda\dot{\gamma})^2)^{(n-3)/2}\,\frac{\partial\dot{\gamma}}{\partial w^j} \tag{2.39}$$

$$\frac{\partial\mu}{\partial h^j} = \frac{\partial\mu}{\partial\dot{\gamma}}\frac{\partial\dot{\gamma}}{\partial h^j} = (\mu_o-\mu_\infty)(n-1)\lambda^2\,\dot{\gamma}[1-(\lambda\dot{\gamma})^2)^{(n-3)/2}\,\frac{\partial\dot{\gamma}}{\partial h^j} \tag{2.40}$$

The second invariant of the rate-of-strain tensor for three dimensional flow is:

$$|\dot{\gamma}| = [2u_x^2 + 2v_y^2 + 2w_z^2 + (u_y+v_x)^2 + (u_z+w_x)^2 + (v_z+w_y)^2]^{1/2} \tag{2.41}$$

and its derivatives w.r.t u,v,w and h are

$$\frac{\partial \dot{\gamma}}{\partial u^j} = [2u_x N_x^i + (u_y + v_x)N_y^i + (u_z + w_x)N_z^i] \frac{1}{\dot{\gamma}} \tag{2.42}$$

$$\frac{\partial \dot{\gamma}}{\partial v^j} = [(u_y + v_x)N_x^i + 2v_y N_y^i + (v_z + w_y)N_z^i] \frac{1}{\dot{\gamma}} \tag{2.43}$$

$$\frac{\partial \dot{\gamma}}{\partial w^j} = [(u_z + w_x)N_x^i + (v_z + w_y)N_y^i + 2w_z N_z^i] \frac{1}{\dot{\gamma}} \tag{2.44}$$

$$\frac{\partial \dot{\gamma}}{\partial h^j} = \left[2u_x \frac{\partial u_x}{\partial h^j} + 2\, v_y \frac{\partial v_y}{\partial h^j} + 2\, w_z \frac{\partial w_z}{\partial h^j} + (u_y + v_x)\left(\frac{\partial u_y}{\partial h^j} + \frac{\partial v_x}{\partial h^j} \right) \right.$$

$$\left. + (u_z + w_x)\left(\frac{\partial u_z}{\partial h^j} + \frac{\partial w_x}{\partial h^j} \right) + (v_z + w_y)\left(\frac{\partial v_z}{\partial h^j} + \frac{\partial w_y}{\partial h^j} \right) \right] \frac{1}{\dot{\gamma}} \tag{2.45}$$

2.5 FREE SURFACE UPDATE

Free surface flows are non-linear problems because the position of the free surface is unknown a priori and its calculation has to be included in the numerical procedure. The free surface update scheme has an impact on the number of non-linear iterations required because it implicitly dictates the non-linear iteration policy. This section summarizes the free surface handling techniques used in this thesis. These are the pathline method approach (Tran -Cong and Phan-Thien, 1988; section 2.5.1), the spine method (Kistler, 1984; section 2.5.2) and a hybrid of the two (section 2.5.3).

2.5.1 Pathline Method

The fact that the free surface is a material surface and each material point on it follows a pathline, provides an alternative technique for the free surface construction that has been used by many workers (Nickell et al., 1974; Reddy and Tanner, 1978; Crochet and

Keunings, 1980; Mavridis et al., 1986; Mavridis, 1988) in two dimensional approximations and lately three dimensional approximations (Tran-Cong and Phan-Thien, 1988).

The pathline method updates the free surface by solving

$$\frac{u}{dx} = \frac{v}{dy} = \frac{w}{dz} \tag{2.46}$$

for all pathlines on the free surface.

This method requires a knowledge of the velocity field and decouples the free surface calculation from the calculation of the field variables through a Picard type iteration. The problem can then be reduced to a (u-v-w-p-T) formulation with the free surface calculated separately after every non-linear iteration, based on the latest velocity information where we calculate

$$\Delta y = \int v \frac{dx}{u} \qquad \text{and} \qquad \Delta z = \int w \frac{dx}{u} \tag{2.47}$$

with the x-nodal coordinates fixed because of the finite element grid construction.

The calculation of pathlines is cheap in terms of CPU cost because it does not involve the solution of large systems of simultaneous equations. However, the convergence rate of the decoupled technique is slow because of the Picard-like iteration scheme (linear convergence rate) and the procedure generally needs a large number of iterations (about 15 non-linear iterations) to achieve convergence.

The integrations of equations (2.47) are performed at the element level through the isoparametric mapping using Gaussian quadrature.

In many cases, when the initial starting conditions are not within the radius of convergence of the Newton-Raphson iteration, the pathline approach is used to provide start-up approximations. Then, the Newton-Raphson iteration is employed to accelerate the convergence to the solution.

2.5.2 Spine Method

As has already been discussed (paragraph 2.3), the spines are predefined straight lines in space and also form the interelement boundaries in each y-z cross section (Figures 2.2, 2.4a).

The main advantage of the spine method over the pathline method is that the calculation of the field unknowns and the free surface parameters can be performed simultaneously (u-v-w-p-h-T formulation) and the Newton-Raphson iteration scheme can be implemented to reduce the number of the non-linear iterations required. This is very important because of the large size of the three dimensional problems and the high computational cost that is involved.

However, in highly nonlinear cases the Newton-Raphson method cannot always converge and a strategy where we start with the pathline approach and then switch to the spine method using the same grid has proved effective in some cases.

Although the application of the spine method is quite straightforward in parametrizing two dimensional free surface flows, in the formulation of three dimensional free surface flows some difficulties arise. The three dimensional free surface formulation is faced with the movement of the free surface in three dimensions and with the existence of sharp corners in the die geometries. When material is extruded from geometries where sharp corners are present and there are no surface tension effects, the extrudate tends to form edges (Tran-Cong and Phan-Thien, 1988; see also Chapters 3, 5, 6) corresponding to the die corners. The material redistributes near the region of the corners and the location of the corner point in the extrudate poses a numerical problem for the spine approach with quadratic approximation of the free surface. Because of the three dimensional movement of the free surface, the corner point is not very clearly defined unless it lies on a spine. This is because the spines, as used in this analysis, have a predefined, fixed orientation in space and consequently cannot follow the

path of the corner point. Also, the spine method with quadratic approximation of the free surface does not guarantee continuity of the free surface shape across interelement boundaries. The pathline method, on the other hand, is capable of defining the corner point location since it simply constructs the path of the corner material point but then convergence is slow.

To overcome these difficulties, a combination of the two methods was developed in a hybrid spine/pathline approach.

2.5.3 Hybrid Spine/Pathline Method

The spine method was implemented so that the spines no longer form the element sides (Figure 2.4b), but rather only the free surface nodes are allowed to move along the spine. Then, after the k-th Newton-Raphson iteration, the pathline approach is used to update the orientation of spines and their new direction is calculated as follows (see also Figure 2.5).

The pathlines of the free surface are constructed, and the solution of equation (2.46) defines a new vector of free-surface coordinates $\underline{x}_p$.

Instead of updating the free surface as

$$\underline{x}^{k+1} = \underline{x}_p \tag{2.48}$$

which is the pure pathline method, the corresponding free-surface node is allowed to run along a spine which is defined as the line which connects the $\underline{x}^k$ and $\underline{x}_p$ points. Thus, after every non-linear iteration, a new base point and orientation of each spine is defined, based on the information given by the pathline construction of the free surface (Figure 2.6). The values of the h parameters are then reset accordingly and the next Newton-Raphson non-linear iteration is performed.

This procedure forces the free surface nodes toward the direction which the pathline method predicts but we are still able to solve for the whole set of unknowns (u,v,w,p,h,T)

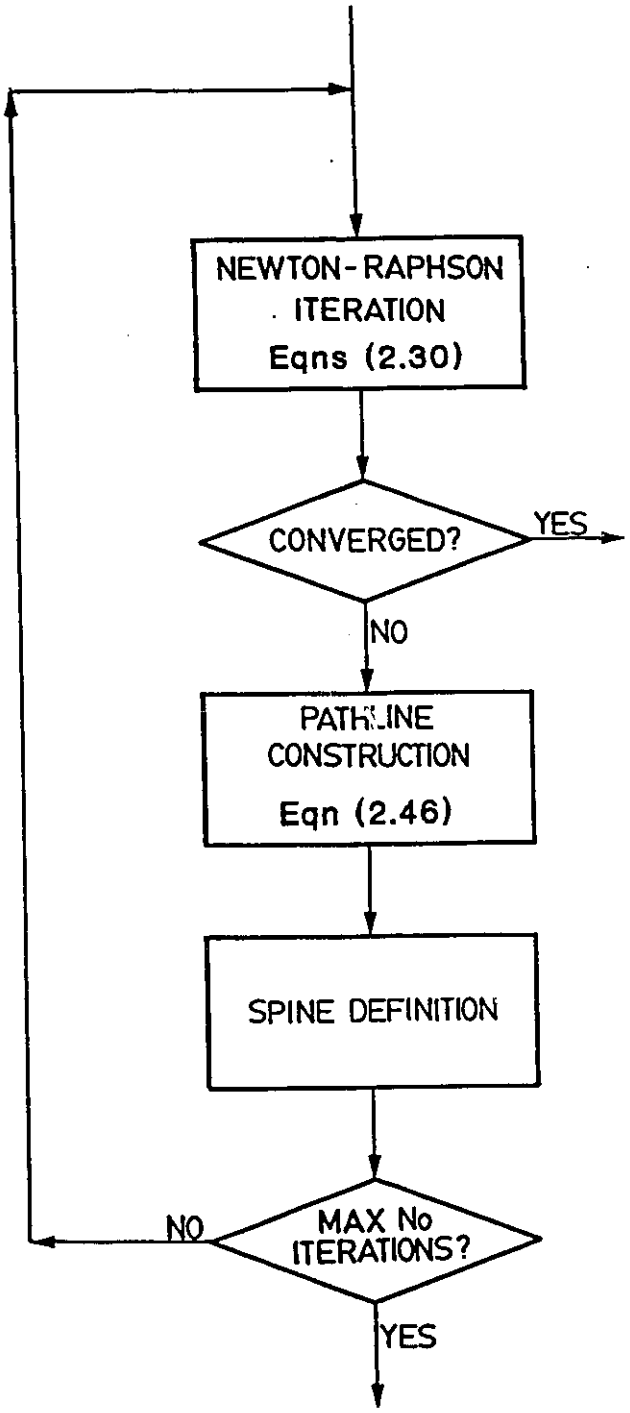

Figure 2.5 Schematic of the hybrid spine/pathline approach procedure.

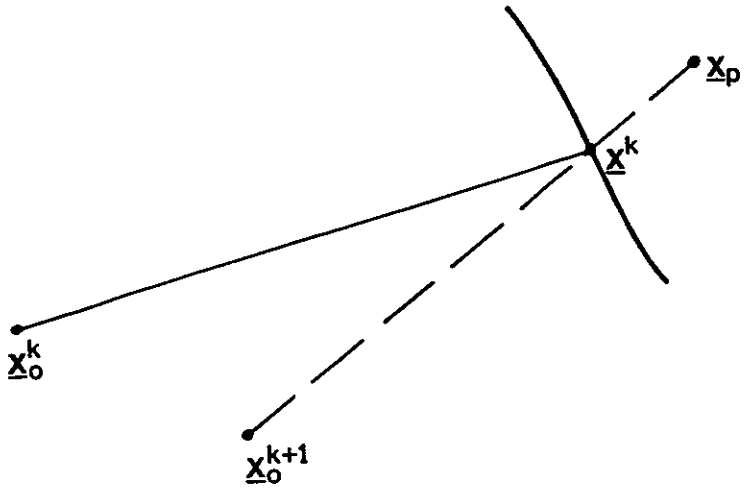

Figure 2.6 Schematic of the spine construction in the hybrid spine/pathline method.

simultaneously using the Newton-Raphson iteration. This procedure required 6 fewer non-linear iterations than the pure pathline method for the problems used (9 total non-linear iterations compared to 15 required by the pure pathline approach) to meet the convergence criteria.

Since the hybrid spine/pathline approach is based on the Newton-Raphson iteration it suffers from the same convergence difficulties of the method. Newton-Raphson has a small radius of convergence, and in highly non-linear cases some start-up iterations with the pathline method alone are required.

2.6 NUMERICAL CONSIDERATIONS

At each non-linear iteration the resulting linear system of equations (2.30) is solved with the frontal solver of Taylor and Hughes (1981). The original version of the solver was slightly modified to increase vectorization and optimize I/O operations with much improved performance for vector computers (see Appendix C).

The three dimensional analysis gives rise to large systems of equations because of the high number of unknowns involved. The computational cost depends on storage requirements, construction and assembly of the element-level Jacobian matrices, and solution of the assembled matrix problem. The most critical parameters affecting the CPU time requirements is the frontwidth which is tied to the y-z density of the grid, and the total number of equations. A compromise between accuracy and cost must be done because of the large size of the three dimensional problems.

Due to the large scale of the three dimensional problems use of vector processing computers is essential. In this thesis most of the production runs were executed on the CRAY-X/MP 2/4 at the University of Toronto as well as on an FPS-264 at McMaster University.

Vectorization of the codes leads to very favorable performances. Storage requirements are high at the order of 1 million words and out-of-core storage has been extensively used.

The Newton-Raphson iteration is employed, where possible, since it minimizes the number of iterations required for convergence. The Jacobian was constructed using analytical derivatives of the finite element equations in all cases.

Tolerances are set so that the maximum relative update of all the calculated variables (velocities, pressure, temperature, free surface coordinates) is less than 10^{-2} for convergence, unless otherwise noted.

In all cases, initial estimates for the velocity and temperature fields are obtained by solving the corresponding isothermal Newtonian case with the extrudate having the shape of the die. Once these initial estimates are obtained, the non-linear procedure is initiated. This policy leads to convergence problems for the Newton-Raphson iteration when the problem is highly non-linear. No convergence difficulties occurred when the pathline free surface update was used.

In all cases the upstream profile is assigned as the fully developed, one dimensional flow with viscous heating. The Galerkin formulation over the same two-dimensional grid that was assigned to the inlet of the three-dimensional solution was used for the input profile calculation.

In all cases studied in this thesis, Reynolds Number was always less than 10^{-2} which is typical of polymer processing flows.

CHAPTER 3

THREE DIMENSIONAL ANALYSIS OF EXTRUDATE SWELLING

3.1 INTRODUCTION

The term "extrudate swell" is the term used to describe the increase of the diameter of a liquid jet as it emerges from an orifice, die or duct. It is of importance in the polymer processing industry (films and pipes, coatings, profiles) since the extrusion of viscoelastic materials like polymer melts involves high extrudate swelling which may have an impact on product quality.

Experience and intuition are still major factors in the design of process equipment especially where complex three-dimensional geometries are involved (profile extrusion) and some typical problems and examples in that direction are discussed by Schenkel (1966) and Tadmor and Gogos (1979).

The swelling phenomenon is not limited to viscoelastic fluids but it is known that Newtonian fluids exhibit swell at very low Reynolds Numbers ($Re < 10$) and the experimentally observed swelling for axisymmetric geometry at zero Reynolds number was about 13.5% (Batchelor et al., 1973).

The numerical simulation of the phenomenon has been an active research area for the past 15 years and a brief review of numerical investigations of the swelling phenomenon are reported in section 1.2.1. Although many polymer processing operations involve the extrusion of melts out of complex geometries, 3-D simulation has lagged behind mainly because of the complexity and the large scale of the numerical problem. Serious viscoelastic model deficiencies also limit progress in the area.

Studies on the isothermal extrudate swelling out of dies with square, triangular and rectangular cross-section have been recently presented (Tran-Cong and Phan-Thien, 1988, Boundary Element method; Shiojima and Shimazaki, 1987, Finite Element method). An investigation of isothermal and non-isothermal extrusion is presented in this Chapter for a number of different die geometric shapes. The u-v-w-P-h-T formulation presented in Chapter 2 is used to study the effects of the 3-D geometry, imposed non-isothermal conditions and viscous heating due to viscous dissipation. Important 3-D effects such as extrudate bending, layer thickness variation and extrudate distortion because of temperature gradients inside the die are reported. Extrudate bending in isothermal flows due to asymmetry of the die shape is numerically shown and experimentally verified.

3.2 EXTRUDATE SWELLING BEHAVIOUR OF ISOTHERMAL NEWTONIAN FLOWS

This section studies the isothermal free surface flow of Newtonian creeping jets as those emerge out of several typical 3-D die geometries. A schematic of the flow with the boundary conditions is given in Figure 3.1.

The governing equations, boundary conditions and the mathematical formulation are discussed in Chapter 2 for the more general case of non- isothermal flows and are not repeated here. In this section a Galerkin/finite element u-v-w-p-h formulation with the spine free surface representation is used. The formulation follows that of Chapter 2 and Appendix A but there are no contributions of the energy equation (pure isothermal flow).

Because of the nonexistence of a profound reference point in some die shapes, the swelling ratio is always defined as

$$\text{swelling ratio} = (h^i_{final} - h^i_{initial})/(h^i_{initial})$$

along the i-th spine.

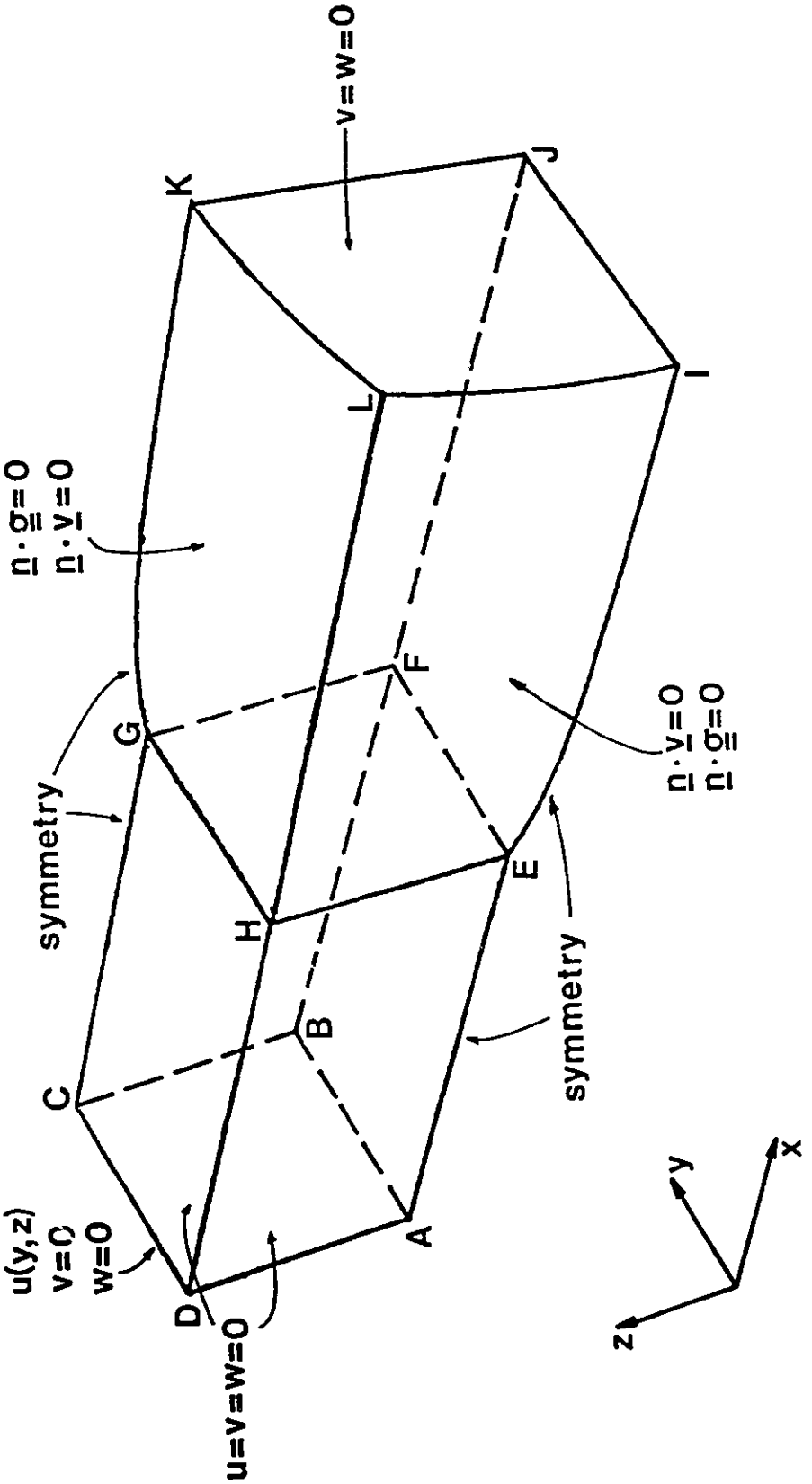

Figure 3.1 Emergence of a three-dimensional jet and boundary conditions.

3.2.1 Numerical Considerations

Although the constitutive equation of the Newtonian fluid is linear, the existence of the free surface renders the problem nonlinear since its shape is not known a priori and must be solved for. An iterative scheme is required and in this part the Newton-Raphson iteration is used since the spine approach for the free surface parametrization allows for the simultaneous solution of the full set of unknowns (for details see section 2.5.2).

The Jacobian for the Newton-Raphson iteration is calculated using analytical derivatives of the finite element equations (Appendix A).

The Newton-Raphson scheme converges with a quadratic rate of convergence normally within four to six iterations for the problems studied here. The first iteration, with a fixed free surface, is performed to obtain initial estimates of the velocities and pressure and does not enter the iteration count. The initial shape of the free surface is given as that of the die exit in all problems. The method is relatively robust since convergence was always attained for the problems investigated but fewer iterations may have been needed if a better estimate of the extrudate shape was supplied. Termination criterion is that the maximum relative update of all the calculated variables be less than 10^{-6}.

The resulting system of simultaneous equations at each iteration was on the order of 8,000-17,000 equations and was solved with a frontal solver by Taylor and Hughes (1981). Frontwidths were on the order of 400-750 and depend on the (y-z) density of the grid.

Details on the size of the problems with respect to the number of elements, number of nodes, number of variables and the total CPU times are given in Table 3.1. The use of a highly vectorized solver may lead to significant reduction of the CPU time requirements since over 70% of the total CPU time was spent in the frontal solver routine for all the problems dealt with.

The density of the grid along the downstream direction has an impact on the accuracy of the calculated swelling ratio and determines the size of the problem. The grid density along the downstream direction used in all problems dealt with in this section is shown in Figure 2.2 and consists of 15 "bands" of three dimensional elements. The corresponding 31 divisions are

$$x = 0.0, 1.0, 2.0, 2.5, 3.0, 3.25, 3.5, 3.65, 3.8, 3.9, 4.0$$
$$4.05, 4.1, 4.125, 4.15, 4.175, 4.2, 4.25, 4.3, 4.4, 4.5$$
$$4.65, 4.8, 5.0, 5.2, 5.45, 5.7, 6.2, 6.7, 7.7, 8.7$$

and the jet emerges from the $x = 4.15$ division in all cases.

Table 3.1 Size of the Isothermal Free Surface Problems

Problem	Elements	Nodes	Unknowns	Frontwidth	Iterations	CPU time*
Circular	480	3,999	11,120	522	4	680
Square	720	5,859	16,500	726	5	1,150
4:1 Rectangle	495	4,340	11,885	550	6	3,550**
Triangle	405	3,286	9,068	443	5	387
Bow-Tie	660	5,673	15,830	701	7	1,400

* CPU seconds on the CRAY-XMP 2/2, University of Toronto Center for Large- Scale Computation

** CPU seconds on the FPS-264, McMaster University

3.2.2 Cylindrical Die

The 3-D finite element implementation is assessed by comparing the predicted swelling ratios against experimental and 2-D theoretical predictions. The flow out of a circular die, which can also be studied in its axisymmetric version, is considered. The problem is solved

as fully three dimensional and the calculated swelling ratio with the 3-D code is 13.5%. This result establishes the validity of the approach since it is in full agreement with corresponding experimental and theoretical predictions (Batchelor et al. (1973), Gear et al. (1983) and Tanner (1985)).

3.2.3 Square Die

The extrusion of a Newtonian fluid from a square die is investigated. The shape of the die renders the problem three dimensional and due to symmetry only one quarter of the flow domain is considered.

A perspective view of the final three dimensional grid is shown in Figure 3.2. Because of the die geometric characteristics, the swelling of the material is not uniform and a maximum swell of 18.41% at the planes of symmetry with a minimum swell of 2.9% at the corner occurs (Figure 3.3). These results were predicted for a mesh of 720 elements, 5,859 nodes and 16,500 unknowns. For a less dense mesh of 480 elements, 3,999 nodes and 11,120 unknowns, a maximum swell of 18.9% and a minimum swell of 2.99% are predicted which are within 3% of the more dense grid predictions. The boundary element study by Tran-Cong and Phan-Thien (1988), predicts a lower swell (18% compared to 18.4%) at the flat regions but a higher swell (3.4% compared to 2.9%) at the corners.

The pressure and downstream velocity distribution is shown in Figures 3.4-3.6 along the centerline, along the corner points and along the center of the flat face (symmetry plane) for the square die problem. No acceleration of the centerline fluid is predicted (Figure 3.4) in contrast to the prediction of Bush and Phan-Thien (1985). The fluid at the centerline flows with constant velocity in the region of fully developed flow until it reaches the region of the die exit and then it monotonically decelerates to the plug flow value. The pressure distribution along the center of the face exhibits the well known (Caswell and Viriyayuthakorn

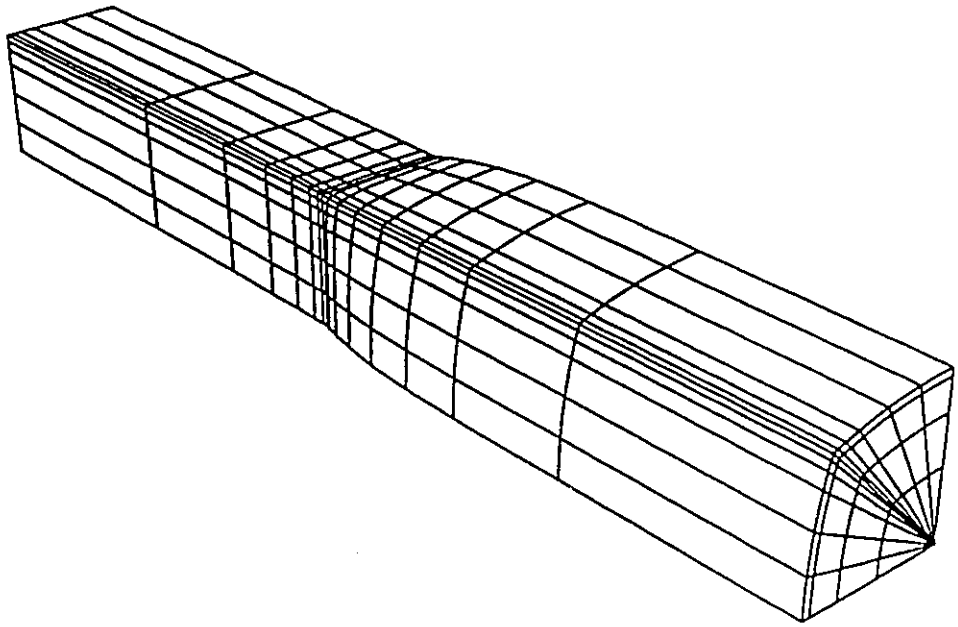

Figure 3.2 Perspective view of the three-dimensional extrudate swell from a square die.

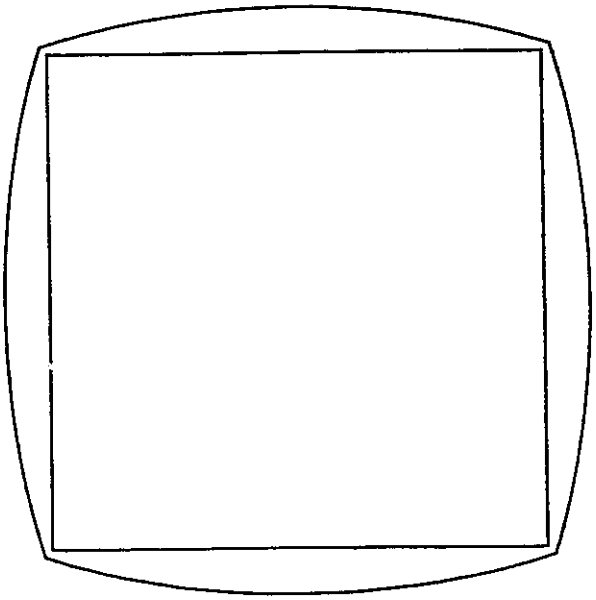

a

Spine	Swelling Ratio
1	18.41
2	18.11
3	17.21
4	15.81
5	13.88
6	11.57
7	8.91
8	7.48
9	6.02
10	5.12
11	4.20
12	3.57
13	2.90
14–25	symmetric

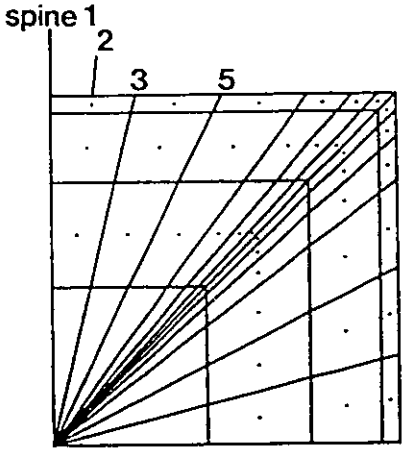

b

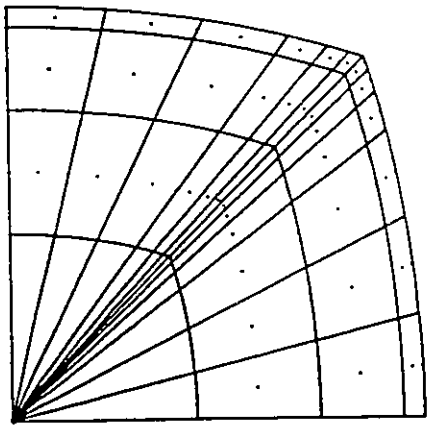

c

Figure 3.3 Extrudate swell from a square die: a) superposed die shape and final shape of the extrudate; b) initial grid; c) final grid.

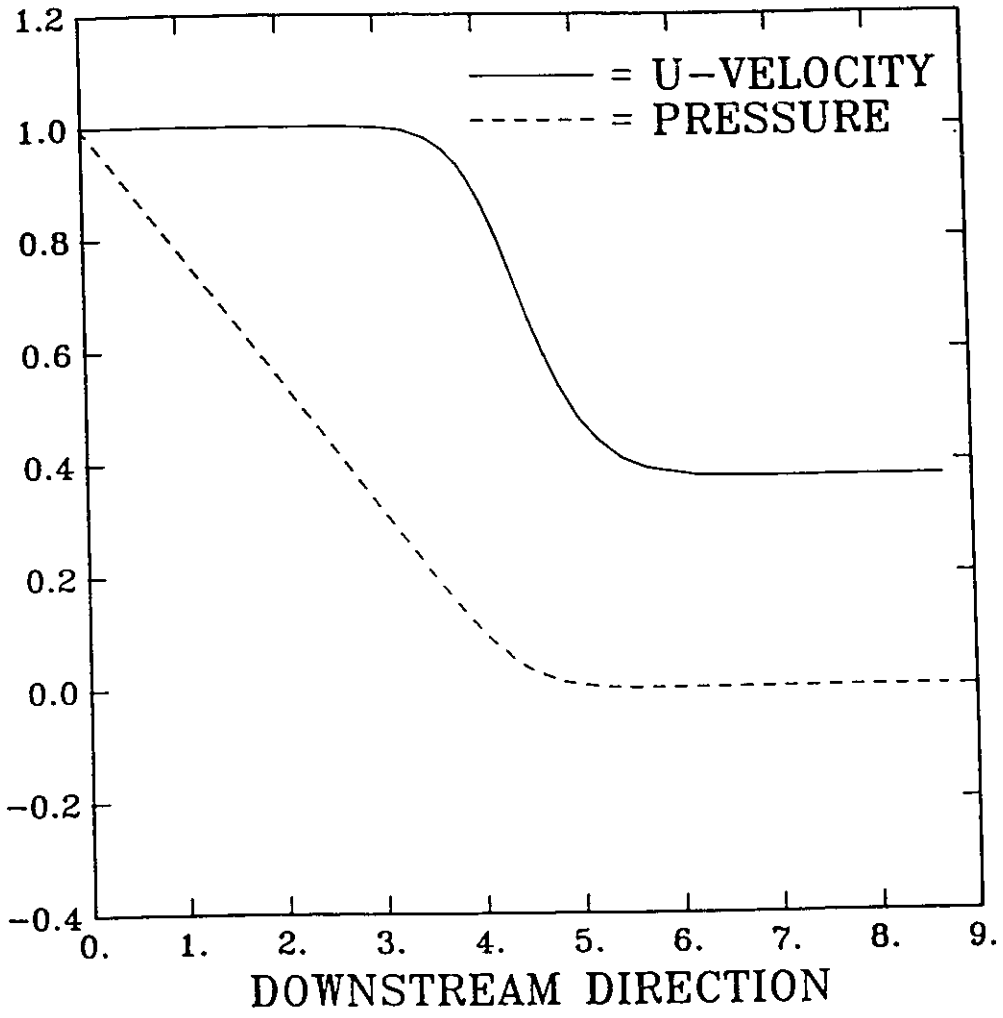

Figure 3.4 Extrudate swell from a square die: normalized downstream velocity and pressure and pressure distribution along the centerline.

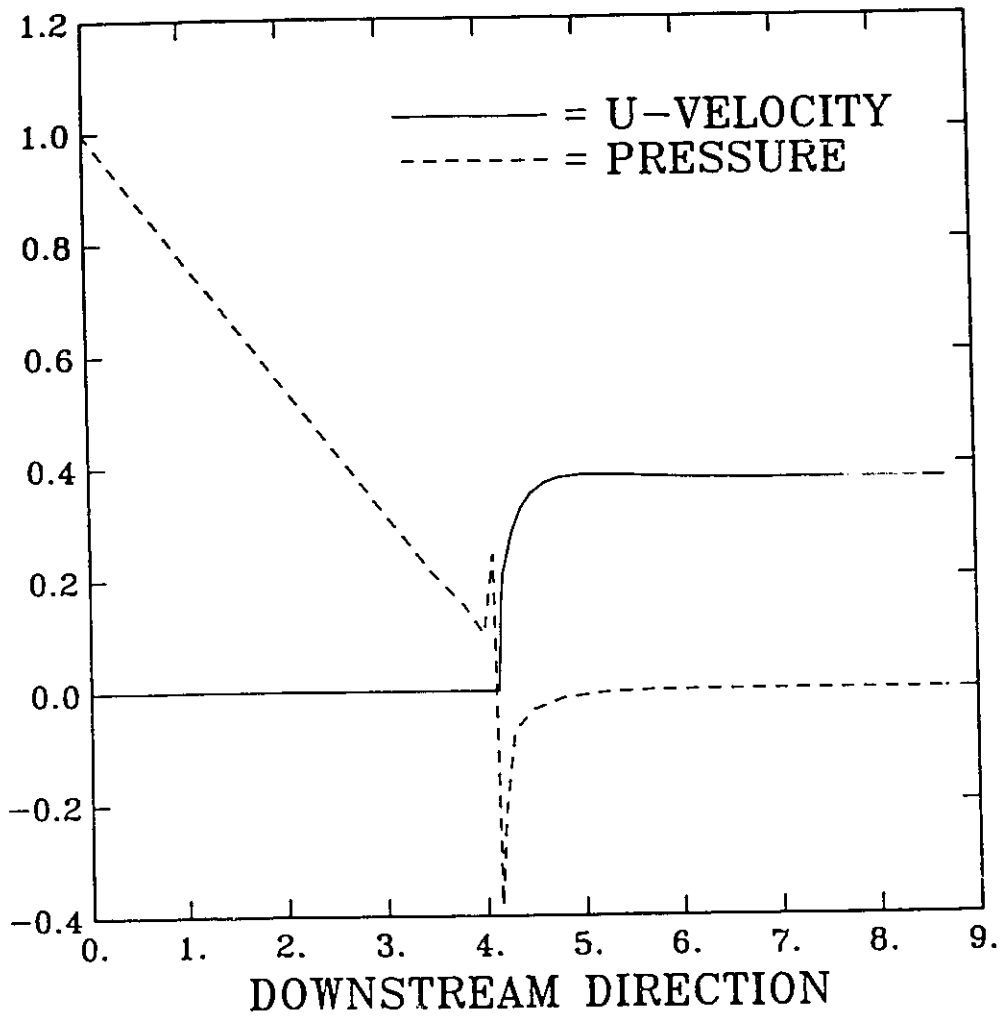

Figure 3.5 Extrudate swell from a square die: normalized downstream velocity and pressure and pressure distribution along the center of the flat face (scale the same as in Figure 3.4).

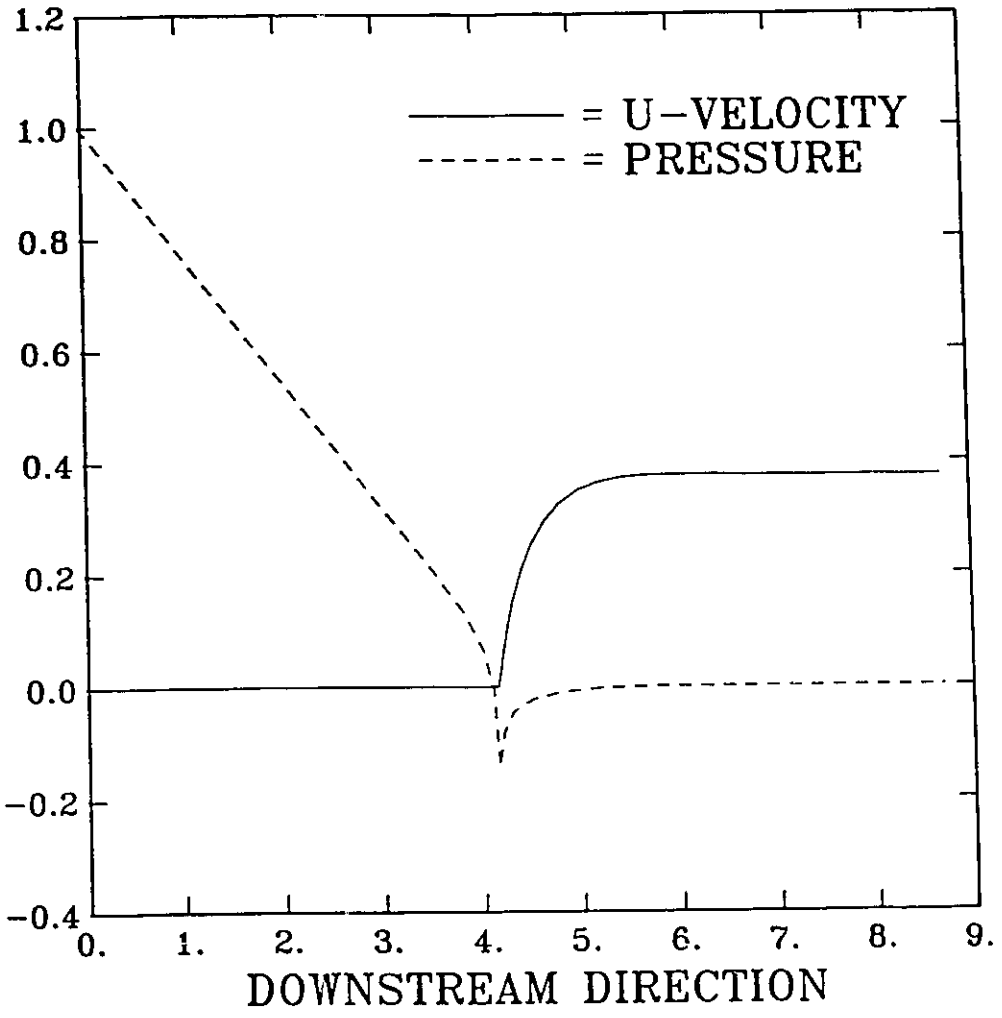

Figure 3.6 Extrudate swell from a square die: normalized downstream velocity and pressure and pressure distribution along the corner points (scale the same as in Figure 3.4).

(1983); Mitsoulis et al. 1984) behaviour of the corresponding two dimensional solution of the swell from a slit (Figure 3.5). The pressure exhibits a discontinuous increase before the exit of the die, where it takes negative value, while the pressure distribution along the corner points (Figure 3.6) does not exhibit this increase but rather drops smoothly to a negative value probably because of the force balance in that region. The same behaviour of the pressure discontinuity was observed in all the problems where a sharp corner was present.

In the absence of surface tension effects, which is the case with the highly viscous polymer melts, the extrudate tends to sustain a sharp corner point downstream which corresponds to the die corner point. In the square die geometry, this point is located on the diagonal due to symmetry and is clearly defined. The 3-D studies by Tran-Cong and Phan-Thien (1988) and Shiojima and Shimazaki (1987) have also reported this effect.

3.2.4 Rectangular Die

The free surface flow out of a rectangular die of aspect ratio 4:1 is considered and a perspective view is shown in Figure 3.7. One quarter of the flow domain is dealt with taking advantage of the symmetric shape. It is interesting that as the material exits the die, it actually contracts at the corners, while it exhibits large swell at the symmetry planes (Figure 3.8). The material redistributes near the regions of the sharp corners and is pushed inward to keep the force balance as the flow field changes.

The distorted free surface shape has to do with the position of the "extrudate corner point" in the absence of surface tension effects. The wiggles on the free surface are also attributed to the C^0 approximation of the free surface (slope is not continuous across inter-element boundaries) with the spine method. The spine approach as used in this section, utilizes spines with fixed orientation in space. The result is that this approach cannot follow the movement of the corner point in the cross-flow directions in the sense that the corner point

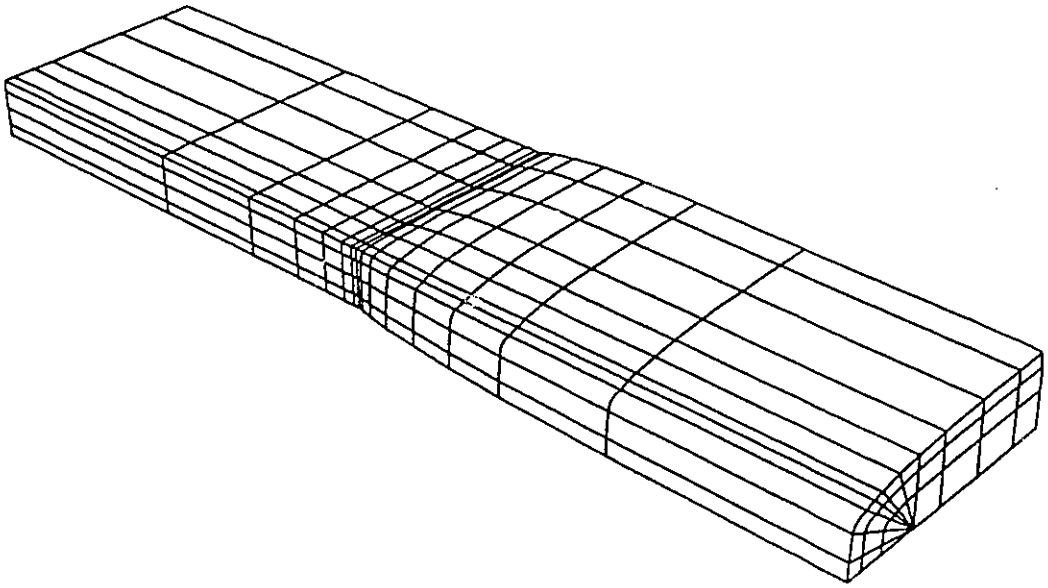

Figure 3.7 Perspective view of the three-dimensional extrudate swell from a rectangular die of aspect ratio 4:1.

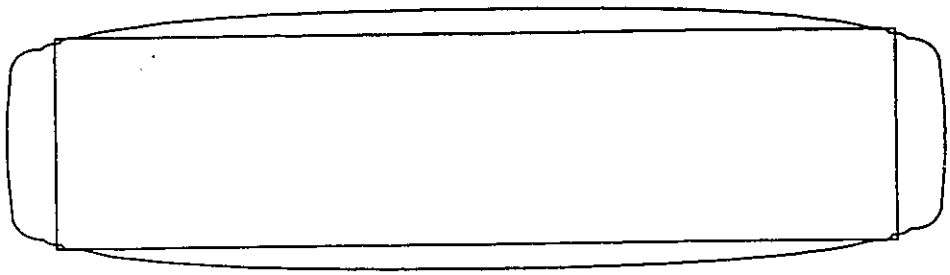

a

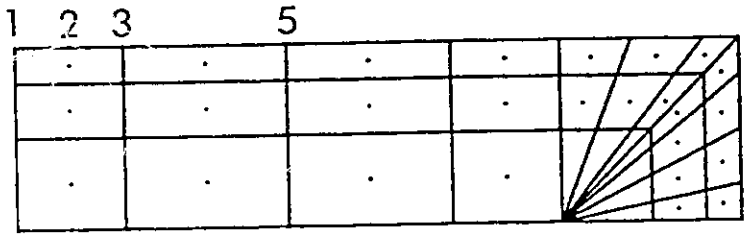

b

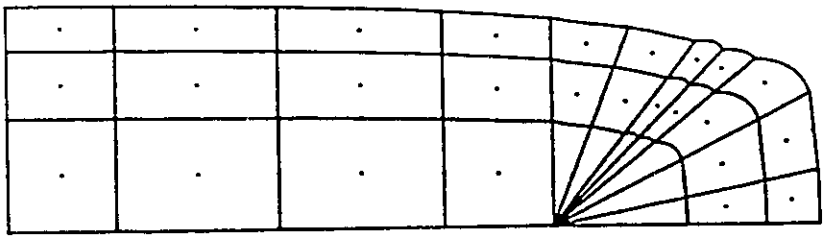

c

Figure 3.8 Extrudate swell from a rectangular die of aspect ratio 4:1: a) superposed die shape and final shape of the extrudate; b) initial grid; c) final grid.

will no longer fall on a spine because of the material redistribution. The corner point is located on the side of the corresponding element between two successive spines and the shape is smoothed because of the quadratic approximation of the free surface.

It is interesting that for this geometry the swelling is more pronounced along the long axis of the die than along the short axis (Shiojima and Shimazaki, 1987; Han, 1971).

3.2.5 Triangular Die

The equilateral triangular geometry was also considered and a slight contraction of 2.6% was observed at the corners in the final shape, Figure 3.9, while the maximum swell of 22.8% occurs at the flat face. The corresponding results of Tran-Cong and Phan-Thien (1988) were 2% contraction at the corner and 20.6% swell at the flat face. As was also the case with the square geometry, it seems that the boundary element method predicts lower swelling ratios at the flat faces but higher at the corners compared to the finite element results.

3.2.6 Bow-Tie Die

A very interesting geometry which finds use in the polymer processing industry to counter-balance the pronounced swelling that is observed at the flat faces of rectangular dies, is the bow-tie shaped geometry (Figures 3.10,3.11). This geometric shape is the result of the experience and intuition of designers and it attempts to restrict the flow in the areas where significant swelling occurs. Here, the width of the die at the neck is set to 80% of the maximum width. It can be seen in Figure 3.11 that the shape of the extrudate approaches the rectangular shape better than the extrudate from a rectangular die.

Tran-Cong and Phan-Thien (1989) also presented a die design scheme which predicts a bow-tie shaped geometry when a square extrudate shape is desired.

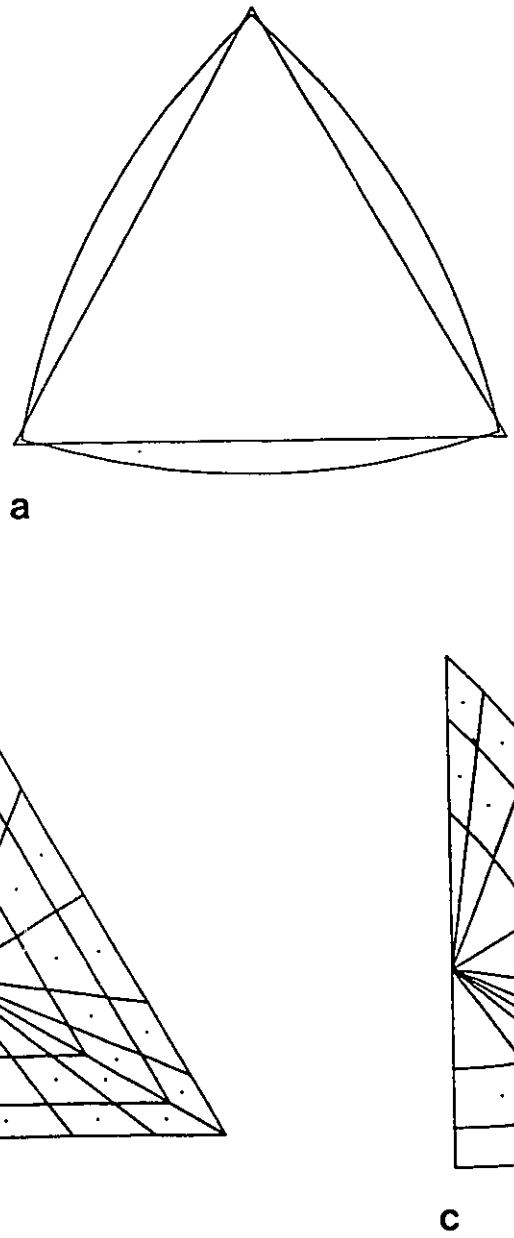

Figure 3.9 Extrudate swell from an equilateral triangular die: a) superposed die shape and final shape of the extrudate; b) initial grid; c) final grid.

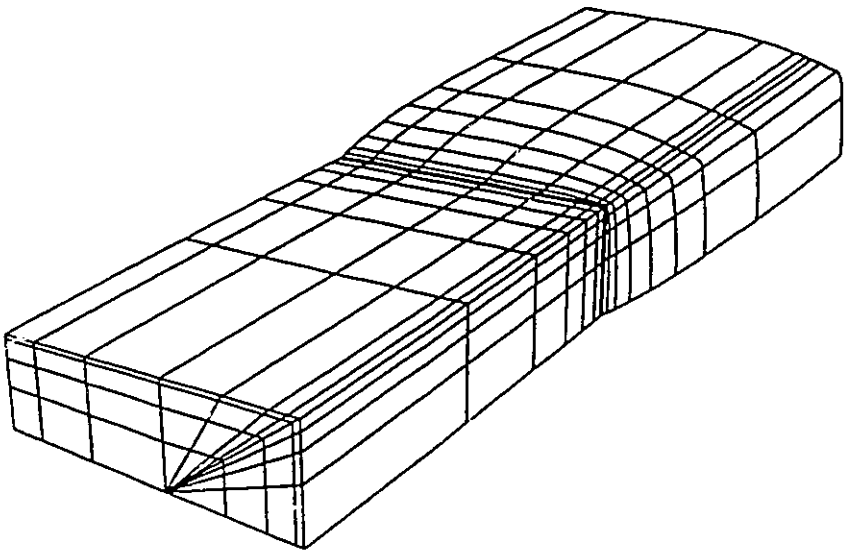

Figure 3.10 Perspective view of the three-dimensional extrudate swell from a bow-tie die.

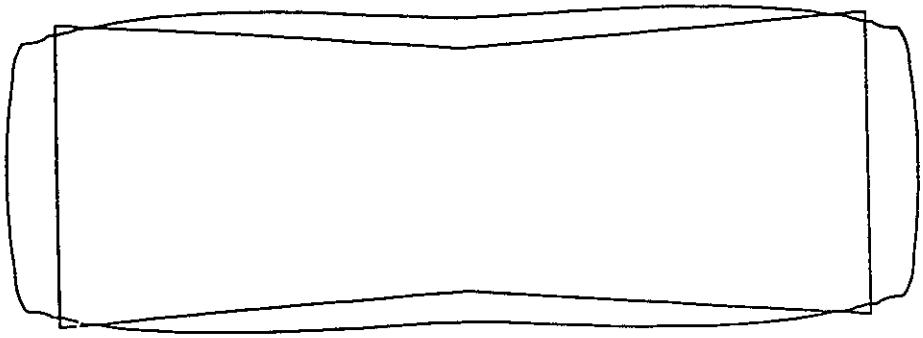

a

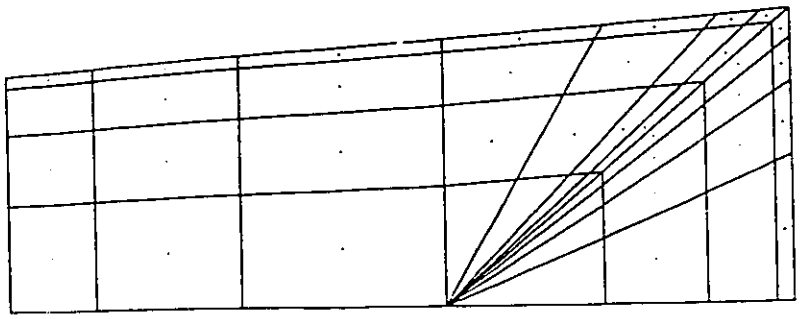

b

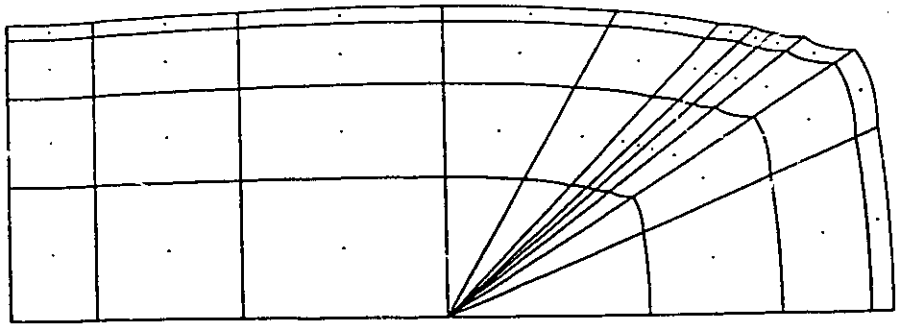

c

Figure 3.11 Extrudate swell from a bow-tie die: a) superposed die shape and final shape of the extrudate; b) initial grid; c) final grid.

3.3 EXTRUDATE SWELLING BEHAVIOUR IN NON-ISOTHERMAL NEWTONIAN FLOWS

Non-isothermal exit flows of molten polymeric materials are encountered in a number of polymer processing operations such as film and pipe extrusion, wire coating, fiber spinning, etc., because of the high melting point of polymeric materials. Apart from material properties (viscosity function, elasticity), processing conditions such as flowrate, temperature and die shape affect the extrudate shape.

A large number of publications deal with the two-dimensional extrusion from planar or round dies. The effects of thermal properties of generalized Newtonian fluids on extrudate swell were studied by Phuoc and Tanner (1980), Ben-Sabar and Caswell (1981), and Huynh (1983). They have demonstrated that non-isothermal conditions can induce high swelling ratios, an effect known as thermally induced extrudate swelling, because of the temperature dependence of the viscous properties of the materials. The non-isothermal extrudate swell of elastic fluids was the subject of studies by Finlayson and McClelland (1985, 1988), Sugeng et al. (1987), Milthorpe and Tanner (1987) and Vlcek and Vlachopoulos (1989), where the coupling between temperature-induced swelling and stress-induced swelling was examined. All the cited work has so far concentrated on the two-dimensional problem of the thermally induced swelling and its interactions with the stress field.

This section studies the problem from a different perspective and focuses on the three-dimensional extrudate phenomena that viscous dissipation and/or temperature differences induce. These include the thermally induced extrudate swelling out of three-dimensional geometries and the extrudate bending and distortion as a result of asymmetric temperature gradients across the die. Such conditions can, for example, be induced by cooling or heating part of the die walls, a practice that is common in the industry. As will be shown, a temperature difference can also arise when a die comprises different geometric shapes and

there is uneven viscous heat generation in the geometrically different regions. Generally, an asymmetric geometric shape can by itself give rise to extrudate bending. Although the effect of polymer melt elasticity on the swelling behaviour is of major importance, this work intends to provide an insight into the viscous mechanisms that induce the three-dimensional phenomena by studying the extrusion of inelastic Newtonian fluids with an exponential dependency of viscosity on temperature.

The Galerkin/finite element u-v-w-p-h-T formulation that is used in this section is presented in extent in Chapter 2 and Appendix A. A schematic of the flow is given in Figure 2.1 and the governing equations and boundary conditions are also presented in Chapter 2.

3.3.1 Numerical Considerations

The problem is rendered non-linear both because of the need to calculate the unknown a priori free surface shape and the additional non-linearity introduced by the exponential dependence of viscosity on temperature (eqn. 2.5). The complication introduced by the material redistribution in the extrudate with the corresponding corner point movement is tackled by the use of the pathline approach and the hybrid spine/pathline approach (section 2.5) depending on the problem characteristics.

The Newton-Raphson method is used when the spine or the hybrid spine/pathline methods are followed and the Picard iteration scheme is used when the pure pathline approach is employed. Because of the slower convergence in that case, tolerances are set so that the maximum relative update of all the calculated variables is less than 10^{-2} for convergence.

In all cases, the initial estimates for the velocity and temperature fields are calculated by solving the Newtonian isothermal case with the extrudate having the shape of the die at the die exit. Once these initial estimates are obtained, the non-linear solution procedure is initiated. This policy leads to convergence problems for the Newton-Raphson iteration when

the problem is highly non-linear. No convergence difficulties occurred when the pathline free surface update was used.

In all cases the upstream profile is assigned as the fully developed, one dimensional flow with viscous heating. The Galerkin formulation over the same 2-D grid that is assigned to the inlet of the 3-D problem is used for the input profile boundary condition calculation.

The size of the non-isothermal problems with respect to the number of elements, number of nodes, number of degrees of freedom and frontwidth is given in Table 3.2.

Table 3.2 Size of the Non-Isothermal Free Surface Problems

Problem	Elements	Nodes	Unknowns	Frontwidth
Round Die	78	783	2,696	223
Square Die				
Isothermal walls	132	1,242	4,454	351
Non-isothermal walls	264	2,277	8,492	549
Rectangular die	176	1,863	6,441	467
Flat die	66	805	2,667	253
Key-hole die				
Isothermal	363	3,358	8,922	538
Non-Isothermal	363	3,358	12,190	710

3.3.2 Test Case. Round Die

The first die shape considered was circular. Here the 3-D implementation is assessed by reproducing, with the three-dimensional code, the predictions of Phuoc and Tanner (1980), who solved the axisymmetric version of the problem. Only three elements were used in the radial direction (Figure 3.12) compared to five in the previously mentioned work. Figure 3.12a is a perspective plot of the U = 30mm/s case and Figure 3.12b shows the effect of the average velocity on the extrudate swell. As the average velocity increases, the viscous

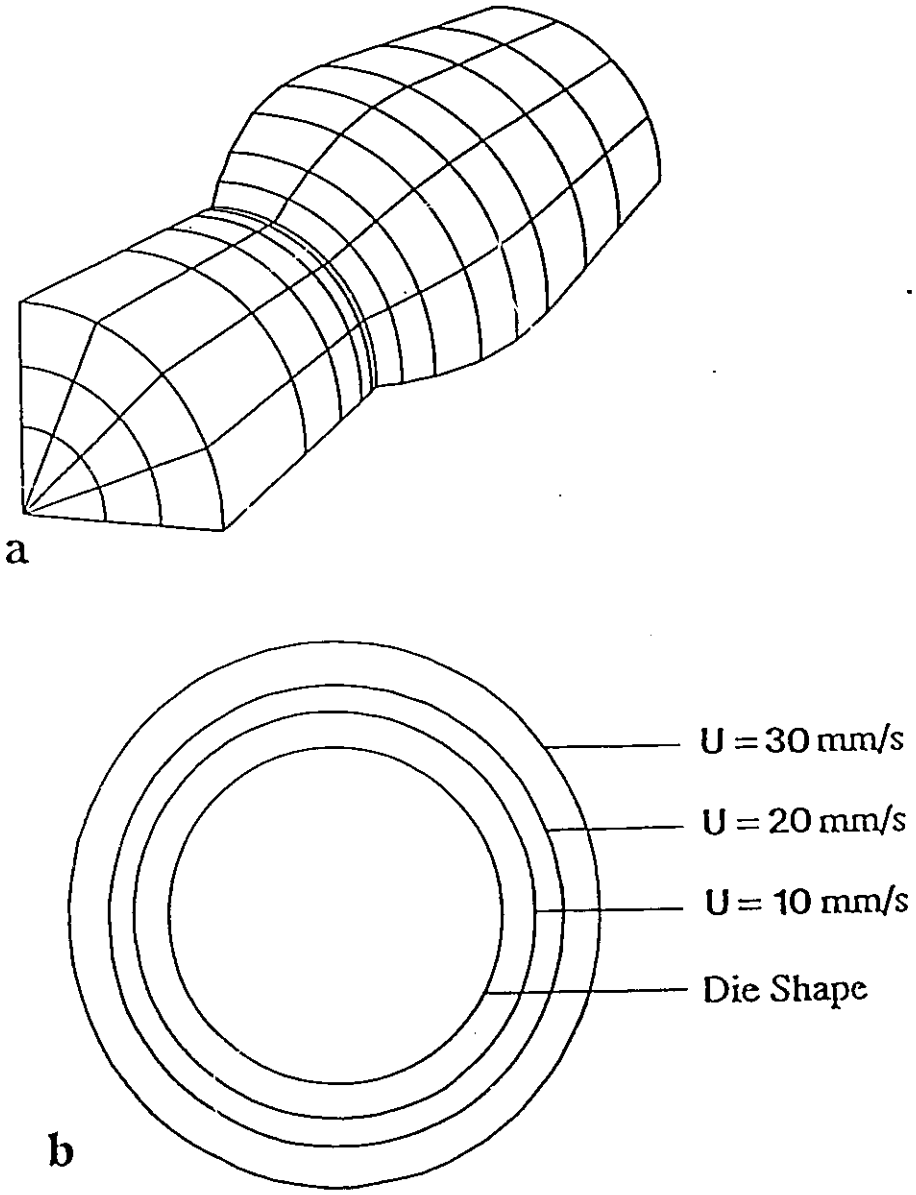

Figure 3.12 Non-isothermal extrudate swell out of round dies: a) perspective view when average velocity is 30mm/s, b) effect of the average velocity on extrudate swell.

dissipation inside the die increases as well and results in the more pronounced swelling via a viscous mechanism. The calculated swelling ratios with the three dimensional code (Table 3.3) were in good agreement with those reported by Phuoc and Tanner (1980).

The spine approach with full Newton-Raphson iteration was used.

Table 3.3 Swelling of Extrudate. Round Die

Average Velocity (mm/s)	Swelling Ratio (%) present work	Swelling Ratio (%) Phuoc and Tanner (1980)
10	21	20
20	37	38
30	62	70

3.3.3 Material Properties

For the remaining part of this investigation the physical properties of a typical polystyrene are used:

$\rho = 940$ Kg/m^3 $\quad k = 0.15$ W/m/K $\quad C = 2100$ J/Kg/K

$\mu_{190°C} = 1.4\,10^4$ Kg/m/s $\quad \alpha = 0.021$ 1/K.

The reference wall temperature is set to $T_w = 190°C$ and the ambient temperature to the room temperature of $T_\infty = 25°C$. The value of $hR/k = 0.72$ given by Acierno et al. (1971) and used by Phuoc and Tanner (1980) is utilized.

3.3.4 Square Die

The non-isothermal extrusion out of a square die with a side of $L = 1$mm is considered.

3.3.4.1 Uniformly Isothermal Walls

The die walls are isothermal at a temperature of $T_w = 190°C$ and the thermally-induced swelling behaviour is examined as the average velocity (characteristic velocity) increases.

Figure 3.13a shows a perspective view of extrusion out of a square and Figure 3.13b shows the effect of the increased average velocity on the amount of swelling. As the average velocity increases, viscous dissipation increases within the die and the generated temperature difference gives rise to a viscosity difference which in turn induces the pronounced swelling.

The flow is symmetric along the centerline and the diagonals and only one eighth of the flow domain was discretized. The spine approach was successfully used to parametrize the relatively simple geometry.

3.3.4.2 Non-Isothermal Walls

Two different non-isothermal situations are examined as shown in Figure 3.14. In both cases the vertical walls are held at a temperature of 190°C but the horizontal walls are heated to 230°C in the first case (Figures 3.14a,b) and are cooled to 160°C in the second case (Figures 3.14c,d). The characteristic (average) velocity is set to $U = 25mm/s$ which corresponds to a $Pe = 329$ and a $Br = 0.354$.

Figures 3.14b and 3.14d show that the maximum swelling along the vertical walls is in both cases approximately the same due to the fact that this part of the die is kept at the same thermal conditions. However, when the horizontal walls are heated, the material in that region swells less (Figure 3.14b) while it swells more when the horizontal wall is cooled (Figure 3.14d). Note that the shape of the extrudate is no longer symmetric with respect to the diagonal. There is uneven material distribution and the corner point moves in different direction in the two cases but is always forced toward the cooler side (Figures 3.14b,3.14d).

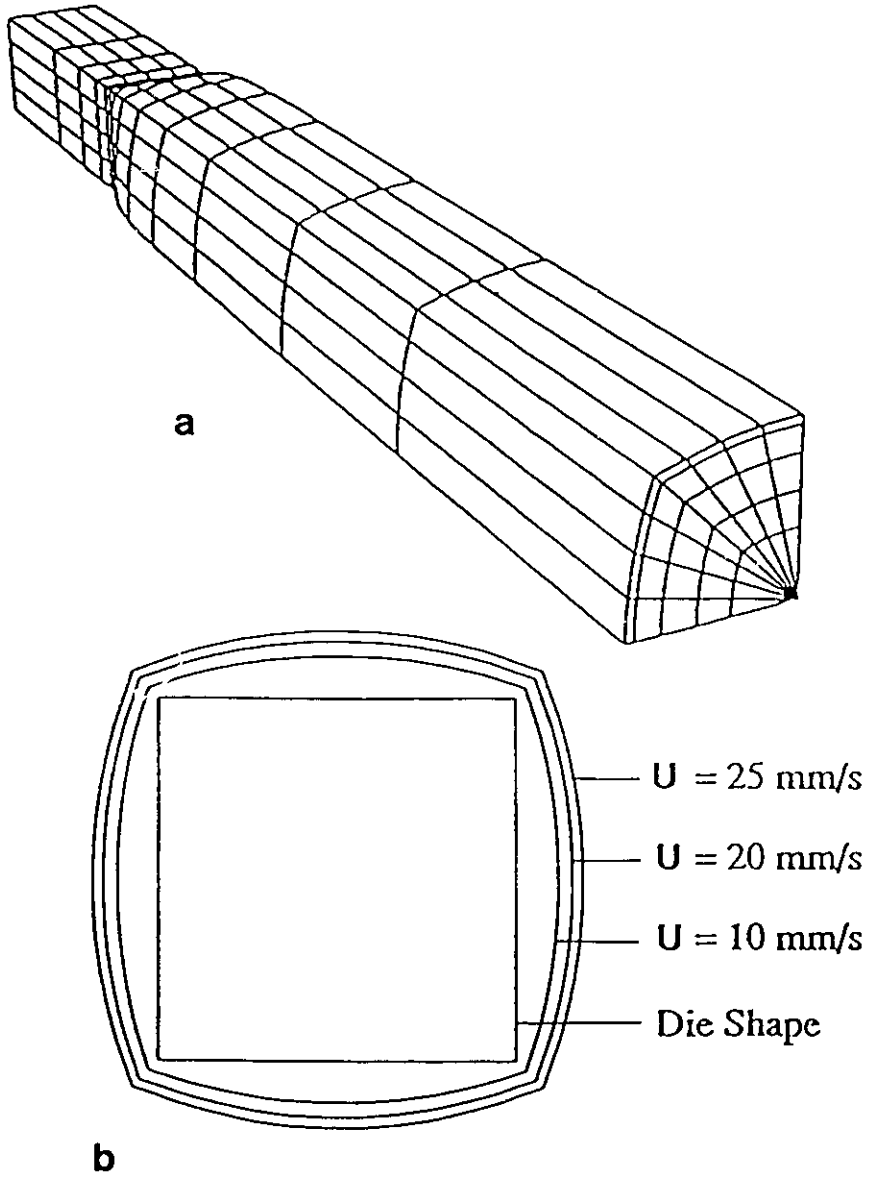

Figure 3.13 Non-isothermal extrudate swell out of square dies: a) perspective view when average velocity is 25mm/s, b) effect of the average velocity on extrudate swell.

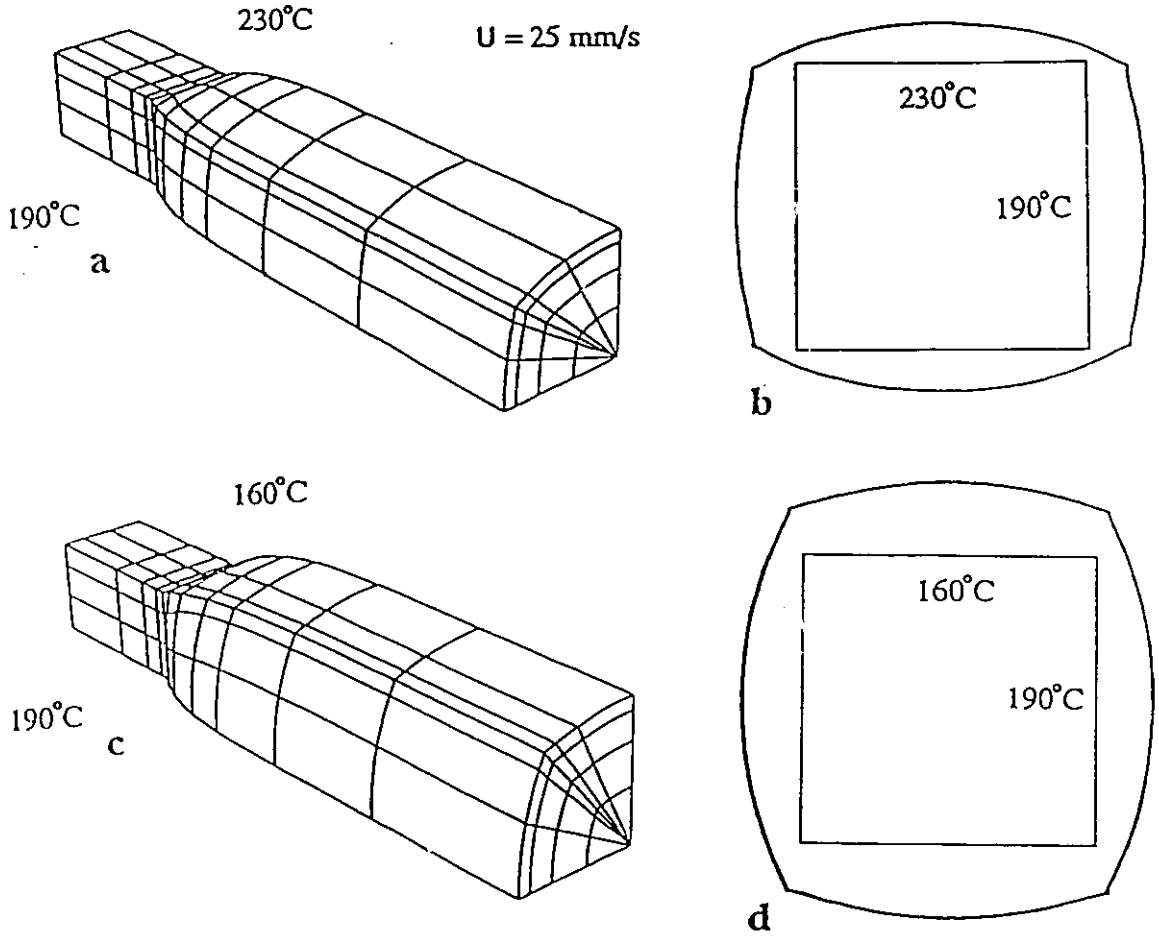

Figure 3.14 Non-isothermal extrudate swell and discortion out of square dies with the walls at different temperatures; average velocity U = 25mm/s; a) perspective view and b) final extrudate and die shape, horizontal walls at 230°C, vertical walls at 190°C; c) perspective view and d) final extrudate and die shape, horizontal walls at 160°C, vertical walls at 190°C.

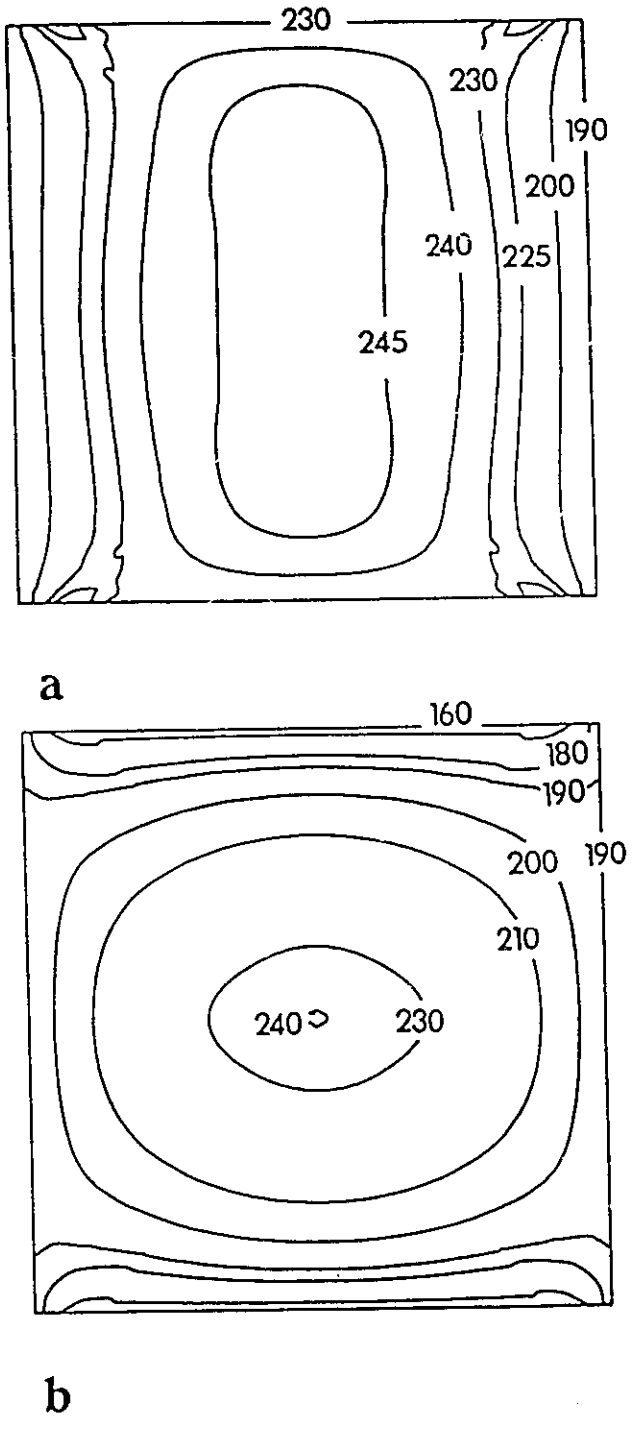

Figure 3.15 Temperature contours within the square dies of Figure 3.13: a) horizontal walls at 230°C; b) horizontal walls at 160°C.

The temperature distribution within the die for both cases is shown in Figure 3.15 and provides an insight on the mechanisms of the flow. In Figure 3.15a there is a $\Delta T_h = 55°C$ along the horizontal direction while there is a $\Delta T_v = 15°C$ along the vertical direction. The low ΔT_v does not induce a high swelling ratio and there is a flow of the faster moving (because of lower viscosity) material of the warmer side toward the cooler (more viscous) side. The flow rearranges in the extrudate and gives both the higher swelling ratio of the cooler side and the corner point movement. The same mechanism holds for the second case of Figure 3.15b, but the magnitude of the temperature differences is reversed in this case.

The problem required 5 pathline iterations followed by 4 Newton-Raphson - spine iterations to converge.

3.3.5 Non-Isothermal Flat Film Extrusion

The non-isothermal extrusion of flat film is considered. Film bending and film thickness variation because of imposed temperature gradients by heating or cooling the walls is displayed.

3.3.5.1 Flat Film Bending

It has been observed experimentally (Southern and Ballman, 1973) and shown numerically (Mavridis et al., 1988) that in the stratified flow of polymer melts, an existing viscosity difference induces the extrudate to bend towards the side of the more viscous material. White and Ide (1975) attribute the "kneeing effect", the bending of a polymer melt when it is extruded through a spinnerette, to a viscosity difference induced by a radial temperature variation.

It is shown that this explanation is valid for the non-isothermal flow out of a flat die when a temperature difference across the die width is imposed (Figure 3.16). The bottom wall

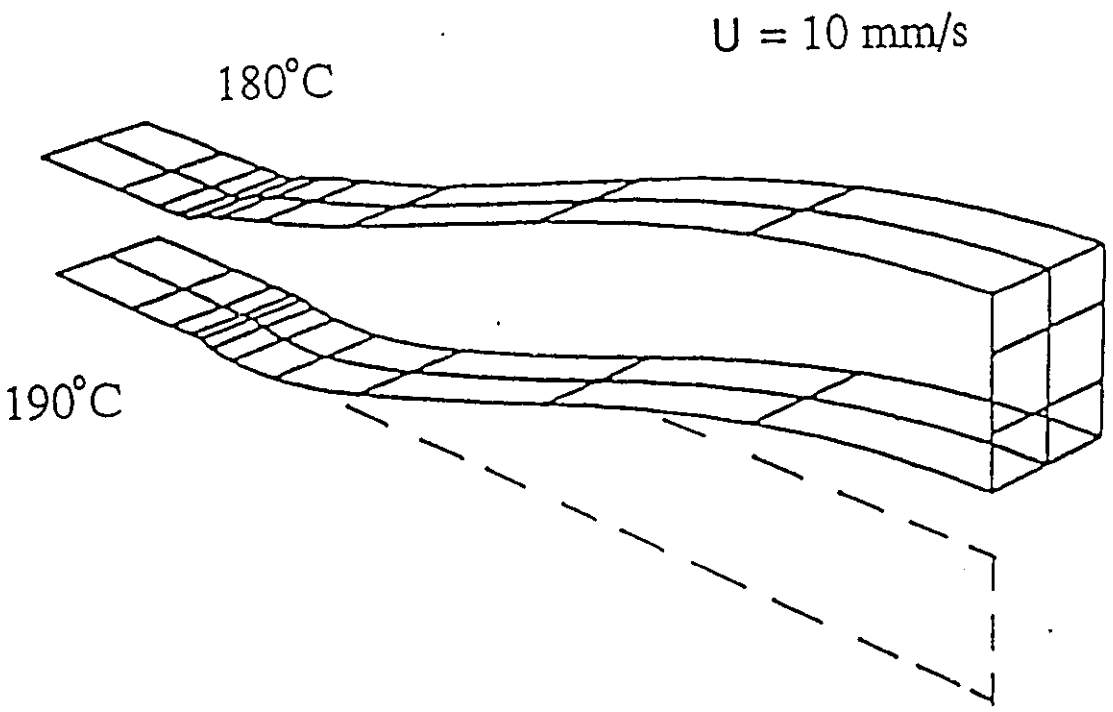

Figure 3.16 Non-isothermal extrudate swell out of a flat die. Extrudate bending because of imposed temperature difference across the die. Upper wall at 180°C, lower wall at 190°C.

of the die is kept at 190°C while the upper wall is at 180°C. The die gap is 1mm and the scaling factors are L=1mm and U=10mm/s (average velocity). The die is assumed to be long in the third direction so that the flow is basically two-dimensional.

Figure 3.16 shows that the material immediately after exiting the die exhibits swell, but as the flow rearranges it bends towards the cooler wall side. There is definitely a viscosity variation because of the imposed temperature difference and the functional dependency of viscosity on temperature. At the cooler wall, viscosity is relatively higher, and the material bends in that direction.

A temperature difference of 10°C was enough to deflect the film by more than one characteristic length (Figure 3.16) which shows that even small temperature differences may give rise to film uniformity or stability problems.

3.3.5.2 Film Thickness Variation

Film thickness variation in a situation where the central part of the flat die walls is kept at 190°C while the rest is at 160°C is studied. The conditions are shown in Figure 3.17 where the thermal conditions are imposed on both the upper and lower walls and therefore no bending of the film occurs. The die extends in both the right and left side where symmetry conditions are imposed.

Because of the higher temperature the material in the central part is thinning and therefore its viscosity is lower compared to the material at the sides. This gives rise to lower swelling ratios at the central region as opposed to the regions of the sides were the material swells significantly through the thermally induced swelling mechanism. This is a typical example of how temperature differences that are imposed by heating or cooling the die walls or may occur because of faulty equipment performance, may affect the film thickness variation.

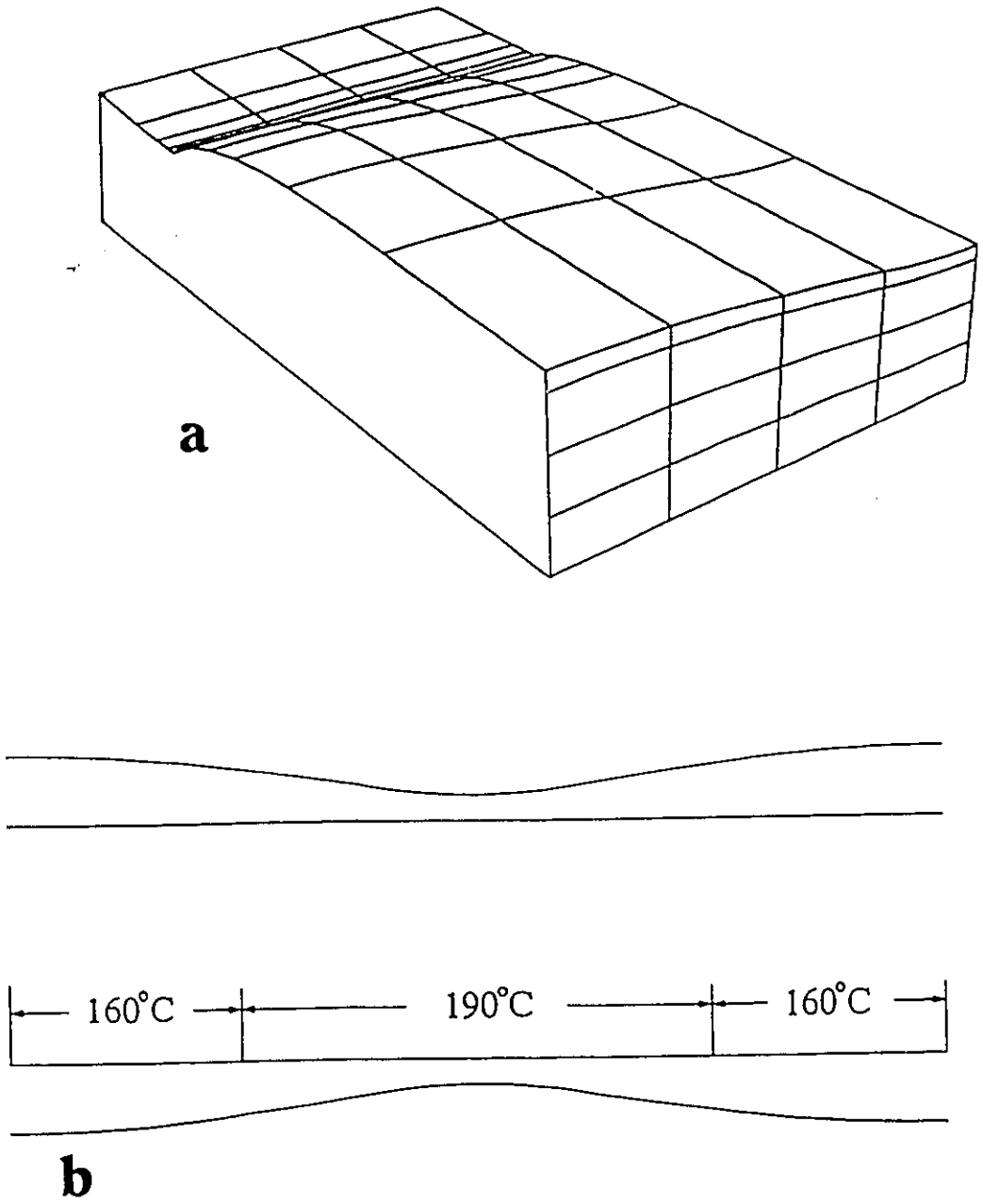

Figure 3.17 Non-isothermal swell out of a flat die. Film thickness variation because of non-uniform die wall temperature: a) perspective view; b) superposed die and final film shape.

3.3.6 Rectangular Die. Distortion and Bending

The situation where the melt is extruded through a rectangular die of aspect ratio 1:4 (Figure 3.18) is examined. The die walls are at 190°C except a portion at the center of the upper wall which is heated to 230°C. The length scale of L=1mm equals the side width of the die.

The temperature difference across the die causes the extrudate not only to swell but to distort significantly (Figure 3.18). The upper wall corners move outward and downward and the surface material distributes quite unevenly.

As the average velocity is increased, the bending decreases but the distortion increases as does the overall cross-sectional area of the extrudate. This trend can be explained in light of the temperature distribution within the die. Figure 3.19 shows temperature contours within the die of the three cases presented in Figure 3.18. In Figure 3.19a, for the lower average velocity of 10mm/s, there is a high temperature difference across the die center in the vertical direction which is responsible for the high bending, but the temperature difference near the corner walls is not large, so the distortion in the horizontal direction is not as pronounced. As the average velocity increases, the induced viscous heating makes the temperature and correspondingly the viscosity distribution more uniform within the core of the flow (Figure 3.19b, 3.19c). Lower viscosity material (because of higher temperature) is found near the bottom wall and therefore less pronounced bending is expected. On the other hand, the regions near the corners have higher temperature differences and the distortion becomes more pronounced. The maximum encountered temperature rises, because of viscous dissipation, and the higher temperature in the core of the material gives rise to higher overall swelling so that the cross-sectional area of the extrudate becomes larger (Figure 3.18).

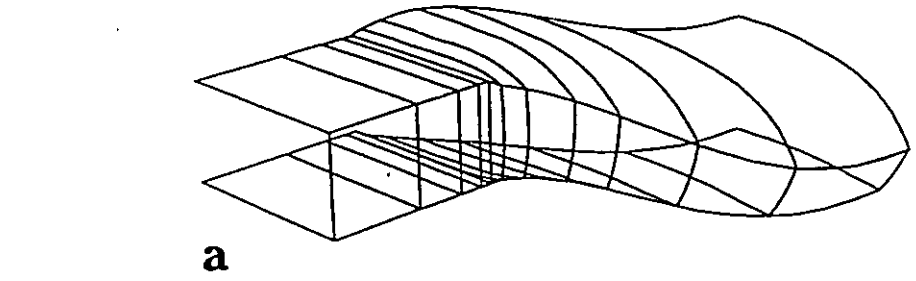

a

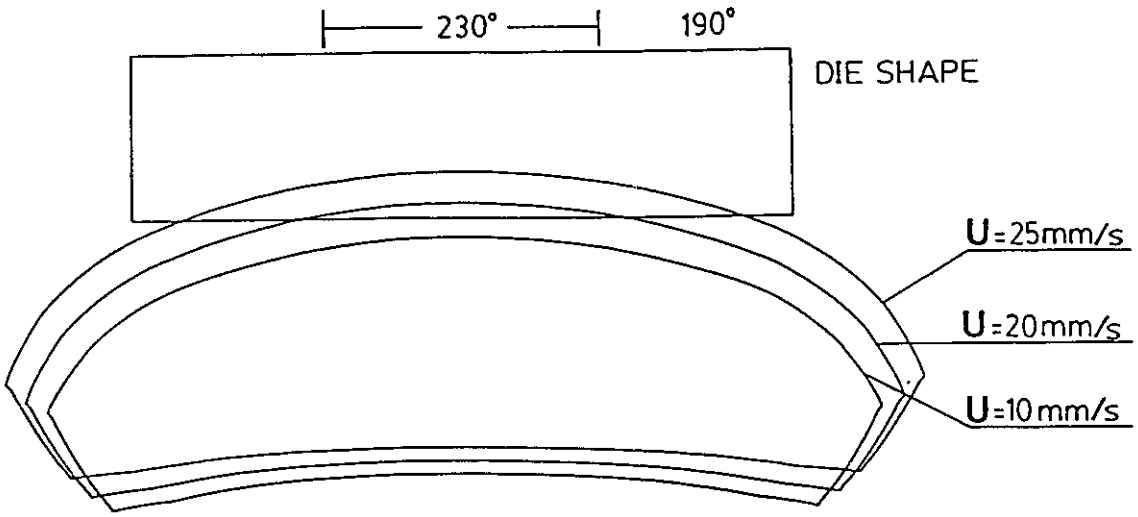

b

Figure 3.18 Extrudate bending and distortion out of a 4:1 rectangular die; part of the upper wall is heated to 230°C: a) perspective view, average velocity U = 25mm/s; b) superposed final extrudate shape and initial die shape; effect of the average velocity on the extrudate bending, distortion and swell.

U = 10 mm/s

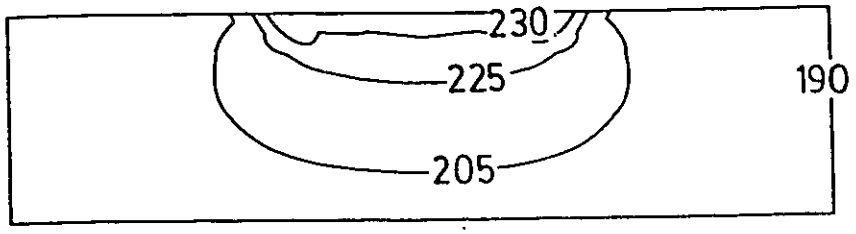

a

U = 20 mm/s

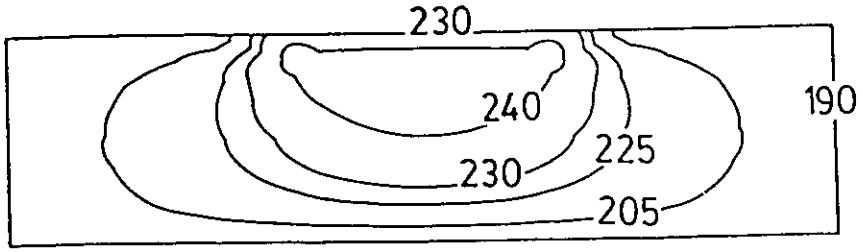

b

U = 25 mm/s

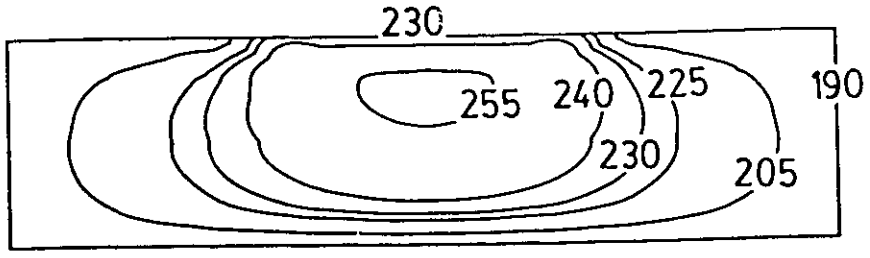

c

Figure 3.19 Temperature contours within the rectangular die of Figure 3.17: a) average velocity U = 10mm/s; b) average velocity U = 20mm/s; c) average velocity U = 25mm/s.

3.3.7 Key-Hole Die

The flow out of a key-hole shaped die is studied (Figure 3.20). The die comprises a round part of radius R=1mm and a rectangular part of height H=0.6mm. The overall horizontal dimension of the die is 3R and the characteristic length is defined as L=R=1mm. This complex three dimensional geometry, because of the presence of geometrically different regions, gives rise to different flow regimes in each region of the die. The effects of geometry and non-isothermal conditions are examined in three flow situations.

3.3.7.1 Non-isothermal Flow. Uniformly Isothermal Walls

The flow is non-isothermal due to viscous heating but the die walls are kept at a uniform temperature of 190°C (Figure 3.20).

Due to the die shape, the non-uniform flow distribution gives rise to unequal heat generation in the geometrically different regions of the die. Viscous dissipation induces a temperature difference in the horizontal direction. The maximum temperature occurs in the circular region of the die because velocity and viscous dissipation is greater in that region.

As a consequence, there is extrudate bending toward the rectangular side of the die (Figure 3.20, 3.23) where temperature is relatively lower and viscosity is higher.

The final shape of the extrudate shows that the swelling behaviour is different in the two geometric regions of the die and that the far end of the rectangular part is shrinking while the round part expands significantly, owing to the unequal temperature differences.

Figure 3.20 also shows the temperature contours within the die, at x=0.875 L and at x=7.0 L downstream of the die exit respectively.

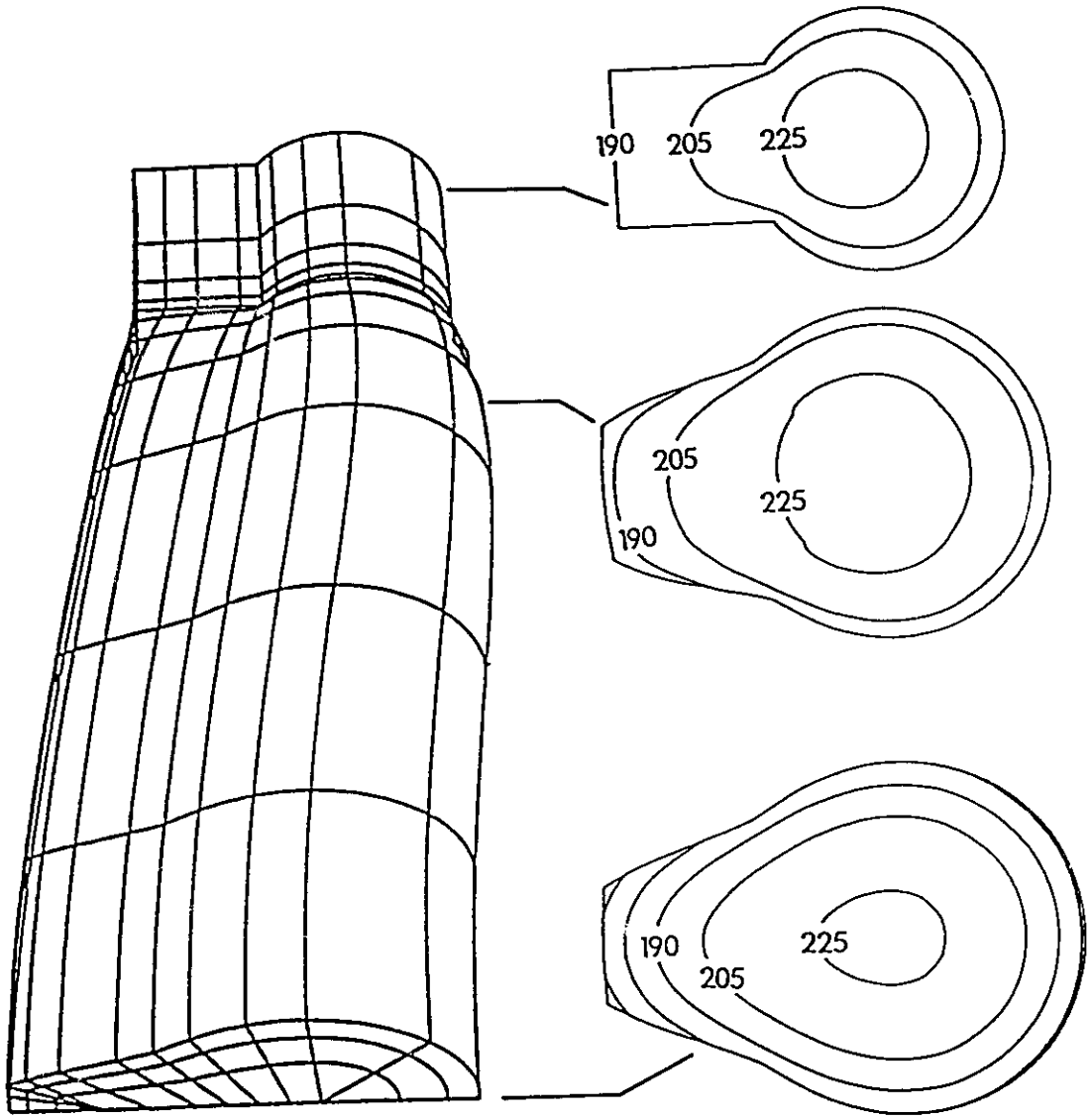

Figure 3.20 Non-isothermal flow out of a key-hole die, average velocity U = 25mm/s. Uniformly isothermal walls at 190°C. Bending due to temperature gradient caused by viscous heating and geometry.

3.3.7.2 Non-isothermal Flow. Non-Uniformly Heated Walls

An example on how changes of thermal conditions may affect the direction of the arising bending phenomena is given. The flow is again non-isothermal, the material is viscously heated but the walls of the rectangular section are kept at an elevated temperature of 230°C relative to the round-part walls which are kept at 190°C (Figure 3.21).

The wall heating generates a different picture of the temperature distribution (Figure 3.21) where there is still a temperature difference across the horizontal direction, but now the maximum temperature is located within the rectangular section of the die as a result of the wall heating.

The direction of the extrudate bending is reversed, and the extrudate bends toward the round part of the die (Figures 3.21, 3.23) because viscosity is higher in the round part of the die due to the lower temperature.

The imposed wall heating gives rise to a final extrudate shape with different characteristics (Figures 3.21, 3.23) compared to the previously studied case (Figures 3.20, 3.23). Here, the rectangular section expands significantly as does the round section of the die.

Figure 3.21 also shows the temperature contours within the die, at $x = 0.875$ L and at $x = 7.0$ L downstream of the die exit respectively.

3.3.7.3 Isothermal Flow

So far it was observed that bending of the extrudate occurs when a viscosity difference is present, either because of the presence of materials with different properties (bicomponent stratified flow) or because of temperature differences. The die geometry is yet another independent factor that may cause extrudate bending.

The isothermal flow through the same key-hole shaped die of the previous cases is examined. The problem reduces to an isothermal Newtonian flow situation, and the analysis

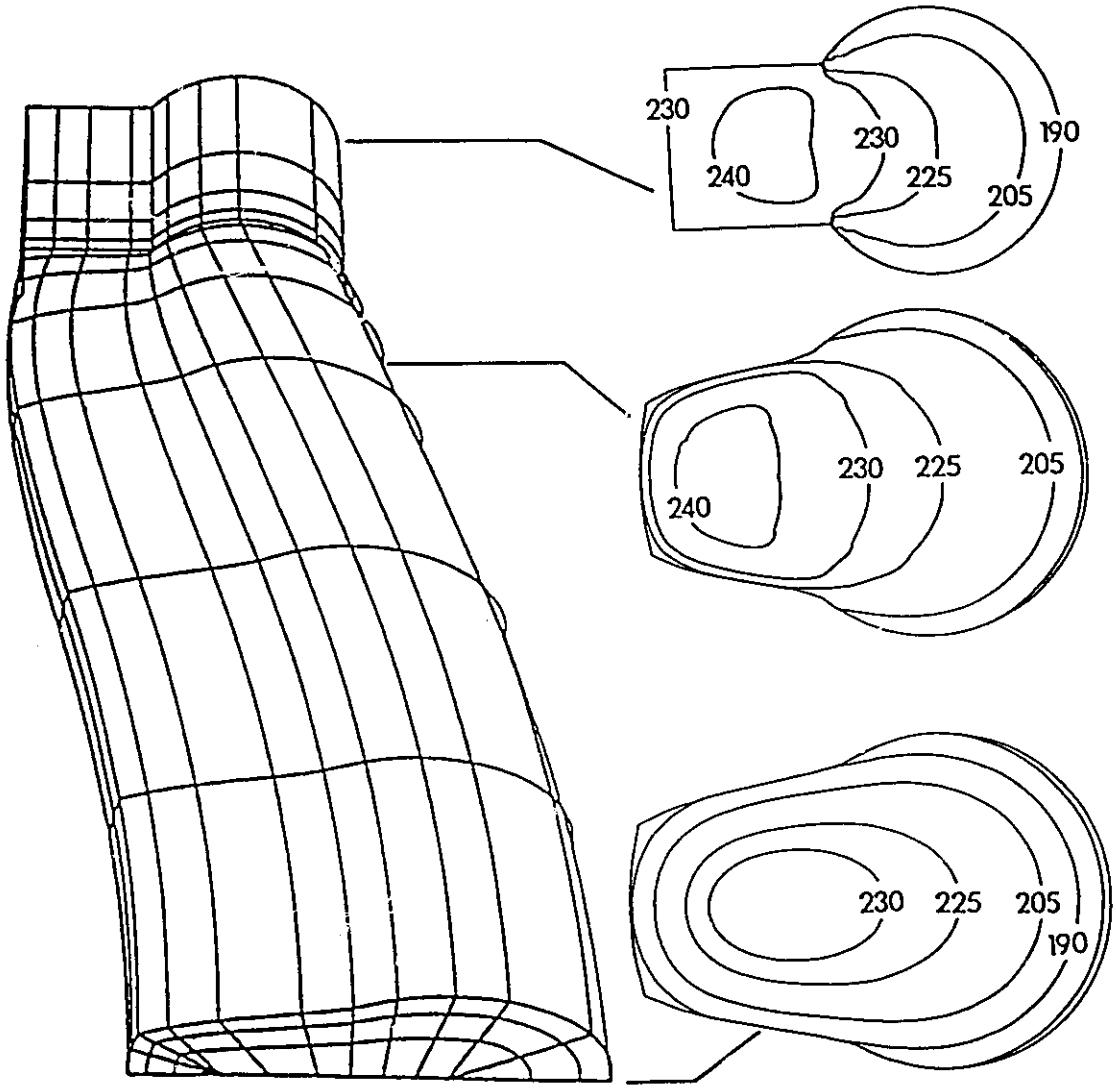

Figure 3.21 Non-isothermal flow out of a key-hole die, average velocity U = 25mm/s. Rectangular section heated at 230°C; round section at 190°C. Bending occurs in the opposite direction than in Figure 3.19.

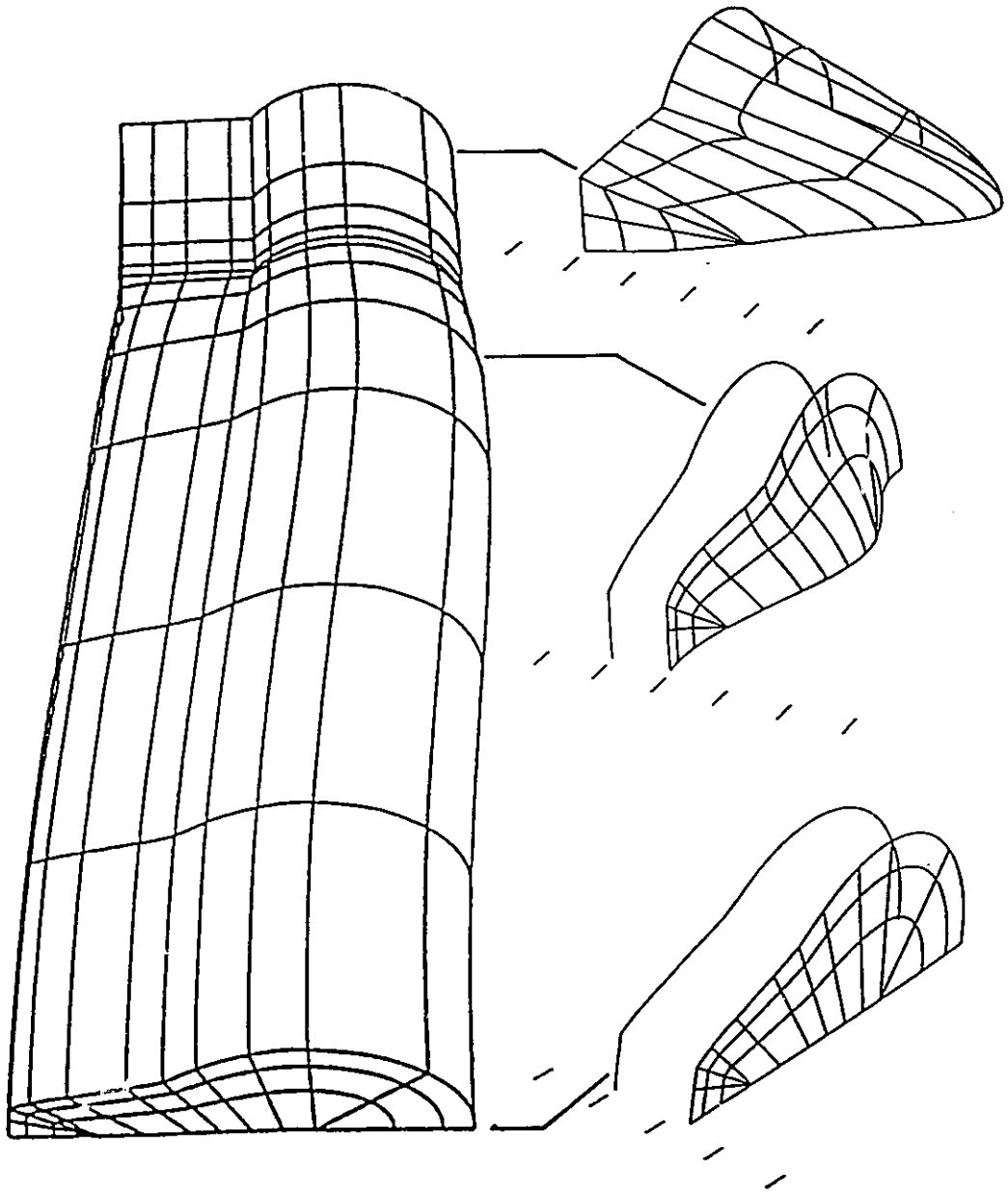

Figure 3.22 Isothermal flow out of a key-hole die. Extrudate bending because of unsymmetric velocity profile.

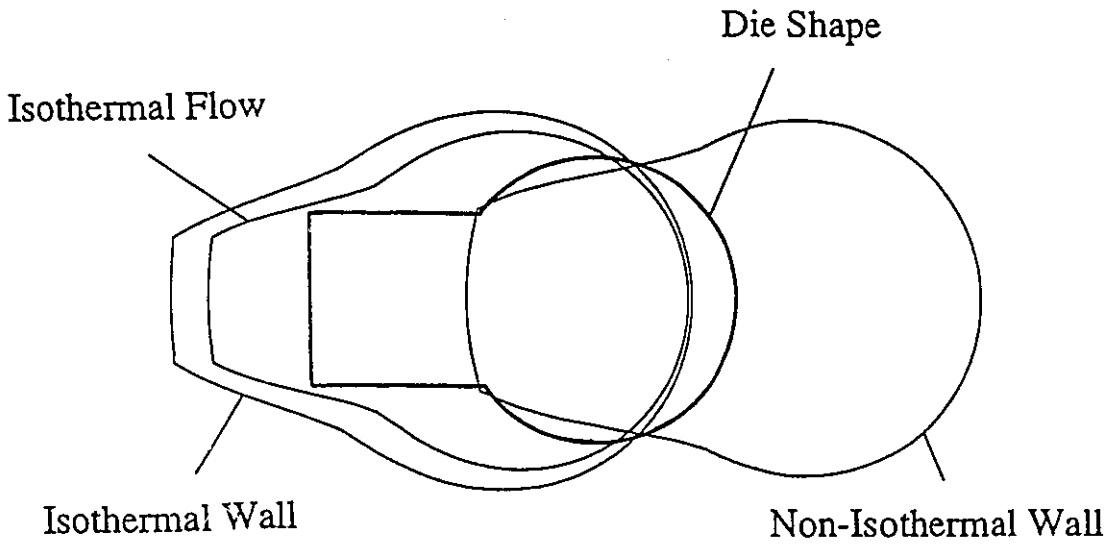

Figure 3.23 Superposed final extrudate shape and die shape for the key-hole dies of Figures 3.20-3.22.

predicts that the extrudate bends toward the rectangular section of the die (Figures 3.22, 3.23) even though no viscosity difference exists.

In this case it is the geometric asymmetry that gives rise to an asymmetric velocity profile (Figure 3.22). The fluid in the round part of the key-hole die is moving faster than it is in the rectangular part. The extrudate bends as a consequence of the fluid rearrangement from the unsymmetric velocity profile to the plug flow profile far downstream.

An experimental investigation that confirmed this prediction was undertaken and is presented next.

3.3.7.4 Experimental Study of Isothermal Flow

To confirm the results of the numerical analysis for the bending of isothermal, creeping Newtonian jets when extruded out of a key-hole shaped die, polystyrene at 190°C was extruded out of a key-hole die under isothermal conditions in an Instron rheometer. The diameter of the experimental die was 4mm and the geometric analogies are the same as in Figures 3.20-3.23.

Figures 3.24a and 3.24b are photographs of the extrudate shape when the polystyrene is extruded downward with an average velocity of 0.042mm/s and 0.127mm/s respectively. The extrudate bends toward the rectangular side in both cases as the analysis predicted.

For the very low extrusion rates studied, no significant contribution of elastic and/or shear thinning properties is expected and therefore the phenomenon is purely viscous Newtonian.

When the extrudate is allowed to emerge in a silicon bath of matching density to eliminate gravity effects, the bending is more obvious. As the average velocity and correspondingly the shearing level was increased, the bending of the extrudate increased

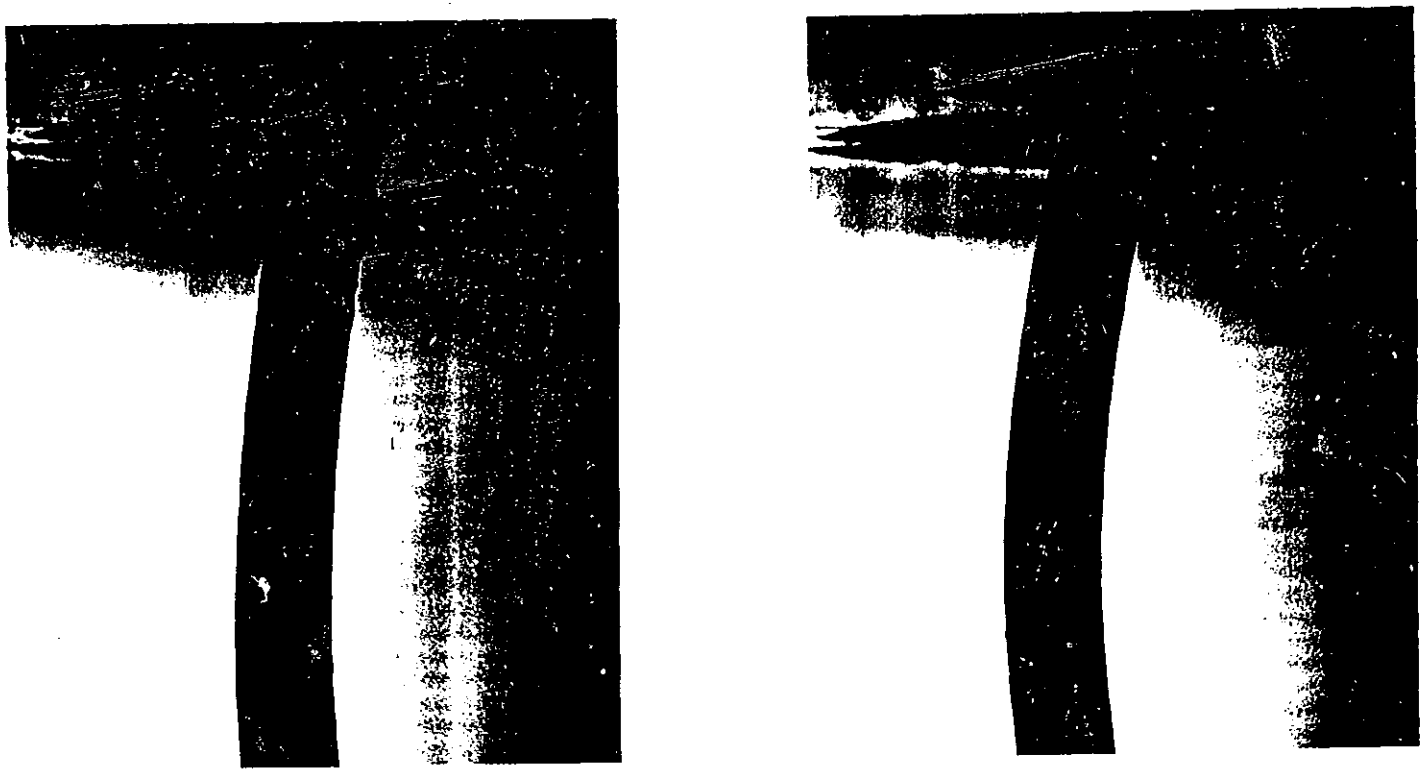

Figure 3.24 Photographs of extrudate bending out of a key-hole die. Isothermal extrusion of polystyrene at 190°C. a) average velocity U = 0.042mm/s, b) average velocity U = 0.127mm/s.

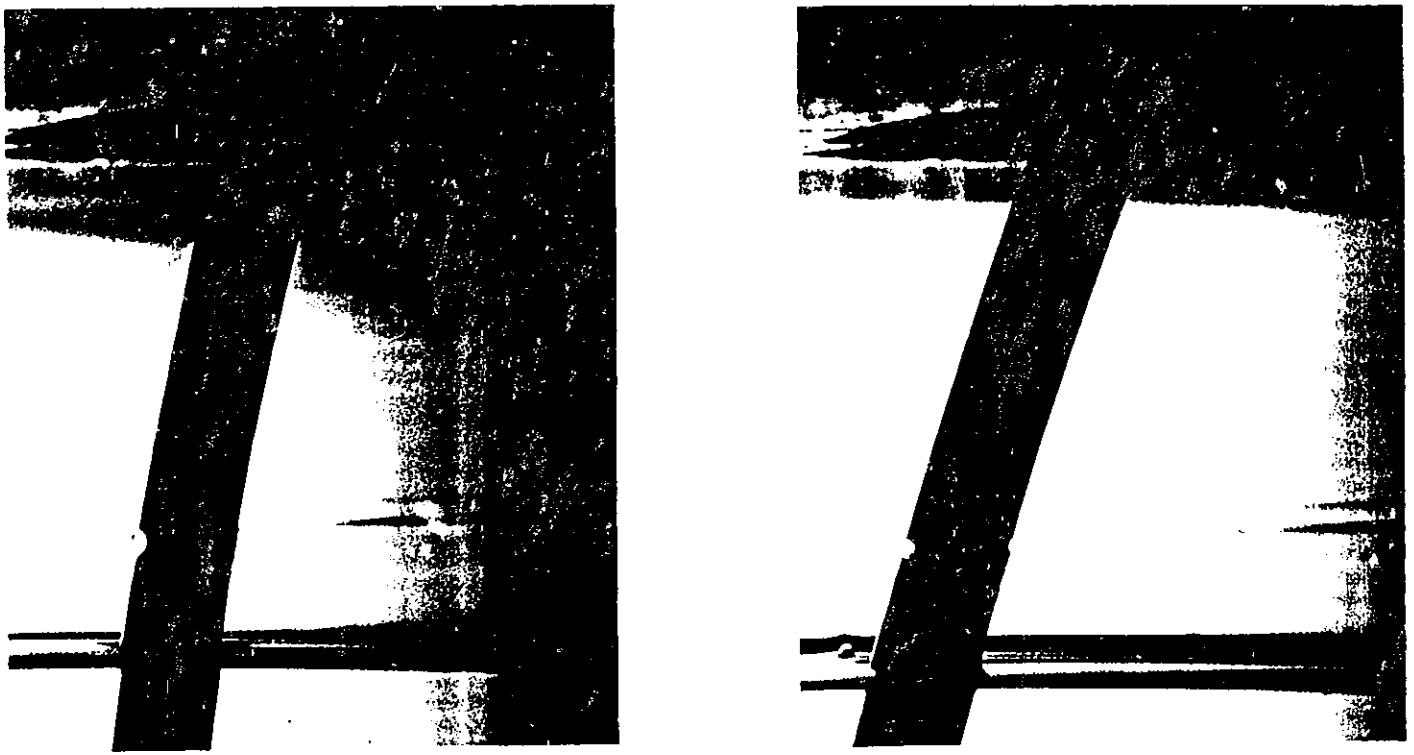

a b

Figure 3.25

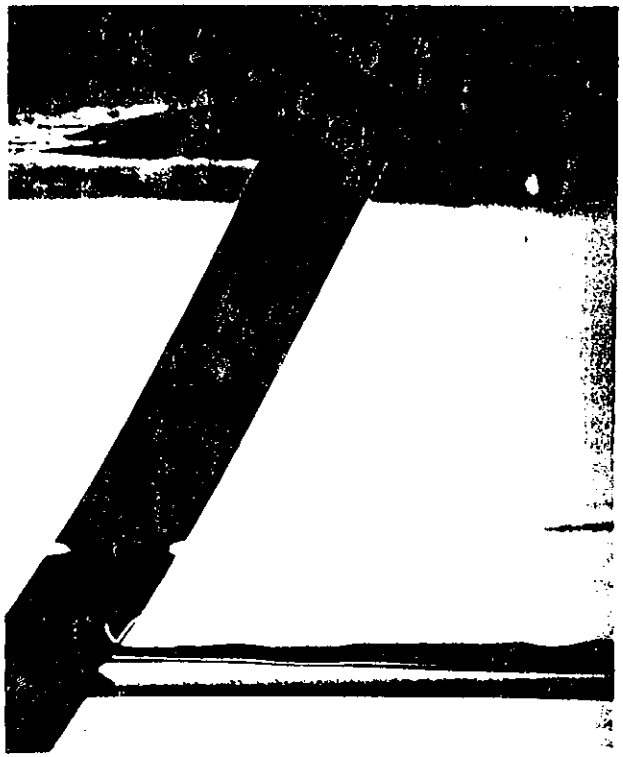

c

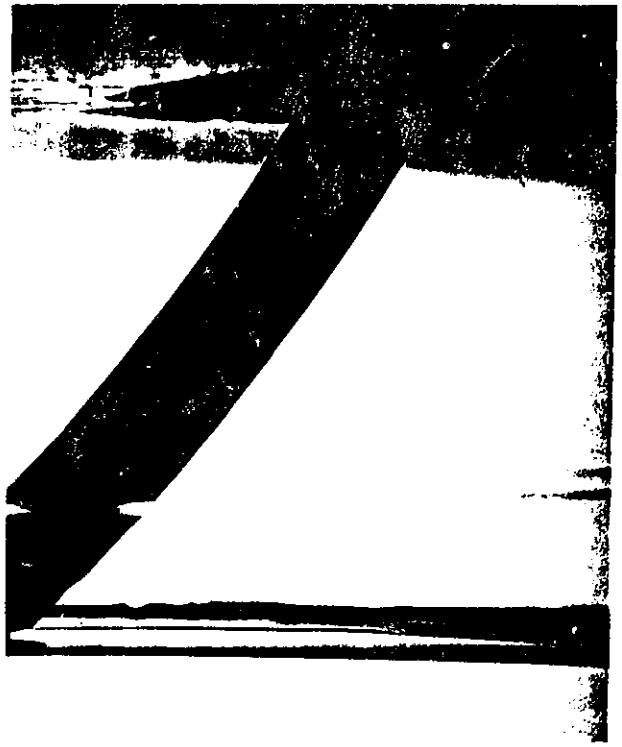

d

Figure 3.25 Photographs of extrudate bending out of a key-hole die. Isothermal extrusion of polystyrene at 190°C. Effect of average velocity; a) U = 0.127mm/s, b) U = 0.42mm/s, c) U = 1.27mm/s and d) U = 4.2mm/s.

dramatically (Figure 3.25). Apparently, as the shearing level increases, the material that is located in areas of higher velocity gradients (round part) is thinning and gives the increasing bending trend. No numerical studies of the shear thinning effect on the extrudate bending were undertaken.

3.4 SUMMARY

The swelling behaviour of creeping, Newtonian jets was studied for several 3-D geometries.

The isothermal study demonstrated the effect of the 3-D geometry on the extrudate swelling behaviour. The presence of geometric singularities (corner points) in the die design results in purely 3-D material redistribution in the extrudate. Generally, the swelling behaviour may be quite uneven and the extrudate shape does not follow exactly the die geometry.

The non-isothermal study displayed the effect of viscous heating and imposed non-isothermal conditions. Where temperature differences arise, pronounced swelling and/or extrudate bending and distortion may occur because of the viscosity-temperature functional relationship. It was shown that geometry may have an effect on the temperature distribution inside the die, because of uneven viscous dissipation, which may result to extrudate bending and unique swelling behaviour.

In the case of unsymmetric geometric shapes, bending of the extrudate may occur even in isothermal flows because of the asymmetry of the velocity profile. This prediction was also verified experimentally for the case of key-hole shaped dies.

Also, the numerical method is robust enough to handle gross movement of the extrudate in space (bending). Not only do the free surface nodal positions move in space but the spines themselves move as well to follow the complex swelling behaviour.

CHAPTER 4

UNIDIRECTIONAL ANALYSIS OF BICOMPONENT FLOWS

4.1 INTRODUCTION

This Chapter presents the analysis of the stratified flow of two immiscible fluids having different viscous properties in long dies of arbitrary shape. The flow is considered in the unidirectional regime with zero Reynolds number. Figure 4.1 presents a schematic of such a bicomponent flow and a literature review is given in section 1.2.2. Mathematically, the problem has a continuum of solutions corresponding to arbitrarily prescribed interface shapes but experimental evidence indicates the existence of a unique interface shape with the less viscous fluid encapsulating the more viscous fluid. With the introduction of the minimum viscous dissipation principle, which postulates that the amount of viscous dissipation is minimized for a given flow rate, the problem becomes a non-linearly constrained optimization problem. A Generalized Reduced Gradient-Galerkin/finite element method combination was developed to tackle the problem of the interface shape calculation when two inelastic fluids are considered. The effect of the viscosity ratio and flow-rate ratio on the interface shape is examined for different die geometries. Inner layer break-up phenomena are indicated and explained for complex die geometries.

4.2 PROBLEM FORMULATION

The process involves the flow of two components forming continuous phases which are separated from each other by continuous boundaries (interfaces, Figure 4.1). Because of the difference in the viscous properties, the less viscous fluid tends to wrap around and

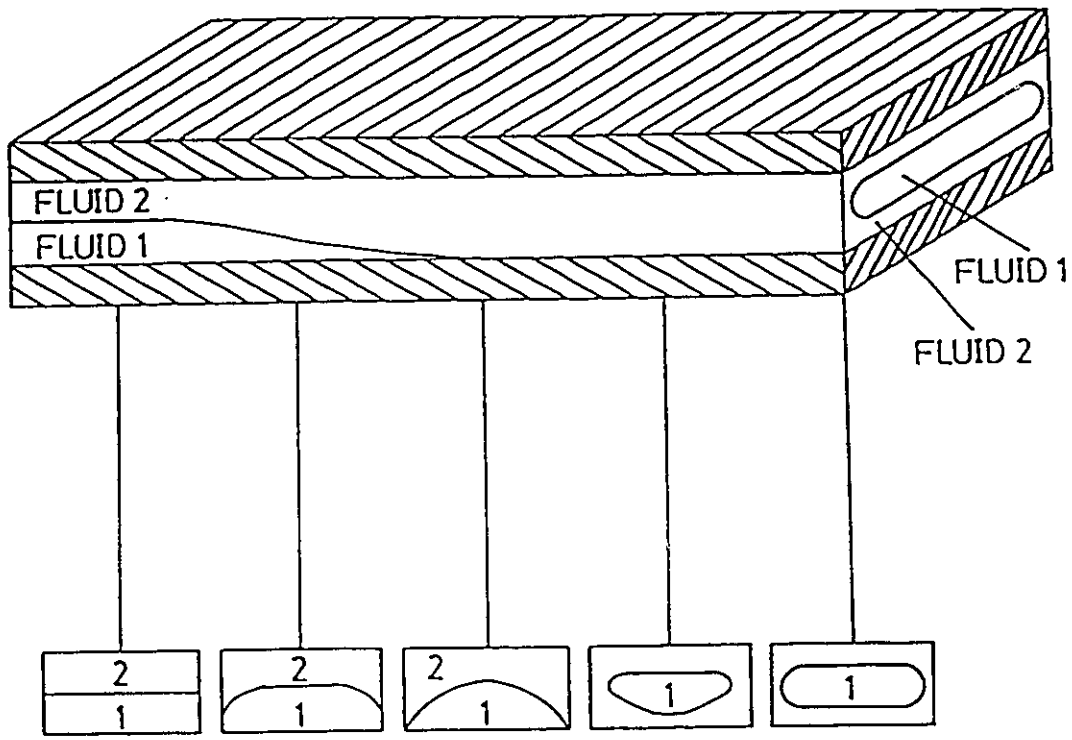

Figure 4.1 Schematic representation of the coextrusion of two immiscible fluids. Fluid 2 is less viscous and encapsulates fluid 1.

encapsulate the more viscous fluid. Here, the problem of the interface shape prediction in the stratified bicomponent flow in long dies of arbitrary cross-section is considered.

4.2.1 Governing Equations

The coextrusion of two immiscible fluids is shown schematically in Figure 4.1. Provided that the die is sufficiently long, the less viscous fluid (fluid 2) encapsulates the more viscous fluid (fluid 1).

The change of the interface shape downstream is a fully three dimensional problem because it occurs in the cross-flow direction and only a small subset will be covered here, namely the unidirectional flow in the fully developed region (far downstream) inside the die. The flow is steady, creeping with no body forces and driven by a prescribed pressure gradient.

The equations governing the flow are the steady Navier-Stokes equations with the velocity and pressure gradient in the x-direction (Fig. 4.2). The density of the two fluids is assumed equal to eliminate any gravitational effects. The two fluids flow in a duct of arbitrary cross-section bounded by the curve Γ. The flow-rates are Q_1 and Q_2 respectively and the ratio of flow-rates is fixed.

The momentum and mass balances reduce to:

$$\frac{\partial}{\partial y'}\left(\mu_i' \frac{\partial u'}{\partial y'}\right) + \frac{\partial}{\partial z'}\left(\mu_i' \frac{\partial u'}{\partial z'}\right) = \frac{\partial P'}{\partial x'}, \qquad \text{in } \Omega_i, \quad i = 1,2 \tag{4.1}$$

$$\frac{Q_1}{Q_2} = \frac{\int_{\Omega_1} u'(y',z')\,d\Omega}{\int_{\Omega_2} u'(y',z')\,d\Omega} = q \tag{4.2}$$

$$u' = 0 \text{ on } \Gamma \tag{4.3}$$

with μ_i' = constant for Newtonian fluids and

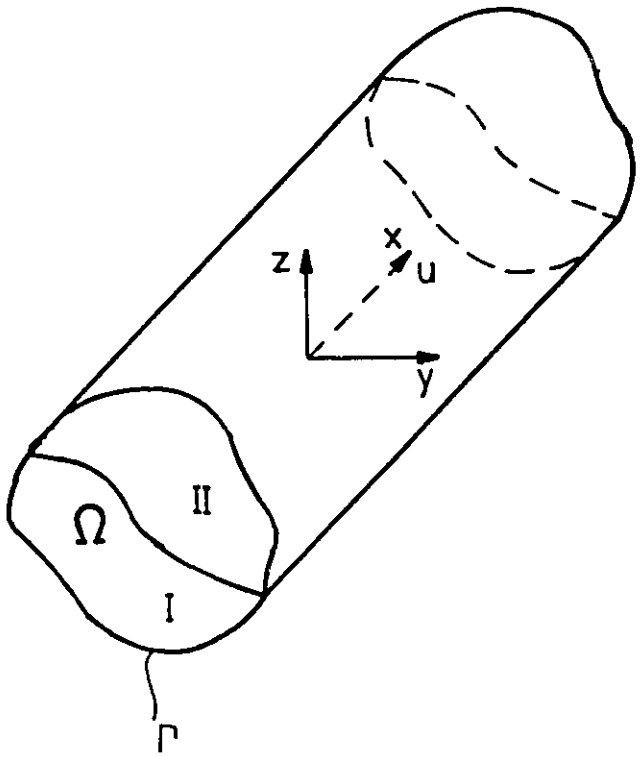

Figure 4.2 Schematic diagram of flow domain.

$$\mu_i' = \mu_{oi}' \left[1 + (\lambda_i \dot{\gamma})^2 \right]^{(n_i - 1)/2} \qquad \text{for Carreau fluids} \tag{4.4}$$

where $\dot{\gamma}$ is the square root of one half the second invariant of the strain- rate tensor

$$\dot{\gamma} = \sqrt{\frac{1}{2} \underline{\underline{\dot{\gamma}}} : \underline{\underline{\dot{\gamma}}}} \tag{4.5}$$

which in this case reduces to

$$\dot{\gamma} = \left[\left(\frac{\partial u'}{\partial y'} \right)^2 + \left(\frac{\partial u'}{\partial z'} \right)^2 \right]^{1/2} \tag{4.6}$$

The system is written in dimensionless form using the following scales :

Length scale	L	characteristic dimension of problem geometry
Viscosity scale	$\mu_c' = \mu_1'$	viscosity of the more viscous fluid for the Newtonian case
	$\mu_c' = \mu_{01}'$	maximum zero shear viscosity of the two Carreau fluids

Velocity scale

$$U = \frac{\left| \frac{\partial P'}{\partial x'} \right| L^2}{\mu_c'}$$

The following dimensionless variables are defined:

$$u = \frac{u'}{U} , \qquad \mu_i = \frac{\mu_i'}{\mu_c'}$$

$$y = \frac{y'}{L} , \qquad z = \frac{z'}{L}$$

and the system is written in dimensionless form as:

$$\frac{\partial}{\partial y}\left(\mu_i \frac{\partial u}{\partial y} \right) + \frac{\partial}{\partial z}\left(\mu_i \frac{\partial u}{\partial z} \right) + 1 = 0 , \qquad \text{in } \Omega_i , \quad i = 1, 2 \tag{4.7}$$

$$\frac{\int_{\Omega_1} u(y,z)\, d\Omega}{\int_{\Omega_2} u(y,z)\, d\Omega} = q \tag{4.8}$$

$$u = 0 \text{ on } \Gamma \tag{4.9}$$

with the dimensionless viscosity for Newtonian and Carreau fluids respectively:

$$\mu_i = \text{constant.}$$

$$\mu_i = \frac{\mu_{oi}}{\mu_c}\left\{1+\left(\lambda_i^2\frac{U^2}{L^2}\right)\left[\left(\frac{\partial u}{\partial y}\right)^2+\left(\frac{\partial u}{\partial z}\right)^2\right]\right\}^{(n_i-1)/2} \tag{4.10}$$

4.2.2 The Minimum Viscous Dissipation Principle

In unidirectional flow and in the absence of surface tension effects which is the case with polymeric materials, the velocity and stress continuity boundary conditions at the interface are automatically satisfied. The number of possible solutions allowed by equations (4.7)-(4.9) is infinite and, moreover, the solution need not be unique (Joseph et al., 1984a, 1984b). On the other hand, experiments indicate that whatever the initial configuration, the low-viscosity material will eventually encapsulate the high-viscosity material (Charles and Redberger, 1962; Everage, 1973; Hasson and Nir, 1970; Minagawa and White, 1975; Southern and Ballman; 1973, White and Lee, 1975; Williams, 1975; Yu and Sparrow, 1969).

The experimentally observed existence of a unique configuration has been explained so far (Everage, 1973; Southern and Ballman, 1973; Williams, 1975; MacLean, 1973) with the aid of the viscous dissipation principle which postulates that the flow chooses a phase configuration and interface shape that in some sense minimize the viscous dissipation for a given flow rate, or, equivalently, maximize the volume flux for a given pressure gradient. The principle has not been proven to be mathematically rigorous for the stratified flow of two or more fluids but is an empirical observation.

In this section, the minimum viscous dissipation principle is adopted in the form of maximizing the flow rate for a prescribed pressure gradient and the problem of interface determination for the flow of two polymers in a die can then be expressed as a non-linear optimization problem:

To determine the vector of unknowns $\underline{X}=(\underline{u},\underline{h})$, i.e. the velocity field $\underline{u}(y,z)$ and the interface position parameters $\underline{h}(y,z)$,

$$\begin{aligned} &\text{Maximize } Q = Q_1 + Q_2 \\ &\text{subject to: Navier-Stokes equations} \\ &\qquad\qquad \text{Flow-rate ratio} \\ &\qquad\qquad \text{Given pressure gradient} \\ &\qquad\qquad \text{Boundary conditions} \end{aligned} \tag{4.11}$$

The velocity $\underline{u}(y,z)$ must vanish on the boundary of the die and be continuous across the interface. The continuity of shear stress across the interface is satisfied automatically as a natural boundary condition. Solution of the optimization problem gives the interface shape and the velocity field.

The Galerkin/finite element method was employed to discretize equations (4.7)-(4.10) into a set of nonlinear algebraic equations. A Generalized Reduced Gradient method was used to solve the optimization problem.

4.2.3 Galerkin/Finite Element Formulation

A typical discretization with the interface parametrization is shown in Figure 4.3. The 6-node isoparametric and 9-node Lagrangian isoparametric elements are used. The interface is parametrized as the distance h^i along the i-th spine. Each spine is defined by a base point and a unit vector $\underline{e}^i$. Interface nodes are defined as $\underline{x}^i_F=\underline{x}^i_F+h^i*\underline{e}^i$, while the other nodes along the spine move in proportion to the interface node.

In the discrete system, the unknowns are the nodal velocities u^i and the interface parameters h^i.

Equations (4.7) and (4.8) are written in the discretized form as :

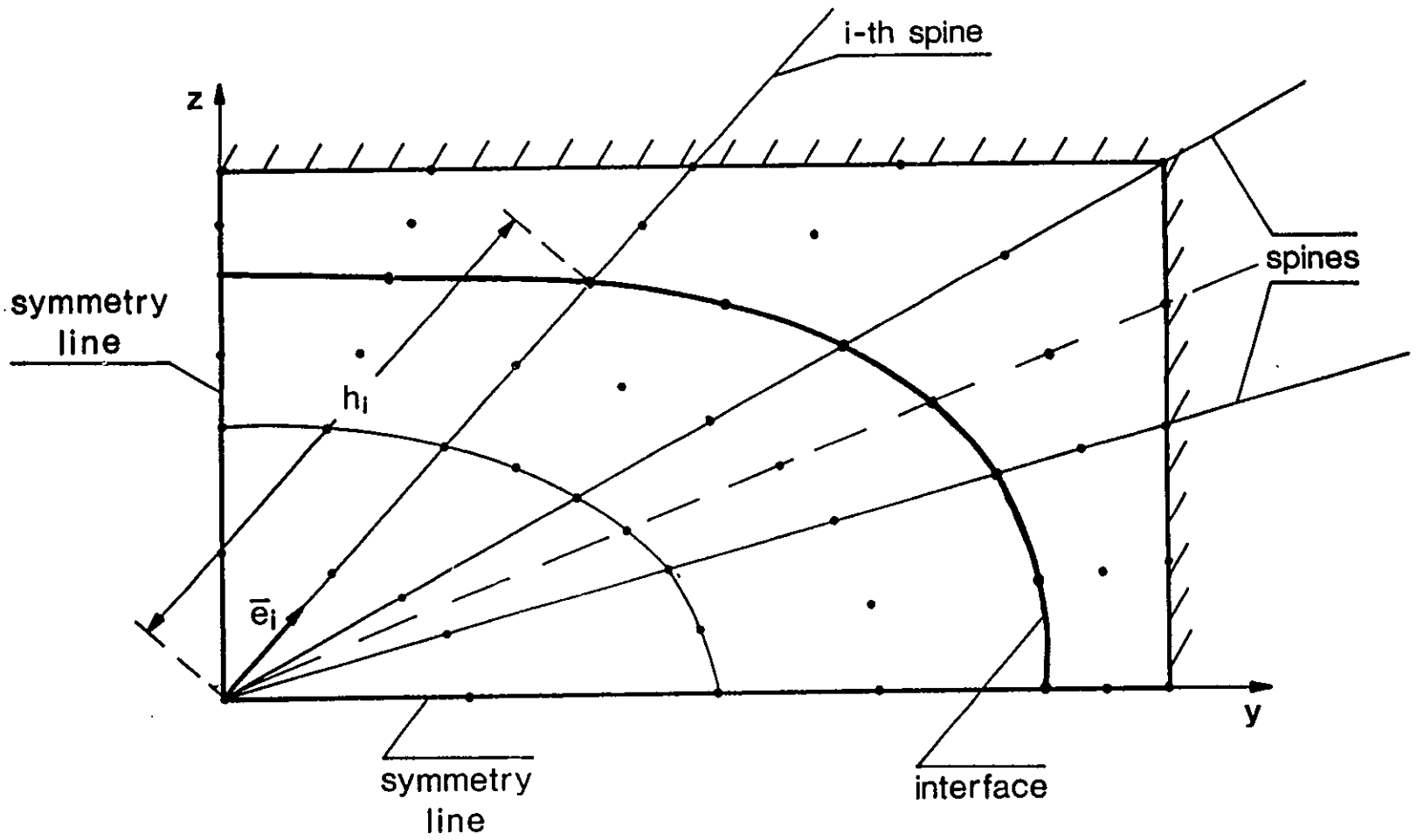

Figure 4.3 Finite element discretization and interface parametrization with spines.

$$R_i = \int_{-1}^{1}\int_{-1}^{1} \{\mu(N^i_y u_y + N^i_z u_z) - N^i\}|J^*|\,d\xi\,d\eta \tag{4.12}$$

$$\sum_1 \int_{-1}^{1}\int_{-1}^{1} u|J^*|\,d\xi\,d\eta - q \sum \int_{-1}^{1}\int_{-1}^{1} u|J^*|\,d\xi\,d\eta = 0 \tag{4.13}$$

where $|J^*| = y_\xi z_\eta - z_\xi y_\eta$ is the determinant of the Jacobian of the isoparametric (y,z)-(ξ,η) transformation.

Derivatives of the equations (4.12,4.13) with respect to nodal variables are computed analytically.

4.2.1 The Optimization Algorithm - GRG method.

A Generalized Reduced Gradient method was used to solve the optimization problem of equations (4.11) and is described in detail in Reklaitis et al. (1983).

The basic idea underlying the GRG method is that it decomposes the set of n unknowns $\underline{X}$ into

$$\underline{X} = (\underline{Y}, \underline{Z})$$

where $\underline{Y}$: a set of m dependent variables which are calculated through the m constraints (Navier-Stokes equations and flow-rate ratio) and

$\underline{Z}$: a set of (n–m) independent variables which are used to calculate a Reduced Gradient for the necessary conditions of optimality.

The total number of unknowns (n) consists of the number of nodal velocities (n_c) and the number of interface parameters (n_h) so that

$$n = n_c + n_h$$

The number of available equations consists of n_c equations for the nodal velocities from the finite element formulation of the Navier-Stokes equations, and the flow rate constraint so that

$$n_a = n_c + 1 = m$$

In the specific implementation, the vector $\underline{Y}$ of dependent variables consists of the nodal velocities and one parameter h which is chosen arbitrarily and the vector $\underline{Z}$ consists of the rest of parameters h.

The Newton-Raphson method of iteration is used to solve the set of non-linear algebraic equations resulting at every step of the optimization procedure and converges normally within 2-5 iterations. In some cases, a strategy of relaxing the tolerances of the constrained equations at the beginning was followed to allow for greater steps toward the optimum. As the procedure was approaching the optimum, the tolerances were gradually decreased to ensure the feasibility of the solution.

4.3 RECTANGULAR DIE OF ASPECT RATIO 2:1

The creeping flow of two Newtonian fluids in a rectangular die of aspect ratio 2:1 is considered (Figure 4.4). The tendency of the less viscous fluid to encapsulate the more viscous fluid is shown and the interface shape for different viscosity and flowrate ratios of the materials is calculated.

4.3.1 Prediction of Encapsulation

The evolution of the interface shape for the case of two Newtonian fluids with equal flow-rates and viscosity ratio (more viscous : less viscous) of 2:1 flowing in a rectangular duct of aspect ratio 2:1 is shown in Figure 4.4 for different steps in the optimization procedure. Figure 4.4a is the starting point with a flat interface in a side-by-side configuration. The method predicts that a more probable configuration would be one where the less viscous fluid would at least partially encapsulate the more viscous fluid (Figure 4.4b). At this point the procedure is stopped and the flow domain is remeshed with the interface ending on the bottom

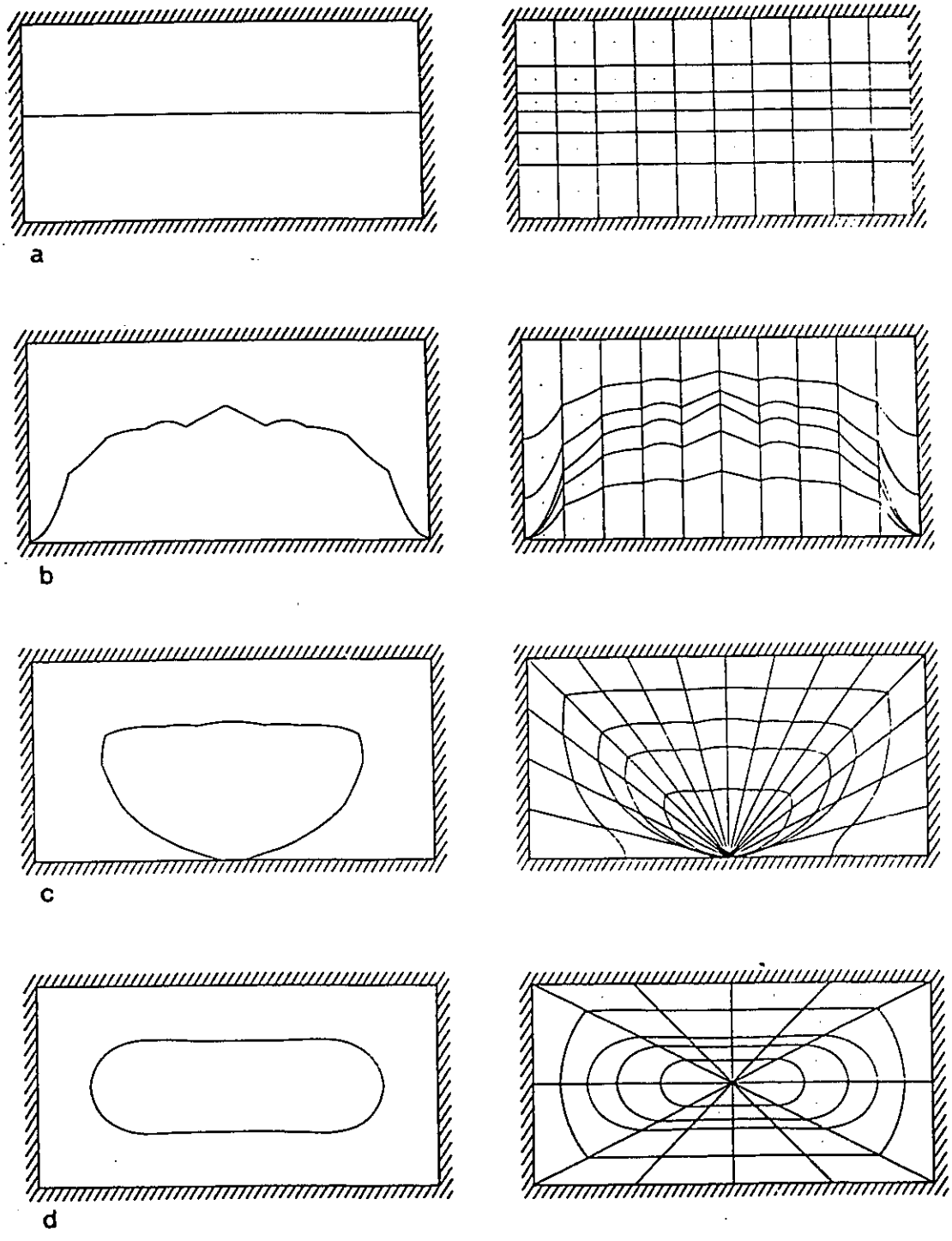

Figure 4.4 Evolution of the interface in the optimization procedure. Newtonian fluids; viscosity ratio 2:1; aspect ratio 2:1.

wall. This reparametrization does not force the solution to a certain direction as is indicated by the minimal change of the reduced gradient. The grid consists of both six-node and nine-node elements and the method predicts the totally encapsulated configuration (Figure 4.4c). The grid collapses into a point on the bottom wall and the procedure is stopped again, and after remeshing, with the more viscous fluid totally encapsulated, the method yields the solution of Figure 4.4d with the more viscous fluid located at the core and the less viscous fluid wetting the walls. This configuration is in agreement with the experimental evidence and produces the maximum flow-rate for the given pressure gradient. The ratio of the total volumetric flow-rate between the encapsulated and the side-by-side configuration was

$$Q_{\text{encapsulated}} / Q_{\text{side-by-side}} = 1.4$$

The method is robust since it is capable of predicting the encapsulated optimum solution even if it starts initially with a side-by-side configuration.

4.3.2 Effect of Flowrate Ratio and Viscosity Ratio on the Interface Shape

The method can be used to study the effect of the flowrate and viscosity ratio on the shape of the core (more viscous) layer, since encapsulated flows occur in a number of industrial processes (multi-layer fibers, profiles and films).

The results of a systematic analysis of the effect of the flow-rate ratio for a constant viscosity ratio in the same rectangular die of aspect ratio 2:1 are shown in Figure 4.5. As the flow-rate ratio is increased, the area occupied by the more viscous core fluid increases and the interface is pushed toward the walls. The curvature of the interface exhibits a reversal in the regions near the center of the flat walls and a similar behaviour is observed when the effect of the viscosity ratio for constant flow-rate ratio is examined in the same geometry (Figure 4.6). This phenomenon is the result of the different shearing that the material experiences in different sections of the die because of the die geometry. The regions near the corners are

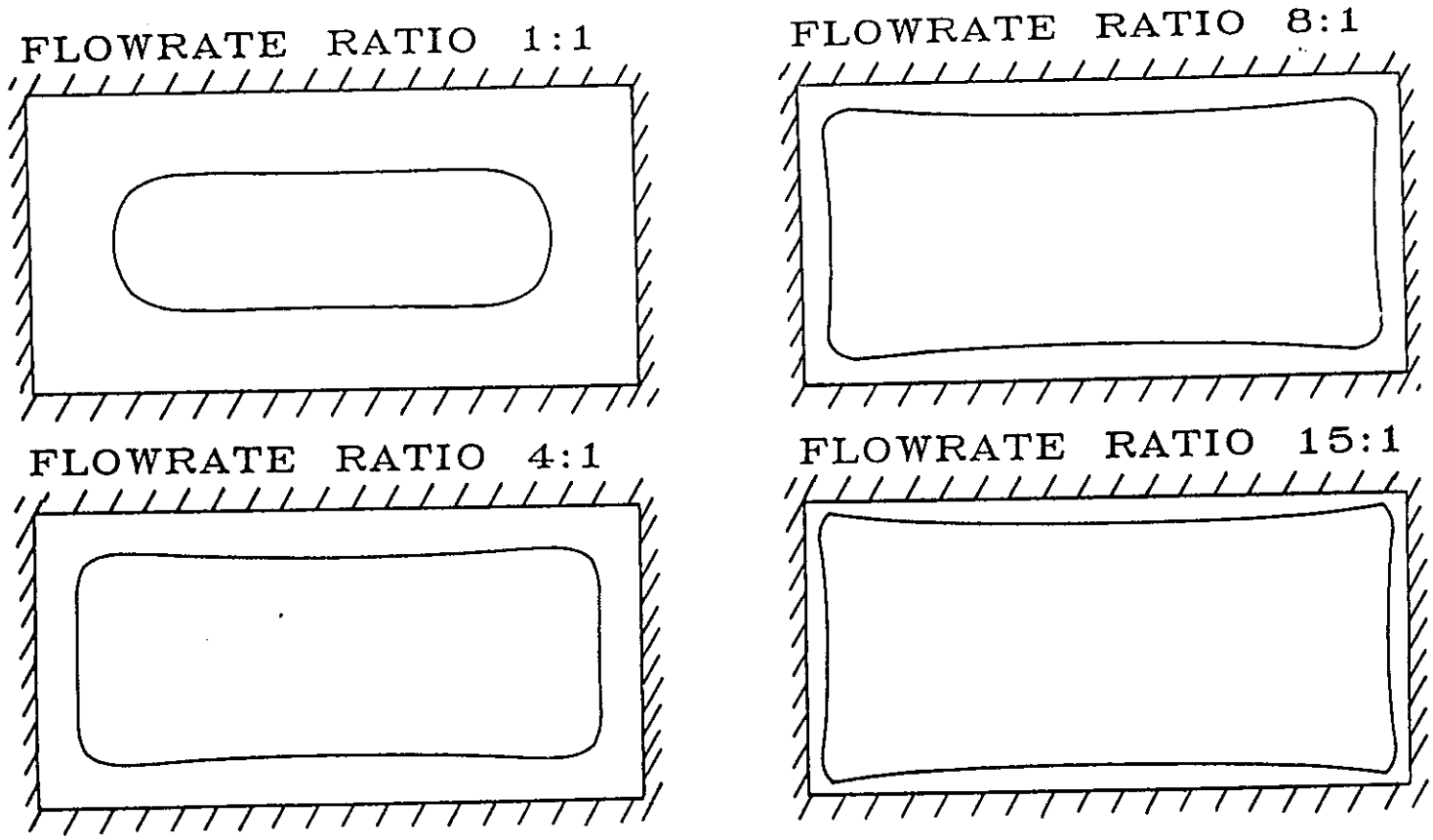

Figure 4.5 Parametric analysis of the effect of the flowrate ratio on the interface shape. Newtonian fluids; viscosity ratio 2:1.

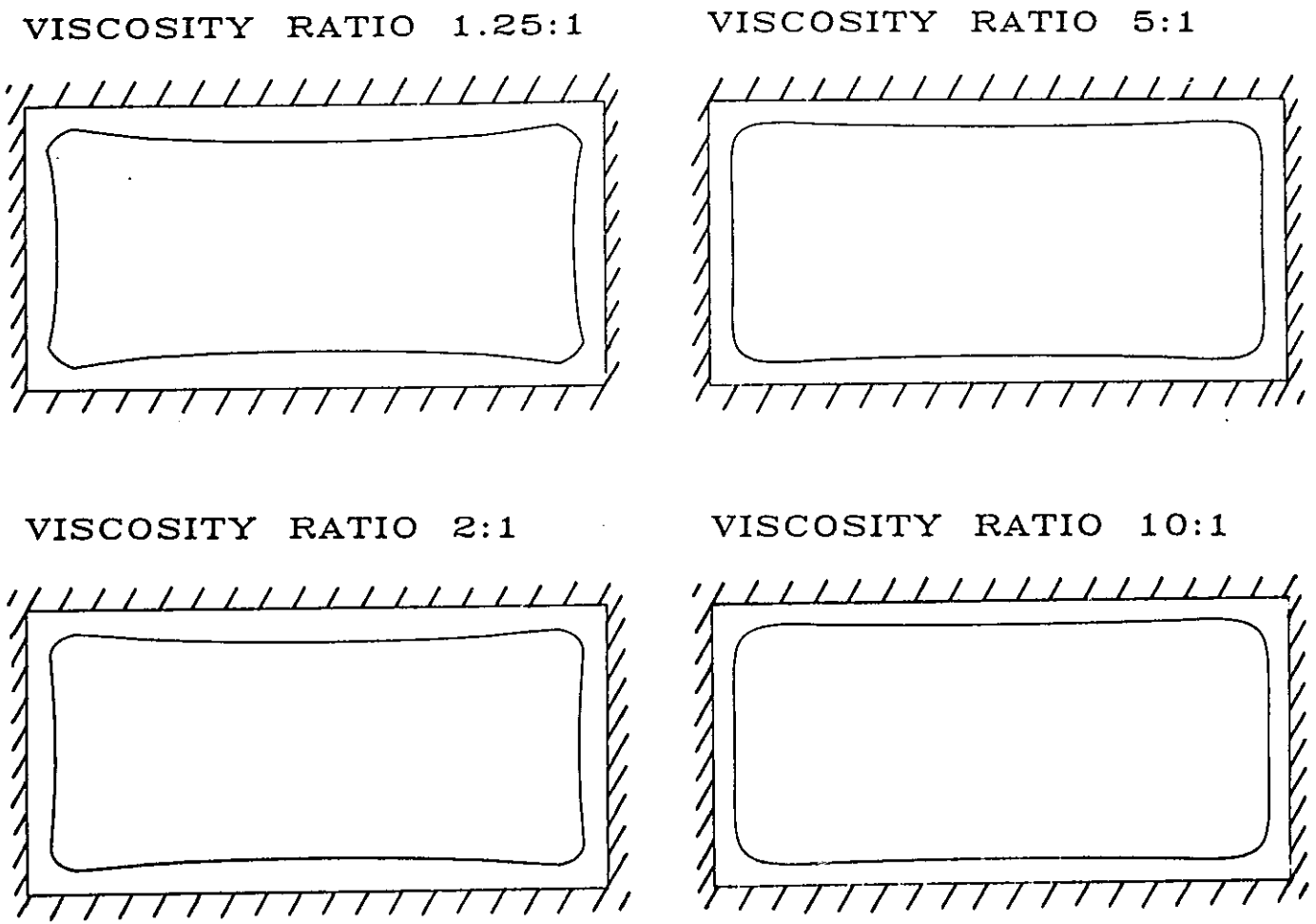

Figure 4.6 Parametric analysis of the effect of the viscosity ratio on the interface shape. Newtonian fluids; flowrate ratio 8:1.

regions of relatively low shear while the regions near the midpoints of the sides are regions of high shear. The more viscous fluid tends to avoid the regions of high shear, where more viscous dissipation occurs due to the steeper gradients, thus giving rise to the different interface shapes.

4.3.3 Shear Thinning Fluids

The phase configuration and interface shape for the stratified flow of two typical Carreau-type shear thinning fluids is considered. The two fluids have the same zero-shear viscosity and their characteristics are given in Table 4.1. Figure 4.7a shows the viscosity curves and Figure 4.7b the predicted interface shape for equal flowrates of the individual fluids.

Because of the shear thinning effects, fluid 2 is less viscous than fluid 1 in the areas of high shearing (near the walls) and the method is capable of predicting the encapsulation of fluid 1 by the less viscous in high shearing fluid 2.

Figures 4.8a and 4.8b show contours of the normalized shear rate and viscosity inside the die. The shearing level is low at the center of the die because of symmetry and is higher in the regions near the center of the flat walls. Correspondingly, viscosity is higher at the center and lower near the walls.

Table 4.1 Characteristics of the Carreau Model Fluids

	μ_0 (N s/m^2)	λ (s)	n
Fluid 1	3200	0.47	0.35
Fluid 2	3200	0.55	0.55

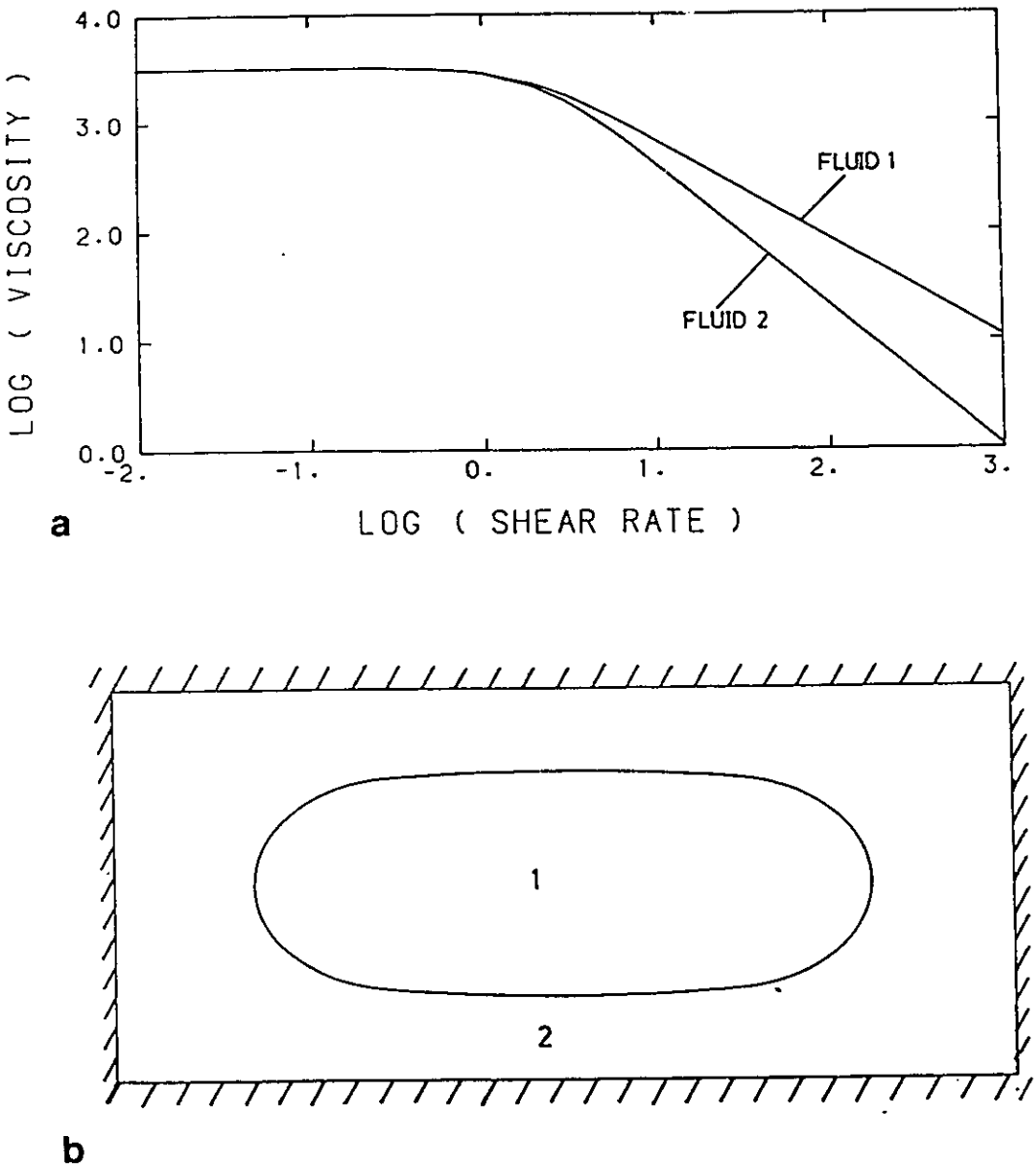

Figure 4.7 a) viscosity curves of two typical Carreau fluids; b) interface shape, die geometry 2cm × 1cm; pressure gradient 10^7 Pa/m.

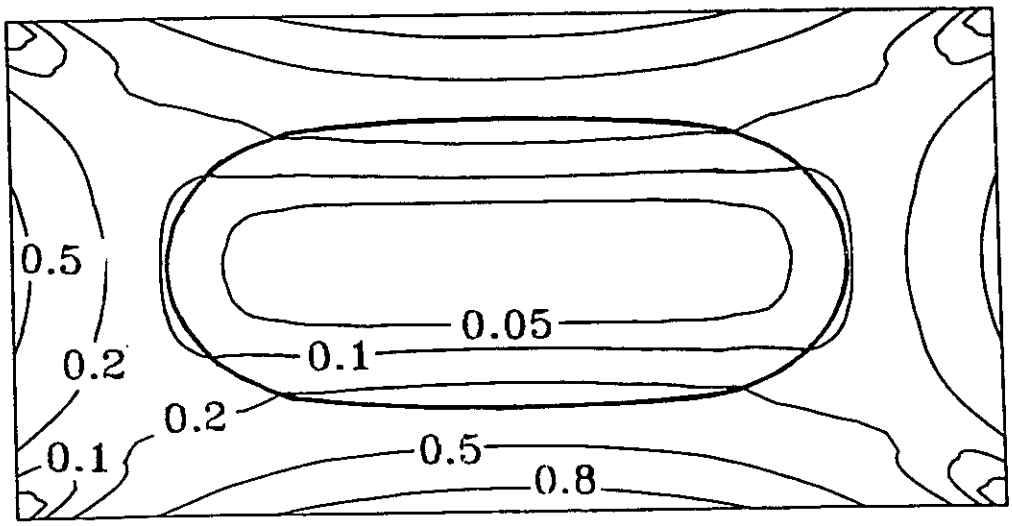

a

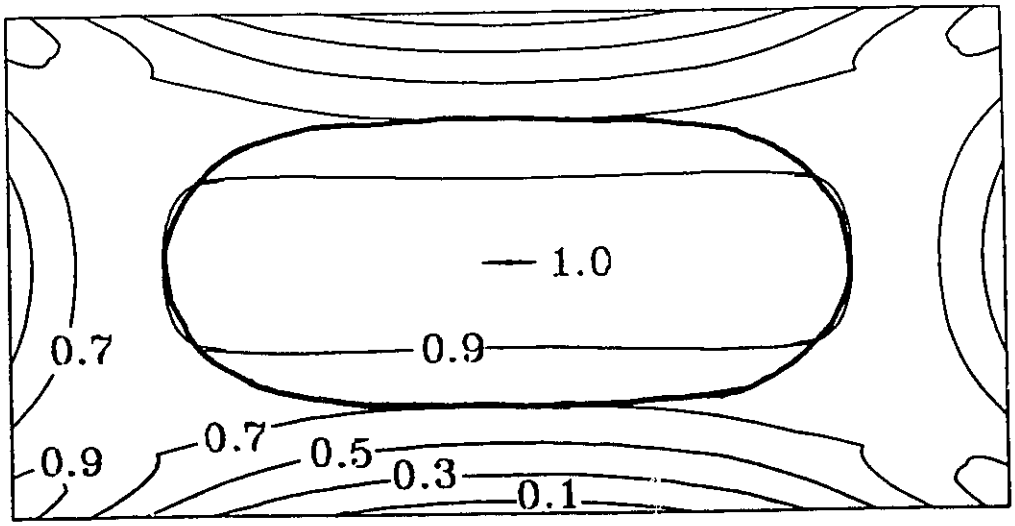

b

Figure 4.8 a) normalized shear rate contours and b) normalized viscosity contours inside the die of Figure 4.7b.

4.4 BOW-TIE DIE

The approach is capable of handling more complex geometries and the stratified flow through a bow-tie type die which is common in industry is examined. The finite element grid is shown in Figure 4.9a and the final interface shape for Newtonian fluids of viscosity ratio 2:1 and flowrate ratio 4:1, in Figure 4.9b.

The inner layer forms a neck at the center of the die following the geometry of the die, but the interface near the corners is smoothed and does not enter far into the corners.

4.5 KEY-HOLE DIE

The stratified flow of two Newtonian fluids with a viscosity ratio of 2:1 through key-hole shaped dies is considered and a typical finite element grid is shown in Figure 4.10. The key-hole die is a complex geometric shape and comprises both a round and a rectangular part. The geometric complexity is expected to give rise to unsymmetric velocity and correspondingly shearing profiles inside the die. The effect of the flowrate ratio is examined and the impact of the geometric shape on the inner layer uniqueness is also addressed.

4.5.1 Effect of Flowrate Ratio

The effect of the flowrate ratio on the interface shape is examined (Figure 4.11). The inner layer does not exactly follow the shape of the die, and is centrally located with the major part located within the round part of the die. As the flowrate ratio increases, the area of flow of the inner layer increases and the interface is pushed toward the walls and into the corners of the rectangular part. The inner layer tends to form a high curvature in the region where the two geometric parts meet since this is expected to be a region of high shearing and would correspondingly induce excessive dissipation.

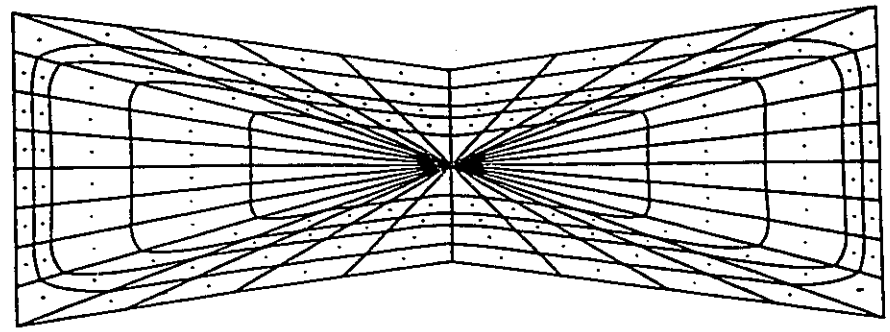

a

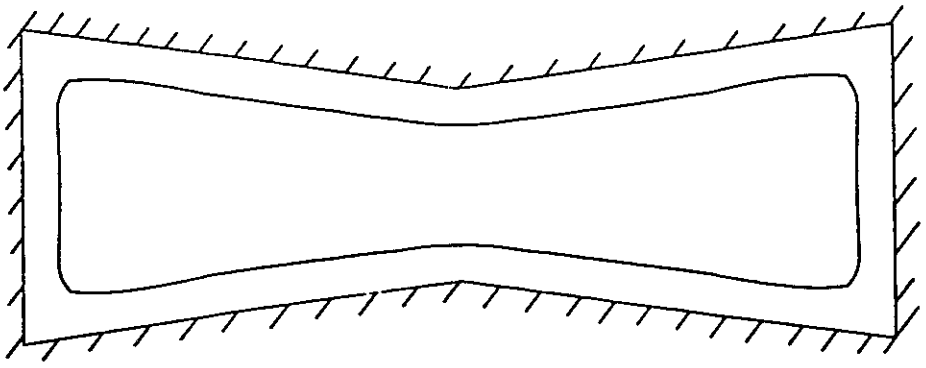

b

Figure 4.9 Bow-tie die geometry. Newtonian fluids; viscosity ratio 2:1; flowrate ratio 4:1. a) finite element grid; b) Interface shape.

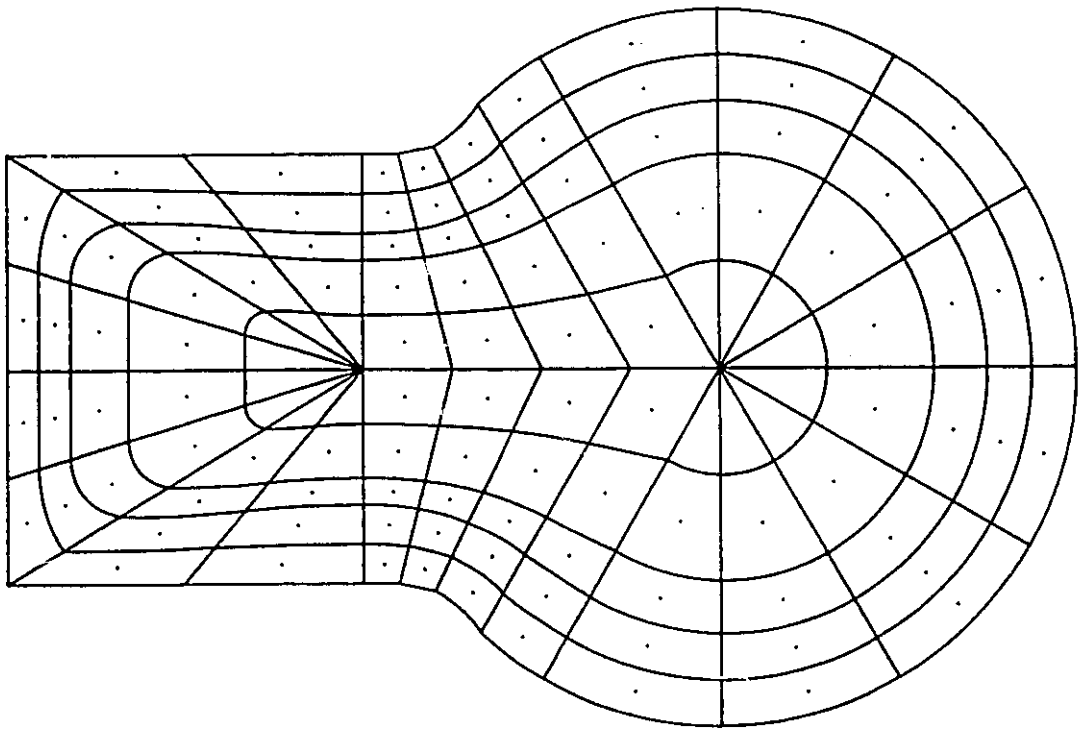

Figure 4.10 Finite element grid for a key-hole type die.

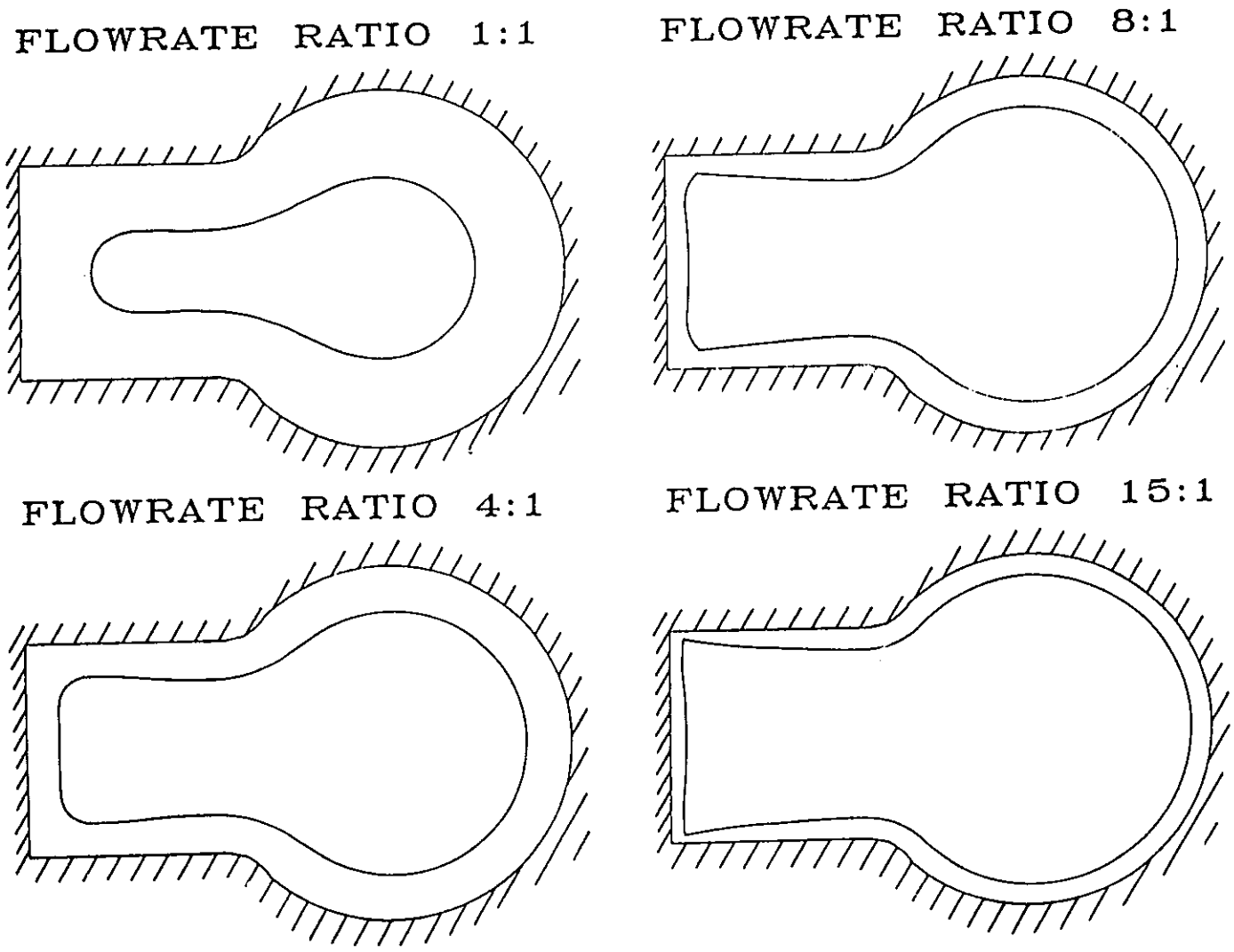

Figure 4.11 Parametric analysis of the effect of the flowrate ratio on the interface shape. Newtonian fluids; viscosity ratio 2:1.

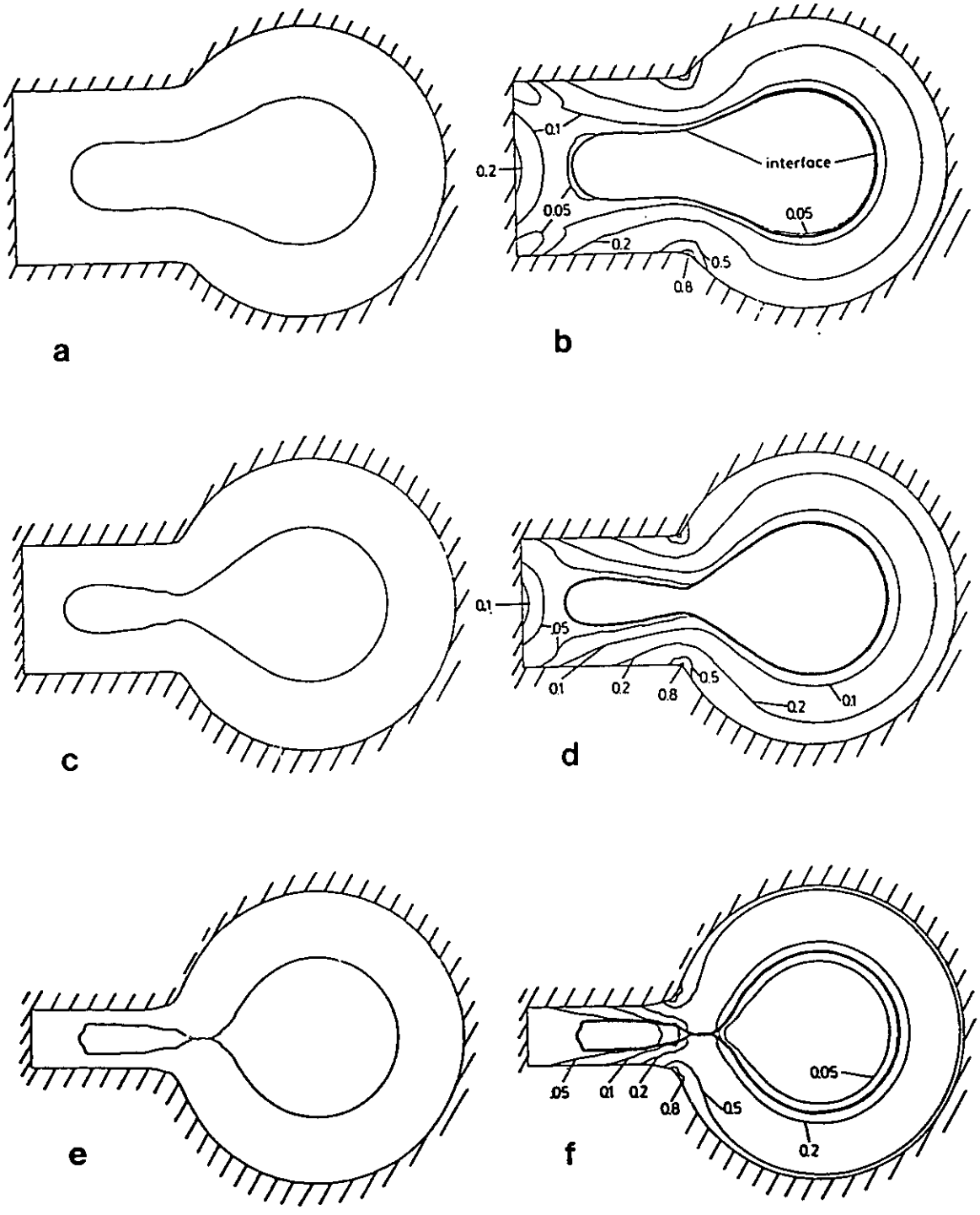

Figure 4.12 Interface shape and contours of normalized shear rate: a),b) wide; c),d) intermediate; and e),f) narrow rectangular section. Newtonian fluids; viscosity ratio 2:1; flowrate ratio 1:1.

4.5.2 Layer Break-Up

The stratified flow through three key-hole dies with different geometric characteristics of the rectangular section is considered (Figure 4.12). The altered geometry changes the shearing distribution inside the die dramatically (Figures 4.12b,d,f) and the effect on the interface shape is severe.

As the rectangular section is narrowed, the inner layer forms a neck (Figure 4.12c) and may even break (Figure 4.12e). To explain this prediction of the optimization procedure, one must consider the shearing distribution inside the die and the corresponding levels of viscous dissipation that would occur. In Figure 3.12b, the inner layer is located within the region of low shear, approximately 5% of the maximum shear observed in the die. In Figure 3.12d, the inner layer is continuous and forms a neck but is still located within the 5% shear region. However, in Figure 4.12f, the die geometry gives rise to two distinct regions of low shear, one located within the round part and another within the rectangular part of the die. Between them, there is a region of relatively higher shear and the inner (more viscous) layer tends to break into two parts to avoid the excessive viscous dissipation that would arise in this area. The more viscous material tends to locate itself within the two regions of low shear and is therefore breaking.

4.6 SUMMARY

A combined Optimization/Finite Element method was developed to allow the simultaneous calculation of the velocity field and interface shape in the unidirectional flow of two immiscible inelastic fluids in a die of arbitrary cross section and very long length.

The method is capable of predicting encapsulation and the effects of viscosity ratio, flowrate ratio and geometry were investigated. Generally, the shape of the interface does not exactly follow that of the die and is a function of the above mentioned factors.

Depending on the geometry, non-unique solutions may exist, and in the flow through complex dies, breakup of the inner (more viscous) layer was indicated for certain die geometries.

The above results have been based on the empirically suggested minimum viscous dissipation principle, but use the fundamental continuity and momentum equations, and are consistent with experimental evidence.

CHAPTER 5

THREE DIMENSIONAL ANALYSIS OF ENCAPSULATED BICOMPONENT STRATIFIED FLOWS

5.1 INTRODUCTION

As was also discussed in Chapter 4, bicomponent stratified flows of molten polymers occur in a number of polymer processing operations, as for example, in the production of bicomponent or biconstituent fibers, in wire and cable coating, etc. The fiber industry for example, has long been involved with the production of structured fibers with a sheath-core configuration (Jeffries, 1971; Paul, 1978; Han, 1981). Here both polymers are not usually exposed to the fiber surface but rather one of the polymers is encased (core) by the other (sheath). The structure is employed when it is desirable for the surface to have the properties of one of the polymers such as luster, dyeability or stability, while the core may contribute to strength or reduced cost. In some cases, the sheath may be used to protect the core from the environment or, if the core material is heat-sensitive, to protect it from coming in contact with the hot die walls by encapsulating it with a more heat-resistive resin. The fiber has normally a circular outer shape, but the core of the filament may have a number of different shapes (Jeffries, 1971; British Patent 1101452; British Patent 1120241; Paul, 1978) depending on the intended use of the product. Other polymer processing areas such as profile extrusion and sheet extrusion also use the same ideas in more complex die geometries.

This chapter intends to study in a 3-D manner, the interface development and the extrudate swelling behaviour of such stratified bicomponent flow systems, examining the effects of different viscosity ratios, flowrate ratios, melt configurations and die geometric shapes.

A three dimensional Galerkin/finite element procedure is used to formulate and study the problem. The existence of both the interface and the external free surface requires special treatment of the unknown free surfaces. The classical spine free surface parametrization is extended to accommodate two spatial unknowns that allows for the simultaneous solution of the field variables and the interface/free surface shapes. Further complications arise from the step change in the fluid properties at the interface and are handled through special numerical techniques.

5.2 GOVERNING EQUATIONS AND BOUNDARY CONDITIONS

The bicomponent stratified flow of immiscible fluids in a sheath-core configuration involves the merging of two fluid streams, their flow inside the die and finally the emergence of the bicomponent system out of the die. Because of the large scale of the three dimensional problems, the overall problem is divided into two sub-problems which are studied separately. The first sub-problem consists of the merging flow of the two fluid streams and the interface shape development in the resulting bicomponent stratified flow inside the die (Figure 5.1). The second sub-problem involves the flow of the bicomponent system out of the die, studies the extrudate swelling behaviour of the bicomponent system and deals with both the interface and the external free surface shape development (Figure 5.2).

The flow fields of the two fluids are governed by the mass and momentum conservation equations in each phase and are coupled through boundary conditions at the interface. The flow is steady, creeping with no body forces and the governing equations written for each fluid are:

$$\nabla \cdot \underline{\tau}_k - \nabla P_k = 0 \quad , \quad k = I,II \tag{5.1}$$

$$\nabla \cdot \underline{v}_k = 0 \quad , \quad k = I,II \tag{5.2}$$

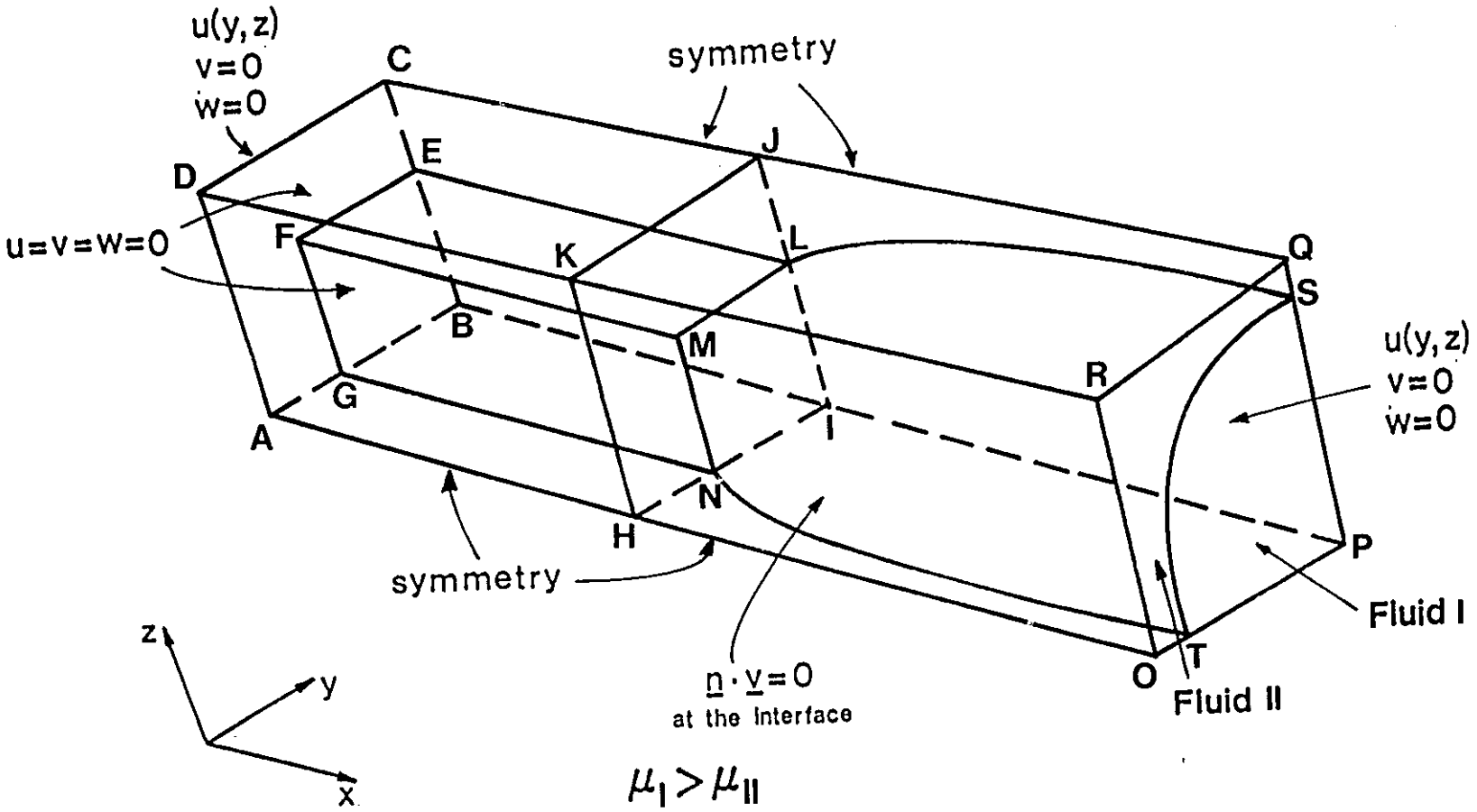

Figure 5.1 Schematic of bicomponent stratified flows with a sheath-core configuration and boundary conditions for the interface development inside the die problem.

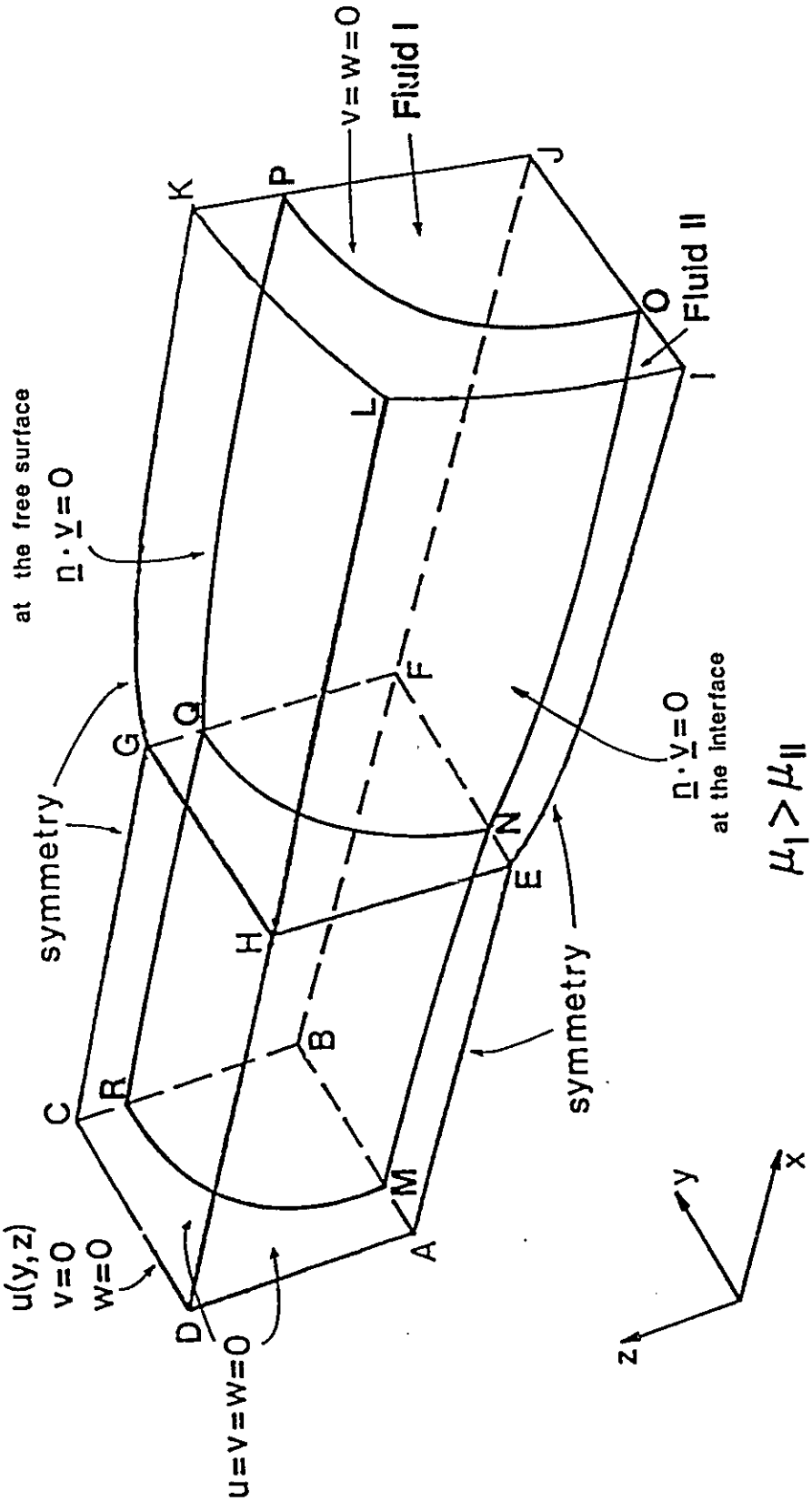

Figure 5.2 Schematic of bicomponent stratified flows with a sheath-core configuration and boundary conditions for the extrudate swelling and interface development outside the die problem.

A characteristic velocity U, length L and the viscosity μ_I of the inner fluid are used to make the variables dimensionless. The extra stress tensor τ is scaled with $\mu_I U/L$ and for the Newtonian case is defined as

$$\tau_{ij} = \mu_k \left[\frac{\partial v_i}{\partial x_j} + \frac{\partial v_j}{\partial x_i} \right], \qquad k = I, II \tag{5.3}$$

Indexes I and II refer to the inner (core) and outer (sheath) layer respectively.

5.2.1 Boundary Conditions. Interface Development Inside the Die

A schematic of the interface development problem for the stratified flow inside the die with the associated boundary conditions is given in Figure 5.1. Initially the two fluids flow through different channels (BEFG-ILMN for fluid I and CDAGFEC-JKHNMLJ for fluid II, Figure 5.1) separated by very thin walls. The two fluids are brought together, the interface LMNTSL forms and its shape changes downstream.

A fully developed profile is assigned initially to each channel (planes CDAGFEC and BEFG, Figure 5.1) which is generated by solving the unidirectional flow problem

$$\frac{\partial}{\partial y}\left(\mu_k \frac{\partial u}{\partial y}\right) + \frac{\partial}{\partial z}\left(\mu_k \frac{\partial u}{\partial z}\right) - \frac{\partial P}{\partial x} = 0, \qquad k = I, II \tag{5.4}$$

for the (y-z) geometry of each channel. The no-slip boundary condition is imposed at the die walls (areas AHORKDA, DKRQJCD Figure 5.1) and the internal channel walls (areas GNMFG, FMLEF).

The two fluids are brought together at the HIJK plane. The velocity boundary conditions at the interface LMNTSL are:

vanishing velocity normal to the interface (kinematic condition),

$$\underline{n} \cdot \underline{v} = 0 \tag{5.5}$$

continuity of tangential velocities,

$$\underline{t}_I \cdot \underline{v}_I = \underline{t}_I \cdot \underline{v}_{II} \tag{5.6}$$

$$\underline{t}_2 \cdot \underline{v}_I = \underline{t}_2 \cdot \underline{v}_{II} \tag{5.7}$$

where $\underline{n}$ is the normal vector and $\underline{t}_1, \underline{t}_2$ the tangential vectors at the interface.

Forces at the interface must be in equilibrium since the interface is a material surface, and the dynamic boundary conditions are

$$\underline{t}_1 \cdot \underline{\underline{g}}_I = \underline{t}_1 \cdot \underline{\underline{g}}_{II} \tag{5.8}$$

$$\underline{t}_2 \cdot \underline{\underline{g}}_I = \underline{t}_2 \cdot \underline{\underline{g}}_{II} \tag{5.9}$$

$$\underline{n} \cdot \underline{\underline{g}}_I = \underline{n} \cdot \underline{\underline{g}}_{II} + 2\,H\,\underline{n}/Ca \tag{5.10}$$

where $H = -\nabla \cdot \underline{n}/2$ is the mean curvature of the interface, and $Ca = \mu_I U/\gamma$ the Capillary number which characterizes the ratio of viscous to surface tension forces and γ is the surface tension.

For short dies, the choice of the downstream boundary condition may have an effect on the extent of the calculated phenomena. The most obvious boundary condition is to assume unidirectional flow downstream (plane OPQR, Figure 5.1), where there are no cross-flow velocities. This policy may limit the study in the sense that the cross-flow veclocities are forced to zero at a finite distance into the die, a fact that may not necessarily be true since it is known that the interface evolution in the highly viscous melt/melt systems is generally a very slow phenomenon (Everage, 1975).

Symmetry conditions are imposed where possible (planes AHOPIBA and BIPQJCB in Figure 5.1) to reduce the size of the problem.

5.2.2 Boundary Conditions. Extrudate Swelling and Interface Development Outside the Die

A schematic of the extrudate swelling of the bicomponent system with the associated boundary conditions is given in Figure 5.2. The two fluids initially flow inside the

die ABCDA-EFGHE, emerge from the die at plane EFGHE, and are separated by the interface MNOPQRM.

A fully developed profile is assigned upstream (plane ABCD Figure 5.2) which is the downstream solution of the interface development inside the die problem (section 5.2.1) that is solved first. At the die walls the no-slip boundary condition is imposed (areas AEHDA, DHGCD Figure 5.2) and at the interface the boundary conditions (5.5-5.10) are imposed.

At the free surface (area EILKGHE), the kinematic condition (eqn. 5.5) is imposed and the free surface is always treated as a force-free surface.

Symmetry conditions are again imposed where possible (planes AEIJFBA and BFJKGCB) to reduce the size of the problem.

Far downstream (plane IJKLI Figure 5.2) the traction free boundary condition

$$\underline{n}\cdot\underline{\underline{\sigma}}_k = 0, \qquad k = I,II \tag{5.11}$$

is imposed and plug flow is assumed.

5.3 MATHEMATICAL FORMULATION

The stratified flow of two immiscible viscous fluids is a class of problems that poses additional complexities over the conventional free surface flows due to a pressure discontinuity and viscous stress jumps at the interface. The discontinuity arises due to the step change of the fluid properties at the interface and/or interfacial surface tension effects.

The presence of two free surfaces (external and internal) complicates the free surface parametrization and requires a special technique where two spatial unknowns per spine are allowed in an extension to the previously explained spine approach (section 2.5.2).

These issues are discussed in detail in this section. The finite element formulation follows the procedure presented in Chapter 2. Only deviations from that procedure, to

accommodate the presence of the second fluid and/or surface tension effects at the interface, will be discussed here.

5.3.1 Pressure Discontinuity at the Interface

The continuity of forces acting at the interface (eqn. 5.8-5.10) does not imply that either the pressure or the stress components are continuous across the interface (Mavridis, 1988; Dheur and Crochet; 1987). Referring to the local coordinate system (normal $\underline{n}$ and tangential $\underline{t}$ to the interface), the normal stress boundary condition (equation 5.10) can be expressed as (Mavridis et al., 1987)

$$(P_{II}-P_I) = 2(\mu_I-\mu_{II})\frac{\partial V_t}{\partial t} + \frac{2H}{Ca} \tag{5.12}$$

Equation 5.12 implies that a pressure discontinuity at the interface occurs either when there are non-negligible surface tension effects ($2H/Ca \neq 0$) or when the two fluids have different viscous properties ($\mu_I-\mu_{II} \neq 0$) which is generally the case for bicomponent flows. The discretization algorithm must be able to take such discontinuities into account.

The pressure discontinuity at the interface is handled either by assigning two pressure variables per node at the interface (double node technique, Mavridis 1988; Mavridis et al. 1987, Mitsoulis, 1986,, u-v-w-P_1-P_2-h_1-h_2 formulation) or by a penalty function formulation where the pressure is discontinuous across interelement boundaries (Dheur and Crochet, 1987; Binding et al., 1987, u-v-w-P-h_1-h_2 formulation). Both approaches were used and produced the same interface and extrudate shape for a number of test cases.

In the double-node approach two pressure variables are assigned at each vertex of the 3-d elements along the interface and the pressure is approximated as:

$$P_k^{(e)} = \sum_i N_p^i(\xi, \eta, \zeta) P_k^i \quad , \qquad k = I, II \tag{5.13}$$

where P_k^i are nodal values, N^i_p are linear shape functions and index k denotes the corresponding fluid phase. Velocity is continuous at the interface except for slip condition. The continuity equation residuals are written separately for each fluid

$$R^i_{C,k} = \int_{V_k} (\nabla \cdot \underline{v}_k) N^i_p \, dV \ , \qquad k = I, II \tag{5.14}$$

and in fluid I the contributions of the continuity residual equations are only taken into account with respect to P_1 while the second pressure variable P_2 is set to zero. The same procedure holds for fluid II where contributions are only taken into account for P_2. Pressure can still be continuous across interelement boundaries within each of the fluid phases.

In the penalty formulation approach (Dheur and Crochet, 1987; Binding et al., 1987), the pressure within each element is given by a first order degree polynomial

$$P^{(e)} = a + bx_1 + cx_2 + dx_3 \tag{5.15}$$

where the coefficients a,b,c,d of the polynomial are the pressure degrees of freedom and pressure is by construction discontinuous across interelement boundaries. The introduction of a "penalty parameter" weakens the continuity requirement (eqn. 5.2) and replaces it by

$$R^i_C = \int_V \left\{ \nabla \cdot \underline{v} - \frac{P}{\lambda} \right\} N^i_p \, dV \tag{5.16}$$

where λ, the penalty parameter is large- typically $\lambda = 10^5$-10^9. Physically, this can be equated to simulating the flow of a very slightly compressible fluid.

The penalty formulation allows the elimination of the pressure variables from the global system (Kheshgi and Scriven, 1984, 1985) but it involves costly matrix handling operations when pressure is recovered to be used in the next non-linear iteration. The advantage of the penalty formulation is that it eliminates the introduction of a second pressure variable at the interface to handle the pressure discontinuity, which leads to a reduction of the frontwidth in the system of algebraic equations. The penalty formulation

introduces a higher number of pressure unknowns and is expected to increase the sensitivity of the pressure field calculation.

5.3.2 Interface and Free Surface Parametrization

The interface and free surface parametrization is based on the idea of spines which has been exposed in section 2.5.2. An extension of the classical approach is required since the problem involves two free surfaces (interface and external free surfaces).

In this formulation of the spine method, there are two spatial degrees of freedom (h_1,h_2) associated with each spine. The external free surface node x^i_F is parametrized as the distance h_2^i along the i-th spine while the interface node is parametrized as the distance h_1^i relative to the external free surface node along the same spine (Figure 5.3). Each spine is defined by a base point $\underline{x}^i_0$ and a unit vector $\underline{e}^i$. The external and internal free surface nodes are then defined as

$$\underline{x}^i_F = \underline{x}^i_0 + h_2^{i*}\underline{e}^i \tag{5.17}$$

$$\underline{x}^i_I = \underline{x}^i_0 + h_1^{i*}h_2^{i*}\underline{e}^i \tag{5.18}$$

Other nodal points along the same spine follow the interface and external free surface movement. This is accomplished by allowing the nodal points to be located on fixed proportions along the h_1 and h_2 distances. The spines are only allowed to move on the y-z plane.

The kinematic condition residuals at the interface

$$R^i_{K,I} = \int_{A_I} \{\underline{n} \cdot \underline{v}\} N^i \, dA \tag{5.19}$$

provide the same number of equations as the number of unknown interface parameters h_1. Only elements at the interface from the side of the inner fluid contribute to the kinematic condition residuals of equation 5.19.

The kinematic condition residuals at the external free surface

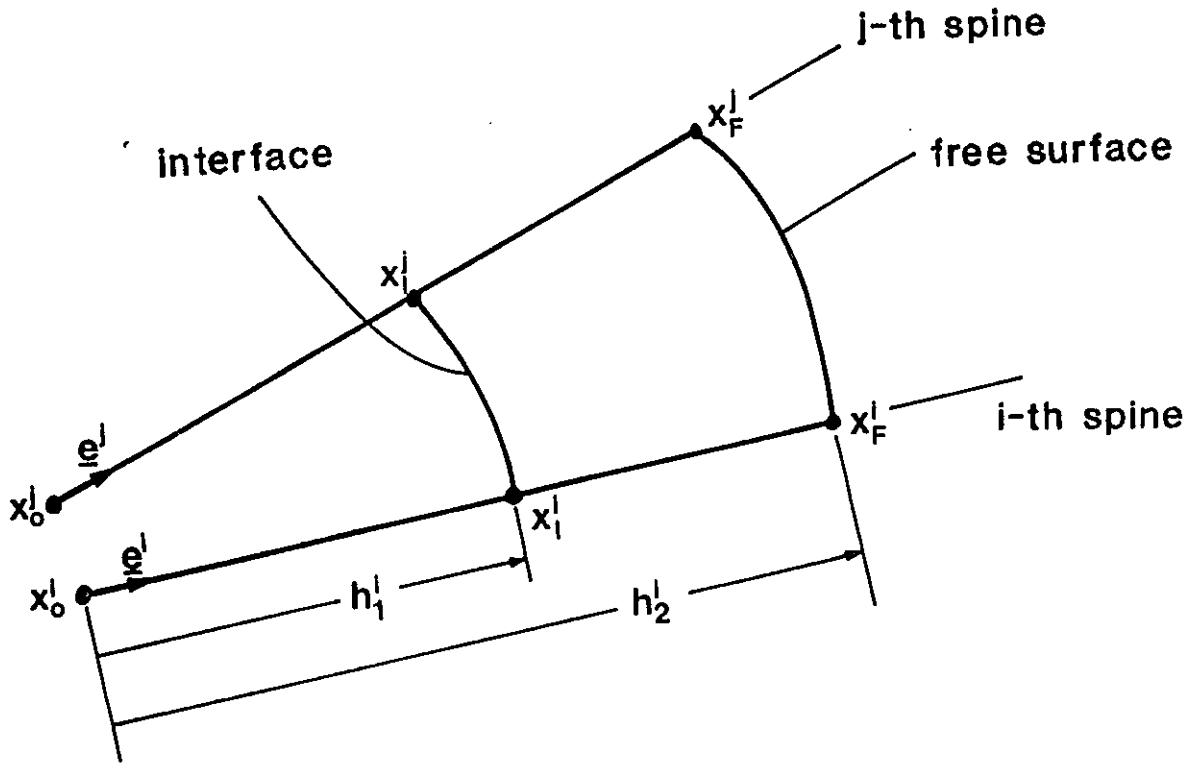

Figure 5.3 Spine definition with two spatial variables per spine.

$$R^i_{K,F} = \int_{A_F} \{\underline{n} \cdot \underline{v}\} N^i \, dA \tag{5.20}$$

provide the same number of equations as the number of unknown external free surface parameters h_2. Only elements at the free surface contribute to the kinematic condition residuals of equation 5.20. Jacobian contributions in the global matrix are taken within every deforming element with respect both to h_1 and h_2. Analytical derivatives are used according to the procedure presented in Appendix A.

5.3.3 Interfacial Surface Tension

In the presence of surface tension effects, the weighted momentum residuals of eqn. 2.18 after the application of the divergence theorem become:

$$R^i_m = \int_V \{\nabla N^i \cdot \underline{\underline{g}}\} dV - \int_{A_I} \{n \cdot \underline{\underline{g}}\} N^i \, dA \tag{5.21}$$

Introducing the boundary condition at the interface between the two melts (equation 5.10) the boundary integral becomes:

$$R^i_{mB} = -\int_{A_I} \{\underline{n} \cdot \underline{\underline{g}}_I\} N^i \, dA = \int_{A_I} \left\{ \frac{1}{Ca} (\nabla \cdot \underline{n}) \underline{n} \right\} N^i \, dA + \int_{A_I} \{\underline{n} \cdot \underline{\underline{g}}_{II}\} N^i \, dA \tag{5.22}$$

or

$$R^i_{mB} = \int_{A_I} \frac{1}{Ca} (\nabla \cdot \underline{n}) \underline{n} \cdot \underline{\underline{d}} \, dA + \int_{A_I} \{\underline{n} \cdot \underline{\underline{g}}_{II}\} N^i \, dA \tag{5.23}$$

where

$$\underline{\underline{d}} = \begin{Bmatrix} N^i & 0 & 0 \\ 0 & N^i & 0 \\ 0 & 0 & N^i \end{Bmatrix} \tag{5.24}$$

Application of the surface divergence theorem (Weatherburn, 1929) yields:

$$R^i_{mB} = \int_{A_I} \frac{1}{Ca} \nabla_{II} \cdot \underline{\underline{d}} \, dA - \oint \underline{m} \cdot \underline{\underline{d}} \, dS + \int_{A_I} \{\underline{n} \cdot \underline{\underline{g}}_{II}\} N^i \, dA \tag{5.25}$$

where $\underline{m}$ is the outward-pointing tangent vector at the boundary of the free surface. The third term in equation 5.25 is neglected since $\underline{n} \cdot \underline{\underline{\sigma}}_{II}$ is zero in the case of a free surface (hydrostatic pressure of a gas $=0$) and is already included in the case of a fluid-fluid interface. The second term gives contributions only at the outflow plane.

The surface divergence is defined as (Weatherburn, 1929; Coyle 1984)

$$\nabla_{II} \cdot \underline{\underline{d}} = \frac{1}{a^2}\left[\underline{r}_1\left(a_{22}\frac{\partial \underline{\underline{d}}}{\partial u} - a_{12}\frac{\partial \underline{\underline{d}}}{\partial v}\right) + \underline{r}_2\left(a_{11}\frac{\partial \underline{\underline{d}}}{\partial v} - a_{12}\frac{\partial \underline{\underline{d}}}{\partial u}\right)\right] \tag{5.26}$$

for a surface defined by $\underline{r}(u,v)$ where $\underline{r}_1 = \partial \underline{r}/\partial u$, $\underline{r}_2 = \partial \underline{r}/\partial v$.

In each element the free surface is represented by

$$\underline{r}(\xi,\eta = 1,\zeta) = x\underline{i} + y\underline{j} + z\underline{k} \tag{5.27}$$

so that

$$\underline{r}_1 = x_\xi \underline{i} + y_\xi \underline{j} + z_\xi \underline{k}, \qquad \underline{r}_2 = x_\zeta \underline{i} + y_\zeta \underline{j} + z_\zeta \underline{k} \tag{5.28}$$

and

$$a_{11} \equiv \underline{r}_1 \cdot \underline{r}_1, \qquad a_{22} \equiv \underline{r}_2 \cdot \underline{r}_2, \qquad a_{12} \equiv \underline{r}_1 \cdot \underline{r}_2$$

$$a = \sqrt{a_{11}a_{22} - a_{12}a_{12}} \tag{5.29}$$

Finally, the momentum boundary integrals become:

$$R^i_{mB} = \frac{1}{Ca}\int_{A_I} \nabla_{II} \cdot \underline{\underline{d}}\, dA - \frac{1}{Ca}\oint m \cdot \underline{\underline{d}}\, dS \tag{5.30}$$

and are non-zero when 1/Ca is non-zero.

5.3.4 Numerical Considerations

The existence of the free surfaces renders the problem nonlinear and the Newton-Raphson iteration is used with the spine approach for the free surface parametrization.

For the interface development inside the die, the first iteration to solve for the velocity and pressure variables is performed with the interface having the shape of the internal channel. The initial position of the internal channel is set so that the flow in the two separate channels (Figure 5.1) is driven by the same pressure gradient in all cases studied.

For the extrudate emergence problem, the first iteration to solve for the velocity and pressure variables is performed with the initial shape of the external free surface assigned as that of the die at the die exit. The initial interface shape is assigned as the one given at the initial inlet profile which is the downstream solution of the previous problem. Termination criterion is that the maximum relative update of all the calculated variables be less than 10^{-6}.

Details on the size of the problems with respect to the number of nodes, number of elements, number of spines, number of unknowns and frontwidth are given in Table 5.1. The penalty formulation, as is adapted in this section, slightly increases the total number of unknowns but reduces the frontwidth of the problem.

Table 5.1 Size of the Bicomponent Encapsulated Problems

Die Geometry	Nodes	Elements	Spines	Unknowns	Frontwidth
Square	5053	600	527	13259	598
Square*	3423	400	357	9807	676
Rectangular	5328	630	555	13747	539
Round	3219	360	333	8074	362
Round**	3219	360	333	8925	325

* Extrudate Swelling Problem
** Penalty Function Formulation

5.3.5 Test Cases

The interface development was studied for the concentric stratified flow of two Newtonian fluids, which admits an analytical solution. For the two cases considered, the predicted interface position downstream is in excellent agreement with the analytical solution predictions and the results are summarized in Table 5.2.

Table 5.2 Interface Development Inside the Die. Test Cases. Concentric Stratified Flow.

Viscosity ratio μ_I/μ_{II}	Flowrate ratio Q_I/Q_{II}	3-D Numerical h_I/R	Analytical h_I/R
4	0.5	0.4419	0.4418
4	2	0.6880	0.6880

The extrudate swelling behaviour was examined for two cases. The free surface flow of a Newtonian bicomponent system with a viscosity ratio of $\mu_I/\mu_{II}=4$ and flowrate ratio $Q_I/Q_{II}=7:3$ out of a round die was considered. The 3-D code predicted a shrinkage of the external free surface of 1.2% and swelling of the internal free surface of 17% which is in close agreement with corresponding 2-D results (Mitsoulis, 1986).

The free surface flow out of a square die when the fluids have equal viscosities and a flowrate ratio of $Q_I/Q_{II}=4$ was considered. Since there is no viscosity mismatch, the flow reduces to the extrusion of a Newtonian fluid out of a square die. The external free surface swells by 18.29% at the midpoints of the flat planes and 2.94% at the corners, in very good agreement with the corresponding results presented in section 3.2.3, Figure 3.3. The interface also exhibits swelling (Figure 5.4) showing the material redistribution in the extrudate, in agreement with the trend presented by Mitsoulis (1986).

5.4 INTERFACE DEVELOPMENT INSIDE THE DIE

This section examines the interface development for Newtonian bicomponent stratified flows inside the die (Figure 5.1). The development and shape of the interface for a set of different outer die geometries, internal channel geometries and flowrate/viscosity ratios is studied.

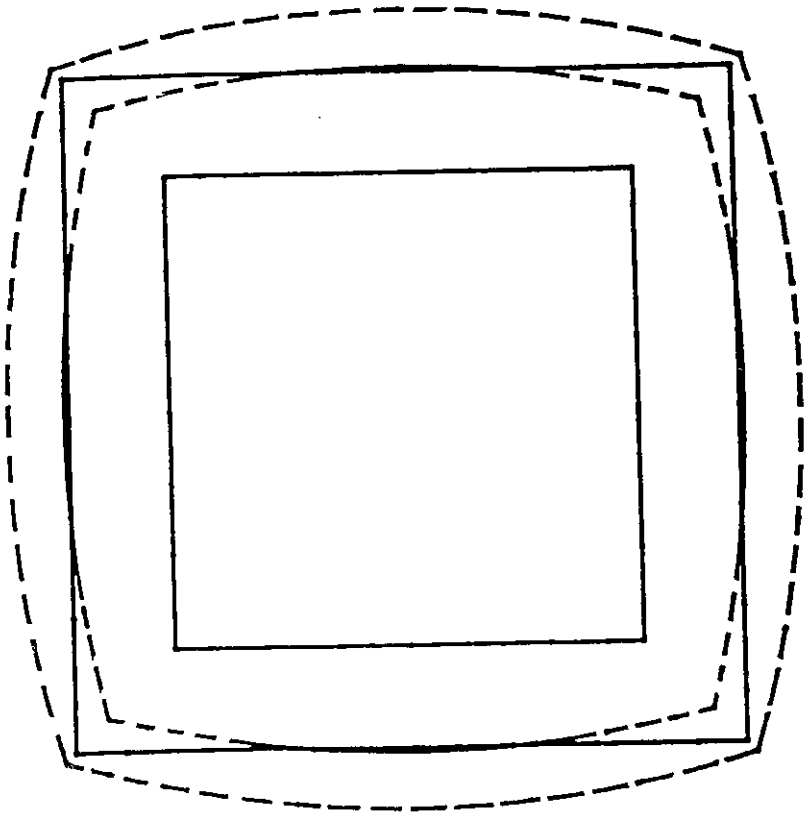

Figure 5.4 Test case. Extrudate swelling out of a square die. The fluids have the same viscosity. Flowrate ratio $Q_I/Q_{II}=4$.

5.4.1 Square Dies

The interface development when the outer die is square is examined. The inner channel that initially separates the two fluids is also square and the flow in the two separate channels upstream is driven by the same pressure gradient. There is flow development right after the fluids are brought together and viscosity and flowrate ratios have an impact on the interface shape and the areas of flow that the two fluids occupy in the fully developed region. Figure 5.5 shows how the initial (y-z) grid upstream (5.5a) is distorted far downstream in the die (5.5b) for a typical case.

Figure 5.6 shows the effect of the flowrate ratio when the viscosity ratio is fixed at $\mu_I/\mu_{II}=4$. For the flowrate ratio of $Q_I/Q_{II}=2$, the interface shrinks near the corners relative to the initial shape (Figure 5.6a). For a flowrate ratio of $Q_I/Q_{II}=8$, the interface swells near the midpoints of the flat plates as the inner material expands but it does not swell at the corner. For the extreme case of flowrate ratio $Q_I/Q_{II}=150:1$, the interface is pushed near the walls. In all three cases, there is flow development and material redistribution inside the die because of the formation of the interface and the acceleration of the fluid as it is flowing away from the inner channel walls. Figure 5.7 shows the (y-z) velocity vectors in the cross section at $x=0.25$ after the fluids merge when $Q_I/Q_{II}=2$. The core of the inner fluid flows outward while both the interface and the outer fluid move inward and result in the interface shrinkage. Figure 5.8a shows the velocity vectors at the same (y-z) plane with Figure 5.7 when $Q_I/Q_{II}=8$. The core of the inner fluid is again flowing outward and so does the interface. The outer fluid near the midpoints of the walls is flowing outward, but near the corner it flows inward. There is material flowing from the area halfway from the corner and the midpoints of the flat plates, toward the direction of the corner in a motion parallel to the die walls (Figure 5.8a). Further downstream however, at $x=0.75$ (Figure 5.8b), as the interface is still expanding, the cross-flow of the outer fluid is directed toward the corner with the same parallel to the die walls

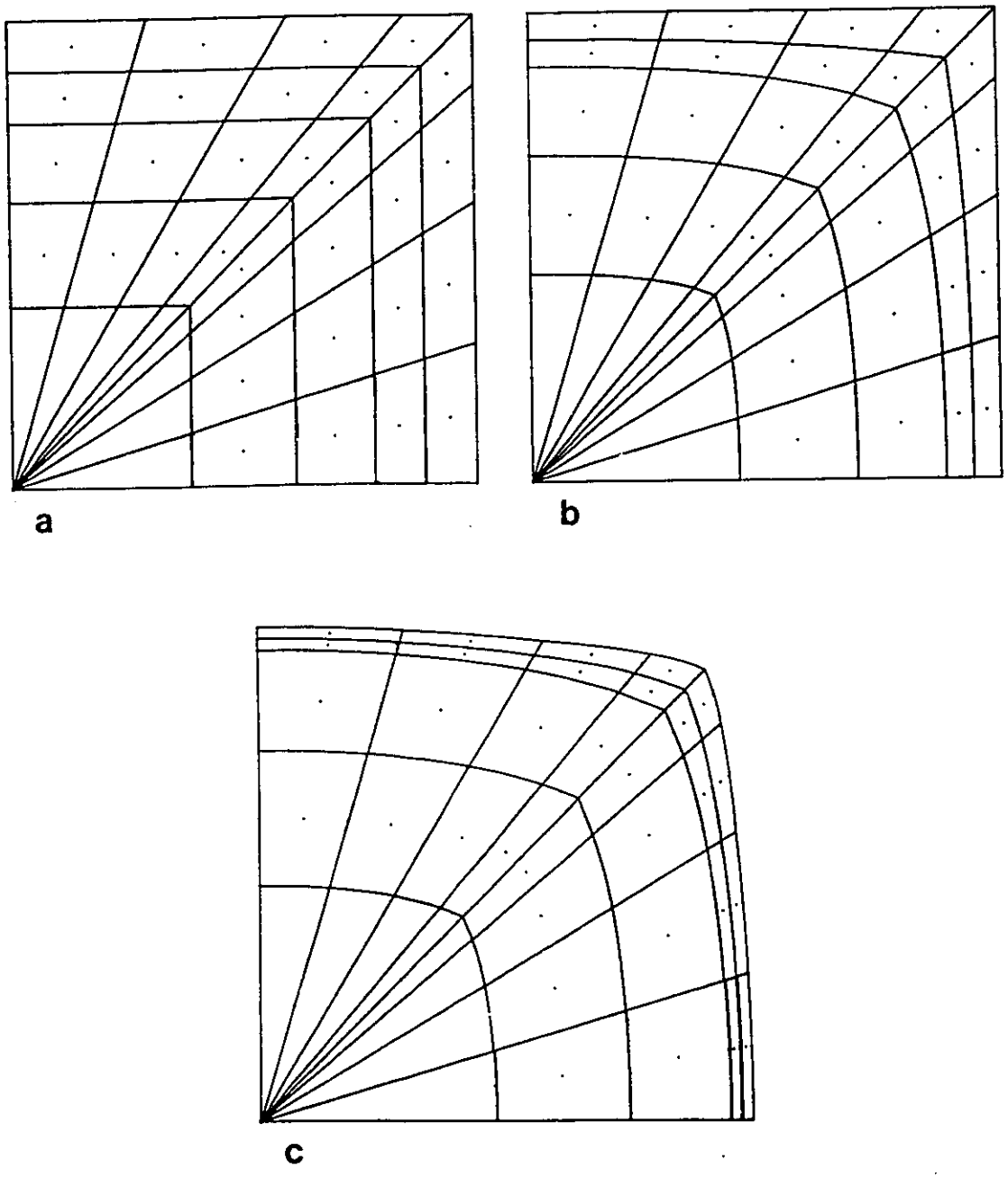

Figure 5.5 Interface development inside and outside the die. Square die, a) initial grid, b) distorted grid at the die exit in the interface development inside the die problem; initial grid in the extrudate swelling problem and c) distorted grid at the extrudate.

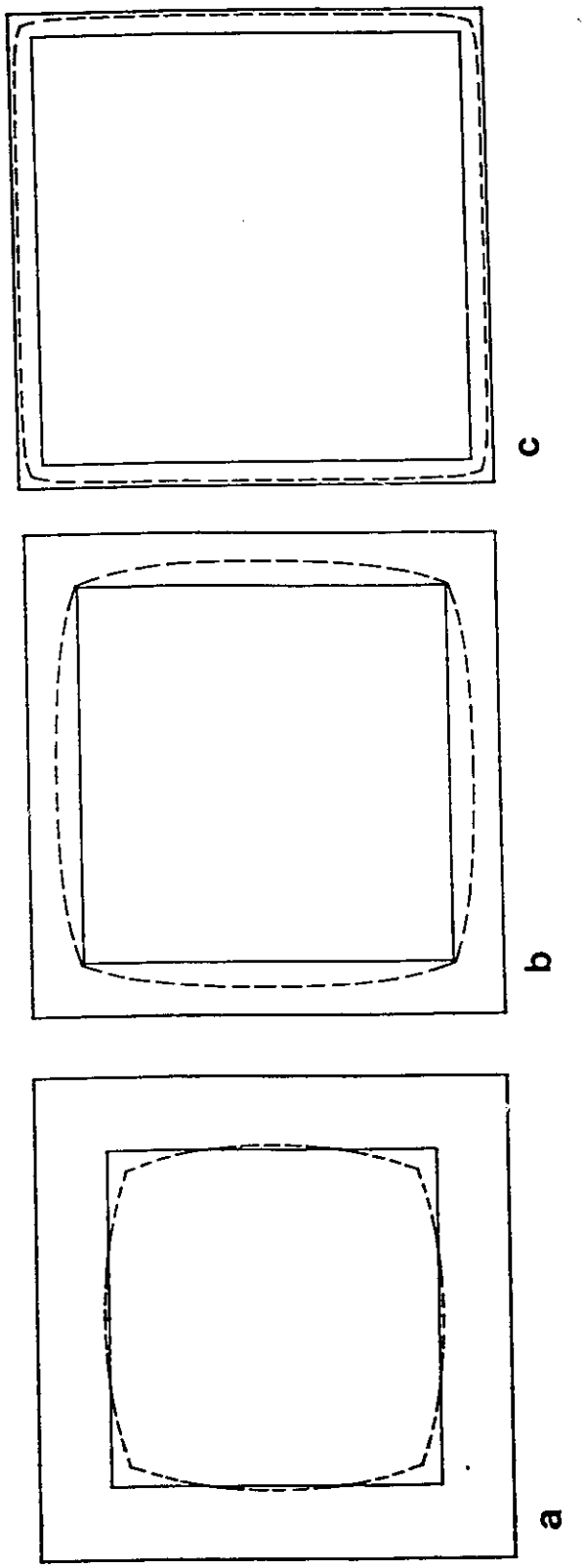

Figure 5.6 Interface development inside the die. Square die. Viscosity ratio $\mu_I/\mu_{II}=4$. Effect of flowrate ratio, a) $Q_I/Q_{II}=2$, b) $Q_I/Q_{II}=8$ and c) $Q_I/Q_{II}=150$.

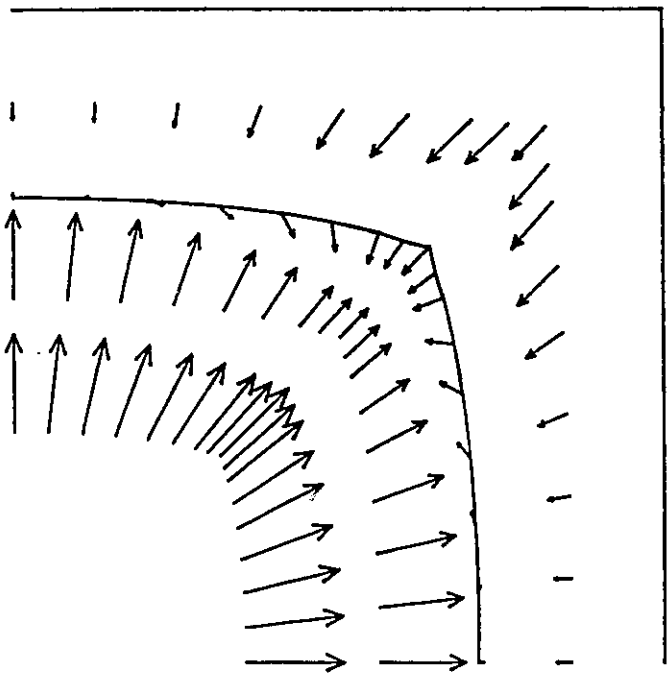

Figure 5.7 Interface development inside the die. Square die. Viscosity ratio $\mu_I/\mu_{II} = 4$, Flowrate ratio $Q_I/Q_{II} = 2$. (y – z) velocity vectors at x = 0.25.

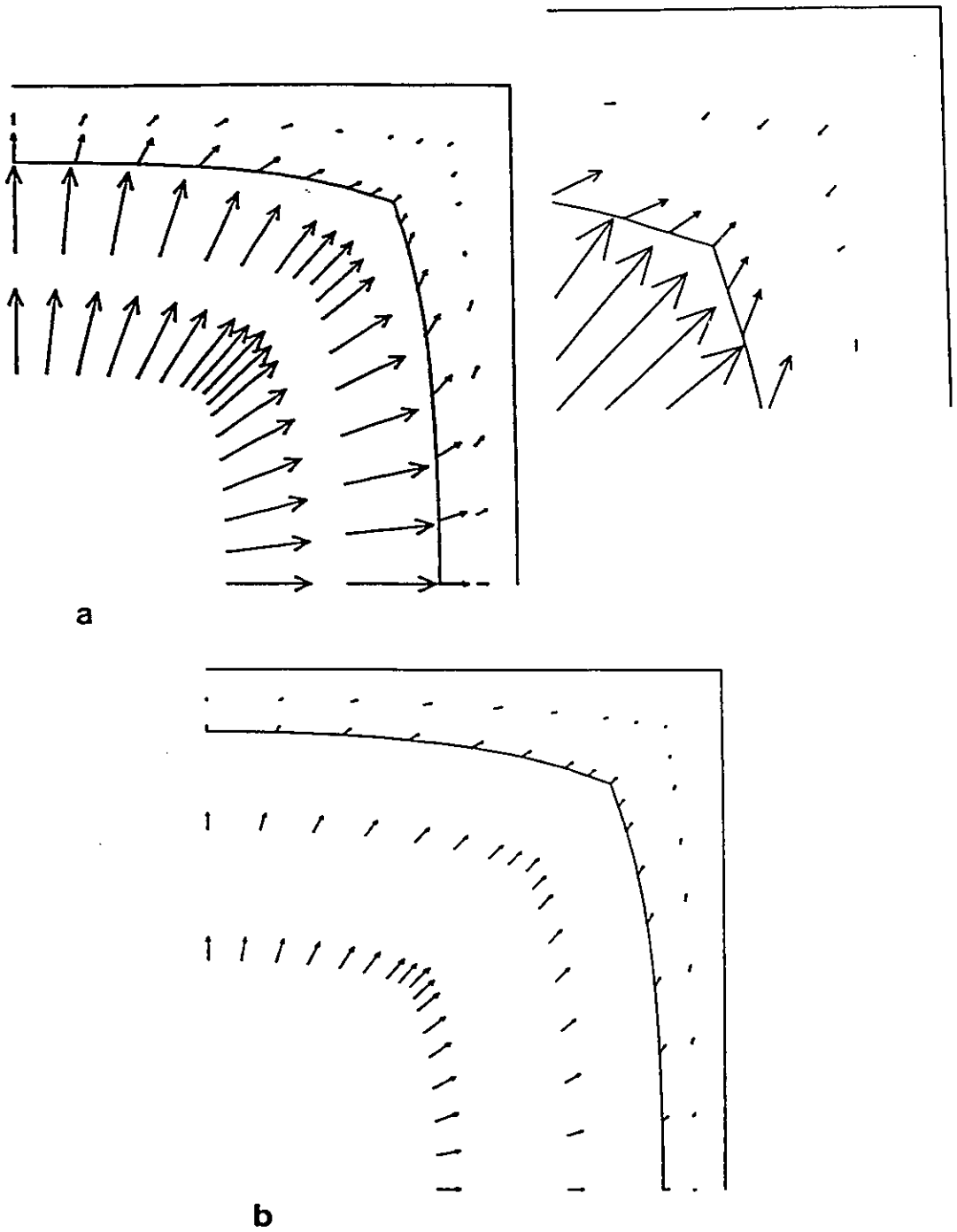

Figure 5.8 Interface development inside the die. Square die. Viscosity ratio $\mu_I/\mu_{II}=4$, Flowrate ratio $Q_I/Q_{II}=8$. (y−z) velocity vectors a) at x=0.25 and b) at x=0.75.

motion. Figures 5.9 and 5.10 present 3-D plots of the downstream component of velocity (x-velocity) for the two cases of $Q_I/Q_{II}=2$ and $Q_I/Q_{II}=8$ respectively, in different stations downstream. Because of the difference in the flow rate ratios, the inner fluid initially flows with a higher velocity, especially in the higher flowrate ratio case (Figure 5.10a). As the interface forms and accelerates, the flow develops and finally far downstream, fully developed flow occurs (Figures 5.9d, 5.10d). Because of the different viscosities, the slope of the velocity profile exhibits a discontinuity at the interface (Figures 5.9, 5.10).

Figure 5.11 presents the effect of the viscosity ratio for a fixed flowrate ratio of $Q_I/Q_{II}=8$. When the less viscous fluid is located at the core (Figure 5.11b), the interface swells relative to the initially assigned shape, but the area of flow of the inner layer is smaller compared to the case when the more viscous layer is located at the core (Figure 5.11a). Although the configuration with the less viscous fluid encapsulated by the more viscous fluid is unstable (Joseph et al., 1984; Han, 1981), the numerical procedure had no difficulty converging to a solution. Figure 5.12 shows 3-D plots of the downstream component of velocity for this set of conditions. The slope of the velocity profile at the interface is different compared to Figure 5.10 because of the different configuration of the materials.

When the more viscous fluid is at the core, in the absence of surface tension effects, the interface tends to form a sharp corner corresponding to the inner channel corner point (Figures 5.6, 5.11a). When the less viscous fluid is at the core, the curvature of the interface is higher in the neighborhood of the corner and the sharp corner tends to disappear (Figure 5.11b).

Table 5.3 summarizes the results with respect to the area of flow that the inner layer occupies. It is seen that for a fixed viscosity ratio, the area ratio is a function of the flowrate ratio.

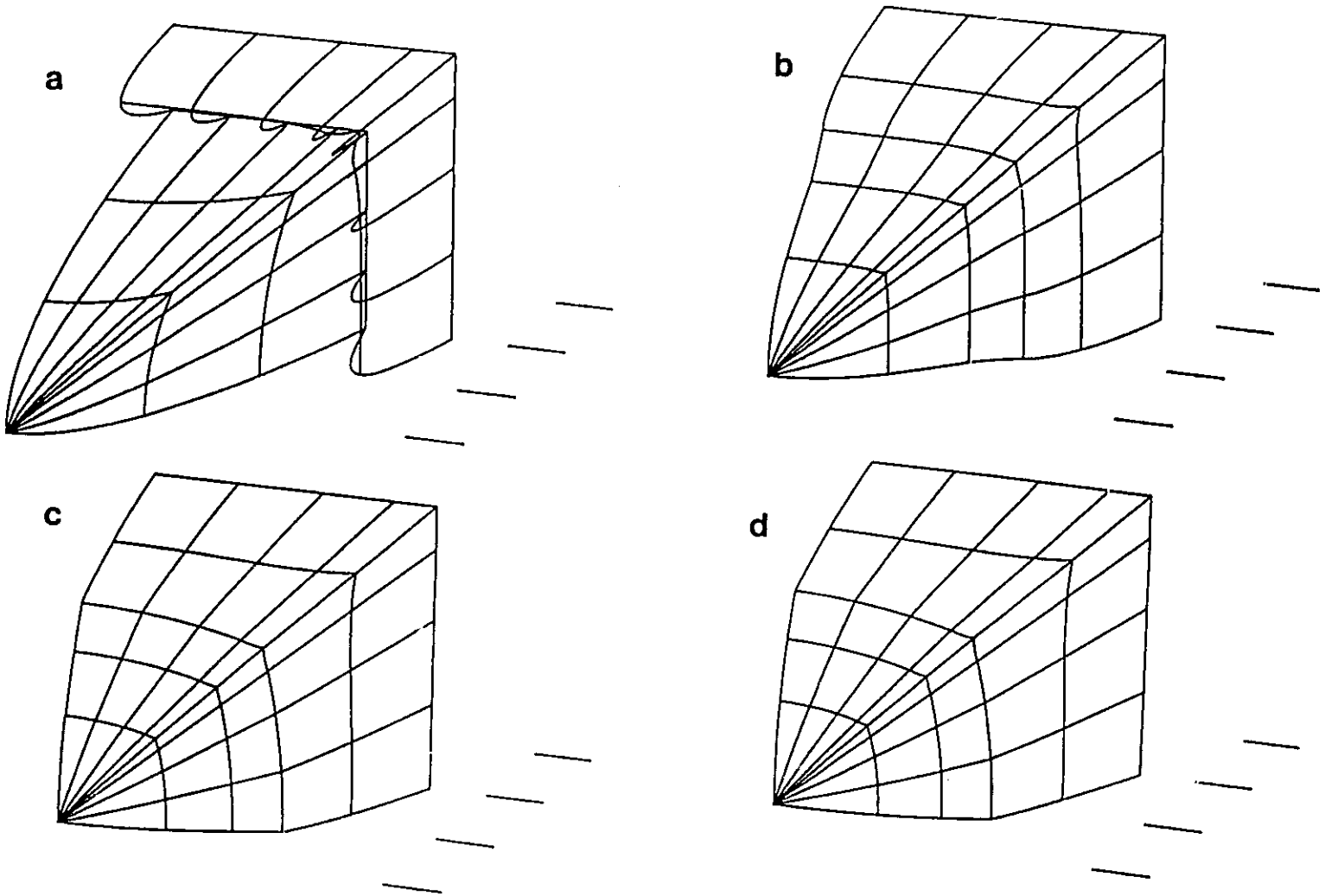

Figure 5.9 Interface development inside the die. Square die. Viscosity ratio $\mu_I/\mu_{II}=4$, Flowrate ratio $Q_I/Q_{II}=2$. Downstream component of velocity at different stations downstream; a) inside the die, b) at $x=0.25$, c) at $x=0.75$ and d) far downstream.

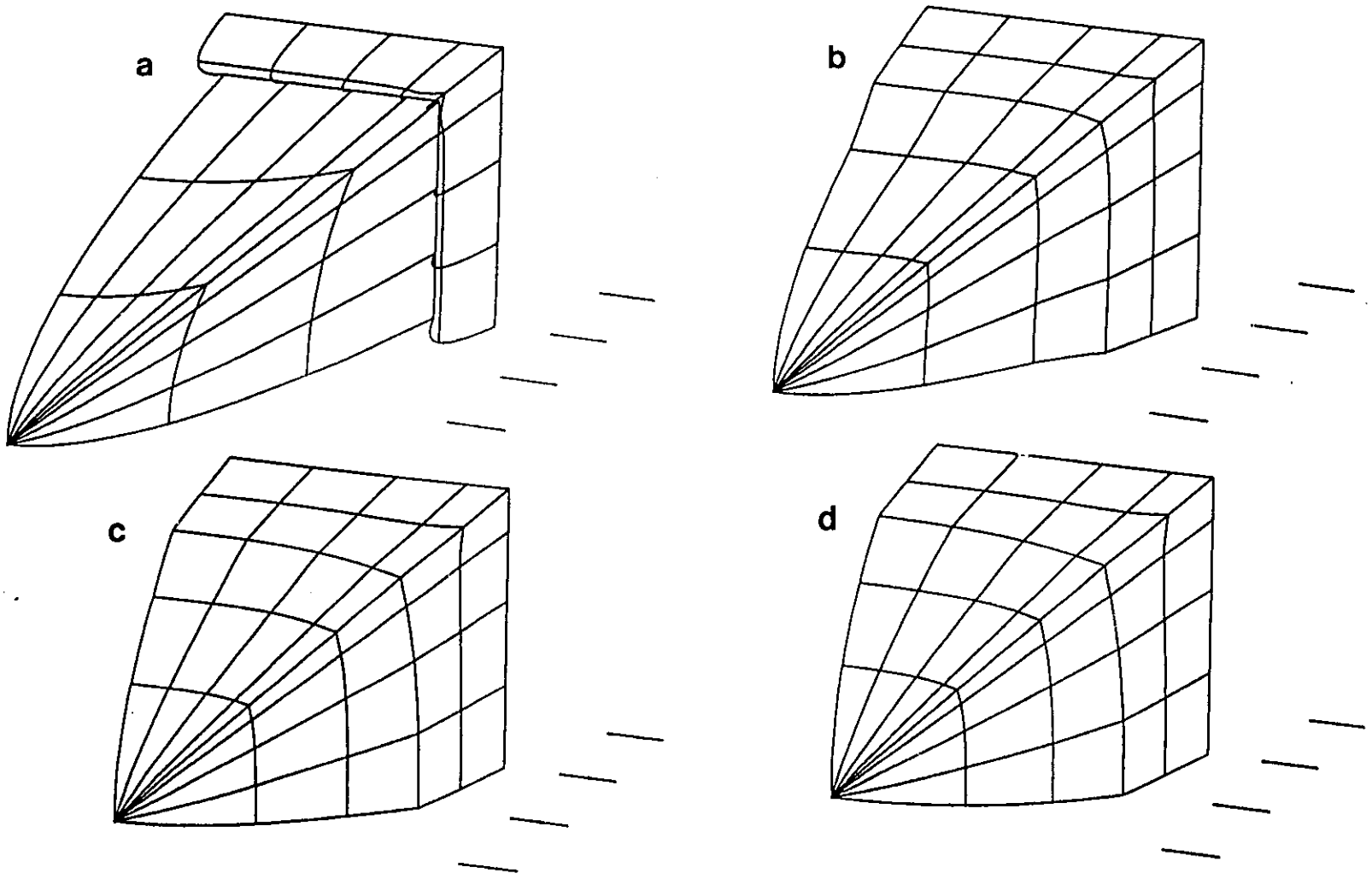

Figure 5.10 Interface development inside the die. Square die. Viscosity ratio $\mu_I/\mu_{II}=4$, Flowrate ratio $Q_I/Q_{II}=8$. Downstream component of velocity at different stations downstream; a) inside the die, b) at $x=0.25$, c) at $x=0.75$ and d) far downstream.

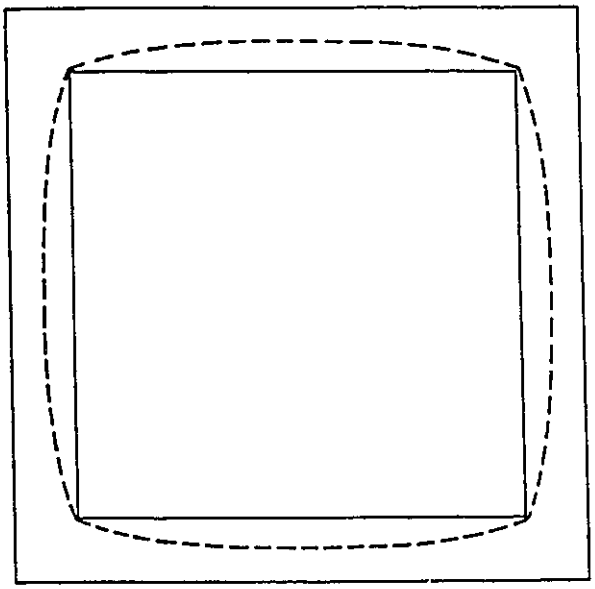

a

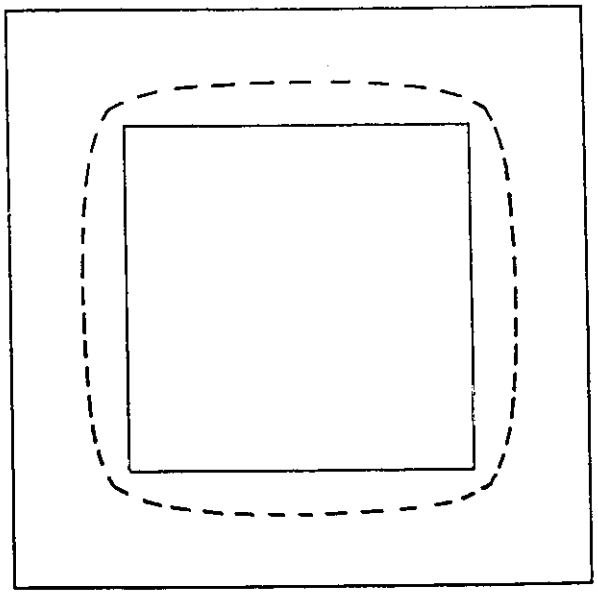

b

Figure 5.11 Interface development inside the die. Square die. Flowrate ratio $Q_I/Q_{II} = 8$. Effect of Viscosity ratio, a) $\mu_I/\mu_{II} = 4$ and b) $\mu_I/\mu_{II} = 0.25$.

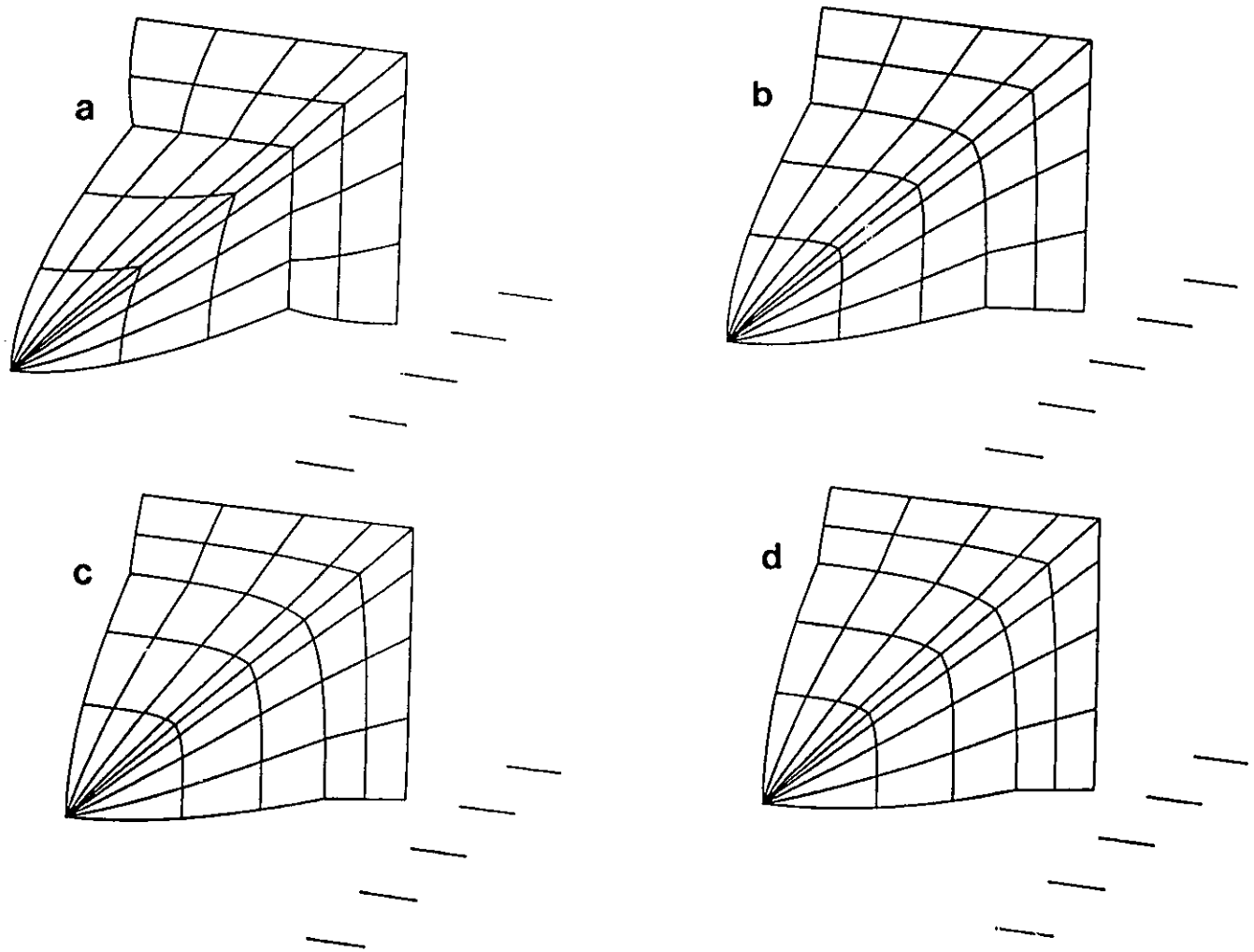

Figure 5.12 Interface development inside the die. Square die. Viscosity ratio $\mu_I/\mu_{II}=0.25$, Flowrate ratio $Q_I/Q_{II}=8$. Downstream component of velocity at different stations downstream; a) inside the die, b) at $x=0.25$, c) at $x=0.75$ and d) far downstream.

Table 5.3 **Encapsulated Flow, Square dies. Areas of Flow of Inner Layer**

Viscosity Ratio μ_I/μ_{II}	Flowrate Ratio Q_I/Q_{II}	Area ratio inner/total	Area ratio inner/outer
4	2	0.46	0.85
4	8	0.73	2.73
4	150	0.95	20.17
0.25	8	0.52	1.10

5.4.2 Rectangular Die

The problem of the interface shape development for a system with a viscosity ratio $\mu_I/\mu_{II}=2$ and flowrate ratio $Q_I/Q_{II}=8$ flowing inside a rectangular die with an aspect ratio of 2:1 is examined.

Figure 5.13 shows the superposed initial and final shapes of the interface. The inner layer expands near the areas of the flat plates but does not expand significantly near the corners.

The result of the 3-D analysis, for a die of finite length, does not fully agree with the result of the optimization procedure that utilizes the minimum viscous dissipation principle (Figure 4.5) which assumes dies of infinite length.

5.4.3 Round Die

The encapsulated flow when the outer geometry is circular is studied. The minimum viscous dissipation principle predicts that irrespective of the initial interface shape, the preferential configuration that minimizes viscous dissipation is a concentric flow, i.e., the shape of the inner layer is circular. The minimum viscous dissipation principle assumes that an infinite die length is available so that the flow attains the optimum configuration. On the other hand, the fiber industry has been producing bicomponent fibers with very complex shapes of the inner layer (Jeffries, 1971; British Patent 1101452; British Patent 1120241;

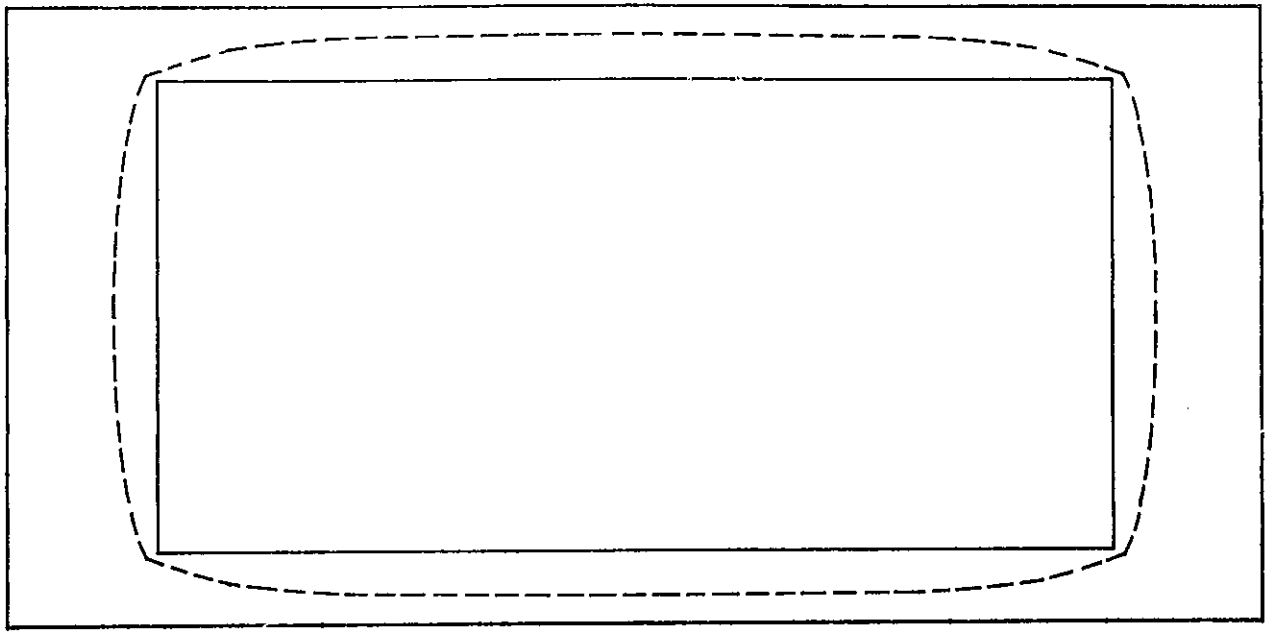

Figure 5.13 Interface development inside the die. Rectangular die of aspect ratio 2:1. Flowrate ratio $Q_I/Q_{II}=8$. Viscosity ratio $\mu_I/\mu_{II}=2$.

Paul, 1978) where sharp corners in the core material shape may exist. Short dies are used in the industry and the interface shape depends on the initial geometry. This section presents results of 3-D studies in relatively short dies ($L/D<25$) that show a dependence of the final interface shape on the initial geometry in the absence of surface tension effects.

Figure 5.14 shows the calculated interface shape for different sets of flow conditions and internal channel shape. Figures 5.14a and 5.14b show that for a nominal viscosity ratio of $\mu_I/\mu_{II}=4$, the interface shape does not change significantly and the sharp corners are retained for both flowrate ratios. Figure 5.14c shows that even for a high viscosity ratio of $\mu_I/\mu_{II}=20$ which induces a significant shrinking of the inner layer, the interface bears the geometric characteristics of the initial geometry and the sharp corners persist. An extreme flowrate ratio of $Q_I/Q_{II}=80$ with a viscosity ratio of $\mu_I/\mu_{II}=1:20$ produces the distorted inner layer shape of Figure 5.14d. There is a small flow development even when the inner layer consists of the same material with the outer layer (Figure 5.14e) because of the effect of the inner channel walls. An octagonal inner channel shape produced an interface shape that is close to the circular (Figure 5.14e) and Figure 5.15 shows a perspective view of the interface development in this case.

Finally, Figure 5.16 shows a study of the effect of interfacial surface tension on a bicomponent system with viscosity ratio $\mu_I/\mu_{II}=25$ and flowrate ratio $Q_I/Q_{II}=4$. Although the viscosity ratio is high, when surface tension at the interface is neglected (Figure 5.16a, $Ca^{-1}=0$) or its effect is not dominant (Figure 5.16b, $Ca^{-1}=10^{-3}$) the interface shape depends on the initial geometric shape. When surface tension effects at the interface become dominant (Figure 5.16c, $Ca^{-1}=10^{-1}$), the interface becomes circular. However, surface tension effects are unlikely to dominate the flow of the highly viscous polymer melts.

The effect of the grid density was studied and there was no indication of dependence of the interface shape on the grid density. However, this study was limited by the large scale of

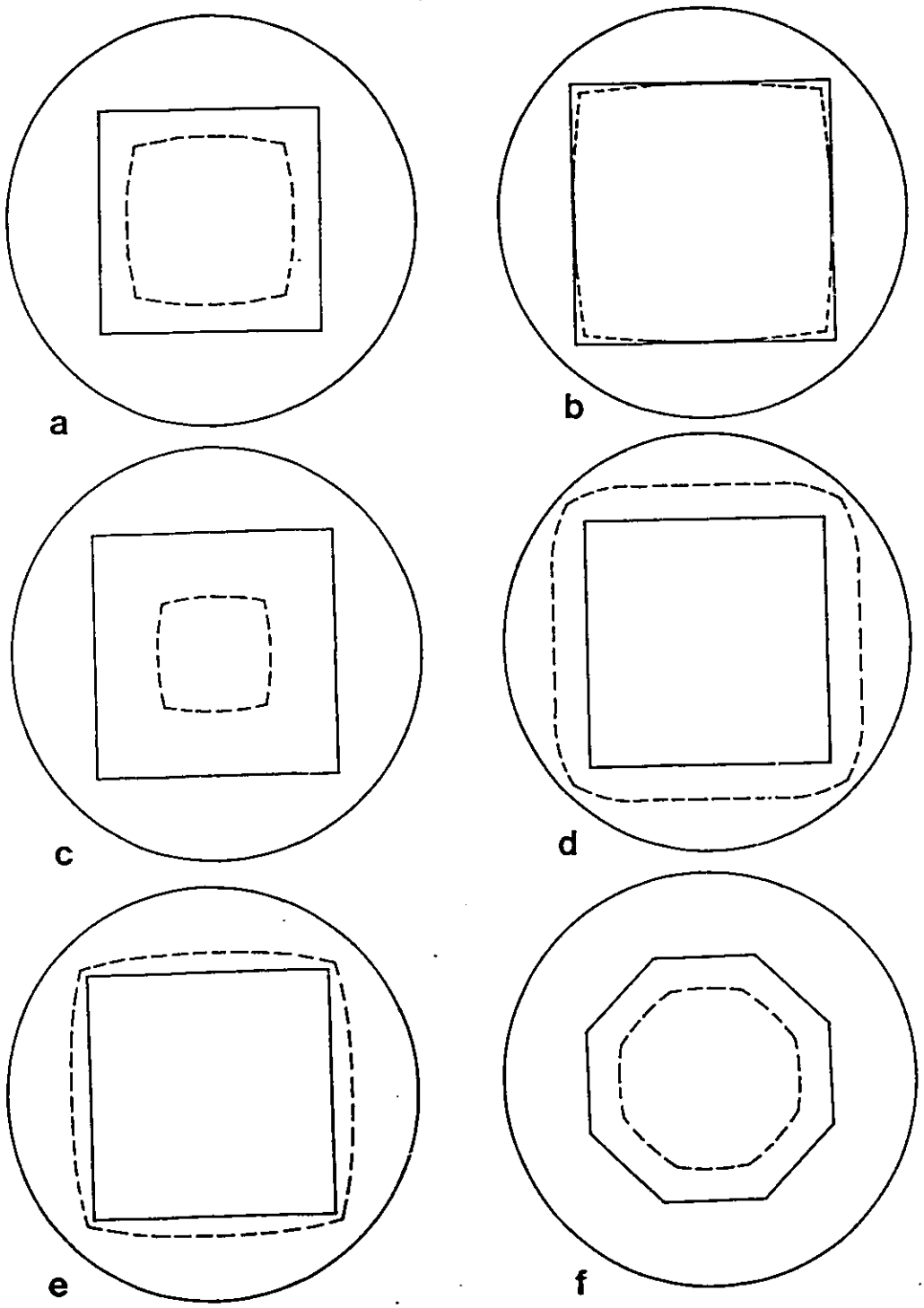

Figure 5.14 Interface development inside the die. Circular die. Square internal channel, a) $\mu_I/\mu_{II}=4$, $Q_I/Q_{II}=0.5$; b) $\mu_I/\mu_{II}=4$, $Q_I/Q_{II}=0.2$; c) $\mu_I/\mu_{II}=20$, $Q_I/Q_{II}=0.2$; d) $\mu_I/\mu_{II}=0.05$, $Q_I/Q_{II}=80$; e) $\mu_I/\mu_{II}=1$, $Q_I/Q_{II}=4$ and f) Octagonal internal channel, $\mu_I/\mu_{II}=4$, $Q_I/Q_{II}=0.5$.

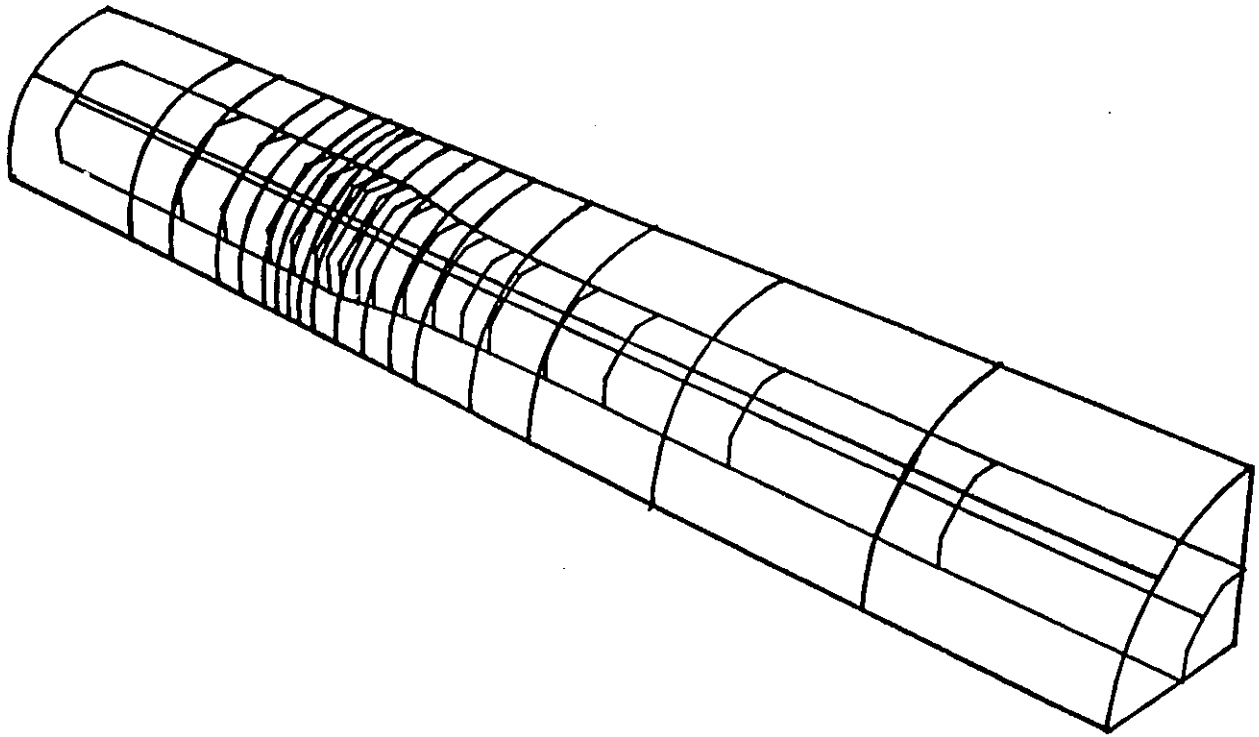

Figure 5.15 Perspective view of interface development inside the die. Same as in Figure 5.14f.

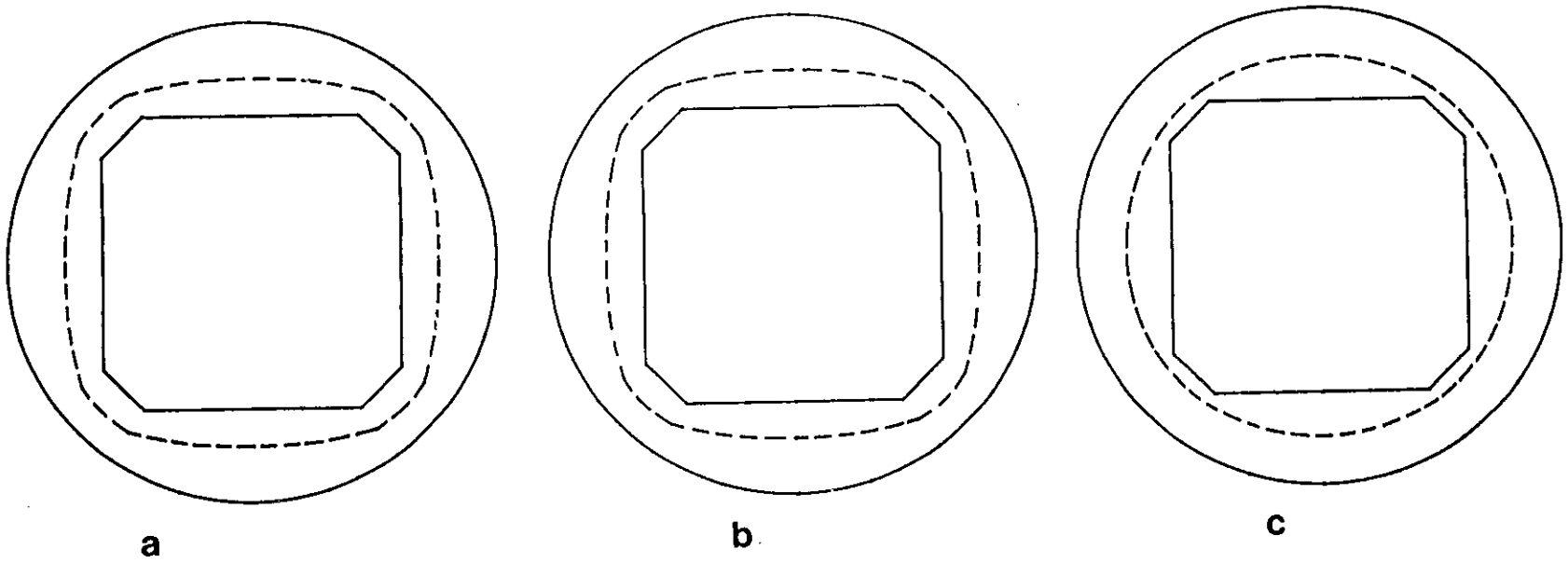

Figure 5.16 Interface development inside the die. Circular die. Effect of interfacial surface tension; a) No surface tension ($Ca^{-1} = 0$), b) $Ca^{-1} = 10^{-3}$ and c) $Ca^{-1} = 10^{-1}$.

the associated problems and more extensive grid studies are needed before a firm conclusion is drawn. There is not sufficient experimental evidence to suggest the interface shape dependence on the initial geometry and clearly more work is needed in the area. The effect of the imposed boundary conditions on the calculated interface shape may be important and this issue is discussed later (see section 6.4.5).

5.5 EXTRUDATE SWELLING AND INTERFACE SHAPE OUTSIDE THE DIE

When the Newtonian bicomponent system emerges from the die, the interface and external free surface exhibit different swelling ratios depending on the flow conditions and layer configuration. Mitsoulis (1986) presented a study for axisymmetric geometry and here the 3-D square die geometry is studied. Figure 5.5b shows the initially assigned grid and Figure 5.5c the final distorted grid in the extrudate for a typical case.

Figure 5.17 presents the swelling behaviour out of square dies for bicomponent systems with viscosity ratio of $\mu_I/\mu_{II}=4$. For the low flowrate ratio of $Q_I/Q_{II}=2$ the external free surface shrinks significantly near the corners while the interface swells (Figure 5.17a). For $Q_I/Q_{II}=8$, the free surface swells at the flat plate regions but still shrinks near the corner points while the interface swells significantly (Figure 5.17b). The (y-z) velocity vectors after the extrudate emerges from the die when $Q_I/Q_{II}=2$ are shown in Figure 5.18. The external free surface tends to move inward initially ($x=0.1$, Figure 5.18a; $x=0.3$, Figure 5.18b) but further downstream ($x=0.8$, Figure 5.18c) the direction is reversed and as the external free surface recovers, there is a tendency of the surface material to slide along the free surface in the direction of the corner point. For $Q_I/Q_{II}=8$, the interface is moving inward initially ($x=0.1$, Figure 5.19a) but it recovers sooner ($x=0.3$, Figure 5.19b) and tends to move outward

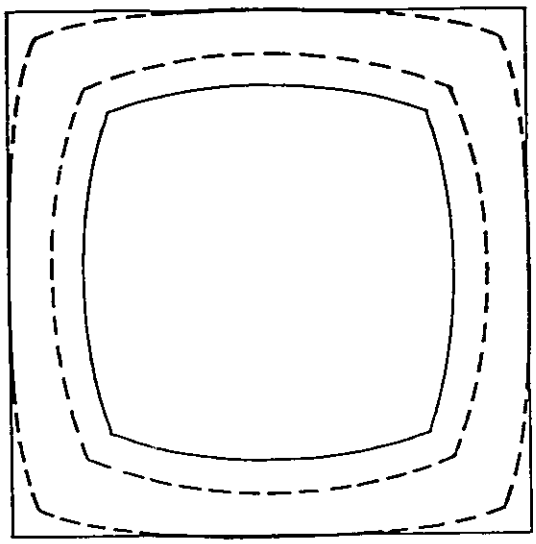

a

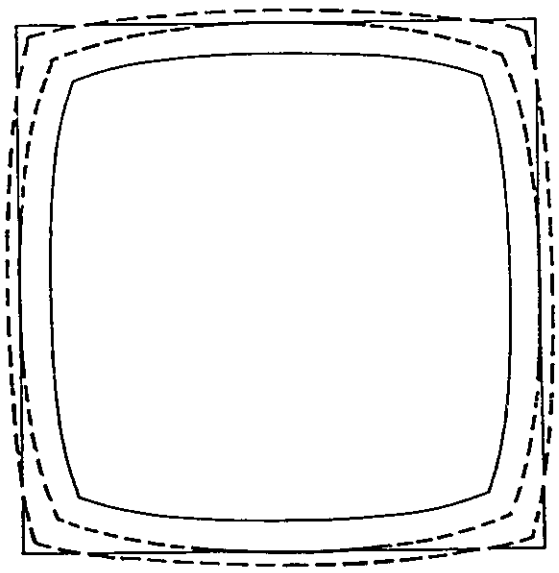

b

Figure 5.17 Extrudate swelling and interface development outside the die. Square die. Viscosity ratio $\mu_I/\mu_{II}=4$. Effect of flowrate ratio, a) $Q_I/Q_{II}=2$ and b) $Q_I/Q_{II}=8$.

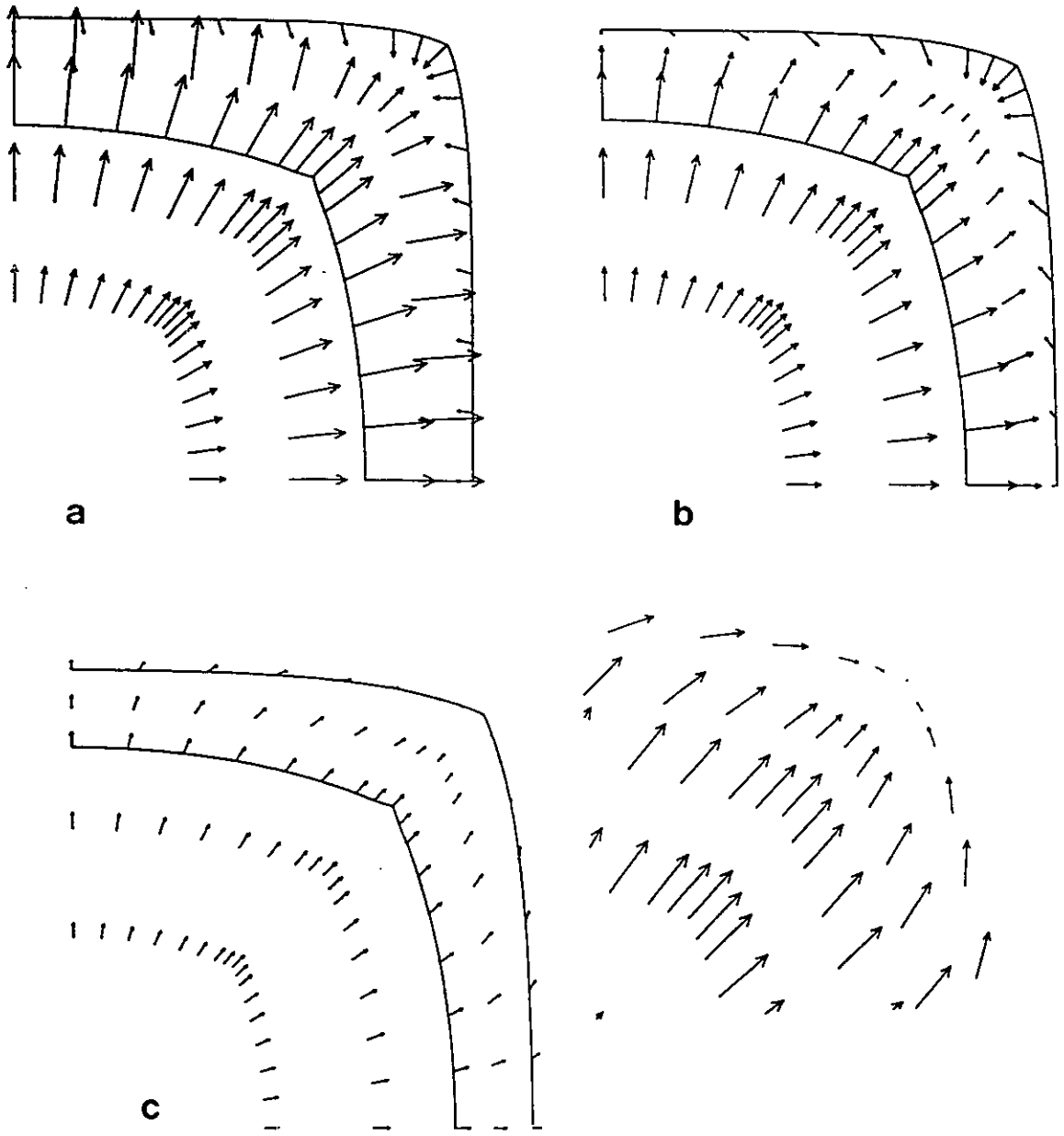

Figure 5.18 Extrudate swelling and interface development outside the die. Square die. Viscosity ratio $\mu_I/\mu_{II}=4$, flowrate ratio $Q_I/Q_{II}=2$. $(y-z)$ velocity vectors, a) at $x=0.1$, b) at $x=0.3$ and c) at $x=0.8$.

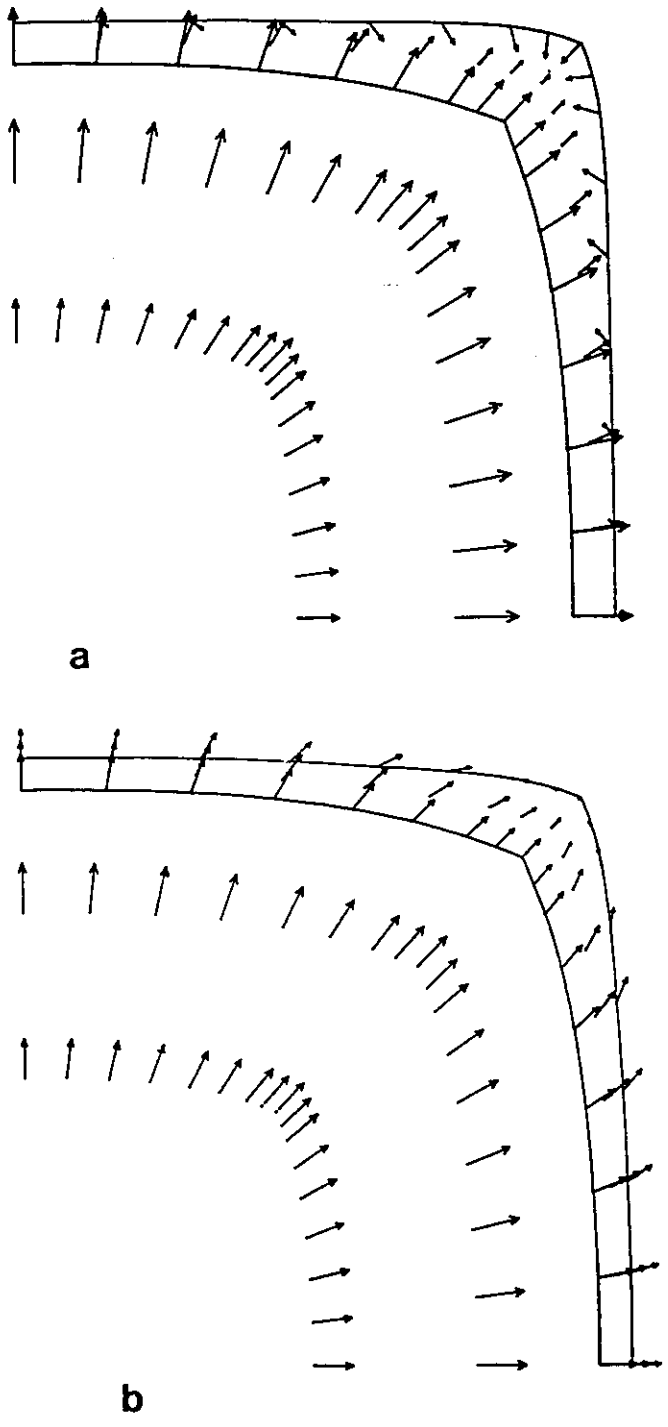

Figure 5.19 Extrudate swelling and interface development outside the die. Square die. Viscosity ratio $\mu_I/\mu_{II}=4$, flowrate ratio $Q_I/Q_{II}=8$. (y−z) velocity vectors, a) at x=0.1 and b) at x=0.3.

with the surface material again tending to redistribute in a sliding-over-the-free surface motion.

The very significant effect of the viscosity ratio on the swelling behaviour is demonstrated in Figures 5.20 and 5.21 for a fixed flowrate ratio of $Q_I/Q_{II}=8$. When the more viscous material is located at the core ($\mu_I/\mu_{II}=4$), the extrudate shrinks (Figures 5.20a, 5.21a). However, when the less viscous material occupies the core ($\mu_I/\mu_{II}=0.25$), the extrudate expands significantly and demonstrates the significant effect that the layer configuration may have on both the interface and the external free surface shapes (Figures 5.20b, 5.21b). Even though there are no surface tension effects, the interface becomes almost round due to the high swelling that the system exhibits. The inner layer corner points disappear completely while they persist on the external free surface. The pronounced swelling is the result of the flow rearrangement in the extrudate and follows the same mechanism with the thermally induced extrudate swelling that was presented in Chapter 3. Generally, when the fluid wetting the walls is more viscous, more pronounced swelling is expected than in the opposite case.

Since the downstream boundary condition assumes plug flow profile, the area ratio in the final extrudate shape equals the ratio of the volumetric flows of the two components and serves as an additional check of the approach. Figure 5.22 shows the downstream component of velocity in different stations downstream corresponding to Figures 5.20a and 5.21a. The material near the core of the flow decelerates as the material near the free surface accelerates and the system finally attains the plug flow profile downstream.

5.6 SHEAR THINNING FLUIDS

The interface development and extrudate swelling behaviour when the fluids follow the shear thinning Carreau-type constitutive relation (eqn. 2.35) is studied (Figure 5.23). The

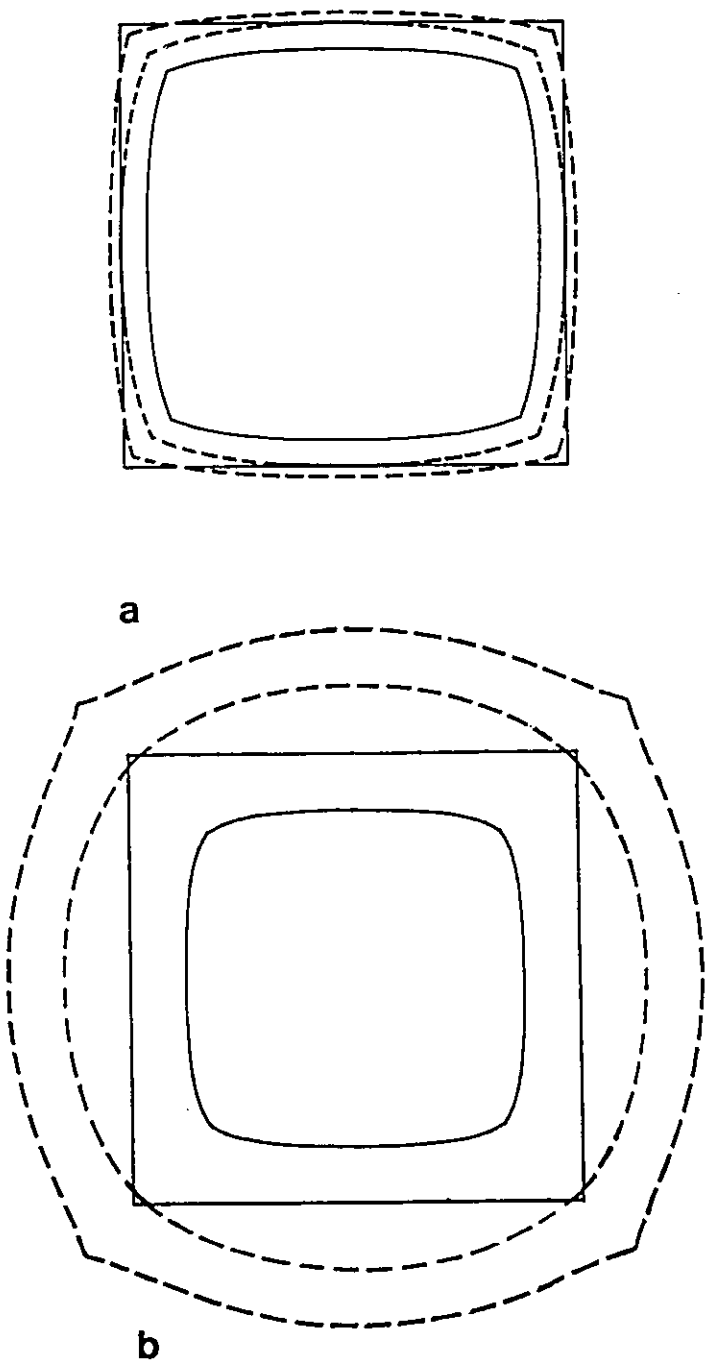

Figure 5.20 Extrudate swelling and interface development outside the die. Square die. Flowrate ratio $Q_I/Q_{II}=8$. Effect of Viscosity ratio, a) $\mu_I/\mu_{II}=4$ and b) $\mu_I/\mu_{II}=0.25$.

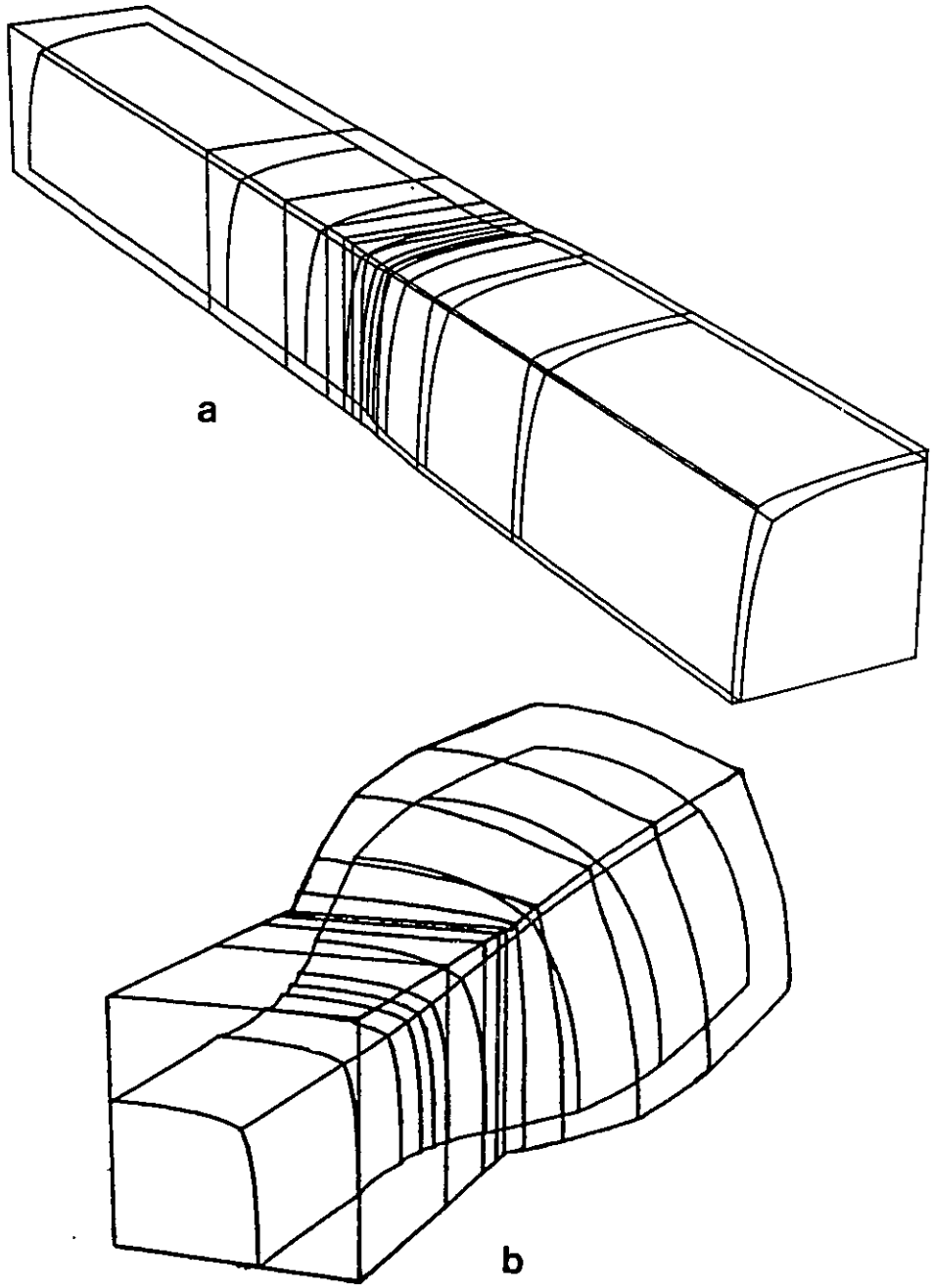

Figure 5.21 Extrudate swelling and interface development outside the die. Square die. Perspective view. Flowrate ratio $Q_I/Q_{II}=8$. Effect of Viscosity ratio, a) $\mu_I/\mu_{II}=4$ and b) $\mu_I/\mu_{II}=0.25$.

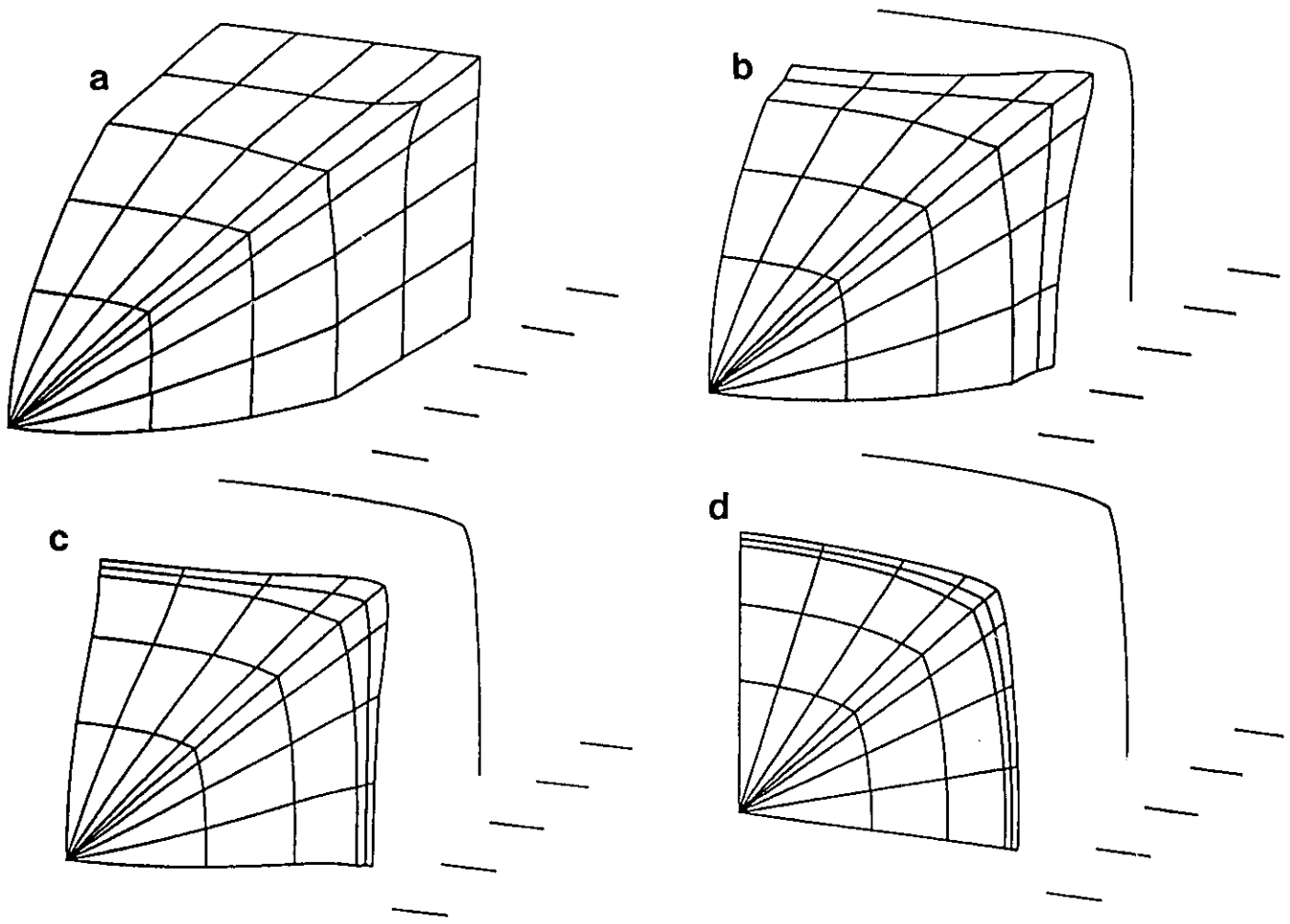

Figure 5.22 Extrudate swelling and interface development outside the die. Square die. Viscosity ratio $\mu_I/\mu_{II}=4$, Flowrate ratio $Q_I/Q_{II}=8$. Downstream component of velocity at different stations downstream; a) inside the die, b) at $x=0.1$, c) at $x=0.3$ and d) far downstream.

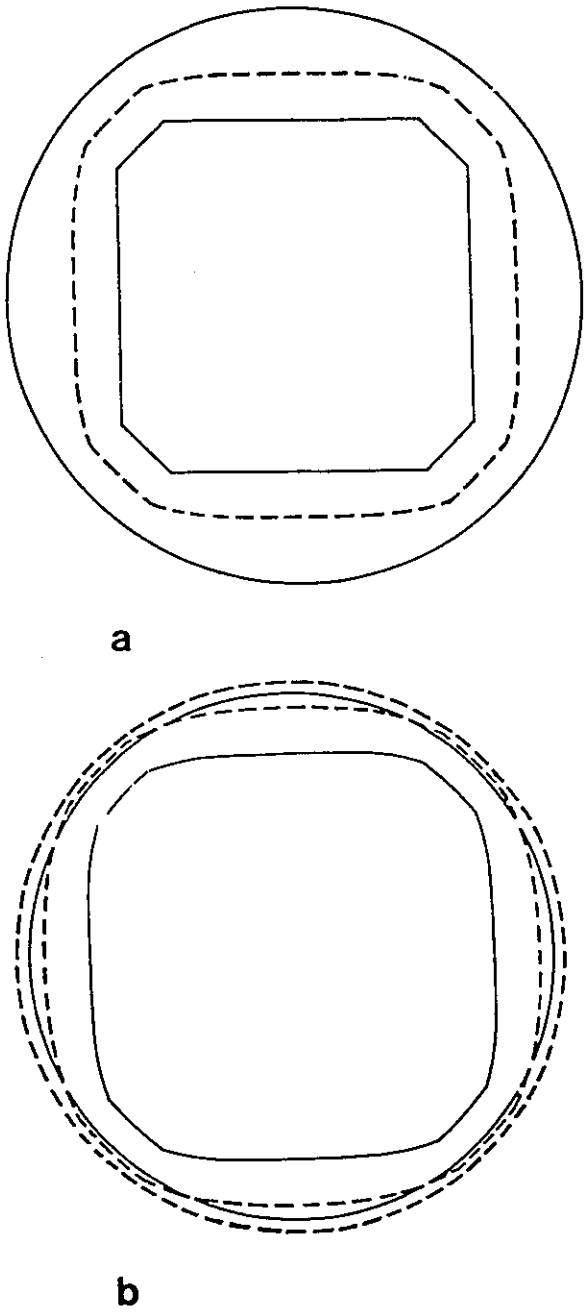

Figure 5.23 Interface development and extrudate swelling behaviour of shear- thinning fluids. Fluid properties are summarized in Table 4.1. Flowrate ratio $Q_I/Q_{II}=8$, a) interface development inside the die and b) Extrudate swelling behaviour and interface development outside the die.

outer die geometry is circular, the flowrate ratio is set to $Q_I/Q_{II}=8$ and the material properties are given in Table 4.1.

The interface shape for the bicomponent stratified flow inside the die is shown in Figure 5.23a. The inner layer expands significantly, but the interface does not become round showing again the dependence on the initial geometric shape.

Upon emerging from the die, the extrudate shape remains round and the system exhibits a low overall swelling which is characteristic of inelastic shear thinning fluids (Tanner, 1985). The interface swells significantly and approaches the free surface. The corner points of the inner layer tend to disappear and the interface shape does not change dramatically.

5.7 SUMMARY

The important class of bicomponent stratified flows with a sheath-core configuration was studied with a fully 3-D approach.

The three dimensional results showed that the inner layer shape depends on the flowrate and viscosity ratios. For the short dies studied, the interface shape was also shown to depend on the initial geometric shape unless dominant interfacial surface tensions effects are present. The assumed downstream boundary condition may have an effect on the calculated interface shape due to the elliptic character of the governing equations and the short grid lengths used.

The extrudate swelling behaviour was demonstrated to depend on the flowrate ratio and more critically on the viscosity ratio. Generally, when the less viscous fluid wets the die walls little swelling or even shrinkage of the extrudate occurs. When the more viscous fluid is wetting the walls pronounced extrudate swelling occurs.

Depending on the flow conditions, the interface shape may change significantly not only during the course of flow inside the die but also in the flow out of the die because of pronounced swelling phenomena.

CHAPTER 6

THREE DIMENSIONAL ANALYSIS OF SIDE-BY-SIDE BICOMPONENT STRATIFIED FLOWS

This chapter contains the numerical studies on the bicomponent stratified flows in a side-by-side configuration. A numerical method for the simulation for this class of problems is presented. The method consists of a Galerkin/finite element discretization of the governing equations with a spine or pathline construction of the internal and/or external free surfaces. The method is applied on the bicomponent stratified flow inside a square die and the flow of the bicomponent system out of the die.

6.1 INTRODUCTION

Stratified flow of molten polymers in a side-by-side configuration is probably the most common form of coextrusion. It is used in the production of multilayer sheet, cast film, blown film, man-made fibers, etc. In a typical coextrusion line, the molten polymers are combined in a layered (side-by-side) manner which is also retained in the final product. Each layer contributes its own physical characteristics (e.g. Oxygen and/or moisture barrier, heat sealability, stiffness, color, etc.) to the system and the result is a product with tailored properties and/or cost effectiveness.

Two possible ways of producing multilayer films or sheets are the tubular blown film process and the flat die coextrusion. Flat die coextrusion in turn, can be divided into two characteristic process groups, the one that first expands the individual layers to the full width of the sheet in separate channels and combines them afterwards (lamination, multimanifold die) and the one that first combines the individual layers and expands them in a single

manifold die (feedblock coextrusion). The more versatile feedblock coextrusion is the most widely used technology since a single-manifold die can be used to make a wide variety of products.

A major problem in the coextrusion process is maintaining the layer structure uniformity. Experimental investigations have so far identified the viscosity difference between the polymer melts to be the controlling factor of the encapsulation effect with the less viscous melt encapsulating the more viscous melt (for an extensive review of relative work see section 1.2.2). The effect occurs predominantly near the die walls and may result in undesirable product properties and increased cost due to the need to trim the film or sheet edges.

Because of the viscosity mismatch, the extrudate of the layered system may exhibit bending (Southern and Ballman, 1973) that may also have an impact on the final product and interface shapes as well as on the winding process stability.

This chapter studies the interface development of stratified bicomponent flow systems in a side-by-side configuration and their extrudate swelling behaviour. A three dimensional Galerkin/finite element algorithm was developed and is used to study the problem in square die geometries. The choice of square die geometries was made in order to approximate the flow in the feedblock method which is the most widely used coextrusion technology (Finch, 1987). The simple geometric characteristics with the low aspect ratios and the long duration of flow are close to practical situations and also facilitate the extremely complex three dimensional analysis. The tendency of the less fluid to wrap around and encapsulate the more viscous fluid during the course of the flow inside the die is demonstrated and the extrudate bending and distortion because of the viscosity mismatch is shown.

Many numerical problems occur because of the complex nature of the 3-D stratified flow. The free surface problem is extremely complicated since there are external free surfaces (corresponding to the sides of the square die) in addition to the interface between the two

fluids. The existence of three-phase (melt/melt/wall) contact lines pose an additional complexity since the physics of the contact lines are not very well understood in the absence of surface tension effects. In simulating this flow, the very slow interface deformation requires very long and dense finite element grids which give rise to extremely large systems of equations and high computation costs.

Differences in the elastic properties of the polymer melts may also contribute to the encapsulation effect (White et al, 1972; Han, 1981; Southern and Ballman; 1975). However, it has been experimentally established that the viscosity difference between the two melts predominates over the elasticity ratio in determining the interface shape (Southern and Ballman, 1973; Lee and White, 1974; Khan and Han, 1976; Han, 1981). Based on this fact, this chapter focuses on the effect of the viscous properties only on the interface deformation phenomena. Melt elasticity differences are believed to cause rugged interface shapes (Southern and Ballman, 1975; Khan and Han, 1977) and contribute to interfacial instabilities (Lee and White, 1974; Pool, 1987). Incorporation of viscoelasticity in the 3-D analysis would complicate further the numerics since viscoelastic models that have been proposed so far are physically questionable (Tanner, 1985) and numerically unstable (Crochet and Keunings, 1982). Furthermore, the need to calculate the stress components would increase the already formidable size of the 3-D numerical problem. Therefore, no studies of the contributions of the elastic properties and/or stability analysis were pursued in this thesis.

6.2 GOVERNING EQUATIONS AND BOUNDARY CONDITIONS

The formulation of the side-by-side stratified flow of immiscible fluids closely follows that outlined in Chapter 5 for the encapsulated case and only the necessary extensions to it are presented here. The flow problem (Figure 6.1) consists of the introduction in a side-by-side manner of two immiscible fluids, the formation of the interface during the course of flow

inside the die and the emergence of the bicomponent system out of the die. The problem is divided into two sub-problems, the interface development inside the die (Figure 6.2) and the extrudate swelling problem (Figure 6.3) which are solved separately to reduce the size of the numerical problem.

The flow fields of the two fluids are governed by the mass and momentum conservation equations in each phase (Eqns. 5.1, 5.2) and are coupled through boundary conditions at the interface.

Throughout this chapter index I refers to the lower and index II to the upper fluid in the bicomponent stratified structure.

A schematic of the interface development problem for the stratified flow inside the die with the associated boundary conditions is given in Figure 6.2. Initially the two fluids flow through different channels (ABFEA-GHLKG for fluid I and EFCDE-KLIJK for fluid II, Figure 6.2) divided by a very thin separation plate (EKLFE). The two fluids are brought together at plane GHIJG, the interface KQRLK forms and the tendency of the less viscous fluid II to encapsulate the more viscous fluid I is shown.

A fully developed profile is assigned initially to each channel (planes ABFEA and EFCDE, Figure 6.2) which is generated by solving the corresponding unidirectional flow problem (eqn. 5.4) for the (y-z) geometry of each channel.

The no-slip boundary condition is imposed at the die walls (areas AGMPJDA and DJPOICD, Figure 6.2) and the thin separation plate (area EKLFE).

The velocity and stress boundary conditions at the interface are given by equations 5.5-5.10, fully developed flow is imposed at the far downstream face (plane MNOPM) and symmetry conditions are imposed where possible to reduce the size of the problem.

A schematic of the extrudate swelling of the bicomponent system with the associated boundary conditions is given in Figure 6.3. The two fluids initially flow inside the

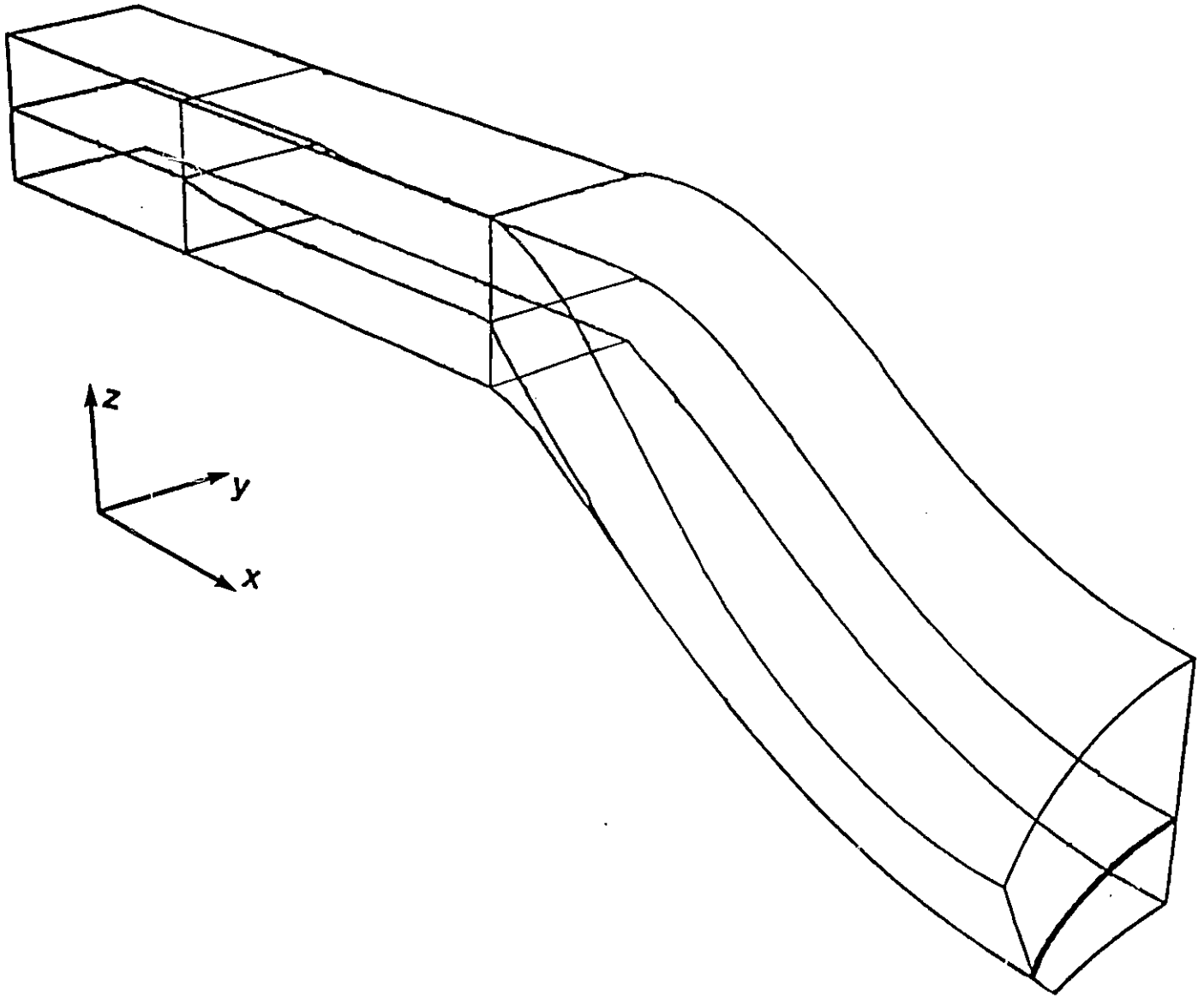

Figure 6.1 Schematic of bicomponent stratified flow in a side-by-side configuration.

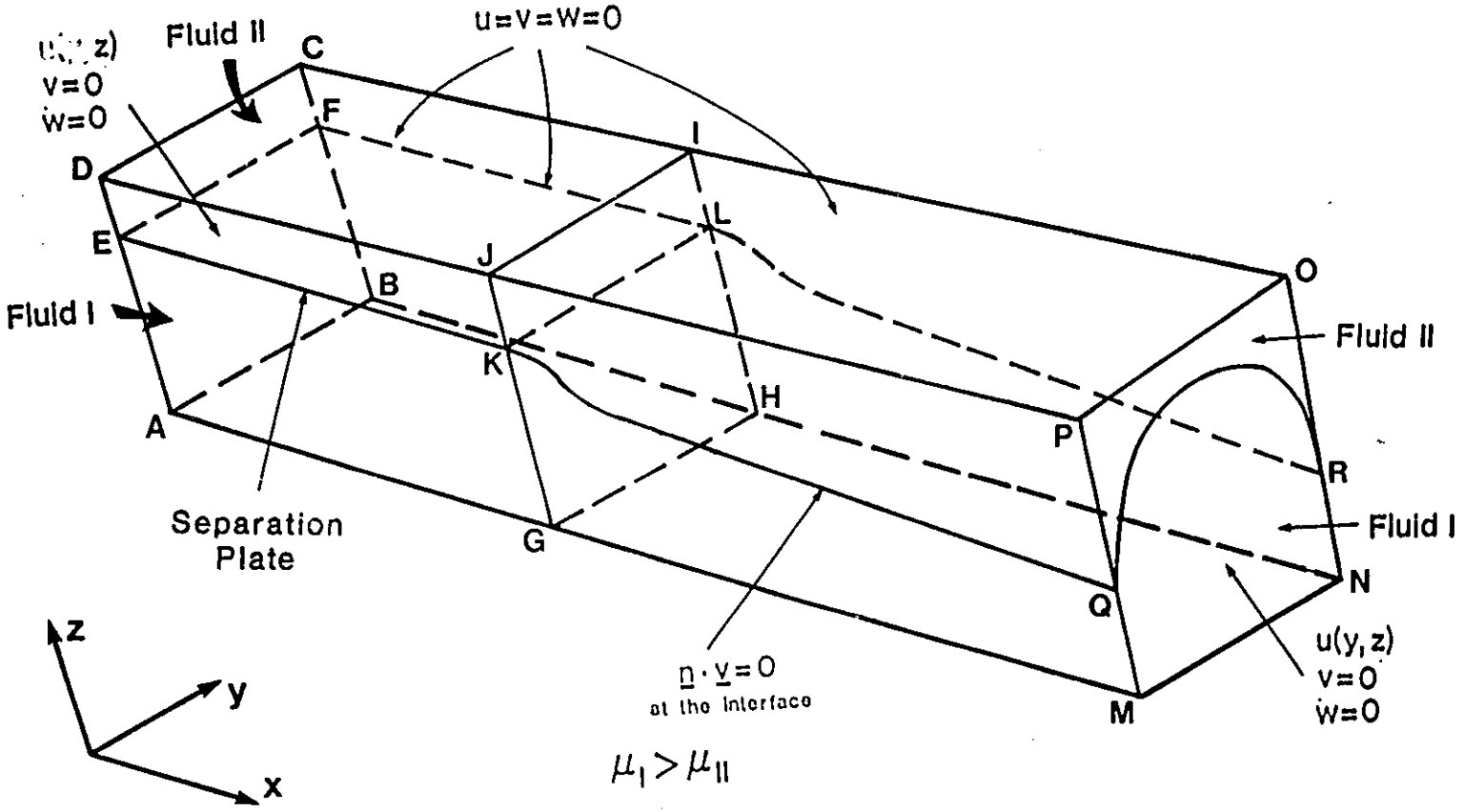

Figure 6.2 Schematic of side-by-side bicomponent flow inside a die. Boundary Conditions.

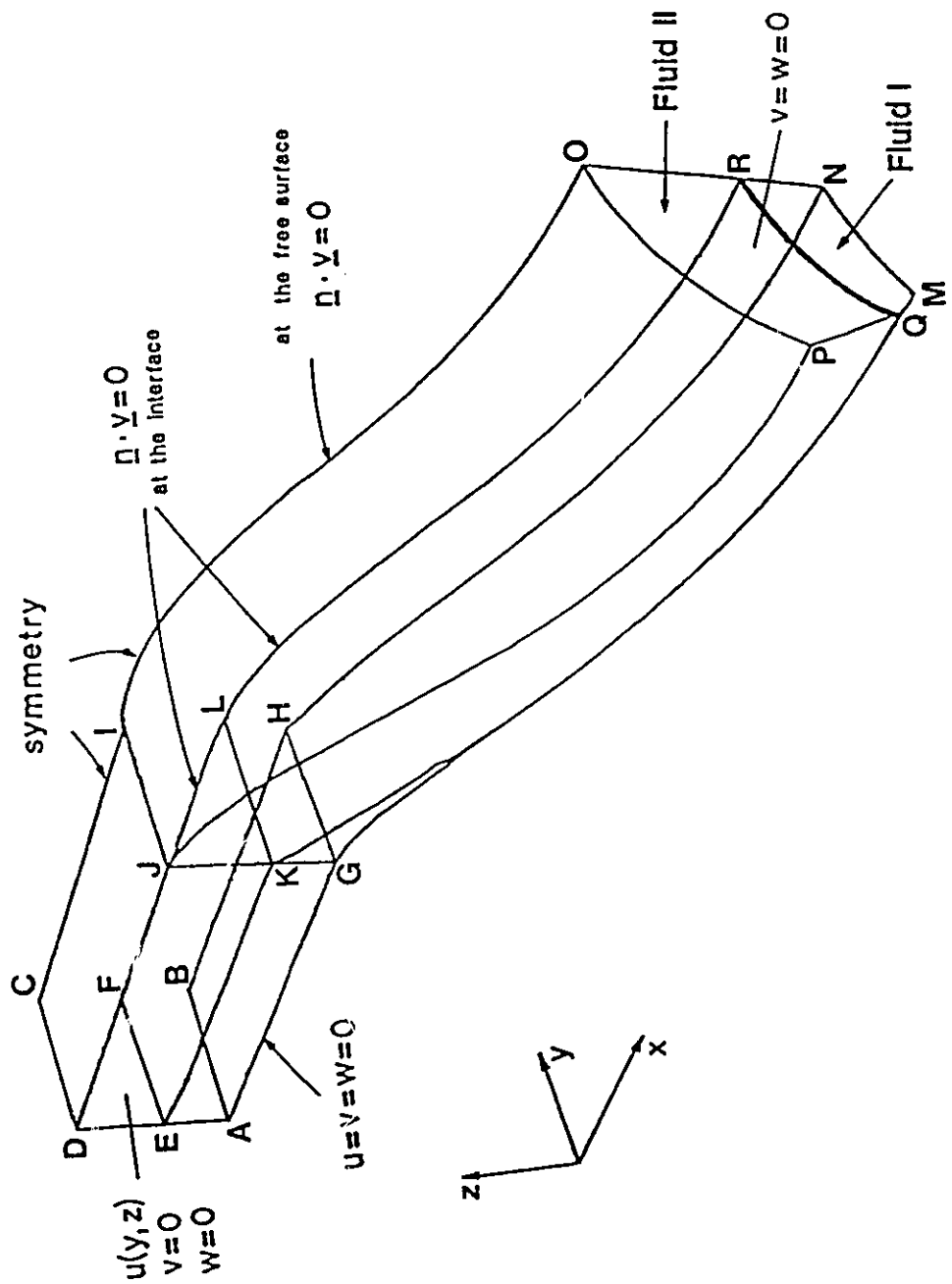

Figure 6.3 Schematic of side-by-side bicomponent flow out of a die. Boundary Conditions.

die ABCDA-GHIJG, emerge from the die at plane GHIJG, and are separated by the interface EKLF.

A fully developed profile is assigned upstream (plane ABCD Figure 6.3) which is the downstream solution of the interface development inside the die problem that is solved first. At the die walls the no-slip boundary condition is imposed (areas AGJDA, DJICD Figure 6.3) and at the interface the boundary conditions (5.5-5.10) are imposed.

At the free surface (areas GMPJG, JPOIJ and HNMGH), the kinematic condition (eqn. 5.5) is imposed and the free surface is always treated as a force-free surface. Symmetry conditions are again imposed where possible to reduce the size of the problem. A wind-up mechanism is assumed far downstream such that it exerts a force in the x-direction only and it is free to translate in the y- and z-directions. A plug velocity profile is assumed at the downstream boundary (plane MNOPM, Figure 6.3) and the draw ratio is set to unity for all the cases studied.

6.3 NUMERICAL COMPLICATIONS AND CONSIDERATIONS

The side-by-side bicomponent stratified flow exhibits the pressure and viscous stress discontinuity at the interface presented in section 5.3, since generally the two fluids have different viscous properties. The double node technique described in section 5.3.1 is used throughout this chapter to handle the pressure discontinuity.

The very complex nature of this type of flow which features a distorted interface because of the encapsulation phenomenon and extrudate bending upon emerging from the die, introduces additional complications to the free surface handling schemes. The melt/melt/solid contact lines, where the interface touches the die walls when the bicomponent system flows inside the die, need a special treatment in the absence of an obvious boundary condition when

no surface tension effects are important. Also, slip at the wall is an additional concern since it is expected to have an effect on the degree of encapsulation.

The numerical aspects of these issues are discussed in detail in this section. The finite element formulation follows the procedure presented in Chapters 2 and 5 and will not be repeated here.

6.3.1 Interface and Free Surface Update Scheme

The interface development inside the die problem examines the merging flow of the two melt streams inside the die (Figure 6.2). The flow is confined and only one unknown free surface exists, namely the interface between the two immiscible fluids. The tendency of the less viscous fluid to encapsulate the more viscous fluid leads to a curved interface, especially near the die walls where encapsulation is more pronounced. The spine parametrization of the interface is very well suited for this problem as long as the fluids remain in the side-by-side configuration which is always the case in this chapter. There is only one spatial variable per spine (only the internal free surface is present) and the spines are defined as straight lines running from the bottom wall to the top wall of the die (Figure 6.4). The spine orientation is kept fixed (Figure 6.4) and very dense grids near the die wall can be constructed. The pathline construction of the internal free surface can also be used but the spine approach is expected to result in fewer non-linear iterations. Also, the pathline approach leads to numerical instabilities when the grid near the wall becomes very fine due to the vanishing magnitude of the velocity components.

The problem of the extrusion out of the die examines the extrudate swelling and bending effects of the layered bicomponent system. The free surface problem is very difficult because multiple free surfaces exist (top, bottom, side external free surfaces and interface). The swelling behaviour of the system is extremely complicated, the extrudate does not only

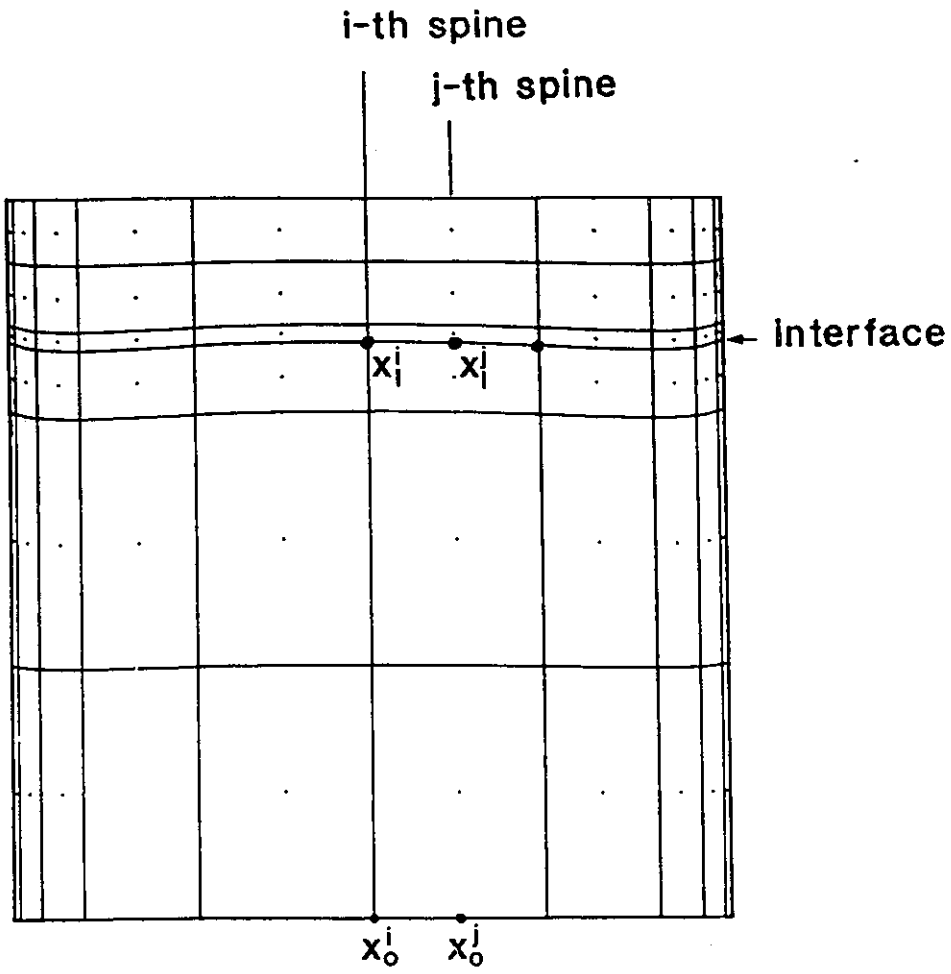

Figure 6.4 Interface parametrization and spine definition in the flow inside the die.

swell but it also bends because of the viscosity difference of the two fluids (Southern and Ballman, 1975; Everage, 1975; Mavridis 1987) and distorts because of the 3-D geometry and the unsymmetric velocity profile inside the die. The finite element grid deforms significantly especially in elements that possess more than one free surfaces (corner elements, interfacial side elements, Figure 6.5). The surface material redistributes in a 3-D manner and in the absence of surface tension effects, the sharp corner points are maintained in the extrudate. The spine approach becomes prohibitively complicated and the less sophisticated and easy to implement pathline method, presented in section 2.5.1, is used for the construction and update of all free surfaces in the extrudate.

It should be noted that for both the spine and pathline approaches, direct use of the calculated interface/free surface position

$$\underline{x}^{k+1} = \underline{f}(\underline{x}^k) \tag{6.1}$$

leads to divergence of the nonlinear iteration procedure. A stabilizing underrelaxation scheme was employed and the free surface coordinates are calculated as

$$\underline{x}^{k+1} = \underline{x}^k + \lambda[\underline{f}(\underline{x}^k) - \underline{x}^k] \tag{6.2}$$

where λ is the relaxation factor and k the iteration index. Values of λ range between 0.2 to 0.8 depending on the nonlinearity of the problem. The interface calculation inside the die was more stable than the free surface calculation in the extrudate in all cases studied.

6.3.2 Contact Line Determination

The existence of three-phase contact lines where the interface between the two fluids meets the die wall, adds a further complication to the 3-D analysis. For the flow inside the die problem, the governing equations with the boundary conditions presented in earlier sections constitute a closed system which allows, in principle, the calculation of the location of every node on the interface. Locating the intersection between the interface and a solid

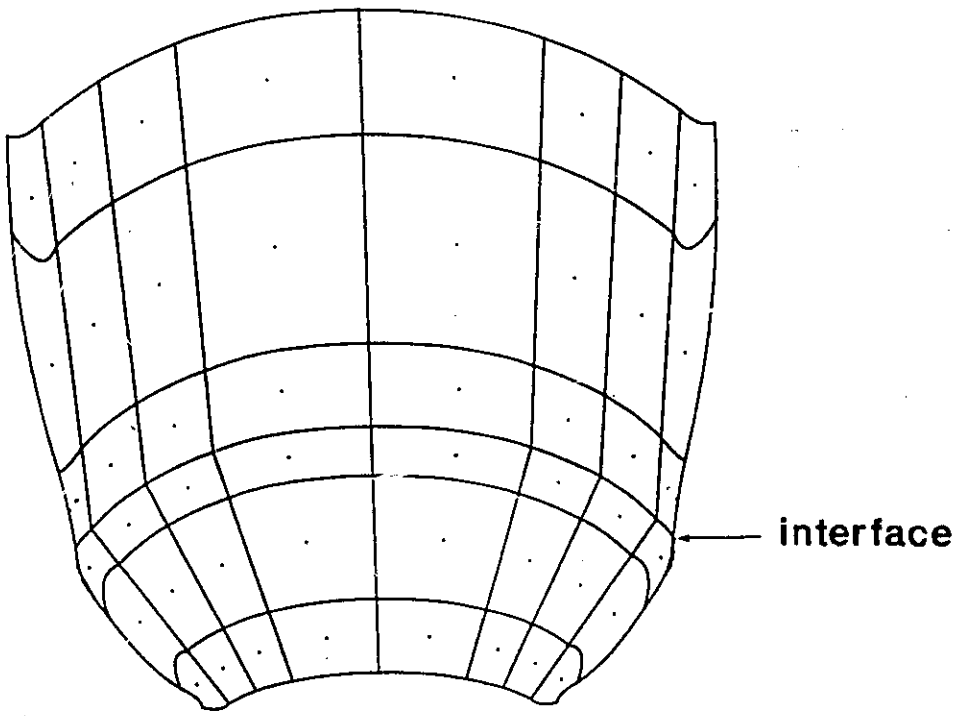

Figure 6.5 Distorted downstream finite element grid. Square die geometry.

boundary is however a difficult problem which has been studied extensively (Kafka and Dussan, 1979; Mavridis et al., 1987; Dheur and Crochet, 1987; Binding et al, 1987). One should distinguish between static contact lines, which do not move with respect to the walls, and dynamic ones which exhibit a uniform translational velocity with respect to them. Surface tension is generally a major factor in this problem but in this thesis the static case in the absence of surface tension effects is considered.

The locations of the contact lines between the interface and the side walls (Figure 6.2, lines KQ and LR) are not known a priori and their calculation needs to be included in the numerical problem since there is no physical hypothesis available that could otherwise determine their position. In principle, the kinematic condition (equation 5.5) is valid at the interface and with respect to the contact point A (Figure 6.6) it becomes

$$\int_I \{\underline{n} \cdot \underline{v}\} N^A \, dS \tag{6.3}$$

Since $\underline{n}$ implicitly refers to the nodal coordinates of the interface, eqn. 6.3 provides the necessary condition for calculating the location of point A. The problem with this approach (Dheur and Crochet, 1987) is that since A is a stagnation point, the velocity components near it are very small and the coefficients of the algebraic equations resulting from (6.3) tend to vanish when the size of the elements near A decreases. Correspondingly, the slope of the last segment of the interface tends to be undetermined and it is usually difficult to obtain convergence of the iterative procedure.

An alternative method which has been used in this thesis is the extrapolation method (Dheur and Crochet, 1987) and is presented in Figure 6.6. The contact point is denoted by A while B,C,D,E etc. denote other nodes on the interface. The extrapolation method consists of forcing the contact point to lie on the cross section of the wall (y_A = constant) with a line that passes through some of the B,C,D,E etc. points, for which the kinematic condition

provides a unique solution. Dheur and Crochet (1987) used a simple linear extension of the segment BC to define the contact point depicted by A' in Figure 6.6, according to

$$z_C - z_A = (z_B - z_A)(y_C - y_A)/(y_B - y_A) \tag{6.4}$$

This technique approaches the true contact point A in the limit as the grid becomes denser near the wall and utilizes information from the two previous nodes B and C only. Higher order extrapolation was attempted in this thesis to take advantage of the quadratic interface parametrization and the curvature information of the previous interfacial nodal points. The contact point A is generally found as the cross section of the wall and a polynomial fitted through the previous interfacial nodal points. The choice of the degree of the polynomial impacts the cost of the method because of the need to calculate the coefficients of the polynomial at each step. It also affects the stability of the non-linear problem and generally use of up to a 3rd order polynomial seems to be a fair compromise. The contact point is then calculated as

$$z_A = a + b y_A + c y_A^2 + d y_A^3 \tag{6.5}$$

and the coefficients a, b, c, d of the polynomial are calculated by using the information provided by points B, C, D, E (Figure 6.4).

Results produced with this policy were not very different compared to results with the linear extrapolation and this motivated the use of the more convenient linear approximation of equation 6.4 throughout this chapter. The most significant effect of the higher order curvature information is on the computed position of the contact point itself which generally results in more pronounced encapsulation.

A study on the effect of the grid density near the contact point proved that the calculated interface position one element away from the wall is accurate to the tolerance limit, although the computed location of the contact point itself may exhibit a grid dependence. As the grid becomes denser near the contact point, the convergence of the non-linear iteration

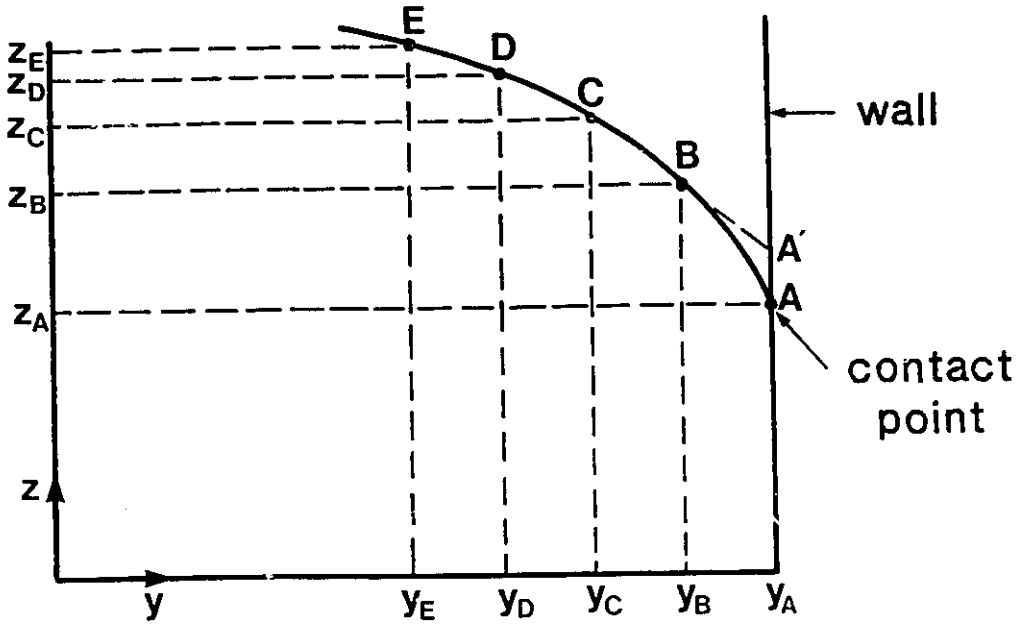

Figure 6.6 Location of the contact point by the extrapolation method.

scheme becomes slow and difficult due to the decreasing magnitude of the velocities near the wall. The treatment of the contact point is expected to be one of the major sources of error in the 3-D finite element analysis and a further fundamental study of the three-phase contact points is essential. Dheur and Crochet (1987) have also shown that any error produced by the contact condition at A is local and its numerical effect is confined within the first row of elements.

6.3.3 Slip at the Wall

The slip of polymer melts at the die walls is experimentally justified (Kraynik and Schowalter, 1981) and the use of a slip boundary condition has been suggested by several researchers (Huh and Scriven, 1971; Huh and Mason, 1977; Dussan, 1979; Silliman and Scriven, 1980) to alleviate the stress singularity at the contact point. The slip boundary condition relates the magnitude of the slip velocity v_s to the applied wall stress τ_w. The simplest approach is the Navier boundary condition:

$$v_s = \beta \tau_w \tag{6.6}$$

where β is the slip coefficient and can be experimentally determined. More complex descriptions for the slip boundary condition are also available, usually power-law relations empirically fitted to experimental data (Chauffoureaux et al, 1979; Lau and Schowalter, 1986; Cohen and Metzner, 1985). The subject of slip at the wall received special attention recently due to its relevance in polymer flow instabilities and the breakdown of viscoelastic computations (Ramamurthy, 1986; Kalika and Denn, 1987; Yeh et al, 1984; Schowalter, 1988; Wesson and Papanastasiou, 1988; Phan-Thien, 1988).

In this work the linear form of the slip boundary condition of eqn. (6.5) is used. The contact points are allowed to exhibit slip at the wall in the z-direction only (Figure 6.6) since

encapsulation occurs along that direction. The dimensionless form of the applied slip condition becomes then:

$$\tau_w = -w/B \tag{6.7}$$

where $B = \beta \mu/L$ is a dimensionless measure of slip, typically a small number below unity. This condition enters the finite element algorithm through a line integral:

$$R^i_{z,s} = \int_I \left\{ \frac{w}{B} \right\} N^i \, dS \tag{6.8}$$

that is added to the w-momentum residual equation (eqn. 2.23). When the no-slip condition is applied, the residual is deleted and the w-velocity is set to zero. When the slip velocity is applied, the w-velocity at the wall is unknown, eqns. (6.8) and (2.23) provide as many algebraic equations as there are unknown slip velocities along the wall and the system is closed.

A stick-slip mechanism at the interface is suspected to be responsible for the occurrence of interfacial flow instabilities (Schrenk et al, 1978) and interfacial slip may be important under certain conditions (Lyngaae-Jorgensen et al, 1988). However, due to the additional complications introduced by the existence of the slip velocities at the interface and the lack of clear experimental data, this issue was not pursued.

6.3.4 Numerical Considerations

The problem is nonlinear due to the existence of the free surfaces. When only the interface is present and the spine method is used, the Newton-Raphson iteration can be employed. A Picard iteration is needed with the pathline method. Depending on the initial conditions, viscosity ratio and flow parameters, convergence problems may occur. In most cases the interface calculation needed an underrelaxation factor of 0.4-0.8 to alleviate convergence problems. The more difficult free surface calculation required underrelaxation factors of 0.2-0.5. In same cases, especially when the additional non-linearity of the shear-thinning constitutive relation is included, the Newton-Raphson with the spine approach failed

to converge directly. A Picard-like procedure where the solution of the field unknowns (velocities, pressures) was decoupled from the free surface calculation was used initially to produce a better estimate before the Newton-Raphson method was employed. Normally 2-3 Picard steps were required to ensure convergence of the Newton-Raphson scheme. The convergence rate of the Newton-Raphson scheme is less than quadratic because the contact point calculation was not included in the global matrix system. The Jacobian for the Newton-Raphson iteration is calculated using analytical derivatives of the finite element equations in all cases.

For the interface development inside the die, the first iteration is either performed with a fixed, flat interface at the position of the separation plate or with a fixed interface curved to the expected direction of encapsulation. Both approaches led to the same solution for a number of test cases showing no dependence of the final results on the initial interface shape.

For the extrudate emergence problem, the first iteration is performed with the initial shape of the external free surface assigned as that of the die at the die exit. The initial interface shape is assigned as the one given at the initial inlet profile which is the downstream solution of the previous problem. This policy leads to convergence difficulties, and use of underrelaxation factors is essential.

Termination requires that the maximum relative update of all the calculated variables be less than 10^{-3}. This policy resulted in a large number of non-linear iterations, normally 10-17 iterations, especially when the Picard-pathline iteration scheme was used. No convergence acceleration techniques were employed in this chapter although this could be a very attractive strategy (see Appendix B) in light of the high cost of the 3-D numerical problems.

6.4 INTERFACE DEVELOPMENT INSIDE THE DIE

This section studies the interface deformation for the bicomponent stratified side-by-side flow of immiscible generalized Newtonian fluids in a square die. The characteristic length scale L equals the width of the die. The actual size of the die and the flowrates of the fluids do not play a role when the Newtonian constitutive relation (eqn. 2.4) is employed, since scaled (dimensionless) quantities are used to describe the flow field.

The effects of viscosity ratio, initial conditions and upstream die design, and slip at the wall on the calculated degree of encapsulation and the interface shape are demonstrated. The effects of the assigned boundary conditions and die length are also discussed.

6.4.1 Effect of Viscosity Ratio. Newtonian Fluids

Numerous experimental investigations (Southern and Ballman, 1973; Everage, 1973; Yu and Han, 1973; Lee and White, 1974; Han, 1981; also Chapter 7) have established that there is a preferential direction in the encapsulation phenomenon and it is always the less viscous fluid that tends to encapsulate the more viscous fluid.

The results of the 3-D analysis are in agreement with the experimental observations as Figures 6.7 and 6.8 illustrate for the square die geometry. The flowrate ratio of the two layers is fixed at $Q_I/Q_{II}=13.2$. In the first case (Figures 6.7a, 6.8a), the viscosity ratio is $\mu_I/\mu_{II}=2.5$ and the numerical simulation shows that the less viscous upper layer tends to encapsulate the more viscous lower layer. In the second case (Figures 6.7b, 6.8b) the configuration of the materials is reversed and the individual flowrates are adjusted accordingly to produce the given flowrate ratio. The interface shape between the two fluids changes and the numerical method shows that again the less viscous fluid (lower fluid in this case) will tend to encapsulate the more viscous fluid (upper). Along the interface the curvature changes as we approach the walls and increases significantly very close to the wall for both configurations

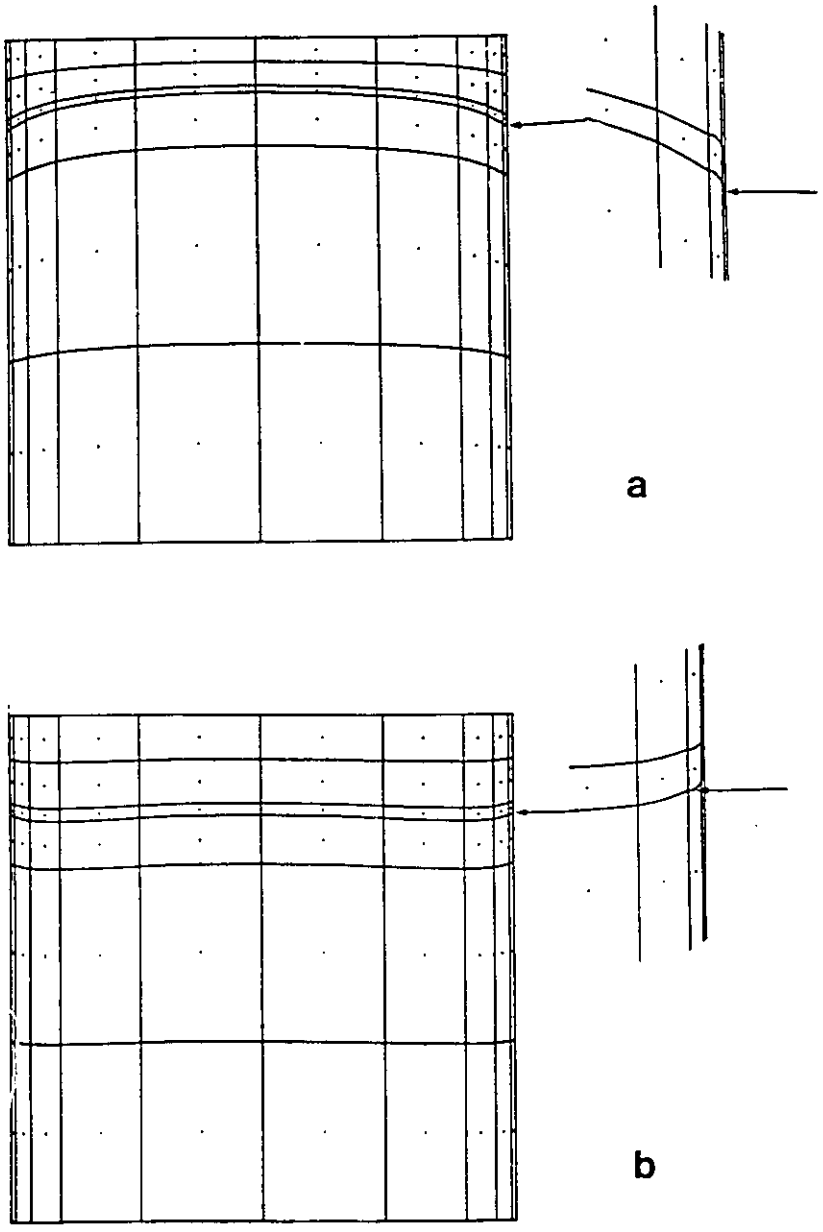

Figure 6.7 Flow inside the die. Effect of viscosity ratio. Downstream finite element grids. Flowrate ratio $Q_I/Q_{II}=13.2$, a) $\mu_I/\mu_{II}=2.5$ and b) $\mu_I/\mu_{II}=0.4$.

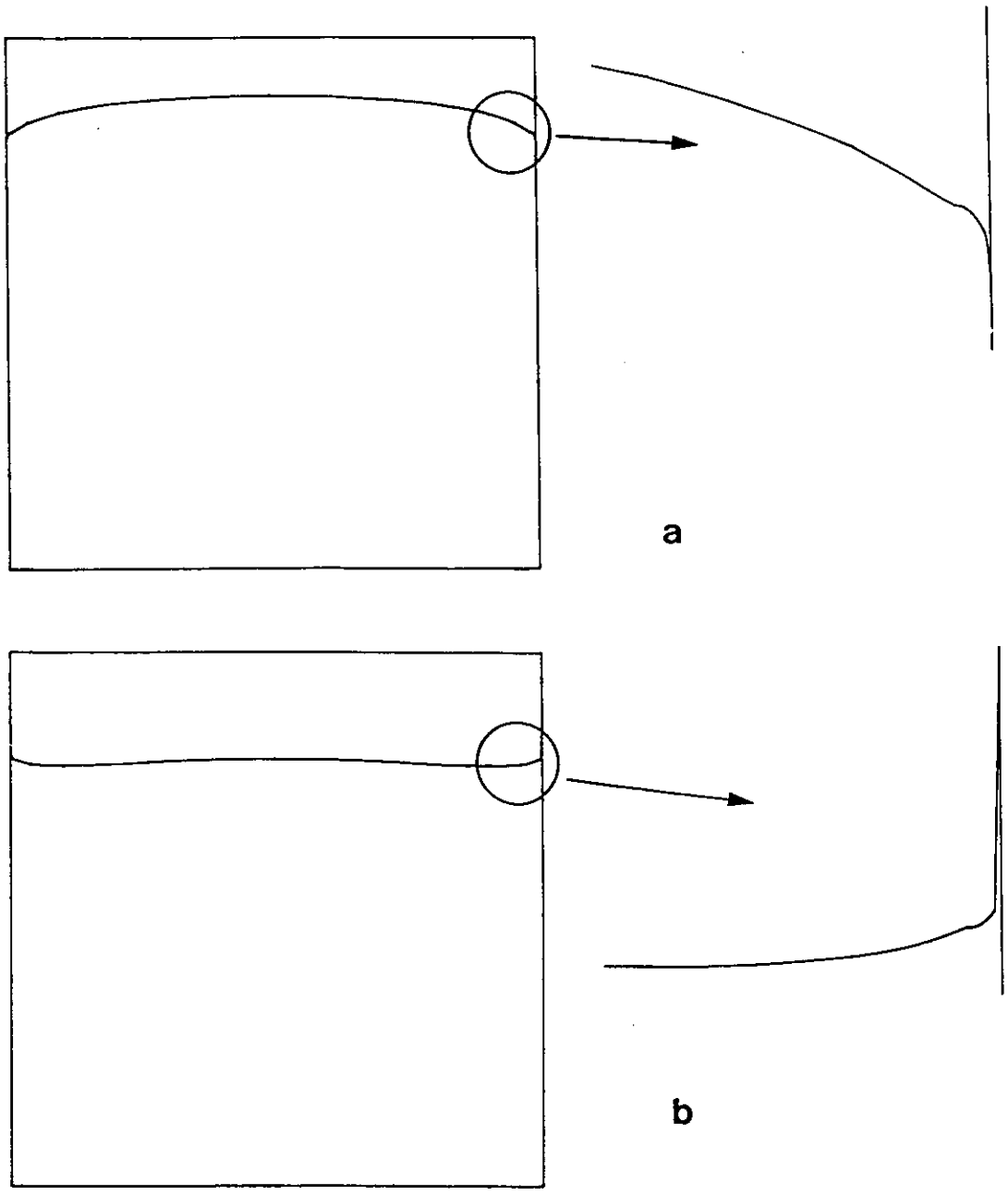

Figure 6.8 Flow inside the die. Effect of viscosity ratio. Interface shape. Flowrate ratio $Q_I/Q_{II}=13.2$, a) $\mu_I/\mu_{II}=2.5$ and b) $\mu_I/\mu_{II}=0.4$.

(Figure 6.8). When the lower fluid is less viscous (Figure 6.8b), the interface exhibits a characteristic waviness. Figure 6.7 also shows the distorted finite element grid at the far downstream plane. The elements near the walls deform significantly due to the higher curvature of the interface. Denser finite element grid is used in that region to filter out the error introduced by the contact point calculation.

The velocity distribution at the far downstream plane, where fully developed flow is assumed, is shown in Figure 6.9. The normalized x-velocity contours show that the velocity distribution is dissimilar in the two cases and the maximum velocity is always located in the lower layer. However, in Figure 6.9a, the velocity contours are elongated in the vertical direction while in Figure 6.9b, they are elongated in the horizontal direction because of the different configuration and viscosities of the materials.

The interface shape change downstream when $\mu_I/\mu_{II}=2.5$ is demonstrated in Figure 6.10 for a distance of one characteristic length downstream the fluid meeting point. The encapsulation seems to start right after the fluid streams merge and progresses downstream. At the center of the die, the interface initially is pushed lower to accommodate the pressure gradients by changing the flow areas (Everage, 1975), but then moves upward and results in an increase of the interface curvature. Figure 6.11 presents the (y-z) velocity vectors on a cross-section at $x=0.02L$ after the fluids meet. In both cases the lower fluid moves upward and the upper fluid downward due to the effect of the separation plate. However, the interface moves in a different direction. A closer look on the cross-flow (y-z) velocity vectors at the interface, shows that for the first case ($Q_I/Q_{II}=13.2$, $\mu_I/\mu_{II}=2.5$, Figure 6.12) the material at the interface initially tends to move upward and to the left (Figure 6.12a, $x=0.02L$) but that direction is reversed to un upward and to the right motion further downstream. In the second case however, ($Q_I/Q_{II}=13.2$, $\mu_I/\mu_{II}=0.4$, Figure 6.13) the initial downward and to the left motion is reversed to an upward but still to the left motion with upper layer material

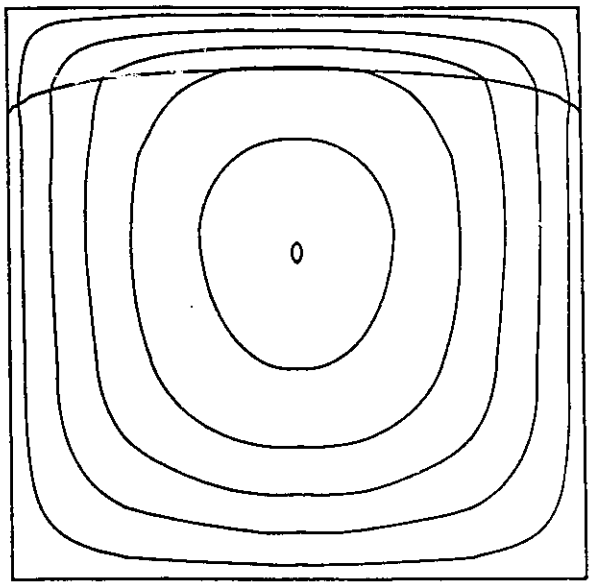

a

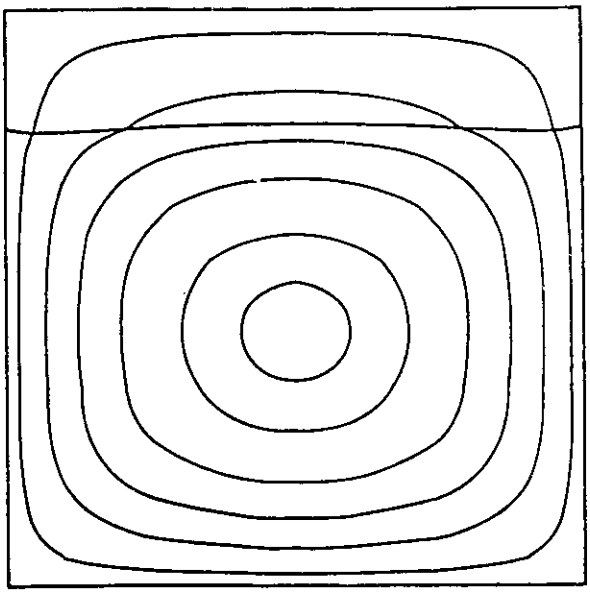

b

Figure 6.9 Flow inside the die. Effect of viscosity ratio. Normalized velocity contours (x-velocity) downstream. Flowrate ratio $Q_I/Q_{II}=13.2$, a) $\mu_I/\mu_{II}=2.5$ and b) $\mu_I/\mu_{II}=0.4$.

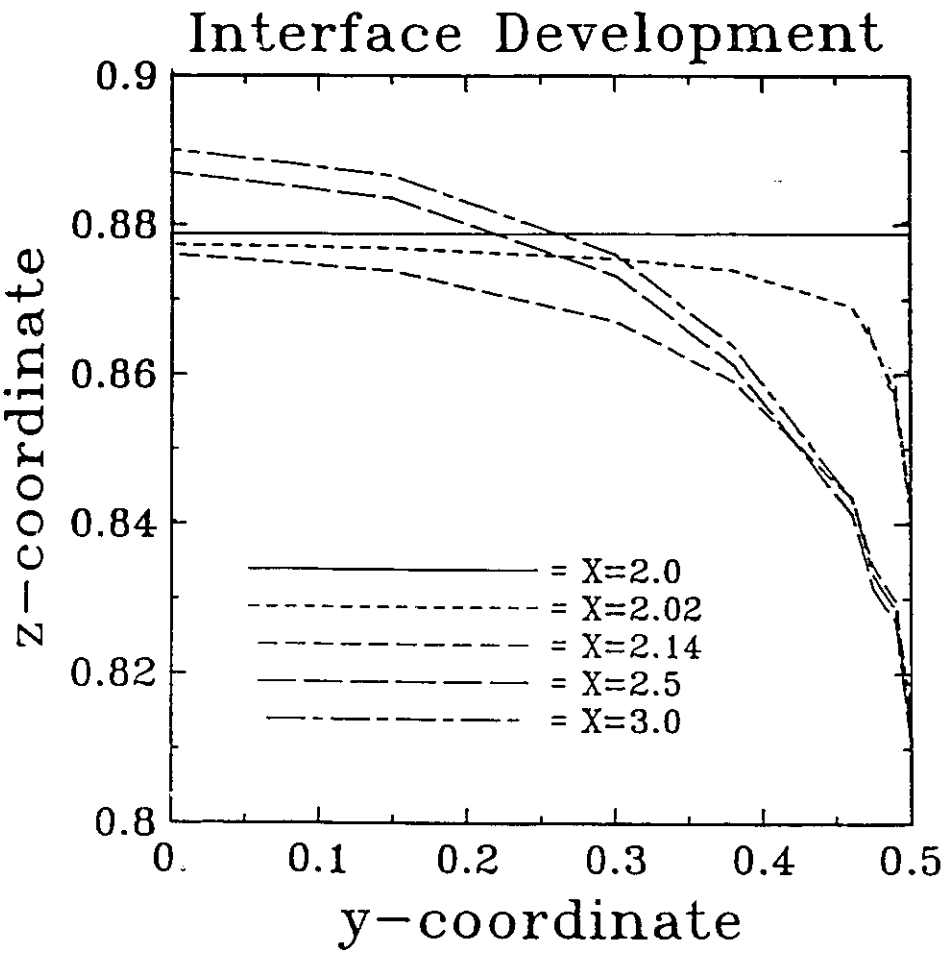

Figure 6.10 Flow inside the die. Interface development downstream. The die wall is at $y=0.5$. Flowrate ratio $Q_I/Q_{II}=13.2$. Viscosity ratio $\mu_I/\mu_{II}=2.5$.

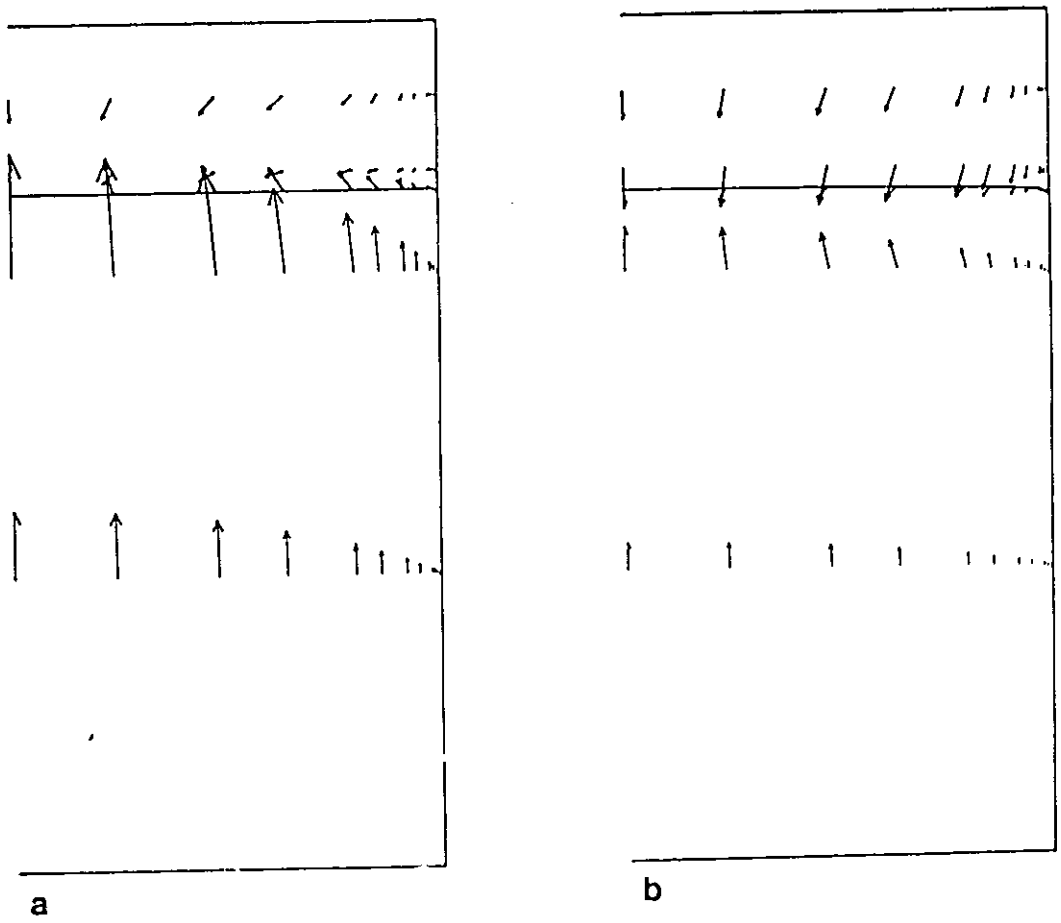

Figure 6.11 Flow inside the die. (y – z) velocity vectors at the cross-section x = 0.02L downstream the merging point. Flowrate ratio $Q_I/Q_{II} = 13.2$, a) $\mu_I/\mu_{II} = 2.5$, b) $\mu_I/\mu_{II} = 0.4$.

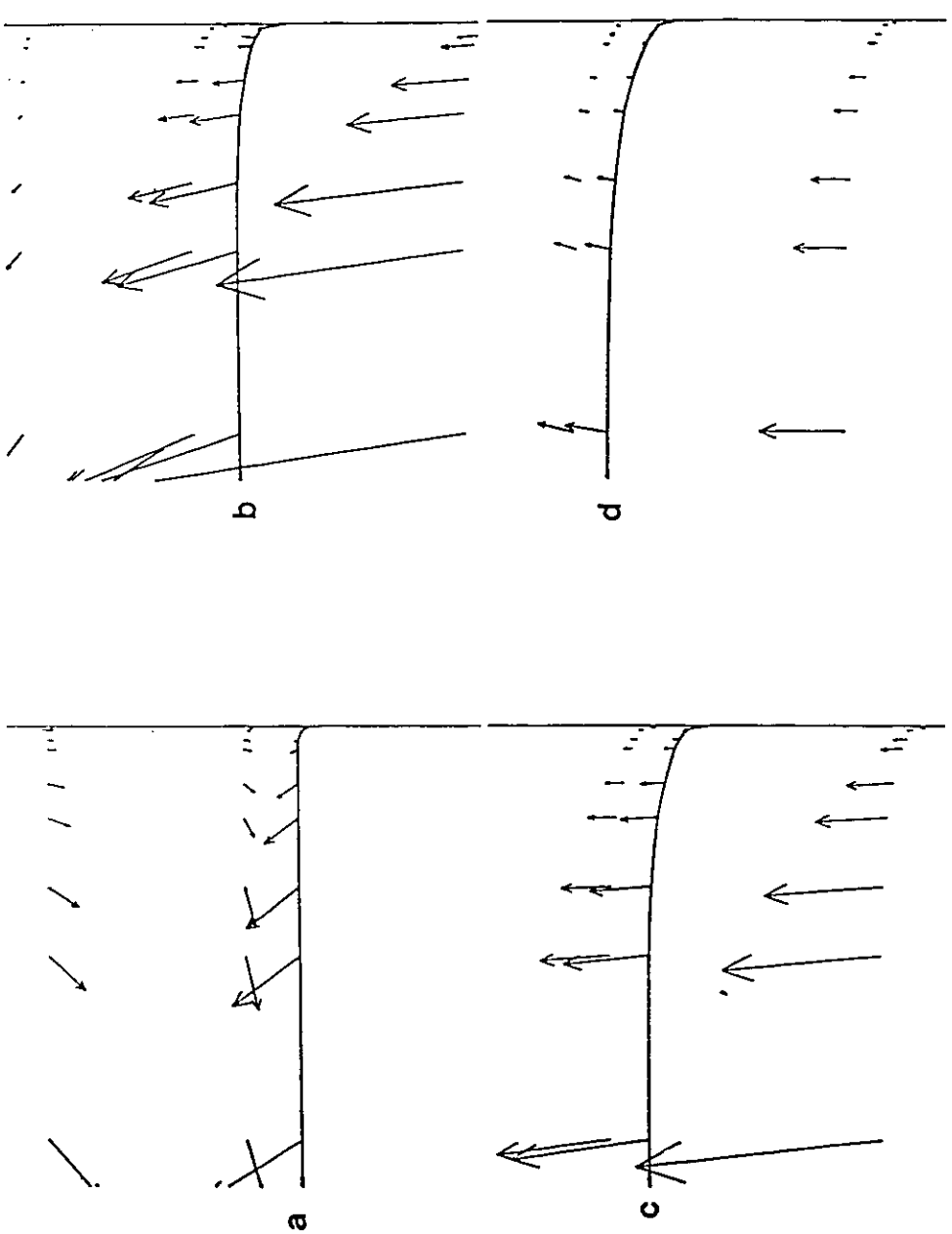

Figure 6.12 Flow inside the die. (y – z) velocity vectors. Flowrate ratio $Q_I/Q_{II} = 13.2$, viscosity ratio $\mu_I/\mu_{II} = 2.5$. a) $x = 0.02L$, b) $x = 0.125L$, c) $x = 0.25L$ and d) $x = 0.5L$.

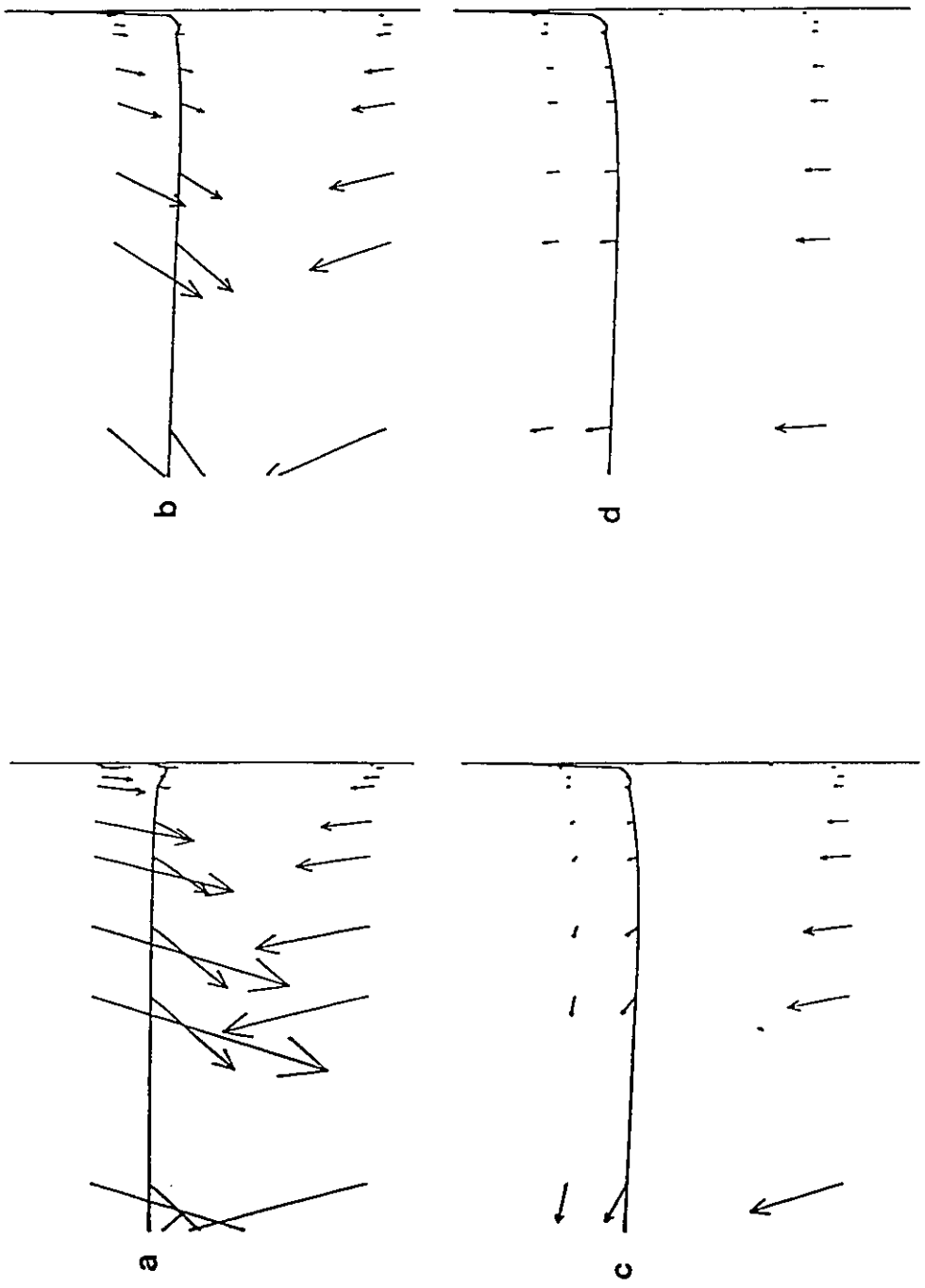

Figure 6.13 Flow inside the die. (y – z) velocity vectors. Flowrate ratio $Q_I/Q_{II} = 13.2$, viscosity ratio $\mu_I/\mu_{II} = 0.4$. a) $x = 0.02L$, b) $x = 0.125L$, c) $x = 0.25L$ and d) $x = 0.5L$.

redistribution in the horizontal direction (Figure 6.13c). Figures 6.14 and 6.15 present the main component of velocity distribution (x-velocity) in different downstream planes. Notice how the initial fully developed profiles inside the two separate channels (Figures 6.14a, 6.15a) change as the interface forms and the material near the interface is accelerating (Figures 6.14b, 6.15b). However, the different viscosities of the materials result in dissimilar velocity profiles far downstream where the discontinuous change of the curvature at the interface in both cases is due to the viscosity mismatch (Figures 6.14d, 6.15d).

Figure 6.16 presents three dimensional plots of the pressure distribution inside the die in different downstream planes. The values plotted are not absolute pressure values because of scaling problems, but are calculated with respect to the lowest occurring pressure at the given cross section, i.e,

$$P^i = P^i - P_{min}, \qquad \text{at } x = \text{fixed} \tag{6.9}$$

$$P_{min} = \text{Min}(P^i), \qquad i=1,\ldots,n_c \tag{6.10}$$

where n_c is the number of nodes on the 2-D cross-section and P_{min} the lowest value of pressure at this cross section. Far upstream, since fully developed flow is assumed in both channels, the pressure is uniform within each channel, but unequal (6.16a). As the fluids meet, a high discontinuity at the interface exists (Figures 6.16b, 6.16c) which is gradually eliminated as the flow becomes fully developed downstream. What is also interesting is that there is a pressure distribution within each layer (Figures 6.16b-6.16e) because of the developing nature of the flow. Far downstream (6.16f), in the fully developed flow regime, the two fluids are driven by the same pressure gradient and there is no pressure discontinuity.

It was experimentally shown that an increase in the viscosity ratio results in more pronounced encapsulation (Minagawa and White, 1975; Lee and White, 1974; Han, 1981). For the square die geometry and a fixed flowrate ratio of $Q_I/Q_{II}=13.2$, the effect of the viscosity ratio on the degree of encapsulation is examined numerically. The degree of encapsulation h_e

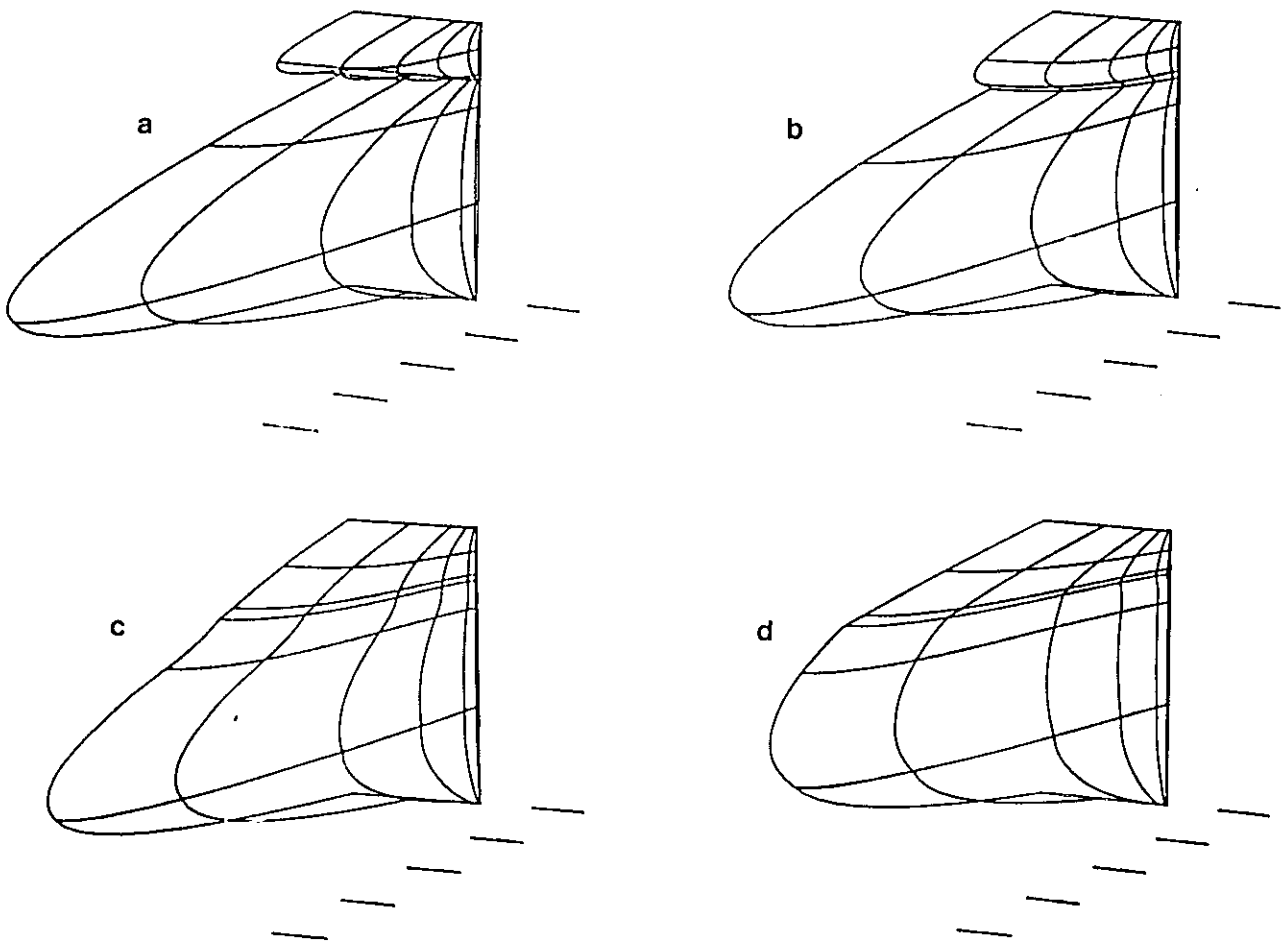

Figure 6.14 Flow inside the die. Downstream component of velocity at different stations downstream. Flowrate ratio $Q_I/Q_{II} = 13.2$, viscosity ratio $\mu_I/\mu_{II} = 2.5$. a) $x = 0.02L$, b) $x = 0.125L$, c) $x = 0.25L$ and d) far downstream.

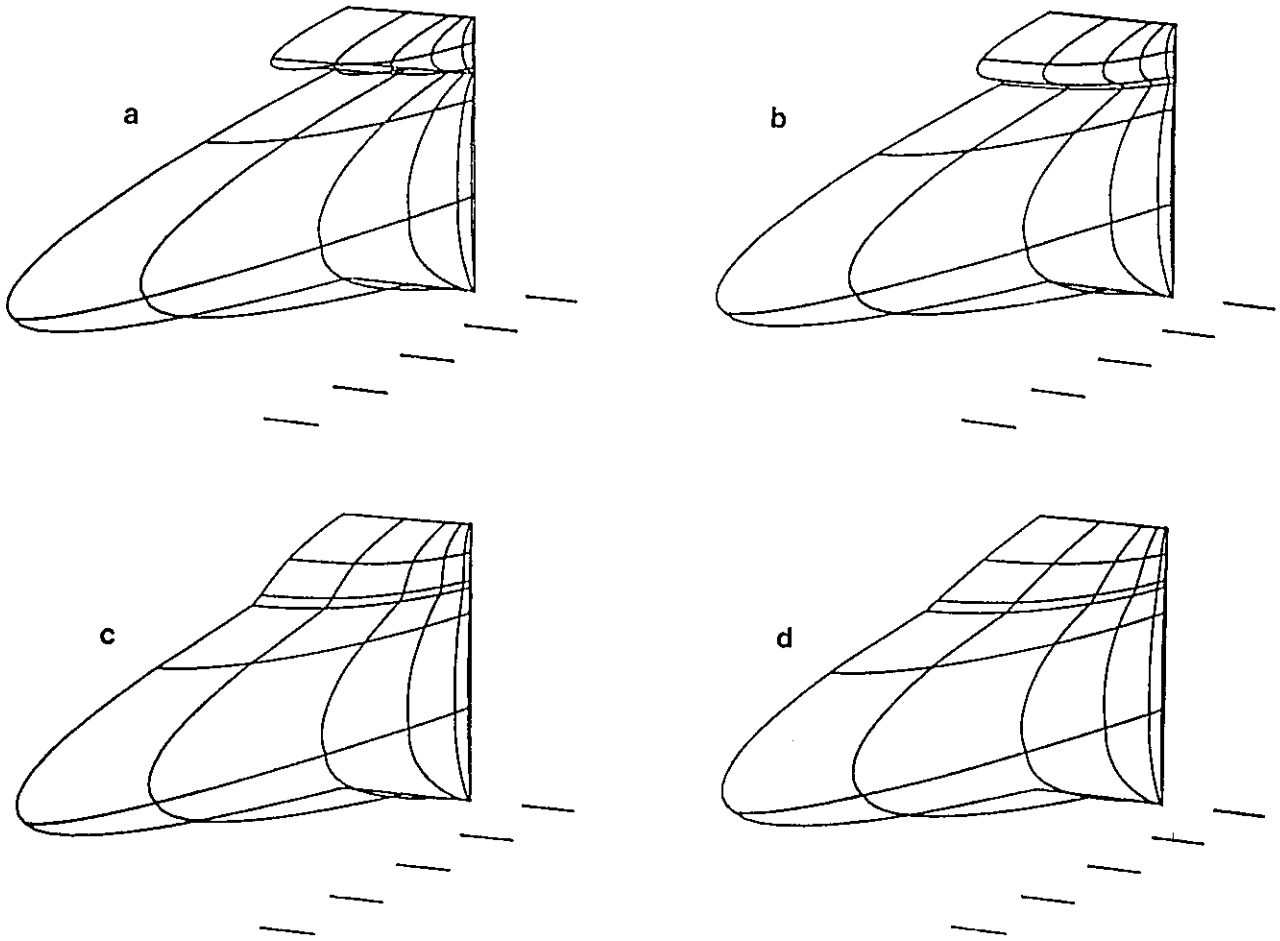

Figure 6.15 Flow inside the die. Downstream component of velocity at different stations downstream. Flowrate ratio $Q_I/Q_{II} = 13.2$, viscosity ratio $\mu_I/\mu_{II} = 0.4$. a) $x = 0.2L$, b) $x = 0.125L$, c) $x = 0.25L$ and d) far downstream.

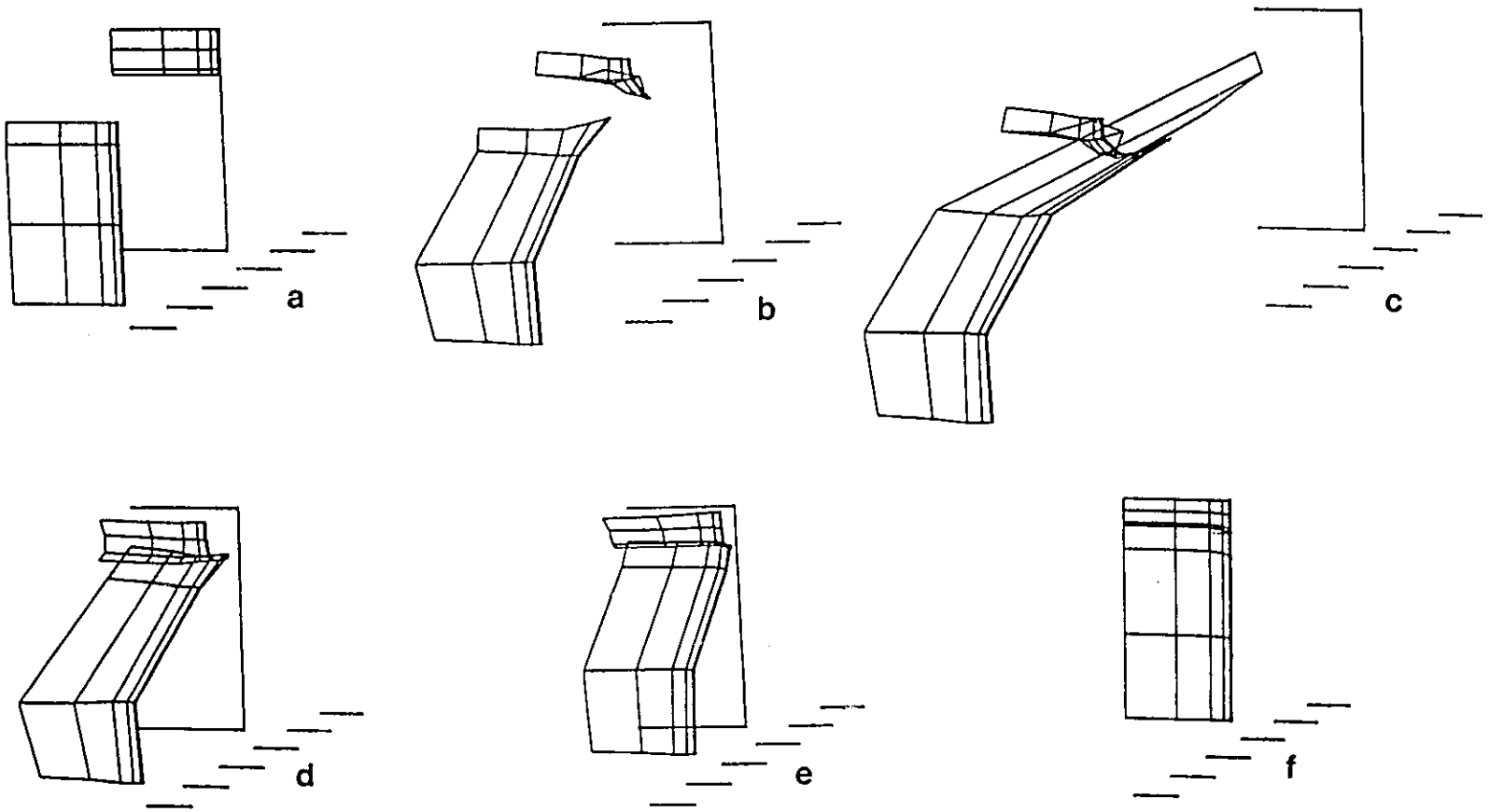

Figure 6.16 Three dimensional plots of the pressure distribution at different stations downstream. Plotted values are scaled as $P = P - P_{min}$. Flowrate ratio $Q_I/Q_{II} = 13.2$, viscosity ratio $\mu_I/\mu_{II} = 2.5$. a) inside the separate channels, b) at the meeting point, c) $x = 0.02L$, d) $x = 0.125L$, e) $x = 0.25L$ and f) far downstream.

is defined as the distance between the contact point at the wall A and the interfacial point B lying on the symmetry line at the center of the die (Figure 6.17). Results are summarized in Table 6.1 and are in agreement with the experimental trend. The degree of encapsulation increases nonlinearly with the viscosity ratio. The results reported in Table 6.1 are for a length of flow of 23 L, a grid of 5265 nodal points, 528 elements and 12071 unknowns with 6 elements in the z-direction (3 elements in the lower fluid) and 4 elements in the y-direction.

Table 6.1 Effect of viscosity ratio on degree of encapsulation

Viscosity Ratio μ_I/μ_{II}	Degree of Encapsulation h_e
1.0	0.018 L
2.5	0.080 L
5.0	0.095 L
20.0	0.134 L

Due to the high flowrate ratio and the separation plate effect, there is a slight interface deformation even when the two layers are the same material ($\mu_I/\mu_{II}=1$). A mesh study was undertaken to establish the margin of error in this case. A more dense grid with 8415 nodes, 880 elements and 20503 unknowns with 8 elements in the z-direction (5 elements in the lower fluid) and 5 elements in the y-direction was used. The denser grid produced a degree of encapsulation of 0.016 which is close to the 0.018 produced by the coarser finite element grid. For equal volumetric flow rates and viscosities, with the separation plate positioned halfway in the die, a perfectly symmetric flow profile with a flat interface downstream resulted.

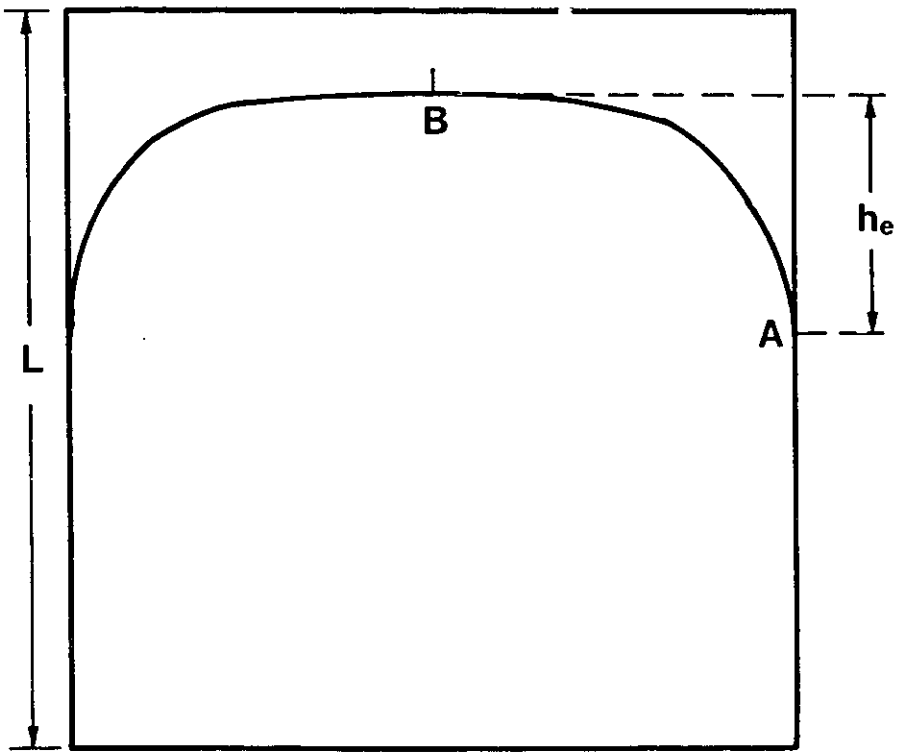

Figure 6.17 Definition of degree of encapsulation h_e.

6.4.2 Effect of Initial Conditions and Die Design.

The most widely used coextrusion method is the feedblock method (Finch, 1987; Pool, 1987) in which two or more polymers are arranged into the desired layer configuration and the layers are subsequently thinned and spread during extrusion through a single-manifold die (U.S. Patent 3,565,985; U.S. Patent 3,557,265; Shrenk and Alfrey, 1978; Michaeli, 1984). Feedports are used to meter layers (Finch, 1987) or in modular feedblock systems (Pool, 1987; Reitemeyer, 1988) a layer control module or adaptor is used to stabilize the individual flows. The idea is that the flow conditions of the layers at the meeting point must be more or less the same. Generally, large pressure or velocity differences are undesirable since they may lead to high stress jumps across the interface which may result in interfacial instability (Schrenk and Alfrey, 1978; Schrenk et al, 1978).

There are generally two approaches in the design of the way the two individual melt streams are brought together in the feedblock or adaptor and are described in terms of the bicomponent flow situation examined here (Figure 6.2). The first approach is to position the separation plate (EKLFE, Figure 6.2) at the height where the interface would be if there were a fully developed flow situation with a flat interface. This policy generally requires unequal pressure gradients to drive the flow in the two separate flow channels which produces a high pressure difference at the interface when the two fluids are brought together. The second approach is to position the separation plate at the height which requires equal pressure gradients in the two separate channels. This policy is not expected to produce high pressure discontinuities at the interface but since the initial flow areas are not necessarily proportional to the required in the bicomponent flow region, this may result in a significant movement of the interface from the initial position.

Figure 6.18 shows the results of the 3-D analysis for these two cases, for a flowrate ratio of $Q_I/Q_{II} = 13.2$ and viscosity ratio of $\mu_I/\mu_{II} = 2.5$. The first approach (6.18a) shows that the

interface, immediately after the meeting point, exhibits an undershoot due tc the sudden flow rearrangement caused by the unequal pressure levels. Such behaviour was also reported in the 2-D studies by Mavridis et al, 1987 and Mitsoulis, 1987. The undershoot of the interface is coupled to the encapsulation effect, is different across the die and its magnitude depends on the distance from the wall. Also near the wall the interface seems to exhibit an overshoot right after the undershoot (spines 1, 2 and 3, see also Figure 6.7). This sudden change of the interface curvature in the downstream direction may be a source of wave or numerical instabilities. In the second approach, the equal pressure gradients in the two channels result in a significant migration of the interface from the initial point (Figure 6.18b), but this movement is monotonic and is therefore more likely to result in a stable flow. Again, the tendency for encapsulation is evident and although the total interface movement is higher, it results in a lower degree of encapsulation.

The interface shape as it changes downstream for the second case is shown in Figure 6.19. The encapsulation starts right after the two fluids meet, the interface deformation becomes more pronounced downstream, with the curvature increasing predominately near the die wall.

6.4.3 Effect of Shearing Level. Carreau-type Fluids

At a given melt temperature, viscosity ratio reversal can be obtained when the two components have viscosities such that crossovers occur in the plots of melt viscosity versus shear rate (Southern and Ballman, 1973; 1975; Han, 1981). Experimental observations (Southern and Ballman, 1973; 1975; Lee and White, 1974) have shown that interface curvature reversal occurred at approximately the shear rate where the viscosity crossover of the two melts also occurred. Therefore, on the basis of experimental evidence, it can be con-

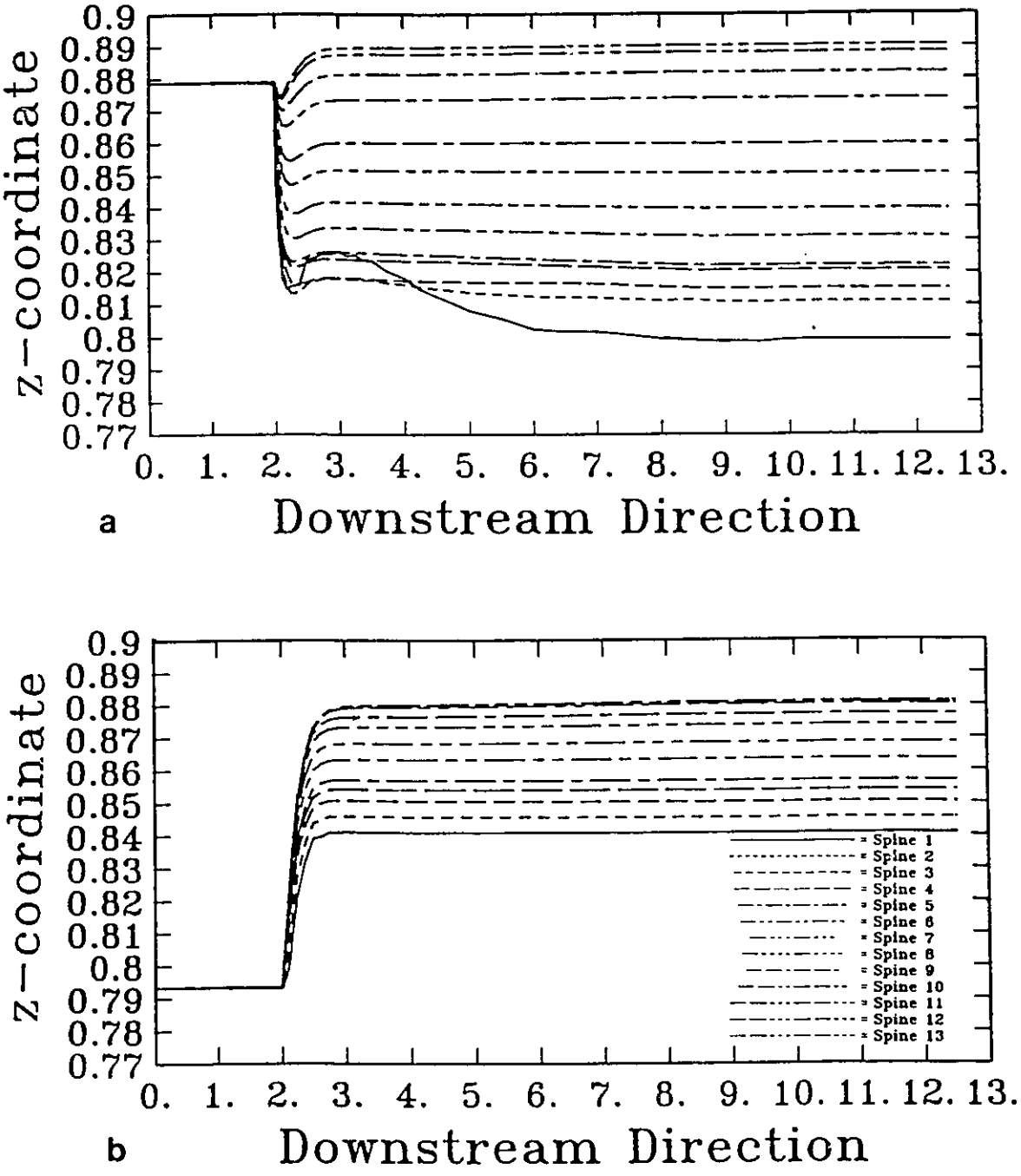

Figure 6.18 Effect of separation plate position. Flowrate ratio $Q_I/Q_{II} = 13.2$, viscosity ratio $\mu_I/\mu_{II} = 2.5$. a) Separation plate where a flat interface would be in the fully developed case, b) equal pressure gradients in the separate fluid channels.

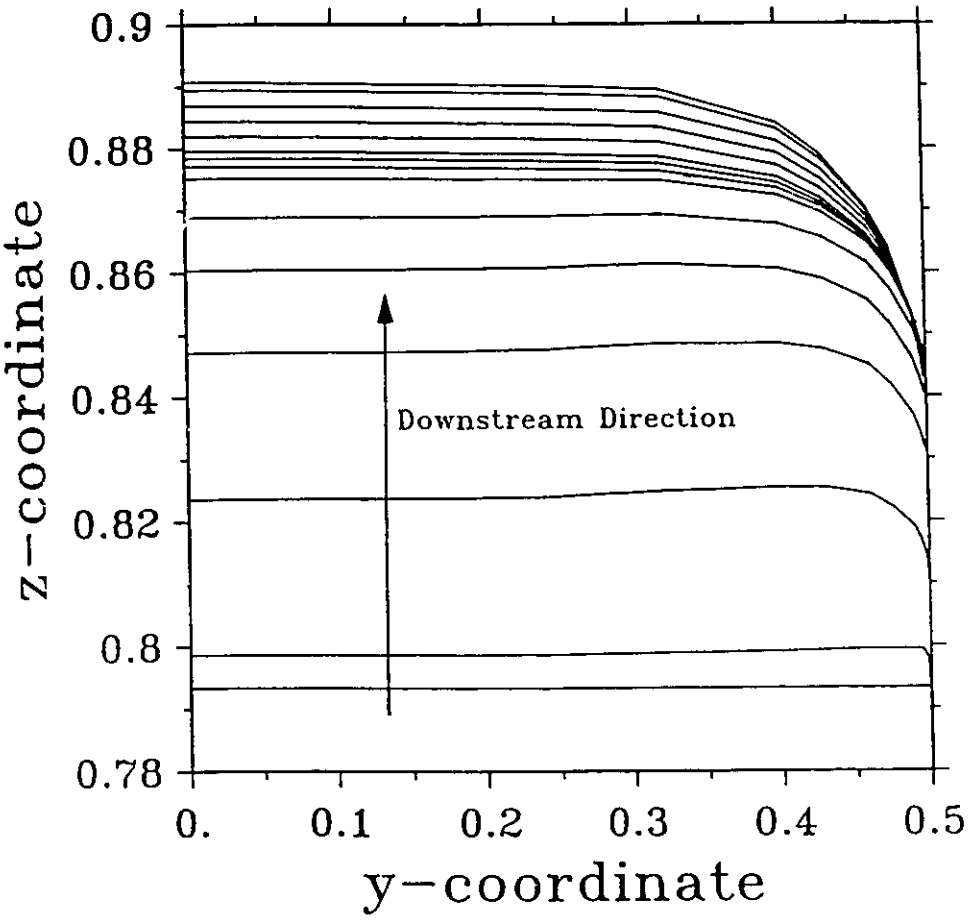

Figure 6.19 Interface development downstream. Flowrate ratio $Q_I/Q_{II} = 13.2$, viscosity ratio $\mu_I/\mu_{II} = 2.5$. Corresponds to Figure 6.18b.

cluded that the viscosity ratio of the two components determines the interface shape in the absence of elastic effects.

This section intends to study numerically the findings of one of the above mentioned experimental analyses. The two polystyrenes reported by Southern and Ballman (1973, 1975) are used and exhibit a viscosity crossover (Figure 6.20) at a shearing level of approximately $\dot{\gamma}=15s^{-1}$. The Carreau-type shear thinning viscosity function was fitted into the reported viscosity-shear rate curves (Southern and Ballman, 1975) and the characteristics of the melts are given in Table 6.2.

Table 6.2 Carreau model characteristics of polystyrenes A and B (after Southern and Ballman, 1975)

	μ_0 (N s/m^2)	λ (s)	n
Polystyrene A	3250	0.47	0.62
Polystyrene B	4580	0.59	0.52

The bicomponent flow in a square die for equal volumetric flowrates of the melts is examined for different characteristic shear rate levels. The shear rate level is calculated as the ratio of the total flowrate over the cross-sectional area and the characteristic length of the die, i.e.,

$$\dot{\gamma}=(Q_I+Q_{II})/L^3 \tag{6.10}$$

In the square die, polystyrene A (Figure 6.20a) forms the upper layer (layer II) and polystyrene B forms the lower layer (layer I).

For the low shearing level of $\dot{\gamma}=0.75s^{-1}$, the upper fluid (fluid A) is less viscous (Figure 6.20a) and tends to encapsulate the more viscous lower fluid (Figure 6.20b). For the high shearing level $\dot{\gamma}=29.8s^{-1}$ the lower fluid (fluid B) becomes less viscous, the interface curvature is reversed and the lower fluid tends to encapsulate the upper (more viscous at high

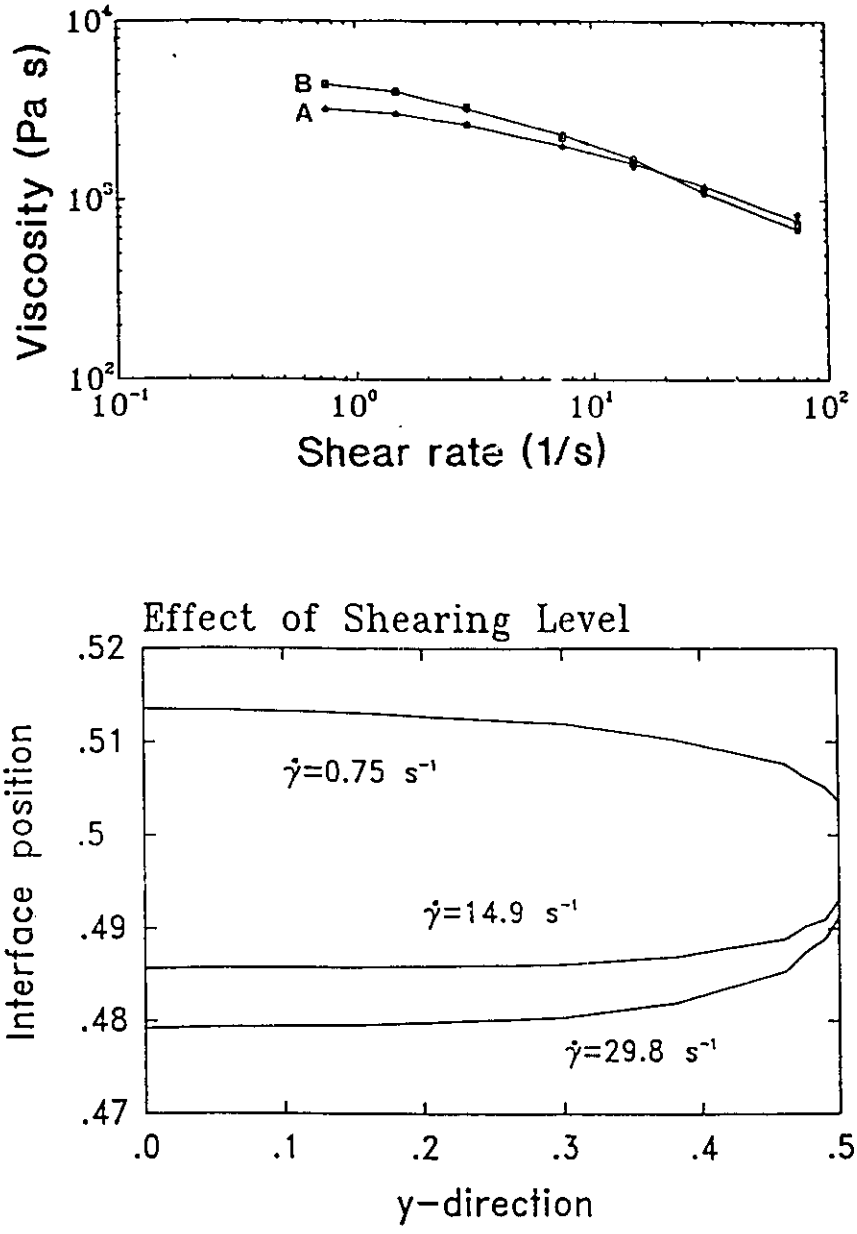

Figure 6.20 Effect of shearing level on the interface shape. Melts A and B exhibit viscosity crossover (see table 6.2). Flowrate ratio $Q_I/Q_{II}=1$. a) viscosity curves, b) interface shape

shearing) fluid. For the intermediate shearing level of $\dot{\gamma}=14.9s^{-1}$, again the lower fluid tends to encapsulate the upper fluid, but the degree of encapsulation is lower.

Southern and Ballman (1973, 1975) for the circular die geometry used in their experimental studies reported an almost flat interface shape when the shear rate was at the crossover point. However, in this study the square geometry results in a shearing distribution along the die walls. Higher shearing than the average is expected near the midpoints of the walls and lower toward the die corners. Since the characteristic shearing level represents an average value in this work and is not the shearing level at the contact lines, the calculated interface is not flat when the characteristic shearing level is set to the cross-over point $\dot{\gamma}=14.9s^{-1}$ (Figure 6.20b).

The nature of the pressure discontinuity at the interface along the symmetry plane is examined and follows the change of the material viscous properties. For $\dot{\gamma}=0.75s^{-1}$, a positive pressure difference exists before the fluids meet ($x\leq 2$, Figure 6.21) and a negative pressure discontinuity occurs at the interface when the fluids are brought together. The pressure discontinuity dissipates downstream as the flow becomes fully developed and is driven by the same pressure gradient. The sign and magnitude of the pressure discontinuity change when the shearing level exceeds the crossover point and the viscosity ratio of the melts is inverted ($\dot{\gamma}=29.8s^{-1}$, Figure 6.21).

The downstream velocity distribution inside the die is also affected by the shearing level. For $\dot{\gamma}=0.75s^{-1}$ the maximum velocity is located very close to the interface in the side of the less viscous upper fluid (Figure 6.22a). For $\dot{\gamma}=14.9s^{-1}$ the maximum velocity migrates toward the lower layer (6.22b) and for $\dot{\gamma}=29.8s^{-1}$ the maximum is located within the lower layer which has become less viscous.

The main component of velocity (x-velocity) in different planes downstream is presented in Figure 6.23. The fully developed flow inside the separate channels (Figure 6.23a)

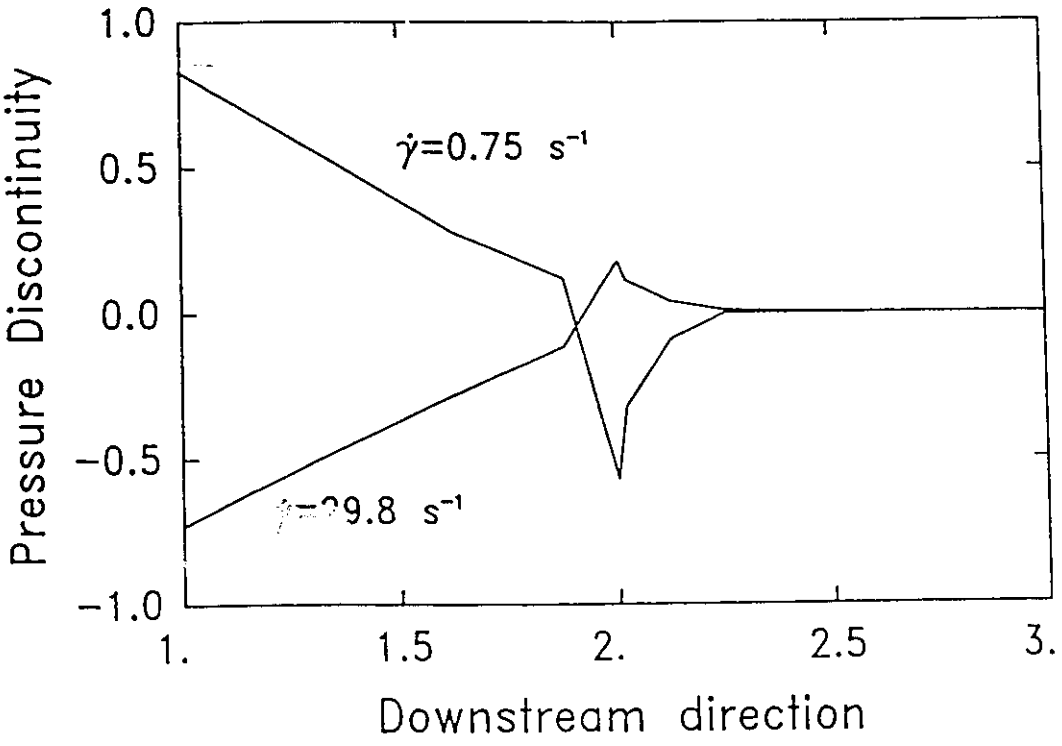

Figure 6.21 Effect of shearing level on the pressure discontinuity at the interface. Corresponds to Figure 6.20.

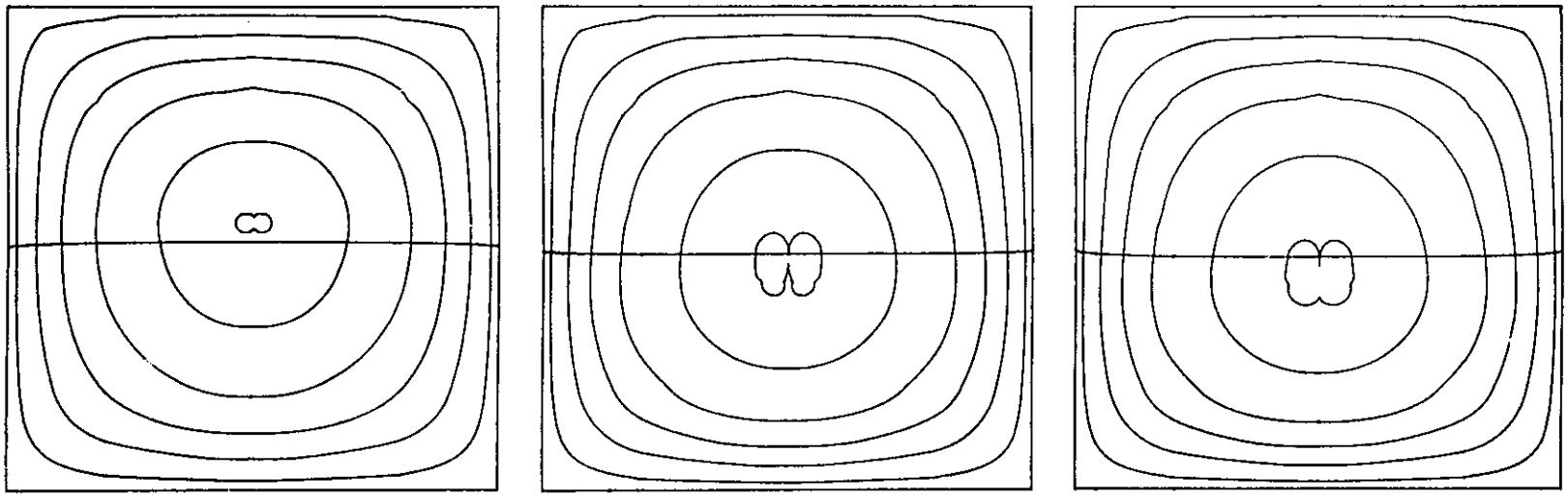

Figure 6.22 Normalized velocity contours (x-velocity) downstream. Flow inside the die. Corresponds to Figure 6.20. a) $\dot{\gamma} = 0.75 s^{-1}$, b) $\dot{\gamma} = 14.9 s^{-1}$ and c) $\dot{\gamma} = 29.8 s^{-1}$.

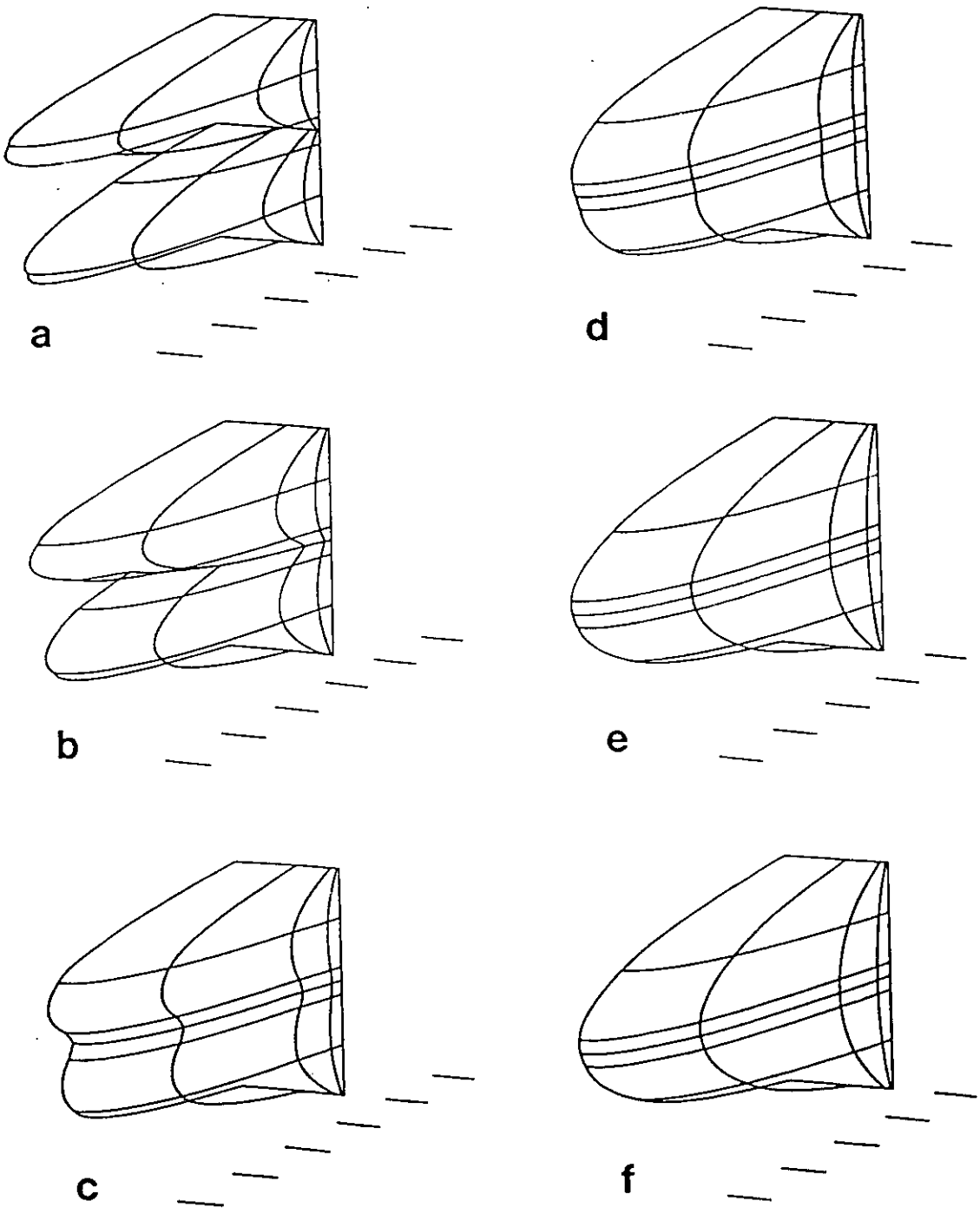

Figure 6.23 Downstream component of velocity at different stations downstream. Corresponds to Figure 6.20. Shearing level $\dot{\gamma}=0.75s^{-1}$. a) inside the different channels, b) $x=0.02L$, c) $x=0.125L$, d) $x=0.25L$, e) $x=0.5L$ and f) far downstream.

is altered by the interface formation and the acceleration of the material at the center of the die (6.23b, c, d, e) until fully developed flow occurs downstream. Notice that because of the very similar viscosities of the two materials, the slope of the velocity at the interface does not change dramatically in the fully developed regime (Figure 6.23f).

6.4.4 Effect of Slip at the Wall

The slip at the wall boundary condition is expected to influence the degree of encapsulation since slip alters the pressure distribution and relieves the stress singularities at the contact points (Mavridis, 1988).

Figure 6.24 gives a representative plot of the behaviour of the computed degree of encapsulation as a function of the slip coefficient B ($B = \beta \mu/L$, see section 6.3.3) which is varied between 10^{-4}-10^{-1}. This figure shows that the degree of encapsulation decreases as the amount of slip increases because the flow near the wall is lubricated and the viscosity difference plays a lesser role. At the limit of perfect slip, no encapsulation would be expected.

6.4.5 Effect of Boundary Conditions

It is known that the interface migration during encapsulation is a very slow irreversible process (Everage, 1975; Han, 1981; Lee and White, 1974; Southern and Ballman, 1973). Generally, a very long die is required for the less viscous fluid to totally encapsulate the more viscous fluid depending on the magnitude of the viscosity ratio. For example, Everage (1975) demonstrated that for stratified flow through a tube, a tube length of more than 20 characteristic lengths (tube diameters) is required before appreciable partial encapsulation is noted, while total encapsulation occurs at the order of 100 characteristic lengths. Everage's investigation proves that there are significant cross-flow velocities which result in the interface shape change, even 100 characteristic lengths downstream. However, parametrizing

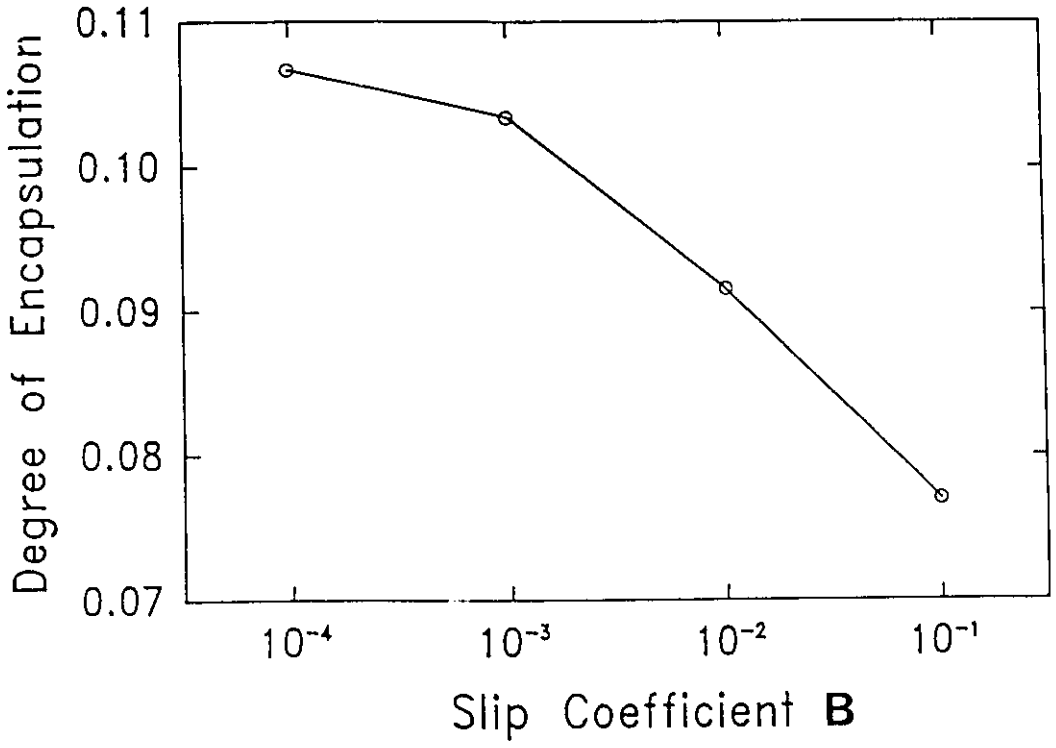

Figure 6.24 Effect of slip at the wall on the degree of encapsulation. Flowrate ratio $Q_I/Q_{II} = 13.2$, viscosity ratio $\mu_I/\mu_{II} = 2.5$.

in a 3-D fashion such a long flow domain would result in a formidable numerical problem. Moreover, the magnitude of the cross-flow velocities is very low compared to the main flow direction velocity, and a very dense grid would be required to capture the details of the flow field. The 3-D study of the problem, in its full extent, is intractable even with today's powerful computers and one is forced to study the problem on a shorter scale.

The finite elements grids used in this section extended up to 23 characteristic lengths downstream. Since we do not actually know what the interface shape will be at the downstream plane, the choice of downstream boundary condition becomes a critical issue. One obvious choice is to assume fully developed flow downstream, i.e. no cross-flow velocities. This policy definitely introduces an error, since we restrict the flow development within the finite length of the die under study. An alternative boundary condition is to require a zero rate of change of the velocity components in the downstream direction, i.e.,

$$\frac{\partial u}{\partial x} = \frac{\partial v}{\partial x} = \frac{\partial w}{\partial x} = 0 \qquad (6.11)$$

Although the boundary condition of eqn. (6.11) allows for non-zero cross-flow velocity components, it again introduces an error since the 3-D nature of the interface shape change does not guarantee the validity of the imposed boundary condition except in the immediate neighborhood of the downstream plane. The calculated degree of encapsulation with this boundary condition changes only in the third decimal place compared to the fully developed flow boundary condition. Further investigation of the effect of the downstream boundary condition was done by solving the full problem (Figure 6.1) and allowing the material to exit the die. The obvious plug flow profile boundary condition at the downstream plane of the extrudate was imposed, but the calculated degree of encapsulation inside the die did not change significantly, although the error would have been expected to dissipate due to the fact that it was introduced far downstream in the extrudate. These results show an insensitivity of the calculated degree of encapsulation with respect to the downstream boundary conditions

examined. The next consideration is then what is the effect of the other boundary conditions, i.e., initial boundary condition, kinematic condition at the interface, contact point and also the grid density and initial interface shape.

The effect of the initial (inflow) boundary condition and the initial interface shape were studied for the case where the fluids are in contact with each other from the beginning instead of bringing the fluids together by first allowing them to flow in separate channels (Figure 6.2). Referring to Figure 6.2, in place of the separation plate (EKLFE), we have the interface of the two fluids and fully developed flow of the two fluids with a flat interface between them is then assigned in the inflow plane (ABCDA). When a flat interface downstream was assigned as the initial guess, no change of the interface shape was computed because the kinematic condition is automatically satisfied. When a curved initial interface was assigned downstream, the cross flow velocities that were artificially introduced by the curved interface shape were driven to zero and the calculated final shape was again flat. This very interesting result shows that the effect of the kinematic condition at the interface is overwhelming and combined with other potential sources of numerical error may be responsible for the small degrees of encapsulation that were computed. It is characteristic that in the numerical study, the encapsulation occurs within the first characteristic lengths of flow after the fluids are brought together (see Figure 6.18 for example) and it is believed that this is caused by a combination of the boundary conditions and the short downstream length of flow considered.

6.4.6 Effect of Grid Length

The extent of the interface deformation from the initial flat interface and the degree of encapsulation depend also on the residence time (duration of flow) in the die as was experimentally shown (Lee and White, 1975; Everage, 1975; Han, 1981; Southern and Ballman,

1973). A study on the effect of the length of flow was examined in one case only, because of the large scale of the numerical problem, with a flowrate ratio of $Q_I/Q_{II}=13.2$ and a viscosity ratio of $\mu_I/\mu_{II}=2.5$. For the square die, a grid consisting of 5259 nodes, 528 elements, 405 spines and 12071 variables was used. For a length of flow of 10L, the computed degree of encapsulation was $h_e=0.077$. For the same grid but for a longer flow path of 23L the calculated degree of encapsulation was higher at $h_e=0.080$. This result is in agreement with the experimental trend, although the computed increase in the extent of encapsulation was small.

6.5 SWELLING BEHAVIOUR AND INTERFACE SHAPE OUTSIDE THE DIE

In addition to interface curvature, a mismatch of component melt viscosities can also produce bending of the extrudate stream to form a significant angle relative to the main flow direction axis (Figure 6.25). This phenomenon occurs due to the unsymmetric velocity profile inside the die that is induced by the viscosity difference, and the flow rearrangement in the extrudate (Southern and Ballman, 1973; Everage, 1975; Mavridis et al, 1987; see also Chapter 3). This section examines the free surface flow of bicomponent side-by-side systems as they emerge from a square or rectangular die under isothermal conditions.

Figure 6.25 shows a perspective view of the flow out of a square die of a system with a viscosity ratio of $\mu_I/\mu_{II}=1.5$ and flowrate ratio $Q_I/Q_{II}=1:1.5$. In agreement with experimental evidence (Southern and Ballman, 1973; Everage, 1975) the bending occurs in the direction of the higher viscosity component. Figure 6.26 presents the initial and distorted final finite element grid. The two fluids exhibit different swelling characteristics and the upper part of the extrudate is wider than the lower (see also Figure 6.27). The side free surface also appears to be distorted near the interface which exhibits a higher curvature than the corresponding upper and lower external free surfaces. The superposed initial and final extrudate

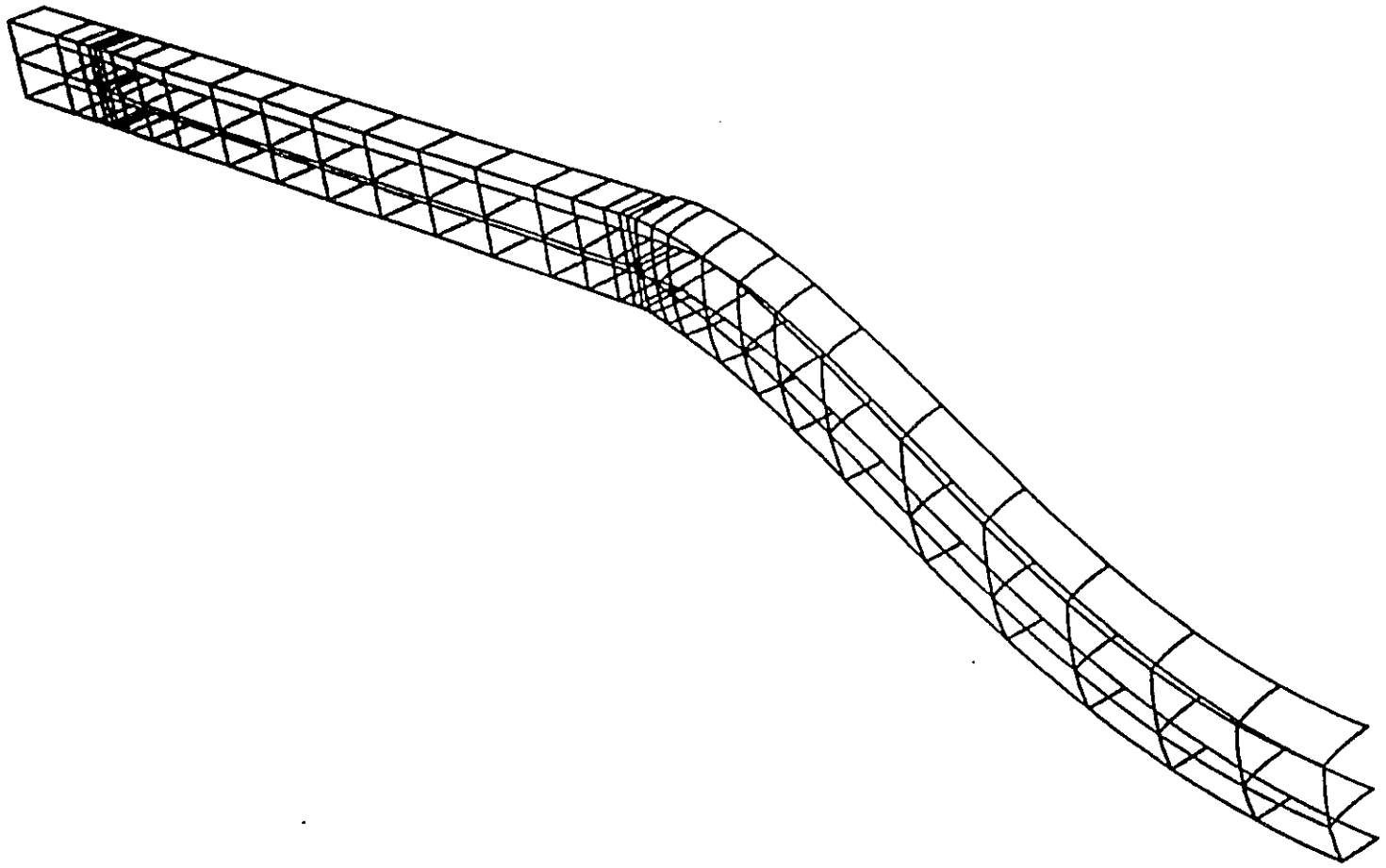

Figure 6.25 Perspective view of the extrudate bending out of a square die. Flowrate ratio $Q_I/Q_{II} = 1{:}1.5$, viscosity ratio $\mu_I/\mu_{II} = 1.5$.

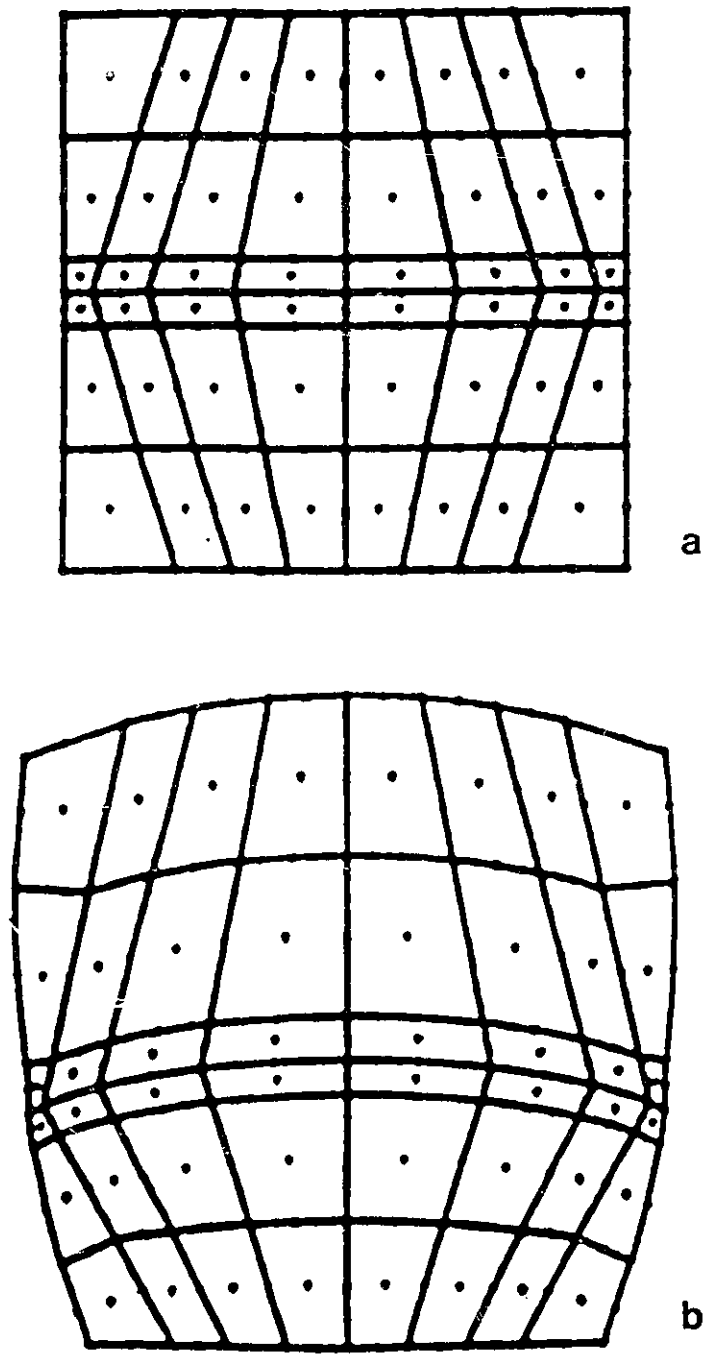

Figure 6.26 Initial and distorted final finite element grid. Same as in Figure 6.25.

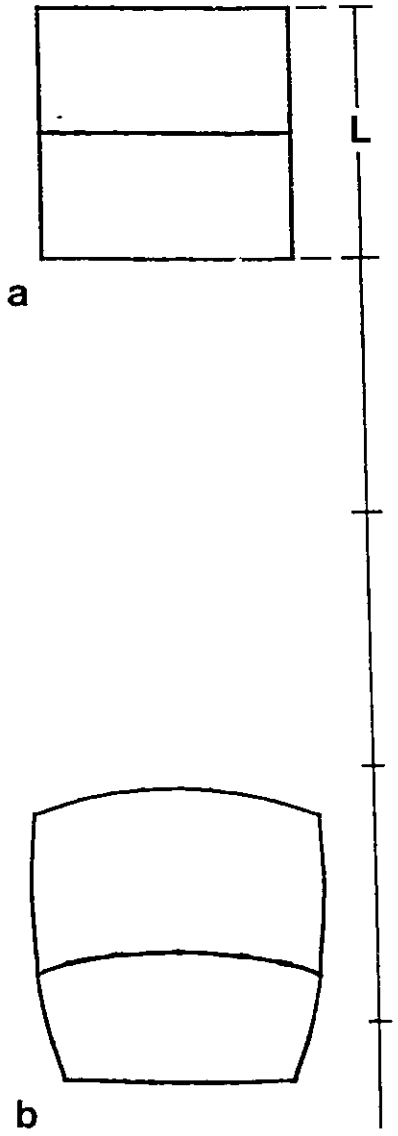

Figure 6.27 Superposed initial die shape and final extrudate shape. Same as in Figure 6.25.

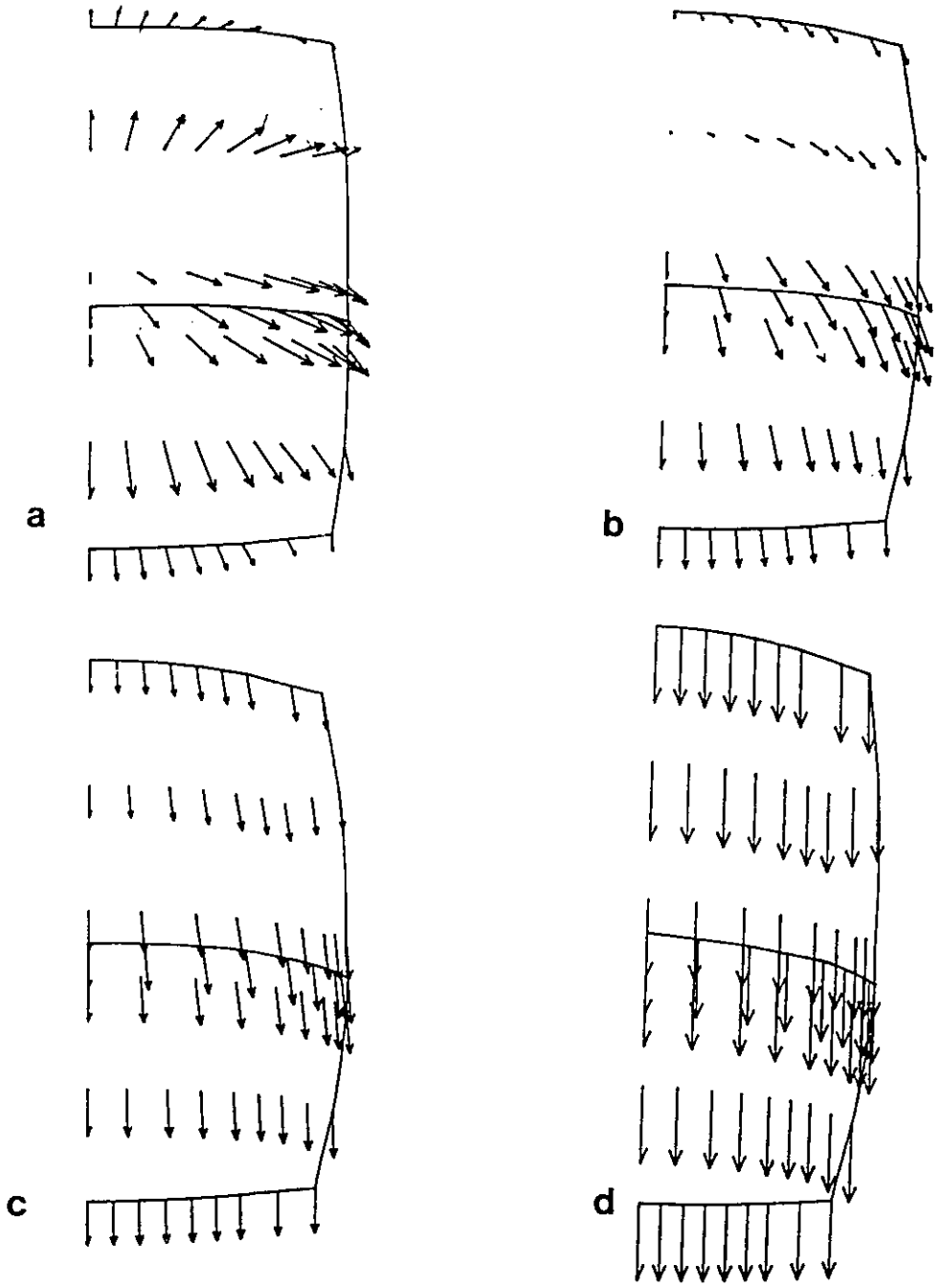

Figure 6.28 (y−z) velocity vectors. Same as in Figure 6.25. a) x=0.125L, b) x=0.375L, c) x=0.625L and d) x=2.75L.

shapes are shown in Figure 6.27. For this problem and an extrudate grid of 23L long, bending of more than three characteristic lengths is computed. The (y-z) velocity vectors in the extrudate at different downstream planes illustrate the mechanisms of the flow (Figure 6.28). At a distance x=0.125L after the extrudate emerges from the die (Figure 6.28a), the upper free surface tends to move upward, resulting in a slight extrudate swelling very near the die exit. The core of the upper fluid moves upward and to the right, a motion that results from the swelling of the upper layer. The lower free surface moves downward, and the core of the lower fluid moves downward and to the right. At x=0.375L (Figure 6.28b), the motion of the upper free surface is already reversed, but the extrudate is still expanding to the right. Further downstream however (Figures 6.28c, 6.28d), the downward bending motion dominates. Notice that the magnitude of the downward velocity becomes approximately the same in the whole cross-section of the extrudate (Figure 6.28d).

Figure 6.29 presents a perspective view and the downstream grid for a rectangular die geometry of aspect ratio 2:1. The viscosity ratio is $\mu_I/\mu_{II}=2$ and the flowrate ratio $Q_I/Q_{II}=0.5$. For this geometry, the extrudate distortion is more pronounced and the high interface curvature in the final extrudate (Figure 6.30b) occurs during the free surface flow out of the die rather than during the flow inside the die. Again the fluids exhibit quite different swelling characteristics with the upper layer expanding significantly to the sides. Figure 6.31 presents the (y-z) velocity vectors inside the extrudate and is characteristic that the interface keeps a high cross-flow velocity at all times. The upper free surface initially moves upward (Figure 6.31a), then material slides along the upper free surface to the right (6.31b) before the bending motion dominates (6.31c).

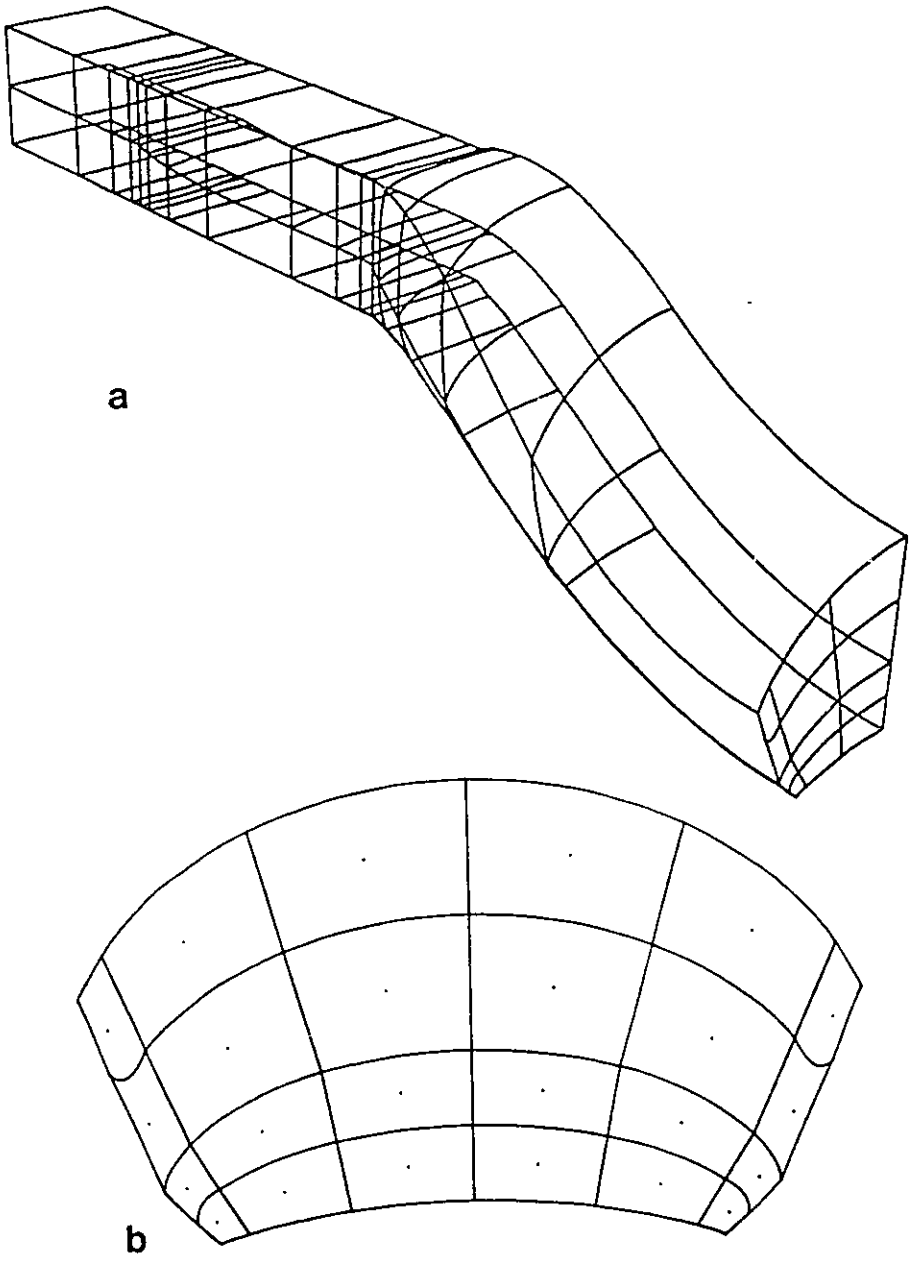

Figure 6.29 Extrudate emergence out of a rectangular die. Aspect ratio 2:1. Flowrate ratio $Q_I/Q_{II}=0.5$, viscosity ratio $\mu_I/\mu_{II}=2$. a) perspective view and b) final downstream finite element grid.

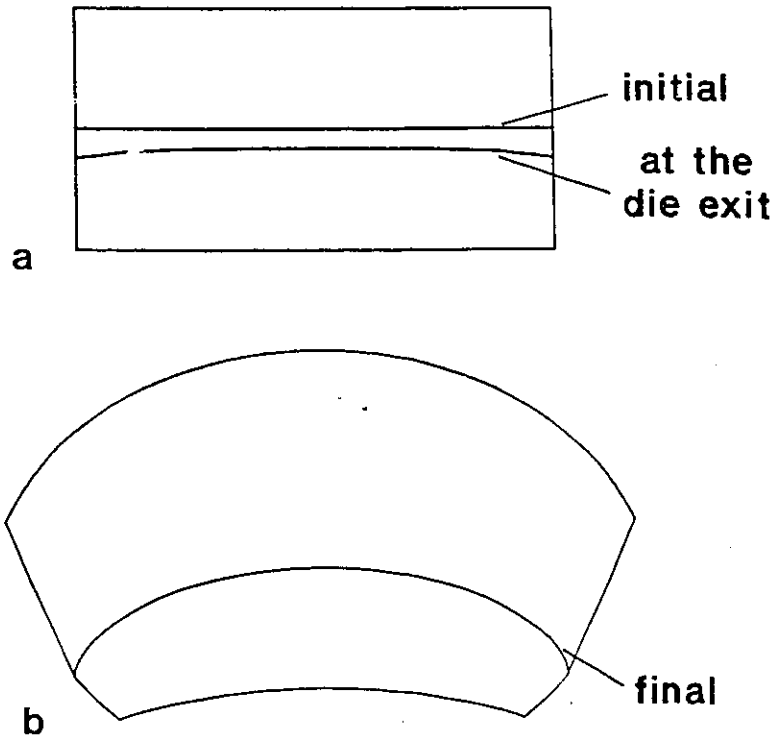

Figure 6.30 Superposed initial die shape and final extrudate shape. Same as in Figure 6.29.

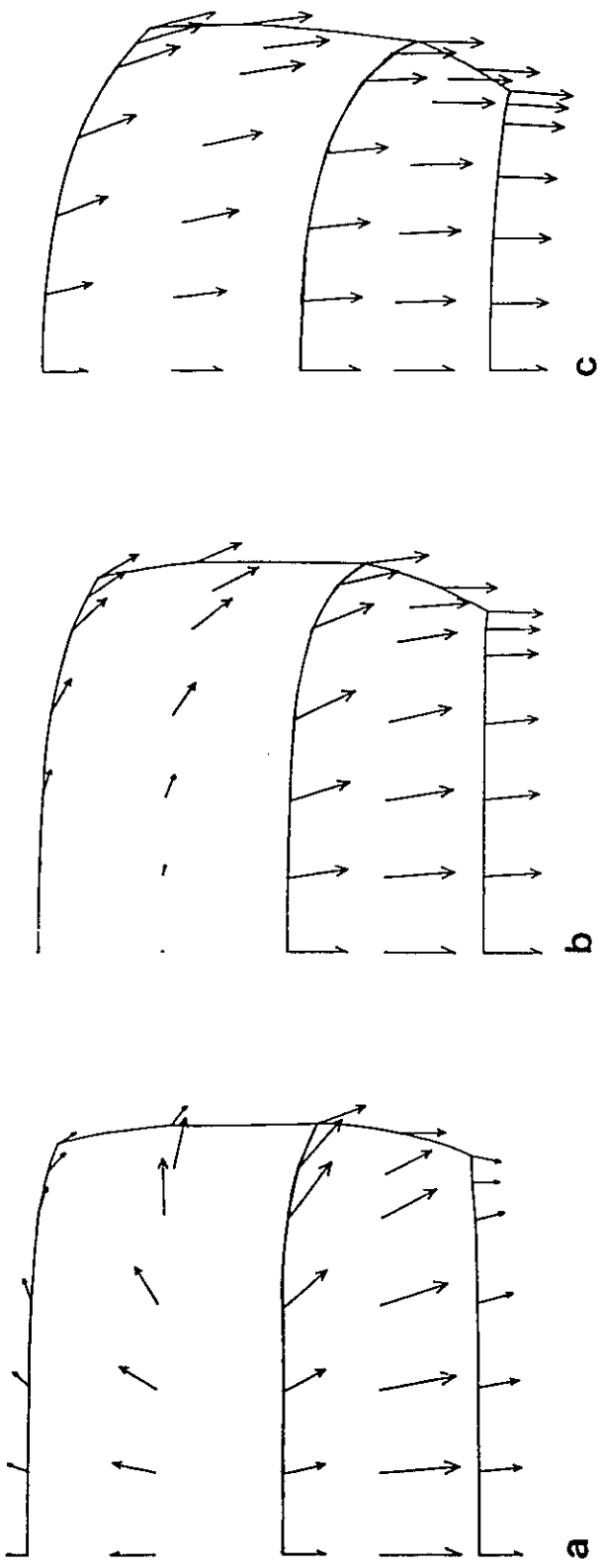

Figure 6.31 (y – z) velocity vectors. Same as in Figure 6.29. a) x = 0.125L, b) x = 0.375L, and c) x = 0.975L.

6.6 SUMMARY

The stratified bicomponent flow in a side-by-side configuration was studied numerically inside and upon leaving a square die. A Galerkin/finite element algorithm was developed to enable the study of the 3-D interface shape evolution during the course of flow inside the die and the bending of the extrudate upon emerging from the die.

Interface deformation occurs due to viscosity differences and the interface shape deviates from the initial flat profile. It was demonstrated that in all cases the less viscous fluid tends to encapsulate the more viscous fluid with the degree of encapsulation increasing with increased viscosity mismatch.

For shear-thinning fluids exhibiting viscosity function crossover, it was demonstrated that interface curvature inversion results if the crossover point is exceeded, in agreement with available experimental evidence.

Slip at the wall was shown to result in reduced encapsulation. Different design policies were discussed and potential sources of instabilities were identified.

The extrudate bending of the bicomponent system as it emerges from the die due to the viscosity mismatch was shown. It was also demonstrated that due to the 3-D die geometry and the stratified nature of the flow, the extrudate shape changes from that of the die profile.

CHAPTER 7

EXPERIMENTAL SIDE-BY-SIDE COEXTRUSION AND NUMERICAL SIMULATION RESULTS

7.1 INTRODUCTION

In Chapter 6, a 3-D Galerkin/finite element formulation was presented that enables the study of bicomponent stratified flows in a side-by-side configuration. It was illustrated there that the method can yield qualitative characteristics of the interface deformation and the encapsulation that results from the viscosity mismatch. The degree of quantitative agreement with experimental evidence was not established.

The results from an experimental investigation of the interface deformation of two typical melts during their course of flow inside a square die are presented. The 3-D numerical method of Chapter 6 is then applied to the experimental conditions to establish the quantitative agreement between experiment and numerical simulation. It is shown that the results of the numerical study agree qualitatively but not quantitatively with the experimental findings. Potential sources of the disagreement are discussed.

7.2 EXPERIMENTAL INVESTIGATION

An experimental investigation of the interface deformation during a side-by- side stratified flow of molten polymers inside a square die is presented. The experiment was performed at the Dow Chemical (Nederland) B.V. facility at Terneusen, The Netherlands, and was made available to the author.

A schematic of the experimental apparatus is shown in Figure 7.1. The molten polymers are fed from two extruders to a Dow modular die (Pool, 1987; Reitemeyer, 1988). The

first part of the feedblock is a "flow programming section", where the flows coming from the extruders are arranged in the desired configuration. The second part is a "flow stabilizing section" where flows are "stabilized" in such a way that their flow conditions at the meeting point are more or less the same either in terms of pressure or velocity at the merging point (Pool, 1987). One policy, for example, is to split the melt flows according to their throughput rates so that they meet at approximately the same velocity (Reitemeyer, 1988).

Figure 7.2 shows a transition channel that connects the feedblock to the square die. The dimensions of the die assembly have been scaled for proprietary reasons. The characteristic length L equals the length of the side of the square die and with respect to Figure 7.2 the other hardware dimensions are:

Length of transition channel	$L_1 = 1.58L$
Initial Height of transition channel	$H = 1.84L$
Width of transition channel	$W = L$
Length of the square die	$L_2 = 7.9L$

The design of the programming and stabilizing sections of the feedblock is proprietary and is not known to the author. The lack of information on the initial flow conditions poses a difficulty to the numerical simulation of the experimental findings. The initial boundary conditions are not exactly known and the adopted boundary conditions may have an effect on the calculated degree of encapsulation. However, the initial boundary conditions are not expected to affect the conclusions of this study.

The viscosity curves of the polymers that were used in this study are shown in Figure 7.3 at the experimental temperature of 220°C. The less viscous polymer is a Dow Styron™ 678E* and the more viscous polymer is a Dow Styron™ 472*. The experiment was

---

* Trademark of the Dow Chemical Company.

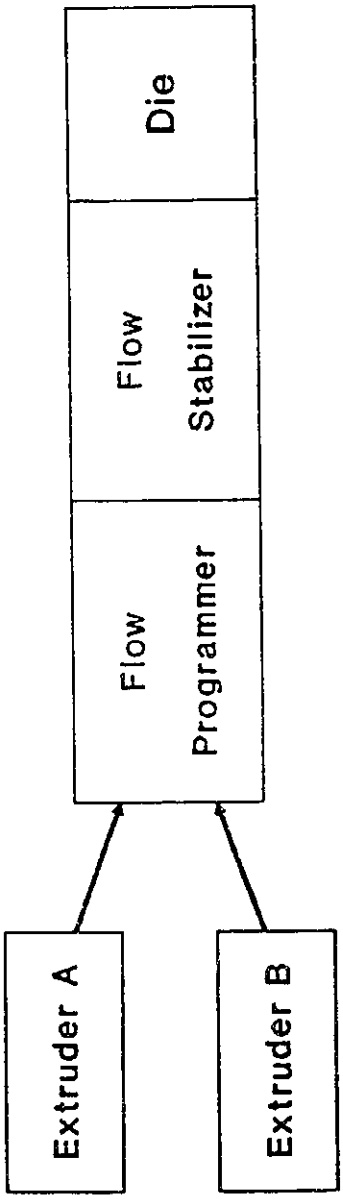

Figure 7.1 Schematic of the hardware set-up for the bicomponent coextrusion experiment.

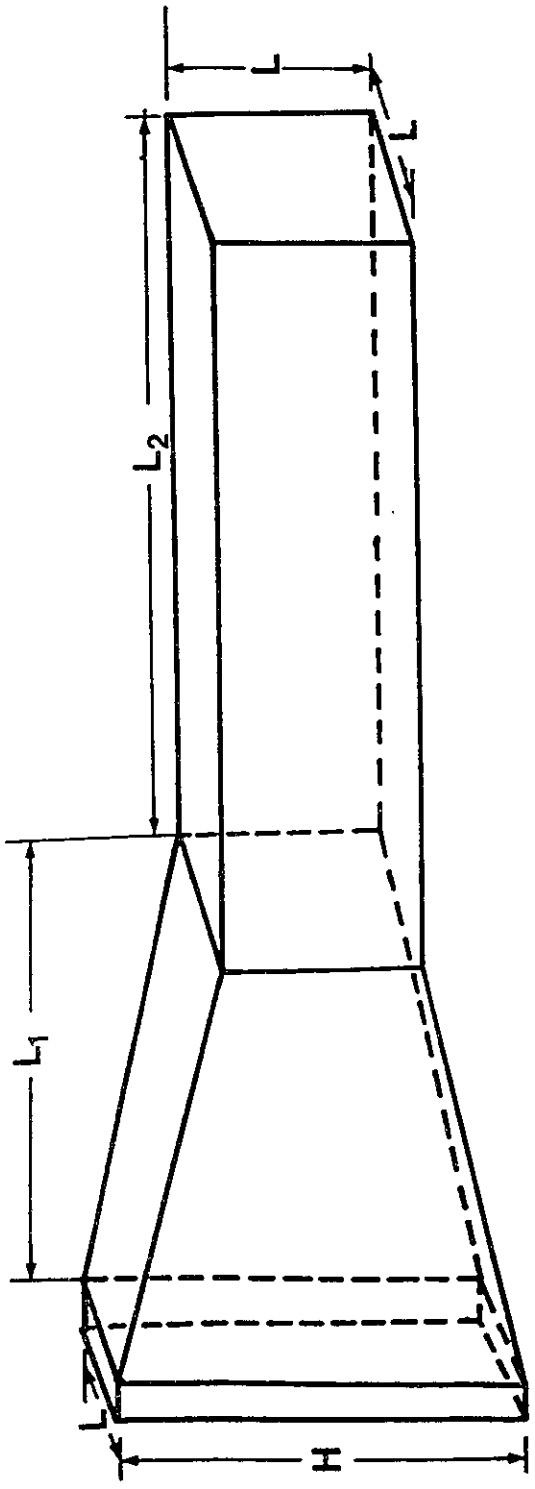

Figure 7.2 Design of the final part in the experimental set-up of Figure 7.1. $L_1 = 1.58L$, $H = 1.84L$, $L_2 = 7.9L$.

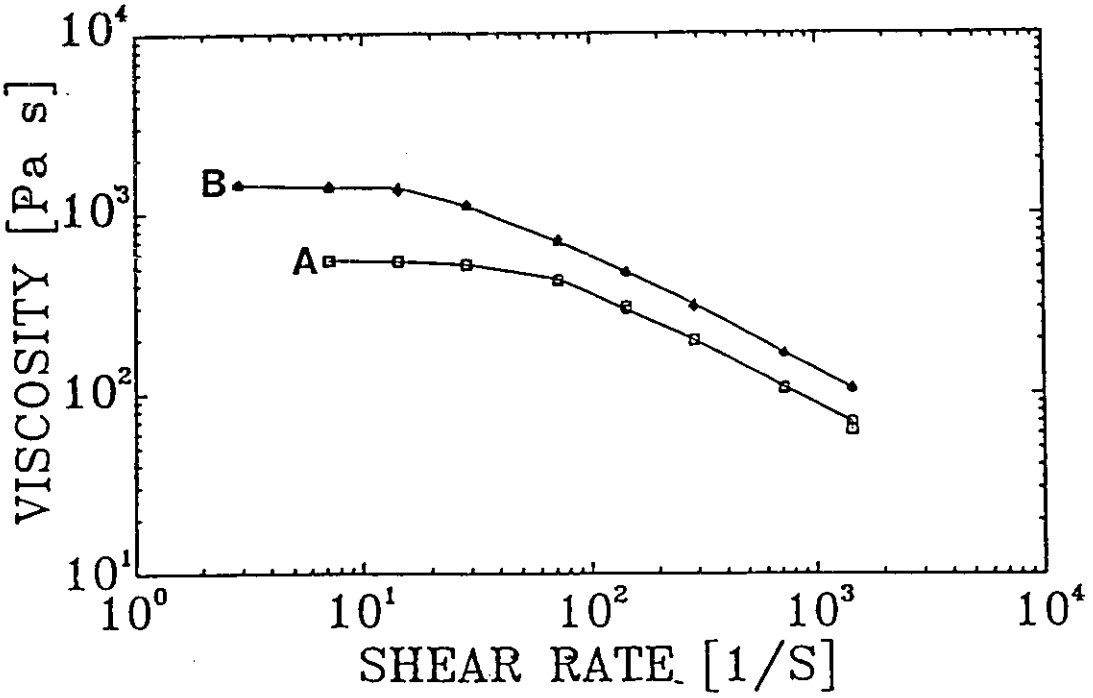

Figure 7.3 Viscosity curves of the polymers used in the Dow experiment at 220°C. A: Dow Styron™ 678E; B: Dow Styron™ 472. Styron is a trademark of the Dow Chemical Company.

performed at a characteristic shear rate of $\dot{\gamma} = 7.5\ s^{-1}$ which is within the shear rate range of the Newtonian plateau for both polymer melts (Figure 7.3).

The polymer melts were brought together under carefully monitored isothermal conditions, the system attained steady-state, the flow was stopped, the die exit was blocked to prevent leakage of the molten polymers and the whole apparatus was then frozen. The feedblock and die were then disassembled, extrudate cross-sections taken and the interface shape was traced. One of the polymers was coloured to facilitate the identification of the extrudate shape. This experimental procedure was designed to study the interface deformation and the resulting degree of encapsulation in addition to previous experimental reports (Everage, 1975; Southern and Ballman, 1975) which examined the interface shape in the extrudate. The interface shape is frozen inside the die instead of the extrudate and extrudate swelling and bending effects which may cause further interface and also free surface distortion are therefore avoided. However, upon solidification polymeric materials may exhibit a small shrinkage due to the different densities between melt and solid phases. A difference in the rate of solidification or the amount of shrinking of the two polymers may result in an interface shape change during the solidification process. Such behaviour usually occurs far downstream in the die and results from that area are not reported.

The layer configuration was such that the less viscous melt A (Figure 7.3) forms the upper layer, while the more viscous melt B forms the lower layer. At the experimental operating conditions (temperature, shear rate) the viscosity ratio between the two melts was approximately (lower:upper) 2.5 and the flowrate ratio was set to (lower:upper) 13.2.

A smooth interface resulted with no diffusion at the interface, interfacial or wave-like instabilities. The evolution of the interface shape inside the square die is shown in Figure 7.4, starting from a distance $x=0.4L$ downstream the square die entrance up to $x=6.71L$. Further downstream, the interface shape was distorted because of material shrinkage and is

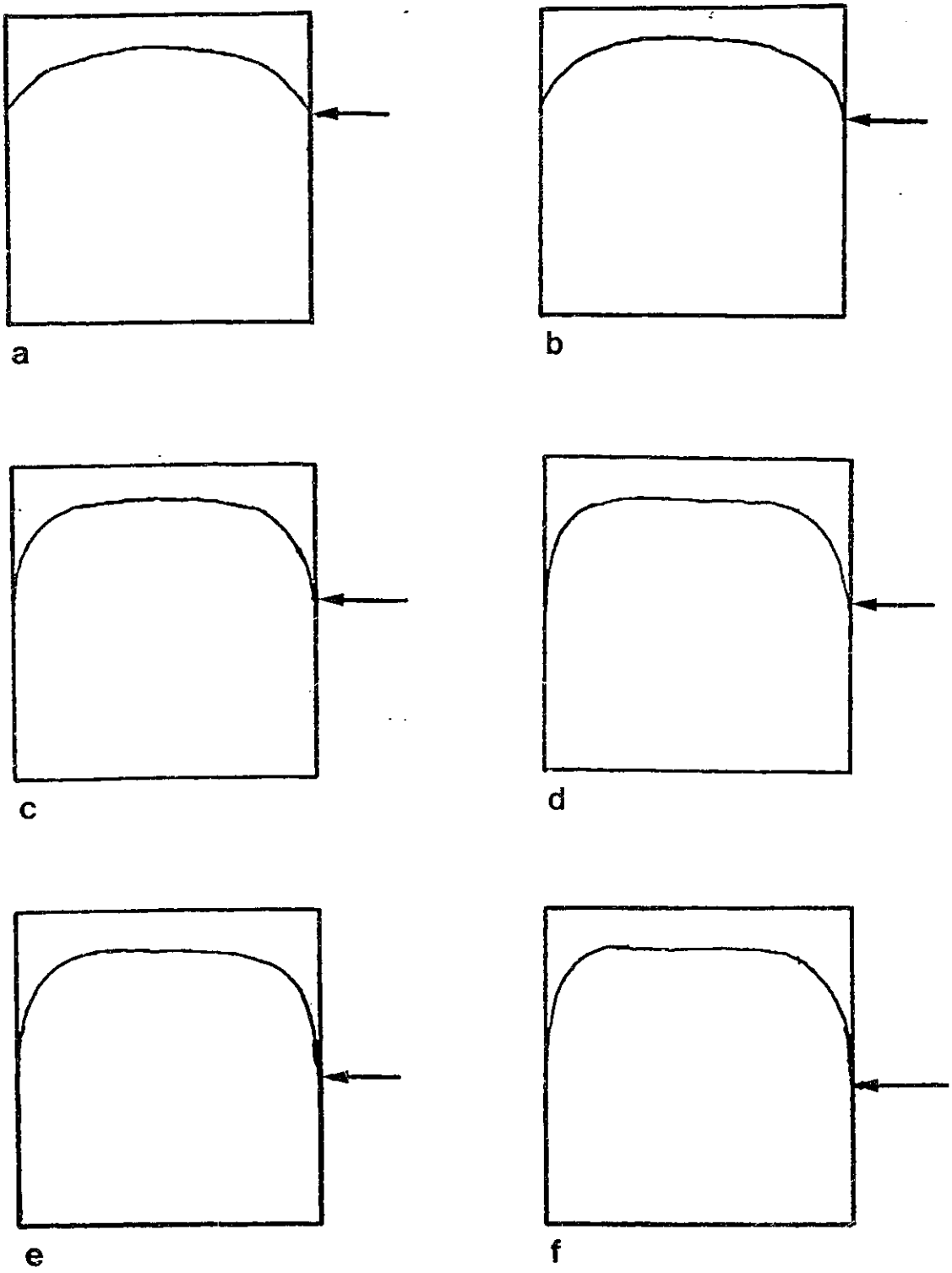

Figure 7.4

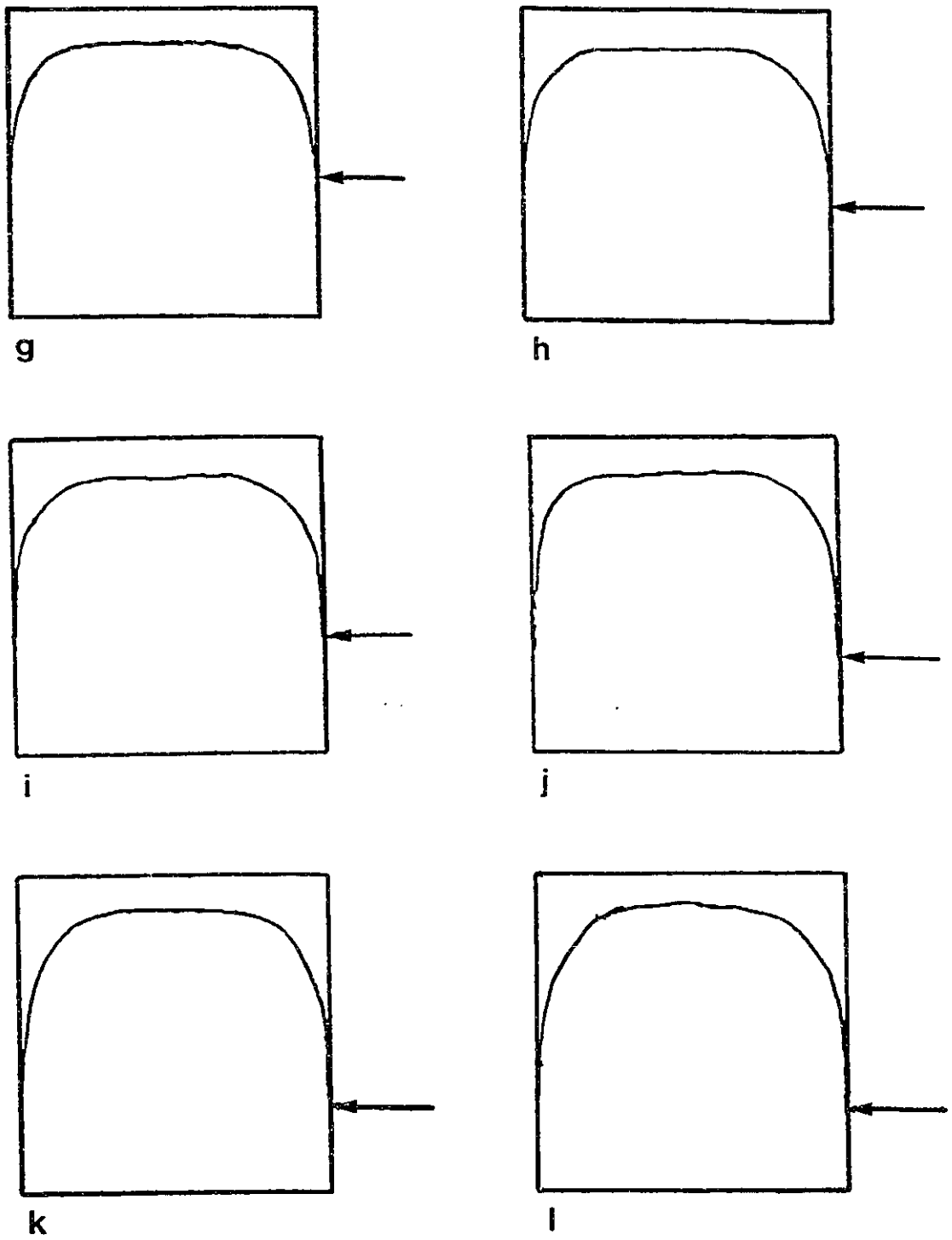

Figure 7.4

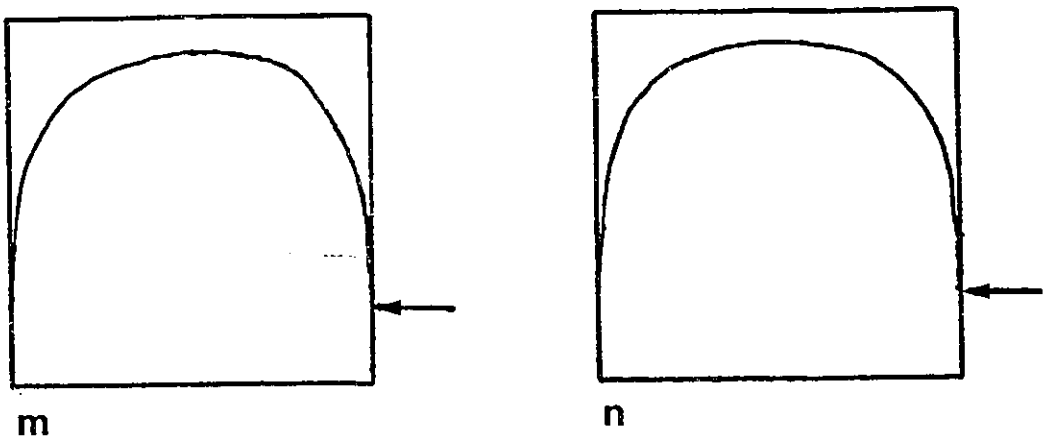

Figure 7.4 Interface shape inside the experimental die. Downstream coordinates are given with respect to the square die entrance (x=0.0). a) x=0.4L, b) x=0.9L, c) x=1.37L, d) x=1.9L, e) x=2.42L, f) x=2.9L, g) x=3.37L, h) x=3.9L, i) x=4.32L, j) x=4.84L, k) x=5.53L, l) x=5.79L, m) x=6.26L, n) x=6.71L.

not reported here. The interface shape inside the square die is shown since no information was released about the interface deformation inside the transition channel.

In agreement with previous experimental evidence (see section 1.2.2), the less viscous upper layer tends to encapsulate the more viscous lower layer. Figures 7.4a to 7.4n show that significant encapsulation occurs during the course of flow in the square die for the relatively low viscosity ratio. The interface curvature increases gradually and initially the interface near the center of the die is almost flat, a condition that persists for a significant length of flow (Figures 7.4c to 7.4k).

It is very interesting that the interface deformation is especially pronounced near the die walls and the encapsulation effect seems to occur within a very thin layer of material next to the walls. This is a very important observation and poses a difficulty to the numerical analysis that is presented in the next section.

7.3 NUMERICAL SIMULATION

A perspective view of the finite element grid that was used in the simulation of the experimental investigation of section 7.2 is shown in Figure 7.5. The grid comprises not only the transition channel and the square die but also a section upstream which intends to simulate the flow stabilizing part of the experimental apparatus (Figure 7.1). In this section the two layers are assumed to flow initially in different channels separated by a thin wall up to the beginning of the transition channel where the melts are brought together. An assumption is made for the purpose of this numerical study, that the separation plate is located at such a height so that the flow of the individual layers in the separate channels is driven by the same

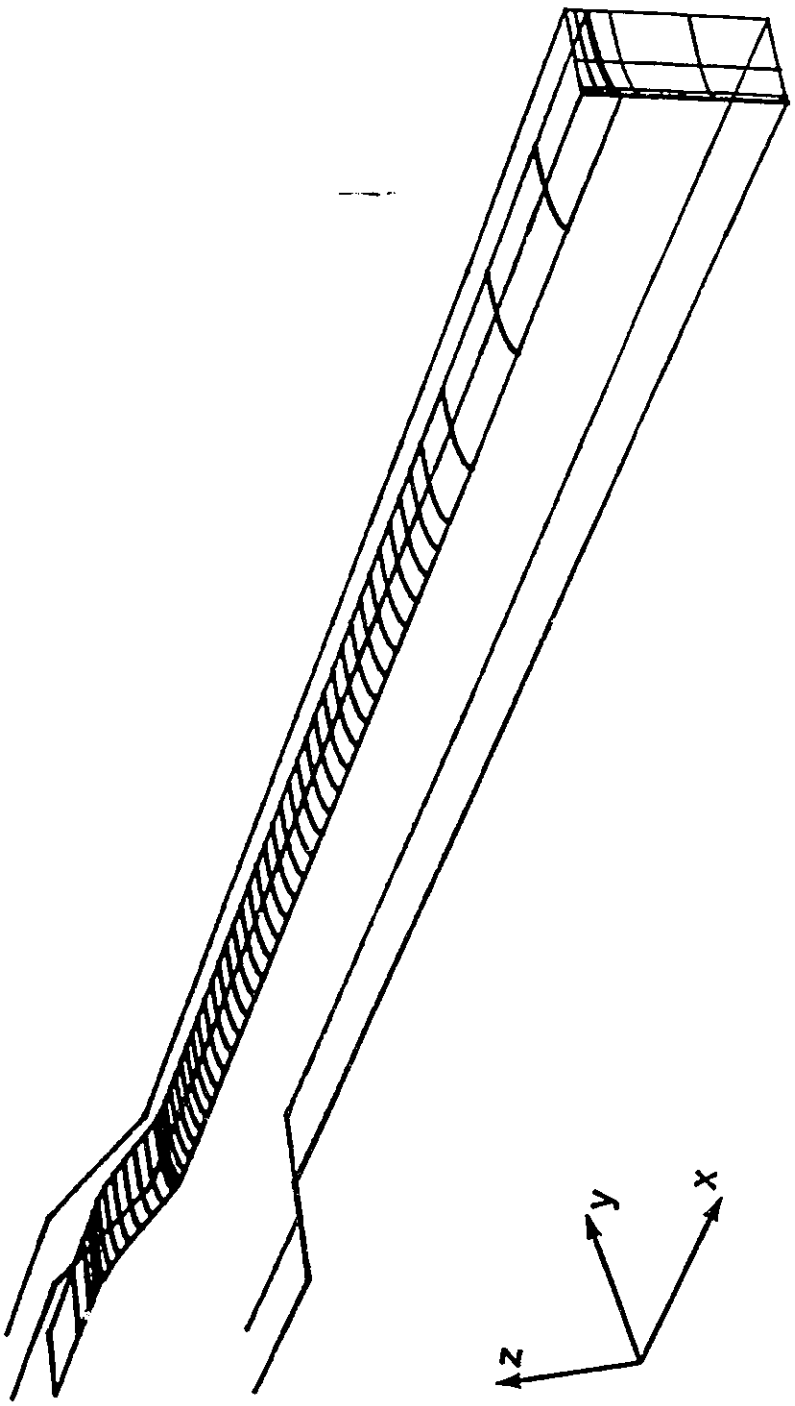

Figure 7.5 Perspective view of the three dimensional grid used in the simulation of Dow's experiment.

pressure gradient. This initial boundary condition may not match exactly the actual design of the Dow modular die that was used in the experiments.

The Carreau shear-thinning model (eqn. 2.35) was fitted to the viscosity curves of Figure 7.3 and in the analysis the melt viscosities are treated as shear-thinning. The characteristic shear rate of the experimental conditions was assigned to the numerical procedure. No thermal effects are considered, since the experiments were carried out under isothermal conditions and no significant viscous dissipation effects are expected for the given processing conditions.

Only half of the flow domain is considered since the square die geometry allows for symmetry. The total grid length is 15L (somewhat longer than the experimental die) and 109 divisions in the downstream direction were used. The grid density in the cross-flow direction is shown in Figure 7.6 and consists of 4 elements in the y-direction (horizontal direction) and 6 elements in the z-direction (vertical direction) with each layer consisting of 3 elements. The resulting numerical problem consists of 1,296 27-node brick elements, 12,753 nodal points, 981 spines and 30,055 unknowns with a frontwidth of 420. No denser grid in the cross-flow (y-z) direction was used although this poses a restriction to the precision of the approach, since it would result in an increase not only of the already very high number of unknowns but also of the frontwidth of the system. The solution of the simultaneous system of equations requires 305 CPU seconds per nonlinear iteration on the Cray X-MP 2/4 of the University of Toronto. Extensive use of disk space was required and the extremely fast Solid State Disk (SSD) was used. Figure 7.6 also shows the deformed finite element grid at the entrance and exit of the square die (Figures 7.6b, 7.6c respectively).

The numerically calculated interface development inside the transition channel and the square die is presented in Figure 7.7. The melts are introduced in a side-by-side manner

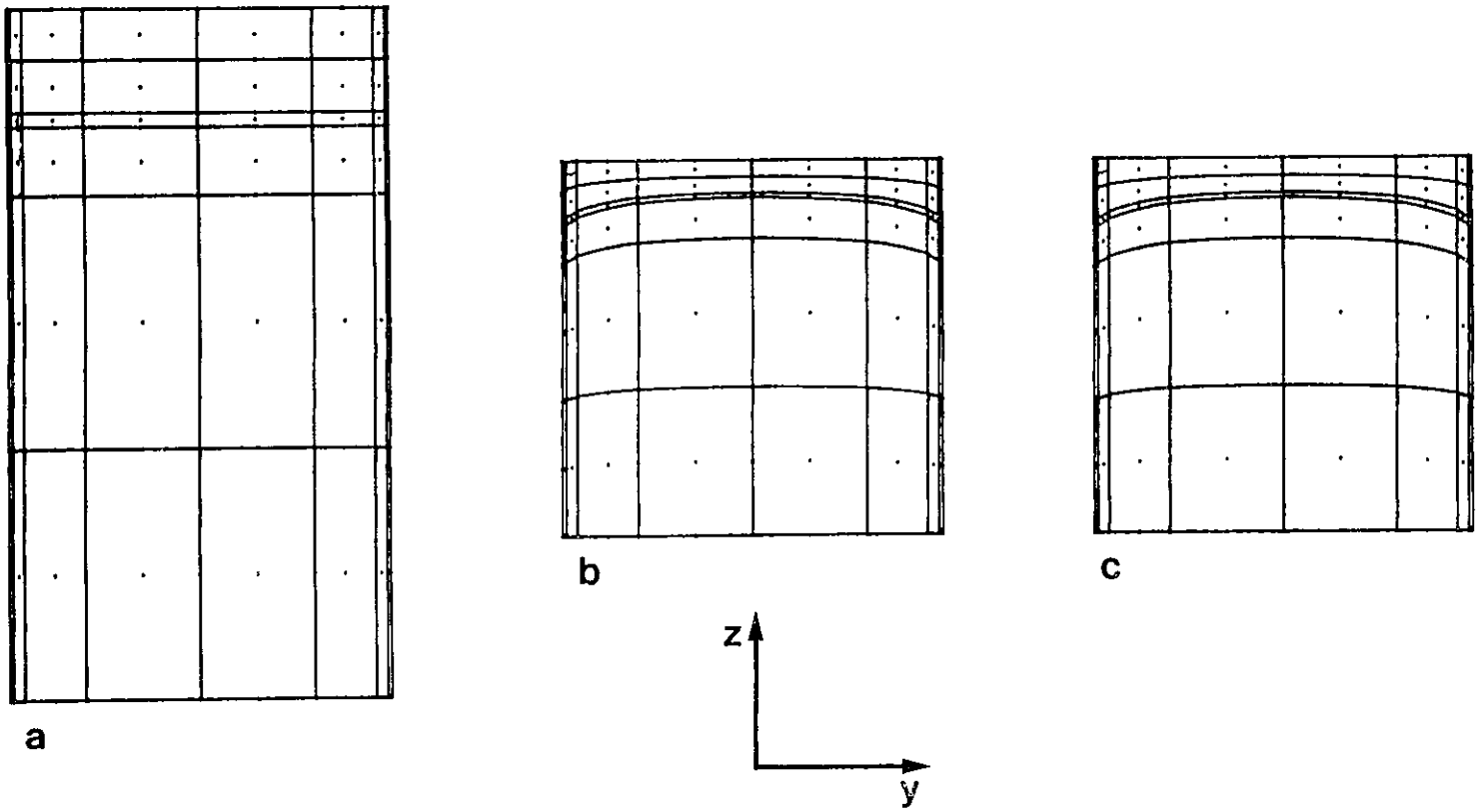

Figure 7.6 Finite element grid. Cross-sectional view. a) Upstream grid, b) distorted grid at the entrance of the square die and c) distorted grid at the downstream plane.

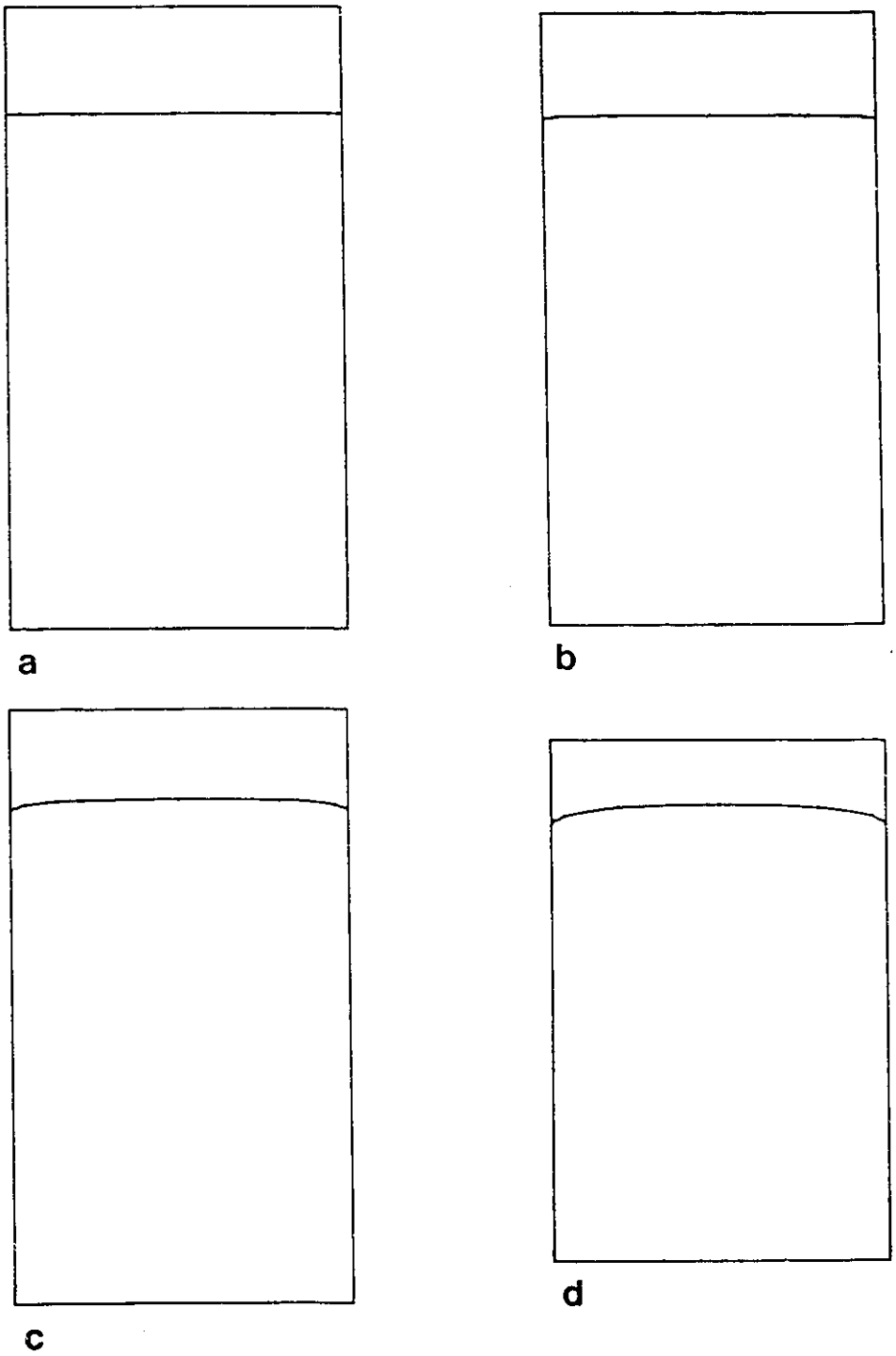

Figure 7.7

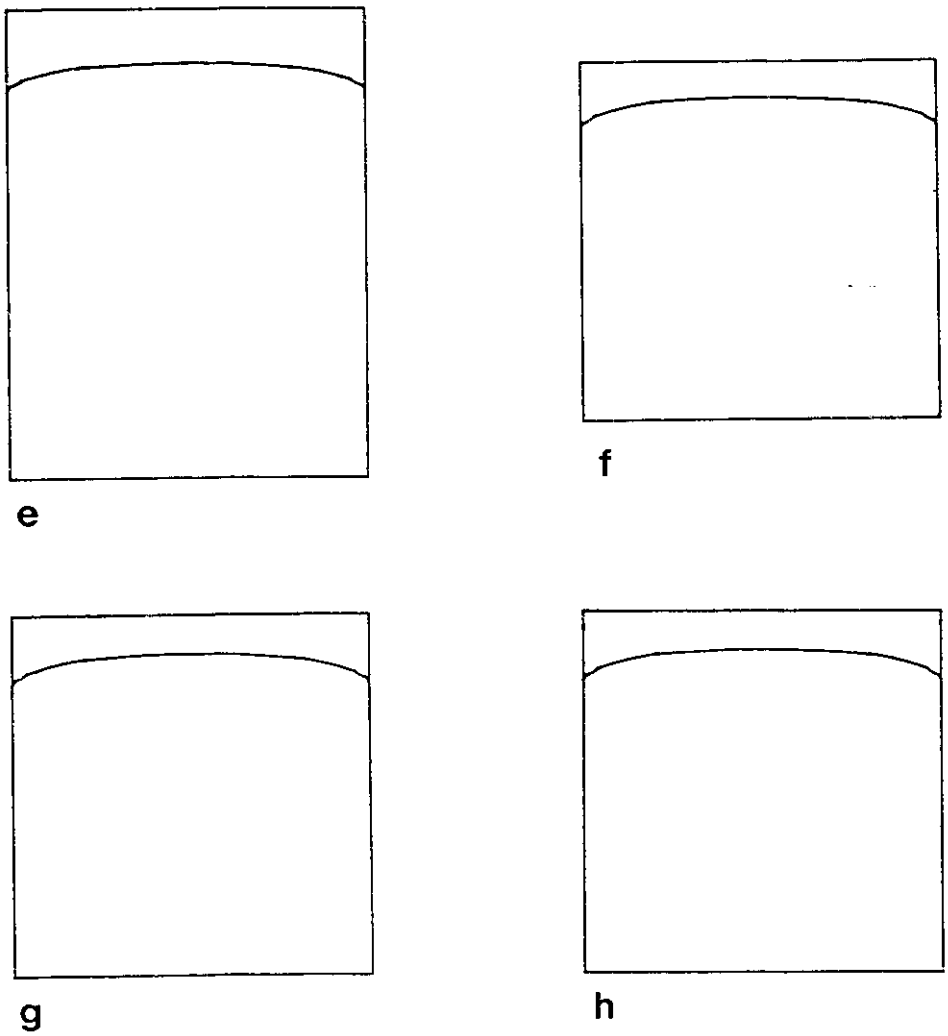

Figure 7.7 Numerically calculated interface shape. a) at the entrance to the converging section (x=0), b) at x=0.05L , c) at x=0.18L, d) at x=0.58L, e) at x=1.0L inside the converging section. f) at the entrance to the square die, g) at 0.42L and h) at 2.42L downstream the die entrance.

with a flat interface initially (Figure 7.7a). Encapsulation occurs during the flow inside the transition channel (Figures 7.7b to 7.7f) and in agreement with the experimental findings, the less viscous upper fluid is encapsulating the more viscous lower fluid. The interface deformation is slight at the beginning (Figures 7.7b, 7.7c) and becomes more pronounced near the walls further downstream. However, no significant increase of the degree of encapsulation was calculated during the course of flow inside the square die (Figures 7.7c to 7.7f), in contrast to the experimental findings. Figure 7.8 also presents the interface development in the downstream direction. Each line gives the interface position along a fixed y-coordinate by connecting the interfacial nodes along a given spine as those are defined by the grid construction of Figure 7.6. Figure 7.7a shows a significant downward migration of the interface from the initially set height due to the effect of the converging geometry of the transition part. At the same time encapsulation is also developing as the spread of the lines demonstrates. The calculated interface shape does not change significantly during the flow inside the square die and only a small tendency of further downward movement of the interface is noted near the wall (Figure 7.8b). Near the entrance of the die, the changing geometry forces a high curvature of the interface in the downstream direction (Figures 7.8b, 7.8c) with a small overshoot of the interface shape. Further downstream the interface is practically leveled in the region near the symmetry plane. Figure 7.8d shows the sudden interface change after the meeting point where the interface near the center of the die overshoots in contrast to the interface near the walls that exhibits a monotonic downward motion.

The initial interface deformation after the layers are brought together is also shown in Figure 7.9. The interface slightly deforms initially and then moves downward because of the converging section geometry.

The pressure discontinuity at the interface along the contact points and the symmetry plane is presented in Figure 7.10. During the flow of the layers in the different

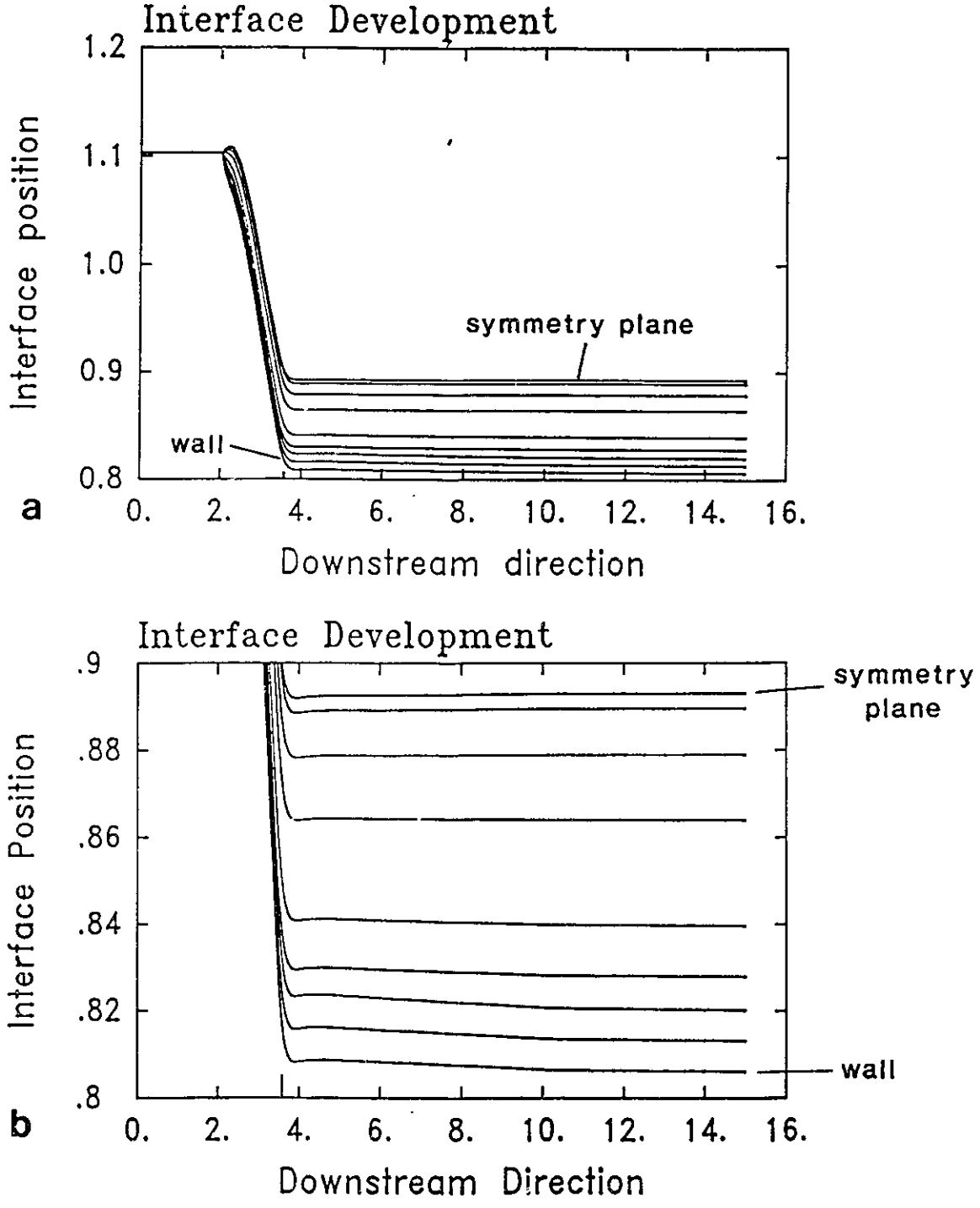
Interface Development
Interface position
1.2
1.1
1.0
0.9
0.8
symmetry plane
wall
a
0.
2.
4.
6.
8.
10.
12.
14.
16.
Downstream direction
Interface Development
Interface Position
.9
.88
.86
.84
.82
.8
symmetry plane
wall
b
0.
2.
4.
6.
8.
10.
12.
14.
16.
Downstream Direction

Figure 7.8

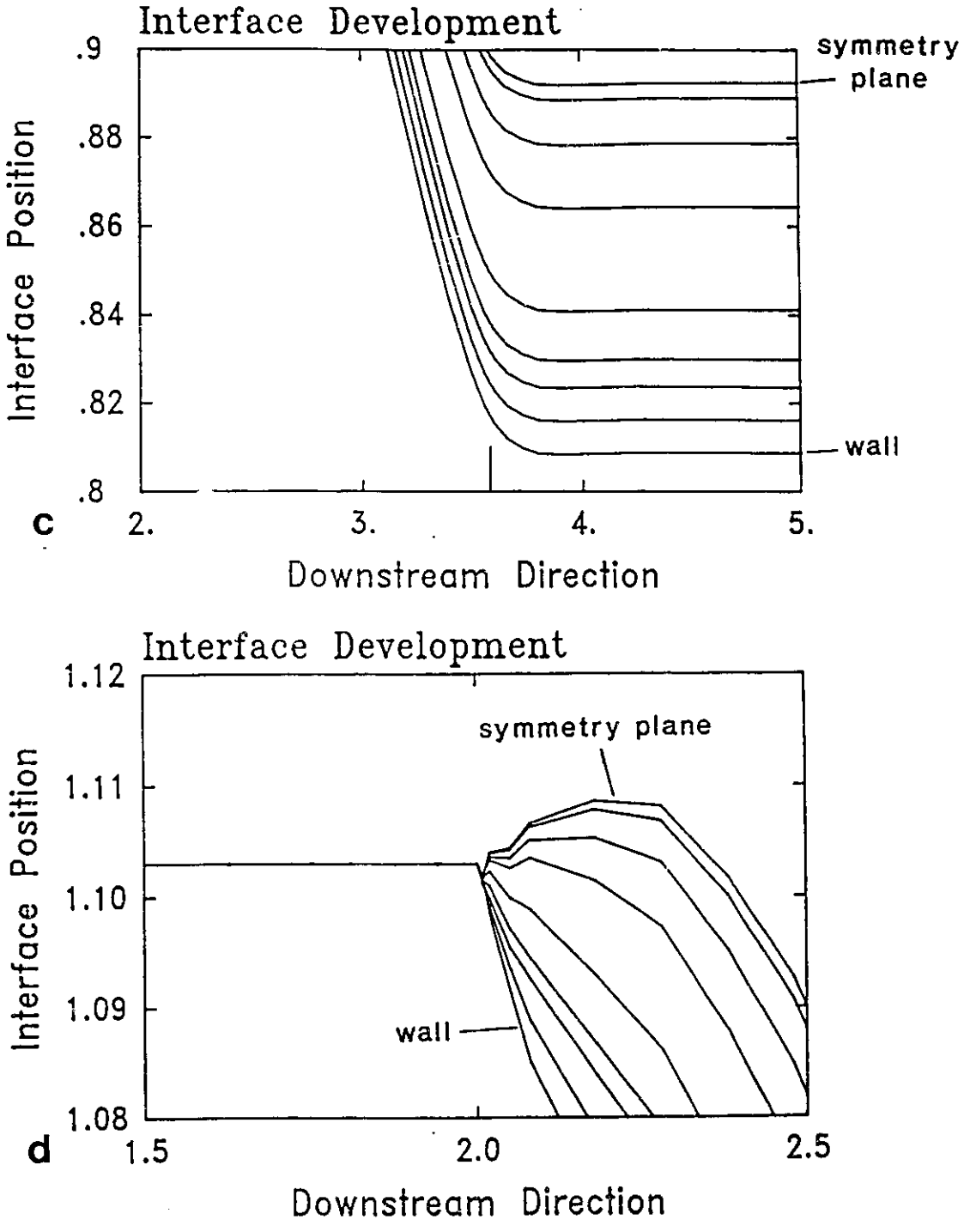

Figure 7.8 Interface development downstream. Lines are for constant y-coordinates from the walls to the symmetry plane. a) Interface development throughout the die, b) and c) near the square die entrance and d) near the merging point.

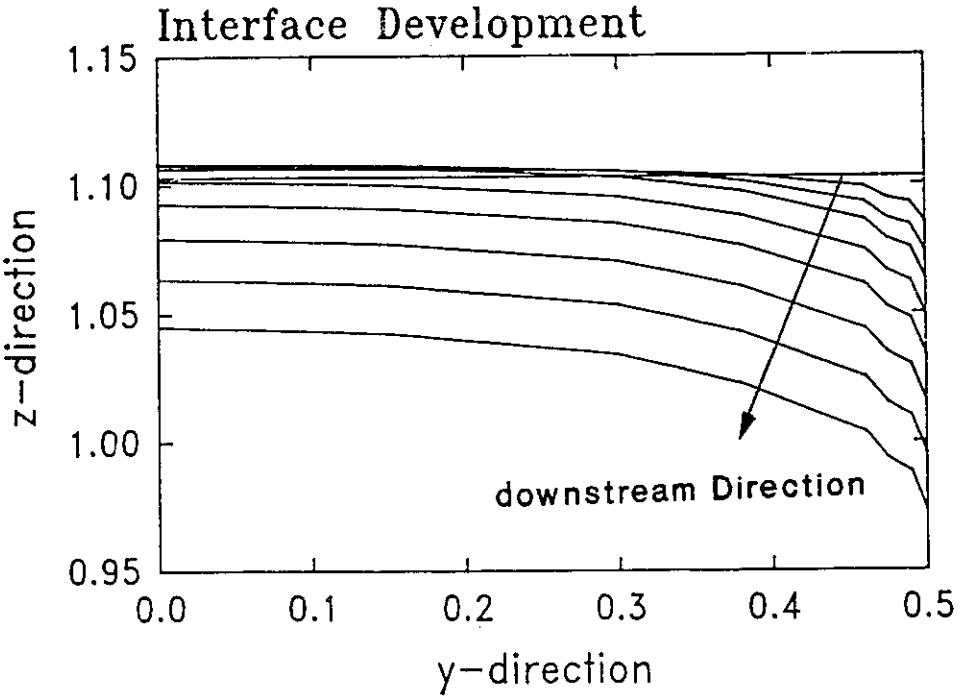

Figure 7.9 Interface shape and deformation in the converging section.

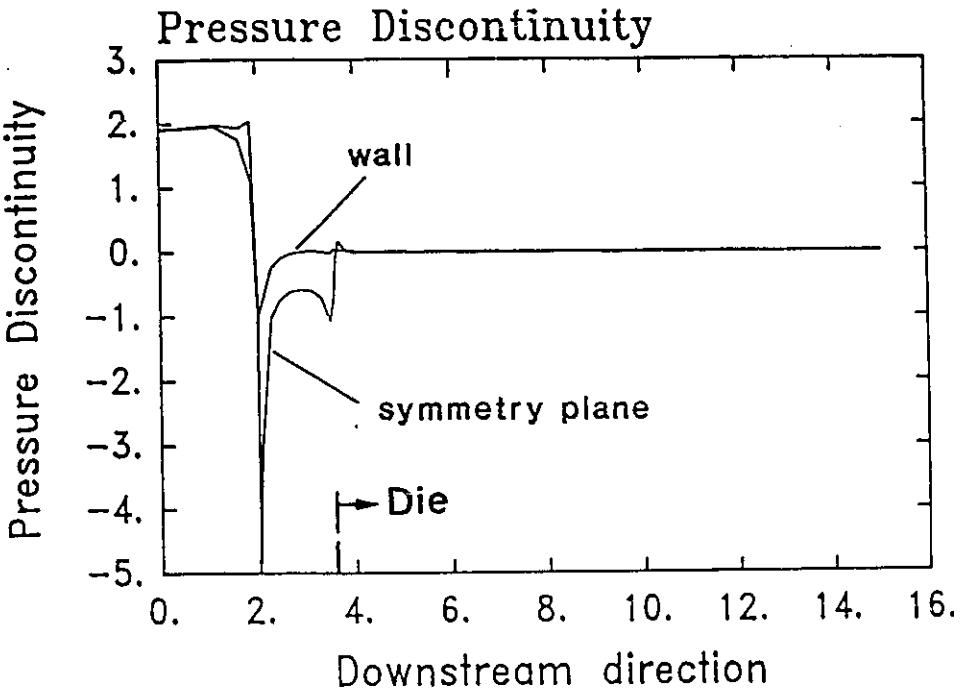

Figure 7.10 Pressure discontinuity at the interface.

channels there exists a significant pressure difference generated by the flow development downstream. At the point where the layers meet, a large negative pressure discontinuity occurs at the interface which is more pronounced at the symmetry plane. As the flow rearranges inside the converging channel, the magnitude of the pressure discontinuity decreases until the entrance of the square die is reached. At the square die entrance a sudden jump of the pressure discontinuity at the interface is exhibited probably because of the effect of the discontinuous change of the geometric shape and the high interface curvature in that region (see Figures 7.8c and 7.8d). Further downstream inside the square die the pressure discontinuity decreases rapidly and finally vanishes as the bicomponent flow develops and is driven by the same pressure gradient.

The development of the individual components of the velocity vector is presented in Figure 7.11 along the interface in the downstream direction. Initially, at the separation plate, velocities are zero but as the fluids are brought together and the interface forms, the fluid at the interface accelerates until the flow fully develops. Figure 7.11a shows that the downstream velocity increases with varying rates along the y-direction (horizontal direction) because of the effect of the die walls. There is a quite complex behaviour of the y- component of velocity (Figure 7.11b) which suggests that in the converging section there is initially flow of material from the region near the walls toward the center of the die, a situation that is soon reversed. After the entrance to the square die however, this behaviour, to a lesser degree, is encountered again. The z-component of velocity (vertical direction, Figure 7.11c) is negative signifying the downward motion of the interface because of the converging geometry. In both Figures 7.10b and 7.10c it is characteristic that the cross-flow velocities are diminishing within a short distance into the square die.

Finally, the calculated and experimentally observed contact point positions are compared in Figure 7.12. It can be seen that although the numerical method is capable of

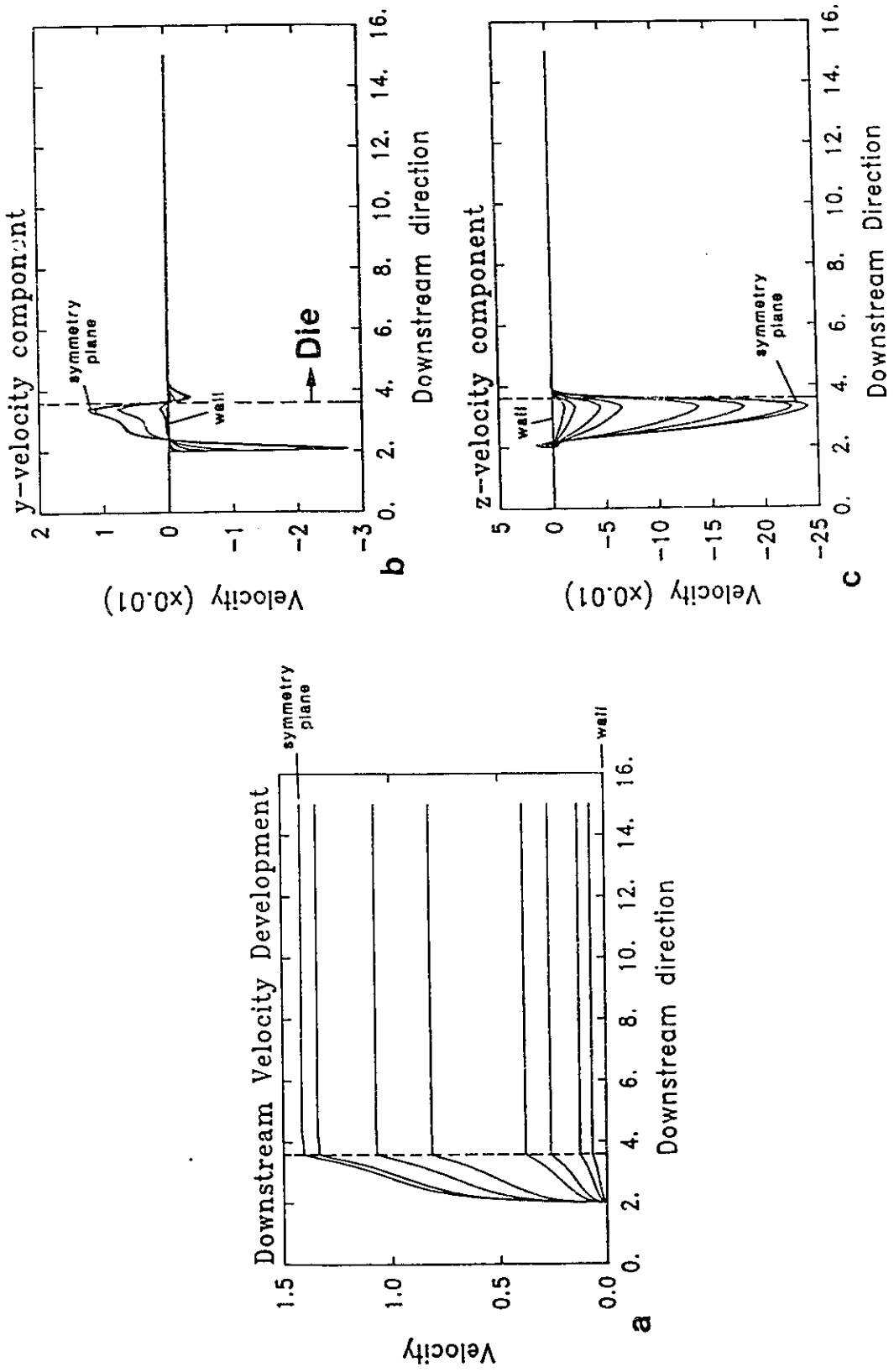

Figure 7.11 Downstream development of the velocity components.

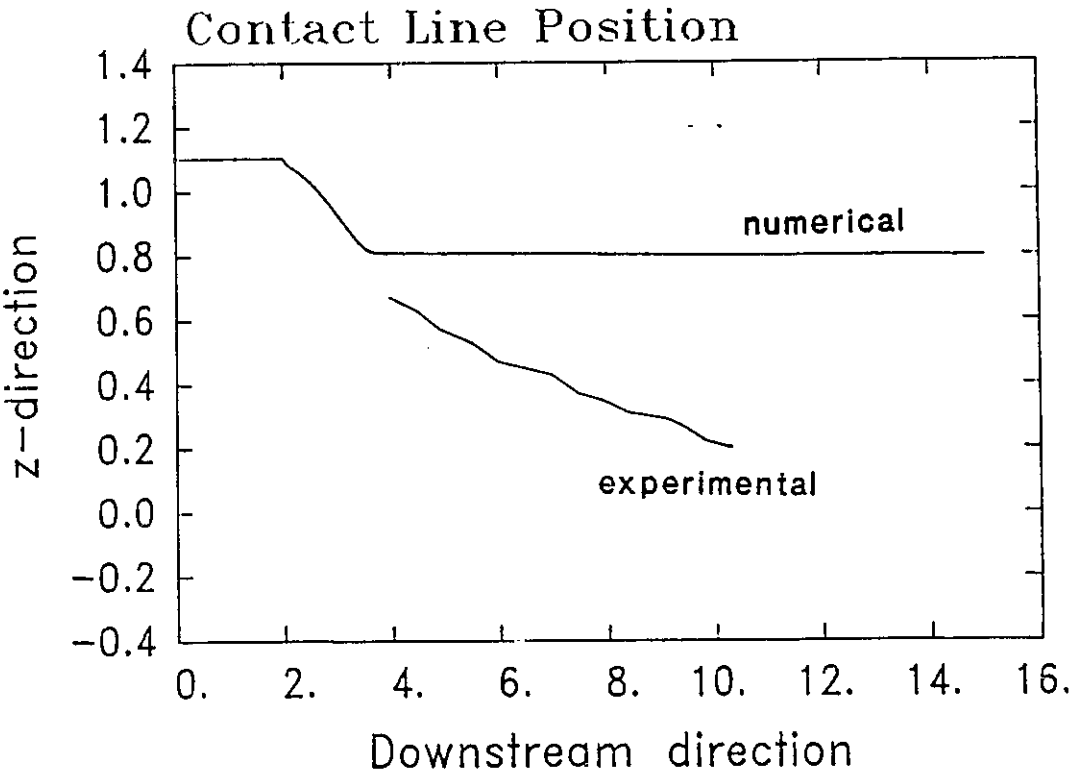

Figure 7.12 Experimentally observed and numerically calculated contact line position.

predicting the qualitative characteristics of the flow, no quantitative agreement with the experimental results is achieved.

7.4 DISCUSSION

The experimental results have shown that although significant encapsulation occurs, it is mainly confined in a small portion of the flow field very close to the die walls (Figure 7.4). In that region of the die, the interface deforms significantly, is elongated and becomes almost parallel to the die walls. This fact raises questions about the correctness of the boundary conditions and the degree of numerical error that is introduced in the numerical approach by the lack of a comprehensive boundary condition at the interface/wall contact lines. The extrapolation technique employed in this thesis (section 6.3) uses information from the interfacial nodes next to the wall to compute the contact point and is dependent on the degree of precision of the interface calculation near the wall. Very dense grids that would better approximate the interface curvature can, in principle, be used but they would result in a dramatic increase of the already formidable size of the three dimensional problem. Also, very dense grids were shown to result in convergence difficulties because of the vanishing magnitude of the velocities near the wall. In light of the experimental findings and the given numerical constraints, a better understanding of the physics of the static contact lines in the absence of surface tension effects becomes imperative.

The experimentally observed increase in the degree of encapsulation questions the downstream boundary condition that was imposed. Unidirectional flow downstream is assumed; a condition that forces the cross-flow velocities, which are responsible for the occurrence of the encapsulation effect, to vanish very rapidly. Zero cross flow velocities, with no change of the interface shape downstream, is an acceptable solution to the governing equations and the kinematic boundary condition at the interface.

The grid density in the downstream direction is an additional consideration because of the small scale of the cross-flow velocities and the slow evolution of the encapsulation. When a dense grid is constructed near the die walls in the (y-z) direction (Figure 7.6), the aspect ratio of the 3-D finite elements increases dramatically unless an equally dense grid is used in the downstream direction. However, to capture the slow encapsulation effect a very long grid is required and in light of the formidable size of the resulting numerical problems, one has to compromise between accuracy and cost.

CHAPTER 8

CONCLUSIONS AND RECOMMENDATIONS

Flow phenomena associated with the extrusion of molten polymers through dies of complex geometric shape have a significant impact on the extrudate shape. A complex die shape and temperature gradients imposed or induced by viscous heat generation give rise to purely three dimensional effects such as extrudate bending and distortion.

In the present thesis, a finite element technique was developed and used to analyze three dimensional extrudate swelling effects of non-isothermal die extrusion flows. The u-v-w-p-h-T formulation presented in Chapter 2 is a powerful numerical technique for the simulation of 3-D non-isothermal free surface flows that enables the simultaneous determination of the flow field (velocities u-v-w, pressure P and temperature T) and the free surface shape (h parameters). An innovative grid generation scheme was developed to allow the parametrization of complex 3-D geometries. The nature of the flow rearrangement in the extrusion out of 3-D dies results in the presence of edges at the extrudate surface when sharp corners exist in the die geometry. To overcome this complexity, a spine-pathline method hybrid scheme that is an extension to the classical spine approach (Kistler, 1984) was developed for the free surface update. This scheme combines the properties of the spine approach that enables the simultaneous solution of the global system of unknowns with the ability of the pathline method to follow the 3-D movement of free surface material points.

This thesis has focused on the effects that occur during extrusion flows because of the viscous properties of the materials. The study was limited to Newtonian and shear thinning fluids of the Carreau type.

The problems studied in this thesis were chosen to help distinguish patterns in the behaviour of the examined flow systems. Table 8.1 summarizes some of the most important results and shows that similar phenomena may occur in completely different flow conditions.

Table 8.1 Summary of Observations of 3-D Problems (Newtonian Fluids)

Die Geometry	Figure Reference	Thermal Effects	Interface	Observation
Flat Film	3.16	Yes	No	Extrudate Bending
Key-Hole	3.20	Yes	No	Extrudate Bending
Key-Hole	3.22	No	No	Extrudate Bending
Square Die	6.25	No	Yes	Extrudate Bending
Square Die	3.13	Yes	No	Pronounced Swelling
Square Die	5.20	No	Yes	Pronounced Swelling
Square Die	6.7	No	Yes	Encapsulation
Square Die*	6.20	No	Yes	Encapsulation

* non-Newtonian fluids

Extrudate bending occurs in non-isothermal flows but also in isothermal flows when the die geometry is not symmetric and in stratified bicomponent systems of side-by-side configuration. Although the flow situations are different, the physics behind the phenomenon are similar and extrudate bending occurs due to unsymmetric velocity profiles inside the die resulting from geometric asymmetries, non-isothermal conditions or the different viscous properties of the materials in the bicomponent case.

Pronounced extrudate swelling occurs when higher viscosity material is wetting the die walls either because of locally lower temperature (thermally induced swelling) or because of the lower viscosity of the outer layer in bicomponent systems.

Encapsulation occurs whenever a viscosity mismatch is present for Newtonian and non-Newtonian materials, with the less viscous fluid always tending to encapsulate the more viscous fluid. The complexity of the numerical problem increases with the presence of the

interface. A rough estimate of the increase in complexity can be given by comparing the CPU time required to solve a bicomponent extrudate swelling problem to the CPU time required to solve a single component problem for a similar die geometry. For a square die geometry, a single component problem requires a CPU time of the order of 1,000 seconds on the CRAY X/MP 2-4. A side-by-side bicomponent problem requires a CPU time of the order of 2,500 seconds on the same computer. The presence of additional unknowns (interface parameters, double-valued pressure variables at the interface) increases the total number of unknowns and the frontwidth of the resulting system of equations. The Picard-like iteration used for the free surface construction in the side-by-side bicomponent flows increases the number of required non-linear iterations with a direct effect on the CPU time requirement. The side-by-side bicomponent flow requires parameterization of half of the flow domain while the single component case study of only a quarter of the flow domain suffices because of symmetry conditions.

The finite element technique was applied in the study of isothermal and non-isothermal flows from dies with complex 3-D shapes (Chapter 3). A number of typical 3-D die shapes were examined (square, rectangular, key-hole, bow-tie) showing that the shape of the extrudate does not exactly follow the shape of the die. The material in the regions of sharp corners swells very little or even contracts while the material near the flat die regions swells significantly.

The mechanisms leading to thermally induced extrudate swelling, bending and distortion of the extrudate were displayed. It was shown that imposed and/or viscous generated temperature differences lead to viscosity differences inside the die which in turn are responsible for the increased swelling or distortion of the extrudate. It has been found through simulation and experiment that the die geometry alone plays an important role in extrudate bending and swelling.

The flow mechanics of bicomponent stratified flows were examined since coextrusion has become a very popular technique of producing polymeric articles with tailored properties. Coextrusion involves the simultaneous flow of more than one polymer melt layer in a single die and the free surface flow of the multicomponent system. Because of the different viscous properties of the materials the interface shape changes during the course of flow inside the die, an effect that may have a severe impact on the layer uniformity and consequently the cost or market value of the final product.

A Generalized Reduced Gradient/Galerkin finite element method combination was developed to study the flow of bicomponent systems through very long dies (Chapter 4). This numerical scheme uses the minimum viscous dissipation principle introduced by Everage (1973) to study the interface shape problem. The method is capable of predicting the encapsulation of the more viscous fluid by the less viscous fluid in agreement with experimental evidence. In complex geometric shapes, break-up of the inner layer may occur because of the shearing distribution inside the die.

The finite element technique of Chapter 2 was extended to enable the fully 3-D study of bicomponent stratified flows. The step change of the viscous properties at the interface generates a pressure and viscous stress discontinuity at the interface and requires special treatment. Both a double-node technique (u-v-w-P_1-P_2-h_1-h_2 formulation) and a penalty function (u-v-w-P-h_1-h_2) formulation were used in this thesis to handle the pressure discontinuity at the interface producing similar results.

The class of the bicomponent stratified flows in an encapsulated configuration was studied in Chapter 5. The complication resulting from the presence of both the interface and the external free surface was handled by the development of an extended spine approach where two spatial variables are assigned to each spine.

The internal interface shape during the course of flow inside short dies was demonstrated to exhibit a dependence on the initial geometric shape unless dominant surface tension effects were present. The interface shape and flow areas of the individual layers were shown to be dependent on the viscosity ratio, flowrate ratio and the material configuration. The swelling behaviour of the bicomponent system also depends on the viscosity and flowrate ratios. Generally, the interface swells significantly which however is not always the case with the external free surface. The layer configuration was shown to have a very important effect on the extrudate shape and swelling ratio. When the less viscous fluid forms the skin with the more viscous fluid located at the core, a slight external free surface swelling or even shrinkage occurs. When the more viscous fluid forms the skin layer, high external free surface swelling results due to fluid rearrangement in the extrudate which alters dramatically the shape of the extrudate and the interface.

The class of bicomponent flows in a side-by-side configuration was studied in Chapter 6. The numerical analysis faces the complicating issue of the static contact line where the melt/melt interface contacts the die walls. An extrapolation method was used to define the contact points in lack of a comprehensive boundary condition at the contact lines. The complicating feature of the extrudate bending due to the viscosity mismatch was handled by the pathline construction of the free surfaces in the extrudate.

The numerically calculated tendency of the less viscous layer to encapsulate the more viscous layer agreed with experimental evidence. The dependence of the degree of encapsulation on the viscosity ratio was studied and it was shown that encapsulation increases with increasing viscosity ratio. The dependence of the interface shape on the viscosity ratio was further investigated for the case of shear thinning fluids exhibiting a viscosity curve crossover point. It was demonstrated that the direction of the interface curvature follows the viscosity ratio and that interface curvature reversal occurs when the crossover point is exceeded, in

agreement with experimental evidence (Southern and Ballman, 1975). The effect of slip at the solid wall was also examined. The bending of the extrudate because of the viscosity stratification and the layered configuration was displayed. Depending on the die geometry, extrudate distortion was shown to occur in addition to the extrudate bending, which may also result in significant interface shape distortion during the free surface flow.

An experimental investigation of the encapsulation effect during the stratified side-by-side flow inside a square die was presented in Chapter 7. The 3-D procedure was applied to the experimental conditions to establish the degree of agreement between experiment and simulation. It was shown that the simulation results are in qualitative but not quantitative agreement with the experimental findings. A number of considerations as to potential sources of the quantitative disagreement were discussed. The presence of numerical singularities and complicating features such as static contact lines in the absence of surface tension effects, downstream boundary conditions for short die flows, finite element grid density etc., probably limit the quantitative extent of the numerical results.

The three dimensional modelling gives rise to problems that require the solution of large systems of equations. The problem size becomes prohibitive even on very fast vector processing computers mainly because of inefficient (non-vectorizable) matrix decomposition techniques. The non-linearity of free surface flow problems requires an iterative solution procedure and the choice of non-linear iteration policy affects directly the cost. Convergence acceleration schemes are available (Appendix B) and a proper non-linear iteration strategy may significantly reduce the cost of the approach.

The finite element methodology adopted in the present work proved to be an extremely powerful tool in analyzing free surface extrusion flows and identifying important effects. The modular structure of the approach allows, with little effort, the incorporation of

more sophisticated constitutive equations and/or free surface handling schemes to study complex flow situations. Further work with this technique is recommended in the following areas:

i) Carefully designed experiments of bicomponent or multicomponent flow coupled with the simulation would help in understanding the contribution of elastic effects on the interface development and their coupling to the viscous effects. Also, the effects that temperature gradients inside the die may have on the interface and free surface shapes would be assessed.

ii) Numerical investigation of the effect of the elastic properties of polymers. This would require the incorporation of an appropriate constitutive equation describing the viscoelastic nature of the polymer melts. The computational cost is expected to be high and there is a need for further improvement of the non-linear iteration policy.

iii) Study of the imposed boundary conditions to the stratified flow problem. The boundary conditions at the contact point, the far downstream plane and at the interface have an effect on the solution due to the elliptic character of the governing equations. The imposed boundary conditions may need to be revised to allow a better quantitative agreement between modelling results and experimental evidence.

iv) Development of more efficient solvers to take advantage of the vector processing operations on supercomputing machines. The current study has shown that over 80% of the total CPU time was spent in the matrix decomposition procedure. Reduction of the memory requirements would also enable the solution of larger systems of equations which would increase the precision and potential of the approach.

v) Investigation of the important issue of the wave-like or incipient interfacial instability because of the different viscoelastic properties of the materials. The effects of viscosity ratio, normal stress ratio, flowrate ratio and the geometric shape would be assessed.

REFERENCES

Acierno, D., Dalton, J.N., Rodriguez, J.M., White, J.L., "Rheological and Heat Transfer Aspects of the Melt Spinning of Monofilament Fibers of Polyethylene and Polystyrene", J. Appl. Pol. Sci., 15, 2395-2415 (1971)

Basu, S., "A Theoretical Analysis of Non-Isothermal Flow in Wire-Coating Co-Extrusion Dies", Pol. Eng. Sci., 21, 1128 (1981)

Batchelor, J., Berry, J.P., Horsfall, F., "Die Swell in Elastic and Viscous Fluids", Polymer, 14, 297-299 (1973)

Ben-Sabar E., Caswell, B., "Heat Transfer Effects in Die Swell", J. Rheology, 25, 537-548 (1981)

Bentwich, M., "Two-Phase Viscous Axial Flow in a Pipe", J. Basic Eng., 86, 669-672 (1964)

Binding, D.M., Walters, K., Dheur, J., Crochet, M.J., "Interfacial Effects in the Flow of Viscous and Elasticoviscous Liquids", Phil. Trans. R. Soc. Lond., A 323, 424-469 (1987)

British Patent No. 1,101,452, "An Improved Spinning Head for the Melt Spinning of Conjugate Filaments", N.V. Onderzoekingsinstituut Research (1968)

British Patent No. 1,120,241, "Composite Filaments and Spinneret for Producing Same", Kanegafuchi Boseki Kabushiki Kaisha (1968)

Broyden, C.G., "A class of methods for solving nonlinear simultaneous equations", Mathematics of Computation, 19, 577-593, (1965)

Bush, M.B. and Phan-Thien, N., "Three Dimensional Viscous Flows with a Free Surface: Flow out of Long Square Die", J. Non-Newt. Fluid Mech., 18, 211-218 (1985)

Carreau, P.J., "Rheological Equations from Molecular Network Theories", Ph.D. Thesis, University of Wisconsin (1968)

Caswell B. and Viriyayuthakorn, M., "Finite Element Simulation of Die Swell for a Maxwell Fluid", J. Non-Newtonian Fluid Mech., 12, 13-29 (1983)

Charles, M.E., Govier, G.W., Hodgson, G.W., "The Horizontal Pipeline Flow of Equal Density Oil-Water Mixtures", Can. J. Chem. Eng., 39, 27 (1961)

Charles, M.E., Lilleleht, L.U., "Co-current Stratified Laminar Flow of Two Immiscible Liquids in a Rectangular Conduit", Can. J. Chem. Eng., 43, 110 (1965)

Charles, M.E., Redberger, P.J., "The Reduction of Pressure Gradients in Oil Pipelines by the Addition of Water : Numerical Analysis of Stratified Flow", Can. J. Chem. Eng., 40, 70 (1962)

Chauffoureaux, J.C., Dehennau, C., Van Rijckevorsel, J., "Flow and Thermal Stability of Rigid PVC", J. Rheol., 23, 1 (1979)

Chin, H.B., Kim, Y.J., Han, C.D., "A Study of Non-Isothermal Flat-Film Coextrusion", Pol. Eng. Reviews, 4, 281 (1984)

Cohen, Y., Metzner, A.B., "Apparent Slip Flow of Polymer Solutions", J. Rheol., 29, 67 (1985)

Coyle, D.J., "The Fluid Mechanics of Roll Coating: Steady Flows, Stability, and Rheology", PhD Thesis, University of Minnesota, Minneapolis (1984)

Crochet, M.J., Davies, M.J. and Walters, K., Numerical Simulation of Non-Newtonian Flow, Elsevier, Amsterdam (1984)

Crochet, M.J. and Keunings, R., "Die Swell of a Maxwell Fluid: Numerical Prediction", J. Non-Newt. Fluid. Mech., 7, 199 (1980)

Crochet, M.J. and Keunings, R., "On Numerical Die Swell Calculation", J. Non-Newtonian Fluid Mech., 10, 85-94 (1982)

Crowe, C.M., Nishio, M., "Convergence Promotion in the Simulation of Chemical Processes - The General Dominant Eigenvalue Method", AIChE J., 21, 528-533, (1975)

Dennis, J., More, J., "Quasi-Newton method, motivation and theory", SIAM Review, 19, 46-89, (1977)

Dheur, J., Crochet, M.J., "Newtonian Stratified Flow Through an Abrubt Expansion", Rheologica Acta, 26, 401-413 (1987)

Dhatt, G., Touzot, G., "The Finite Element Method Displayed", Wiley, New York (1984)

Dongarra, J.J., Bunch, J.R., Moler, C.B., Stewart, G.W., "Linpack Users' Guide", SIAM, Philadelphia, (1979)

Dussan V, E.B., "On the Spreading of Liquids on Solid Surfaces: Static and Dynamic Contact Lines", Ann. Rev. Fluid Mech., 11, 371 (1979)

Engleman, M.S., "Quasi-Newton Methods in Fluid Dynamics", in "Mathematics of Finite Elements and Applications", IV, J.R. Whiteman (Ed.), Academic Press, London, 479-487 (1982)

Engelman, M.S., Strang, G., Bathe, K.J., "The application of quasi-Newton methods in fluid mechanics", Int. J. Num. Methods Eng., 17, 707-718 (1981)

Everage, A.E., "Theory of Stratified Bicomponent Flow of Polymer Melts. I. Equilibrium Newtonian Tube Flow", Trans. Soc. Rheol., 17, 629 (1973)

Everage, A.E., "Theory of Stratified Bicomponent Flow of Polymer Melts. II. Interface Motion in Transient Flow", Trans. Soc. Rheol., 19, 509 (1975)

Finch, C.R, "An Overview of the Coming to Life of Coextrusion", Coextrusion Seminar, SPE Coextrusion IV Conference Program, Arlington Heights, Illinois, October 5-7 (1987)

Finlayson, B.A., McClelland, M.A., "Non-Isothermal Extrudate Swell of Elastic Liquids", in "Numerical Methods in Heat Transfer", R.W. Lewis, Ed., Vol.3, Wiley, New York, 269-287, (1985)

Gartling,D.K., Nickell, R.E.,Tanner, R.I., "A finite element convergence study for accelerating flow problems", Int. J. Num. Methods Eng., 11, 1155-1174 (1977)

Gear, R.L., Keentok, M., Milthorpe, J.F., Tanner, R.I., "The shape of Low Reynolds Number Jets", Phys. Fluids, 26, 7-9 (1983)

Gemmell, A.R., Epstein, N., "Numerical Analysis of Stratified Laminar Flow of Two Immiscible Newtonian Liquids in a Circular Pipe", Can. J. Chem. Eng., 40, 215 (1962)

Han, C.D., Multiphase Flow in Polymer Processing, Academic Press (1981)

Han, C.D.,"Rheology of Shaped Fiber Formation", J. Appl. Pol. Sci., 15, 1091- 1097 (1971)

Han, C.D., Kim, Y.W., "Further Observations of the Interface Shape of Conjugate Fibers", J. Appl. Pol. Sci., 20, 2609 (1976)

Han, C.D., Kim, Y.W., "Use of the Coextrusion Technique for Producing Flame- Retardant and Antistatic Fibers", J. Appl. Pol. Sci., 20, 2913 (1976)

Han, C.D., Rao, D.A., "Studies on Wire Coating Extrusion. II. The Rheology of Wire Coating Coextrusion", Pol. Eng. Sci., 20, 128 (1980)

Han, C.D., Shetty, R., "Studies on Multilayer Film Coextrusion I. The Rheology of Flat Film Coextrusion", Pol. Eng. Sci., 16, 697 (1976)

Hasbani, I., Engelman, M., "Out of core solution of linear equations with non- symmetric coefficient matrix", Computers and Fluids, 7, 13-31, (1979)

Hasson, D., Mann, U., Nir, A., "Annular Flow of two Immiscible Liquids I. Mechanisms", Can. J. Chem. Eng., 48, 514 (1970)

Hasson, D., Nir, A., "Annular Flow of Two Immiscible Liquids II. Analysis of Core-Liquid Ascent", Can. J. Chem. Eng., 48, 521 (1970)

Hickox, C.E., "Instability Due to Viscosity Stratification in Axisymmetric Pipe Flow", Phys. Fluids, 14, 251 (1971)

Hooper, A.P., Boyd, W.G., "Shear-Flow Instability at the Interface Between Two Viscous Fluids", J. Fluid Mech., 128, 507 (1983)

Huebner, K.H., Thornton, E.A., "The Finite Element Method for Engineers", 2nd Ed., Wiley, New York (1982)

Huh, C., and Mason, S.G., "The Steady Movement of a Capillary Meniscus in a Capillary Tube", J. Fluid Mech., 81, 401 (1977)

Huh, C., Scriven, L.E., "Hydrodynamic Model of Steady Movement of a Solid/Liquid/Fluid Contact Line", J. Colloid Interf. Sci., 35, 85 (1971)

Huyakorn, P.S., Taylor, C., Lee, R.L., Gresho, P.M., "A Comparison of Various Mixed Interpolation Finite Elements in the Velocity-Pressure Formulation of the Navier-Stokes Equations", Comp. and Fluids, 6, 25 (1978)

Huynh, B.P., "Some Finite Element Studies of Extrusion", J. Non-Newt. Fluid Mech., 13, 1-20 (1983)

Jeffries, R., "Bicomponent Fibres", Merrow Publishing Co. (1971)

Joseph, D.D., Renardy, M., Renardy, Y., "Instability of the Flow of Two Immiscible Liquids with Different Viscosities in a Pipe", J. Fluid Mech., 141, 309 (1984)

Joseph, D.D., Nguyen, K., Beavers, G.S., "Non-Uniqueness and Stability of the Configuration of Flow of Immiscible Fluids with Different Viscosities", J. Fluid Mech., 141, 319-345 (1984)

Kafka, F.Y., Dussan V., E.B., "On the Interpretation of Contact Angles in Capillaries", J. Fluid Mech., 95, 539 (1979)

Kalika, D.S., Dnn, M.M., "Wall Slip and Extrudate Distortion in Linear Low- Density Polyethylene", J. Rheol., 31, 815 (1987)

Kaniel, S., Stein, J., "Least-Square Acceleration of Iterative Methods for Linear Equations", J. Opt. Theory Appl., 14, 431-437 (1974)

Keunings, R., "Simulation of Viscoelastic Flow", in "Fundamentals of Computer Modelling for Polymer Processing", C.L.Tucker III, Ed., Carl Hanser Verlag (1987)

Khan, A.A., Han, C.D., "On the Interface Deformation in the Stratified Two-Phase Flow of Viscoelastic Fluids", Trans. Soc. Rheol., 20, 595 (1976)

Khan, A.A., Han, C.D., "A Study on the Interfacial Instability in the Stratified Flow of Two Viscoelastic Fluids Through a Rectangular Duct", Trans. Soc. Rheol., 21, 101 (1977)

Kheshgi, H.S., Basaran, O.A., Benner, R.E., Kistler, S.F., Scriven, L.E., "Continuation in a parameter: Experience with viscous and free surface flows", in "Numerical Methods in Laminar and Turbulent Flows", C. Taylor, J.A. Johnson and W.R. Smith (Eds.), Pineridge Press, Swansea, UK (1983)

Kheshgi, H.S., Scriven, L.E., "Penalty Finite Element Analysis of Unsteady Free Surface Flows", in "Finite Elements in Fluids", R.H.Gallagher, J.T. Oden, O.C. Zienkiewicz, T. Kawai, M. Kawahara, Eds., Volume 5, 393-434, John Wiley & Sons (1984)

Kheshgi, H.S., Scriven, L.E., "Variable Penalty Method for Finite Element Analysis of Incompressible Flow", Int. J. Num. Meth. Fluids, 5, 785-803 (1985)

Kistler, S.F., "The Fluid Mechanics of Curtain Coatings and Related Viscous Free Surface Flows with Contact Lines", PhD Thesis, Univ. Minnesota, Minneapolis (1984)

Kistler, S.F., Scriven, L.E., "Coating Flows", in "Computational Analysis of Polymer Processing", J.R.A. Pearson and S.M. Richardson, Eds., Applied Science Pub., London (1983)

Kraynik, A.M., Schowalter, W.R., "Slip at the Wall and Extrudate Roughness with Aqueous Solutions of Polyvinyl Alcohol and Sodium Borate", J. Rheol., 25, 95-114 (1981)

Lau, H.C., Schowalter, W.R., "A Model for Adhesive Failure of Viscoelastic Fluids During Flow", J. Rheol., 30, 193 (1986)

Lee, B.L., White, J.L., "An Experimental Study of Rheological Properties of Polymer Melts in Laminar Shear Flow and of Interface Deformation and Its Mechanisms in Two-Phase Stratified Flow", Trans. Soc. Rheol., 18, 467-492 (1974)

Liu, T-J, "Fully developed flow of power-law fluids in ducts", Industrial Engineering and Chemistry - Fundamentals, 22, 183-186 (1983)

Liu, T-J, "An efficient matrix solver for finite-element analysis of non- newtonian fluid flow problems", Int. J. Num. Methods Fluids, 5, 929-938 (1985)

Lyngaae-Jorgensen, J., Thomsen, L.D., Rasmussen, K., Sondergaard, K., Andersen, F.E., "On the Influence of Interfacial Slip on Melt Flow Properties of Polymer Blends", Intern. Polym. Proc. II, 3/4, 123-130 (1988)

MacLean, D.L., "A Theoretical Analysis of Bicomponent Flow and the Problem of Interface Shape", Trans. Soc. Rheol., 17, 385 (1973)

Matthies, H., Strang, G., "The solution of nonlinear finite element equations", Int. J. Num. Methods Eng., 14, 1613-1616 (1979)

Mavridis, H., "Finite Element Studies in Injection Mold Filling", Ph.D. Thesis, McMaster University, Hamilton, Ont., Canada (1988)

Mavridis, H., Hrymak, A.N., Vlachopoulos, J., "Finite Element Simulation of Fountain Flow in Injection Molding", Polym. Eng. Sci., 26, 449 (1986)

Mavridis, H., Hrymak, A.N., Vlachopoulos, J., "Finite-Element Simulation of Stratified Multiphase Flows", AIChE J., 33, 410 (1987)

McClelland, M.A., Finlayson, B.A., "Heat Transfer Effects in Extrudate Swell of Elastic Liquids", J. Non-Newt. Fluid Mech., 27, 363-374 (1988)

Menges, G., Gesenhues, B. and Schwenzer, C., "A Method of Calculating Die Swell when Designing Profile Dies", Kunststoffe, 75, 14-16(1985)

Michaeli, W., "Extrusion Dies", Hanser Publishers (In English Macmillan, 1984)

Milthorpe J.F., Tanner R.I., "Om the Extrusion of Visco-Elastic Fluids Subject to Viscous Heating", Int. J. Num. Methods Eng., 24, 263-270 (1987)

Minagawa, N., White, J.L., "Co-Extrusion of Unfilled and TiO_2-Filled Polyethylene: Influence of Viscosity and Die Cross-Section on Interface Shape", Pol. Eng. Sci., 15, 825 (1975)

Mitsoulis, E., "Finite Element Analysis of Two-Dimensional Polymer Melt FLows", Ph.D. Thesis, McMaster University, Hamilton, Ont., Canada (1984)

Mitsoulis, E., "Extrudate Swell in Double-Layer Flows", J. Rheol., 30(S), S23 (1986)

Mitsoulis, E., "Multilayer Sheet Coextrusion: Analysis and Design", Adv. Polym. Techn., 8, 225-242 (1988)

Mitsoulis, E., Heng, F.L., "Numerical Simulation of Coextrusion from a Circular Die", J. of Applied Pol. Sci., 34, 1713-1725 (1987)

Mitsoulis, E., Vlachopoulos, J., and Mirza, F.A., "Simulation of Extrudate Swell from Long Slit and Capillary Dies", Pol. Proc. Eng., 2, 153-177 (1984)

Nickell, R.E., Tanner, R.I. and Caswell B., "The Solution of Viscous Incompressible Jet and Free-Surface Flows using Finite-Elemen. Methods", J. Fluid Mech., 65, 189-206 (1974)

OCLCS, "Ontario Centre for Large Scale Computation Course Notes", University of Toronto, Toronto, November 1986

Olson, M.D., Tuann, S.Y., "New finite element results for the square cavity", Computers and Fluids, 7, 123-135 (1979)

Orbach, O., Crowe, C.M., "Convergence Promotion in the Simulation of Chemical Processes with Recycle - the Dominant Eigenvalue Method", Can. J. of Chem. Eng., 49, 509-513 (1971)

Paul, D.R., "Fibers from Polymer Blends", In "Polymer Blends" D.R. Paul, S. Newman, Eds., Volume 2, 167-217, Academic Press (1978)

Phan-Thien, N., "Influence of Wall Slip on Extrudate Swell: A Boundary Element Investigation", J. Non-Newt. Fluid Mech., 26, 327-340 (1988)

Phuoc, H.B., Tanner, R.I., "Thermally-Induced Extrudate Swell", J. Fluid Mech., 98, 253-271 (1980)

Pool, H., "Coextrusion; A Clearly Accepted Polymer Processing Technique", presented at the extruder-Fututre Symposium, Enschede, The Netherlands, August 1987

Ramamurthy, A.V., "Wall slip in Viscous Fluids and Influence of Materials of Construction", J. Rheol., 30, 337 (1986)

Reddy, K.R., Tanner, R.I., "On the Swelling of Extrudate Plane Sheets", J. Rheol., 22, 661 (1978)

Reitemeyer, P.T., "Coextrusionwerkzeuge zum Herstellen von Flachfolien fur den Verpackungsbereich", Kunststoffe, 78, 395-397 (1988)

Reklaitis, G.V., Ravindran, A., Ragsdell, K.M., "Engineering Optimization, Methods and Applications", John Wiley and Sons (1983)

Russell, T.W., Charles, M.E., "The Effect of the Less Viscous Liquid in the Laminar Flow of Two Immiscible Liquids", Can. J. Chem. Eng., 37, 18 (1959)

Russel, T.W., Hodgson, G.W., Govier, G.W., "Horizontal Pipeline Flow of Mixtures of Oil and Water", Can. J. Chem. Eng., 37,9 (1959)

Schenkel, G., Plastics Extrusion Technology and Theory, Elsevier (1966)

Schowalter, W.R., "The Behavior of Complex Fluids at Solid Boundaries", J. Non-Newt. Fluid Mech., 29, 25-36 (1988)

Schrenk, W.J., Alfrey, T. Jr., "Coextruded Multilayer Polymer Films and Sheets", in "Polymer Blends" D.R. Paul, S. Newman, Eds., Volume 1, 129-165, Academic Press (1978)

Schrenk, W.J., Bradley, N.L., Alfrey, T. Jr., Maack, H., "Interfacial Flow Instability in Multilayer Coextrusion", Polym. Eng. Sci., 18, 620-623 (1978)

Schwenzer C., and Menges, G., "Megapus - A Program-Package for the Layout of Extrusion Lines", Proceedings of ANTEC'87 conference, Los Angeles, 109-112 (1987)

Shiojima T., Shimazaki Y., "Three Dimensional Finite Element Analyses for a Maxwell Fluid Using the Penalty Function Method", in "Proceedings of the NUMETA'87", Pande G.N., Middleton J., Eds., Vol. 1, Martinus Nijhoff Publishers, Swansea (1987)

Silliman, W.J., Scriven, L.E., "Separating Flow near a Static Contact Line: Slip at a Wall and Shape of a Free Surface", J. Comput. Phys., 34, 287 (1980)

Sornberger, G., Vergnes, B., Agassant, J.F., "Two Directional Coextrusion Flow of Two Molten Polymers in Flat Dies", Polym. Eng. Sci., 26, 455-460 (1986)

Sornberger, G., Vergnes, B., Agassant, J.F., "Coextrusion Flow of Two Molten Polymers Between Parallel Plates: Non Isothermal Computation and Experimental Study", Pol. Eng. Sci., 26, 682-689 (1986)

Southern, J.H., Ballman, R.L., "Stratified Bicomponent Flow of Polymer Melts in a Tube", Applied Polymer Science, 20, 175-189 (1973)

Southern, J.H., Ballman, R.L., "Additional Observations on Stratified Bicomponent Flow of Polymer Melts in a Tube", J. Polym. Sci., 13, 863-869 (1975)

Southern, J.H., Ballman, R.L., "Preferential Wetting Phenomenon in Bicomponent Polymer Melt Flow", J. Appl. Polym. Sci., 24, 693-701 (1979)

Sugeng, F., Phan-Thien, N., Tanner, R.I., "A Study of Non-Isothermal Non-Newtonian Extrudate Swell by a Mixed Boundary Element and Finite Element Method", J. Rheology, 31, 37-58 (1987)

Tadmor Z., and Gogos C.G., Principles of Polymer Processing, John Wiley & Sons, New York (1979)

Tanner, R.I., Engineering Rheology, Clarendon Press, Oxford (1985)

Tanner, R.I., "The computer simulation of plastics extrusion", Proceedings of the NUMIFORM'86 conference, Gothenburg (1986)

Taylor, C., Hood, P., "A Numerical Solution of the Navier-Stokes Equations Using the Finite Element Technique", Comp. Fluids, 1, 73 (1973)

Taylor, C., Hughes, T.G., "Finite Element Programming of the Navier-Stokes Equations", Pineridge Press Ltd, Swansea(1981)

Than, P.T., Rosso, F., Joseph, D.D., "Instability of Poiseulle Flow of Two Immiscible Liquids with Different Viscosities in a Channel", Int. J. Eng. Sci., 25, 189 (1987)

Tran-Cong, T., and Phan-Thien, N., "Three-Dimensional Study of Extrusion Processes by Boundary Element Method. I. An implementation of high order elements and some Newtonian results", Rheologica Acta, 27, 21-30 (1988a)

Tran-Cong, T., and Phan-Thien, N., "Three-Dimensional Extrusion Processes by Boundary Element Method. II. Extrusion of a viscoelastic fluid", Submitted to Publication in Rheologica Acta, (1988b)

Tran-Cong, T., and Phan-Thien, N., "Die Design by a boundary Element Method", J. Non-Newt. Fluid Mech., 30, 37-46 (1988c)

Uhland, E., "Stratified Two-Phase Flow of Molten Polymers in Circular Dies", Pol. Eng. Sci., 17, 671 (1977)

United States Patent No. 3,557,265, "Method of Extruding Laminates", Chisholm, D.S., Schrenk, W.J., The Dow Chemical Company (1971)

United States Patent No. 3,565,985, "Method of Preparing Multilayer Plastic Articles", Schrenk, W.J., Chisholm, D.S., Cleereman, K.J., Alfrey, T., Jr., The Dow Chemical Company (1971)

Vlcek, J., Vlachopoulos, J., "Effect of Die Wall Cooling or Heating on Extrudate Swell", to appear in Pol. Eng. Sci. (1989)

Waters, N.D., "The Stability of Two Stratified "Power-Law" Liquids in Couette Flow", J. Non-Newt. Fluid Mech., 12, 83 (1983)

Weatherburn, C.E., "Differential Geometry of Three Dimensions", Cambridge University Press, Cambridge (1927)

Wesson, R.D., Papanastasiou, T.C., "Flow Singularity and Slip Velocity in Plane Extrudate Swell Computations", J. Non-Newt. Fluid Mech., 26, 277-295 (1988)

Wheeler, J.A., Wissler, E.H., "The friction factor-Reynolds number relation for the steady flow at pseudoplastic fluids through rectangular ducts", AIChE J., 11, 207-212 (1965)

White, J.L. and Huang D., "Extrudate Swell and Extrusion Pressure Loss of Polymer Melts Flowing through Rectangular and Trapezoidal Dies", Pol. Eng. Sci., 21, 1101-1107 (1981)

White, J.L., Ide, Y., "Rheology and Dynamics of Fiber Formation from Polymer Melts", Appl. Pol. Symposium, 27, 61-102 (1975)

White, J.L., Lee, B.L., "Theory of Interface Distortion in Stratified Two- Phase Flow", Trans. Soc. Rheol., 19, 457-479 (1975)

White, J.L., Lee, B.L., "An Experimental Study of Sandwich Injection Molding of Two Polymer Melts Using Simultaneous Injection", Polym. Eng. Sci., 15, 481- 485 (1975)

White, J.L., Ufford, R.C., Dharod, K.R., Price, R.L., "Experimental and Theoretical Study of the Extrusion of Two-Phase Molten Polymer Systems", J. Appl. Pol. Sci., 16, 1313 (1972)

White, R.E., "An Introduction to the Finite Element Method with Applications to Nonlinear Problems", Wiley, New York, 1985.

Williams, M.C., "Migration of Two Liquid Phases in Capillary Extrusion : An Energy Interpretation", AIChE J., 21, 1204 (1975)

Wong, W.T., Jeng, C.C., "The Stability of Tow Concentric Non-Newtonian Fluids in Circular Pipe Flow", J. Non-Newt. Fluid Mech., 22, 359-380 (1987)

Yeh, P.W., Kim-E, M.E., Armstrong, R.C., Brown, R.A., "Multiple Solutions in the Calculation of Axisymmetric Contraction Flow of an Upper Convevected Fluid", J. Non-Newt. Fluid Mech., 16, 173 (1984)

Yih, C.S., "Instability Due to Viscosity Stratification", J. Fluid Mech., 27, 337 (1967)

Yu, H.S., Sparrow, E.M., "Stratified Laminar Flow in Ducts of Arbitrary Shape", AIChE J., 13, 10 (1967)

Yu, H.S., Sparrow, E.M., "Experiments on Two-Component Stratified Flow in a Horizontal Duct", J. Heat Transfer, 91, 51 (1969)

Yu, T.C., Han, C.D., "Stratified Two-Phase Flow of Molten Polymers", J. Appl. Pol. Sci., 17, 1203 (1973)

Zienkiewicz, O.C., "The Finite Element Method", 3rd Edition, McGraw-Hill, New York (1977)

APPENDIX A

THE FINITE ELEMENT EQUATIONS FOR 3-DIMENSIONAL NON-ISOTHERMAL u–v–w–p–h–T FORMULATION OF FREE SURFACE FLOW

In section 2.3.2, the Galerkin weighted residual equations for u–v–w–p–h–T formulation of non-isothermal free surface flow were derived (eqs. 2.21–2.26).

The Finite Element basis functions $N^i(\xi, \eta, \zeta)$ and $N_p^i(\xi, \eta, \zeta)$ are defined in terms of the local coordinates ξ–η–ζ over the parent element onto which the deformed element is mapped isoparametrically. The explicit form of the finite element basis functions and their derivatives w.r.t. the local system of coordinates ξ–η–ζ are shown in Tables A.1 and A.2 for the 18-node ad 27-node elements respectively.

The Galerkin weighted residual equations and Jacobian entries are listed in Table A.3.

Table A.1 Basis functions and derivatives for 18-node element

Quadratic shape functions

$N^1 = (1-3\,\eta-3\,\zeta+2\,\eta^2+4\,\eta\,\zeta+2\,\zeta^2)\,(-\xi\,(1-\xi)/2)$
$N^2 = (1-3\,\eta-3\,\zeta+2\,\eta^2+4\,\eta\,\zeta+2\,\zeta^2)\,(1-\xi^2)$
$N^3 = (1-3\,\eta-3\,\zeta+2\,\eta^2+4\,\eta\,\zeta+2\,\zeta^2)\,(\xi\,(1+\xi)/2)$
$N^4 = 4\,(\eta-\eta^2-\eta\,\zeta)\,(-\xi\,(1-\xi)/2)$
$N^5 = 4\,(\eta-\eta^2-\eta\,\zeta)\,(1-\xi^2)$
$N^6 = 4\,(\eta-\eta^2-\eta\,\zeta)\,(\xi\,(1+\xi)/2)$
$N^7 = (2\,\eta^2-\eta)\,(-\xi\,(1-\xi)/2)$
$N^8 = (2\,\eta^2-\eta)\,(1-\xi^2)$
$N^9 = (2\,\eta^2-\eta)\,(\xi\,(1+\xi)/2)$
$N^{10} = 4\,(\zeta-\eta\,\zeta-\zeta^2)\,(-\xi\,(1-\xi)/2)$
$N^{11} = 4\,(\zeta-\eta\,\zeta-\zeta^2)\,(1-\xi^2)$
$N^{12} = 4\,(\zeta-\eta\,\zeta-\zeta^2)\,(\xi\,(1+\xi)/2)$
$N^{13} = 4\,\eta\,\zeta\,(-\xi\,(1-\xi)/2)$
$N^{14} = 4\,\eta\,\zeta\,(1-\xi^2)$
$N^{15} = 4\,\eta\,\zeta\,(\xi\,(1+\xi)/2)$
$N^{16} = (2\,\zeta^2-\zeta)\,(-\xi\,(1-\xi)/2)$
$N^{17} = (2\,\zeta^2-\zeta)\,(1-\xi^2)$
$N^{18} = (2\,\zeta^2-\zeta)\,(\xi\,(1+\xi)/2)$

Derivatives w.r.t. ξ

$N_\xi^1 = (1-3\,\eta-3\,\zeta+2\,\eta^2+4\,\eta\,\zeta+2\,\zeta^2)\,(-(1-2\,\xi)/2)$
$N_\xi^2 = (1-3\,\eta-3\,\zeta+2\,\eta^2+4\,\eta\,\zeta+2\,\zeta^2)\,(-2\,\xi)$
$N_\xi^3 = (1-3\,\eta-3\,\zeta+2\,\eta^2+4\,\eta\,\zeta+2\,\zeta^2)\,((1+2\,\xi)/2)$
$N_\xi^4 = (-(1-2\,\xi)/2)\,4\,(\eta-\eta^2-\eta\,\zeta)$
$N_\xi^5 = (-2\,\xi)\,4\,(\eta-\eta^2-\eta\,\zeta)$
$N_\xi^6 = ((1+2\,\xi)/2)\,4\,(\eta-\eta^2-\eta\,\zeta)$
$N_\xi^7 = (-(1-2\,\xi)/2)\,(2\,\eta^2-\eta)$
$N_\xi^8 = (-2\,\xi)\,(2\,\eta^2-\eta)$
$N_\xi^9 = ((1+2\,\xi)/2)\,(2\,\eta^2-\eta)$
$N_\xi^{10} = (-(1-2\,\xi)/2)\,4\,(\zeta-\eta\,\zeta-\zeta^2)$
$N_\xi^{11} = (-2\,\xi)\,4\,(\zeta-\eta\,\zeta-\zeta^2)$
$N_\xi^{12} = ((1+2\,\xi)/2)\,4\,(\zeta-\eta\,\zeta-\zeta^2)$
$N_\xi^{13} = (-(1-2\,\xi)/2)\,4\,\eta\,\zeta$
$N_\xi^{14} = (-2\,\xi)\,4\,\eta\,\zeta$
$N_\xi^{15} = ((1+2\,\xi)/2)\,4\,\eta\,\zeta$
$N_\xi^{16} = (-(1-2\,\xi)/2)\,(2\,\zeta^2-\zeta)$
$N_\xi^{17} = (-2\,\xi)\,(2\,\zeta^2-\zeta)$
$N_\xi^{18} = ((1+2\,\xi)/2)\,(2\,\zeta^2-\zeta)$

Table A.1 (continued)

Derivatives w.r.t. η

$N_\eta^1 = (-3+4\eta+4\zeta)(-\xi(1-\xi)/2)$
$N_\eta^2 = (-3+4\eta+4\zeta)(1-\xi^2)$
$N_\eta^3 = (-3+4\eta+4\zeta)(\xi(1+\xi)/2)$
$N_\eta^4 = 4(1-2\eta-\zeta)(-\xi(1-\xi)/2)$
$N_\eta^5 = 4(1-2\eta-\zeta)(1-\xi^2)$
$N_\eta^6 = 4(1-2\eta-\zeta)(\xi(1+\xi)/2)$
$N_\eta^7 = (-1+4\eta)(-\xi(1-\xi)/2)$
$N_\eta^8 = (-1+4\eta)(1-\xi^2)$
$N_\eta^9 = (-1+4\eta)(\xi(1+\xi)/2)$
$N_\eta^{10} = -4\zeta(-\xi(1-\xi)/2)$
$N_\eta^{11} = -4\zeta(1-\xi^2)$
$N_\eta^{12} = -4\zeta(\xi(1+\xi)/2)$
$N_\eta^{13} = 4\zeta(-\xi(1-\xi)/2)$
$N_\eta^{14} = 4\zeta(1-\xi^2)$
$N_\eta^{15} = 4\zeta(\xi(1+\xi)/2)$
$N_\eta^{16} = 0$
$N_\eta^{17} = 0$
$N_\eta^{18} = 0$

Derivatives w.r.t. ζ

$N_\zeta^1 = (-3+4\eta+4\zeta)(-\xi(1-\xi)/2)$
$N_\zeta^2 = (-3+4\eta+4\zeta)(1-\xi^2)$
$N_\zeta^3 = (-3+4\eta+4\zeta)(\xi(1+\xi)/2)$
$N_\zeta^4 = -4\eta(-\xi(1-\xi)/2)$
$N_\zeta^5 = -4\eta(1-\xi^2)$
$N_\zeta^6 = -4\eta(\xi(1+\xi)/2)$
$N_\zeta^7 = 0$
$N_\zeta^8 = 0$
$N_\zeta^9 = 0$
$N_\zeta^{10} = 4(1-\eta-2\zeta)(-\xi(1-\xi)/2)$
$N_\zeta^{11} = 4(1-\eta-2\zeta)(1-\xi^2)$
$N_\zeta^{12} = 4(1-\eta-2\zeta)(\xi(1+\xi)/2)$
$N_\zeta^{13} = 4\eta(-\xi(1-\xi)/2)$
$N_\zeta^{14} = 4\eta(1-\xi^2)$
$N_\zeta^{15} = 4\eta(\xi(1+\xi)/2)$
$N_\zeta^{16} = (-1+4\zeta)(-\xi(1-\xi)/2)$
$N_\zeta^{17} = (-1+4\zeta)(1-\xi^2)$
$N_\zeta^{18} = (-1+4\zeta)(\xi(1+\xi)/2)$

Table A.1 (continued)

Linear shape functions

$Np^1 = (1-\eta-\zeta)\,(1-\xi)/2$
$Np^3 = (1-\eta-\zeta)\,(1+\xi)/2$
$Np^7 = \eta\,(1-\xi)/2$
$Np^9 = \eta\,(1+\xi)/2$
$Np^{16} = \zeta\,(1-\xi)/2$
$Np^{18} = \zeta\,(1+\xi)/2$

Table A.2 Basis functions and derivatives for 27-node element

Quadratic basis functions

$N^1 = -\xi\,\eta\,\zeta\,(1-\xi)\,(1-\eta)\,(1-\zeta)/8$
$N^2 = \eta\,\zeta\,(1-\xi^2)\,(1-\eta)\,(1-\zeta)/4$
$N^3 = \xi\,\eta\,\zeta\,(1+\xi)\,(1-\eta)\,(1-\zeta)/8$
$N^4 = \xi\,\zeta\,(1-\xi)\,(1-\eta^2)\,(1-\zeta)/4$
$N^5 = -\zeta\,(1-\xi^2)\,(1-\eta^2)\,(1-\zeta)/2$
$N^6 = -\xi\,\zeta\,(1+\xi)\,(1-\eta^2)\,(1-\zeta)/4$
$N^7 = \xi\,\eta\,\zeta\,(1-\xi)\,(1+\eta)\,(1-\zeta)/8$
$N^8 = -\eta\,\zeta\,(1-\xi^2)\,(1+\eta)\,(1-\zeta)/4$
$N^9 = -\xi\,\eta\,\zeta\,(1+\xi)\,(1+\eta)\,(1-\zeta)/8$
$N^{10} = \xi\,\eta\,(1-\xi)\,(1-\eta)\,(1-\zeta^2)/4$
$N^{11} = -\eta\,(1-\xi^2)\,(1-\eta)\,(1-\zeta^2)/2$
$N^{12} = -\xi\,\eta\,(1+\xi)\,(1-\eta)\,(1-\zeta^2)/4$
$N^{13} = -\xi\,(1-\xi)\,(1-\eta^2)\,(1-\zeta^2)/2$
$N^{14} = (1-\xi^2)\,(1-\eta^2)\,(1-\zeta^2)$
$N^{15} = \xi\,(1+\xi)\,(1-\eta^2)\,(1-\zeta^2)/2$
$N^{16} = -\xi\,\eta\,(1-\xi)\,(1+\eta)\,(1-\zeta^2)/4$
$N^{17} = \eta\,(1-\xi^2)\,(1+\eta)\,(1-\zeta^2)/2$
$N^{18} = \xi\,\eta\,(1+\xi)\,(1+\eta)\,(1-\zeta^2)/4$
$N^{19} = \xi\,\eta\,\zeta\,(1-\xi)\,(1-\eta)\,(1+\zeta)/8$
$N^{20} = -\eta\,\zeta\,(1-\xi^2)\,(1-\eta)\,(1+\zeta)/4$
$N^{21} = -\xi\,\eta\,\zeta\,(1+\xi)\,(1-\eta)\,(1+\zeta)/8$
$N^{22} = -\xi\,\zeta\,(1-\xi)\,(1-\eta^2)\,(1+\zeta)/4$
$N^{23} = \zeta\,(1-\xi^2)\,(1-\eta^2)\,(1+\zeta)/2$
$N^{24} = \xi\,\zeta\,(1+\xi)\,(1-\eta^2)\,(1+\zeta)/4$
$N^{25} = -\xi\,\eta\,\zeta\,(1-\xi)\,(1+\eta)\,(1+\zeta)/8$
$N^{26} = \eta\,\zeta\,(1-\xi^2)\,(1+\eta)\,(1+\zeta)/4$
$N^{27} = \xi\,\eta\,\zeta\,(1+\xi)\,(1+\eta)\,(1+\zeta)/8$

Table A.2 (continued)

Derivatives w.r.t. ξ

$N_\xi{}^1 = -\eta\,\zeta\,(1-2\,\xi)\,(1-\eta)\,(1-\zeta)/8$
$N_\xi{}^2 = \eta\,\zeta\,(-2\,\xi)\,(1-\eta)\,(1-\zeta)/4$
$N_\xi{}^3 = \eta\,\zeta\,(1+2\,\xi)\,(1-\eta)\,(1-\zeta)/8$
$N_\xi{}^4 = \zeta\,(1-2\,\xi)\,(1-\eta^2)\,(1-\zeta)/4$
$N_\xi{}^5 = -\zeta\,(-2\,\xi)\,(1-\eta^2)\,(1-\zeta)/2$
$N_\xi{}^6 = -\zeta\,(1+2\,\xi)\,(1-\eta^2)\,(1-\zeta)/4$
$N_\xi{}^7 = \eta\,\zeta\,(1-2\,\xi)\,(1+\eta)\,(1-\zeta)/8$
$N_\xi{}^8 = -\eta\,\zeta\,(-2\,\xi)\,(1+\eta)\,(1-\zeta)/4$
$N_\xi{}^9 = -\eta\,\zeta\,(1+2\,\xi)\,(1+\eta)\,(1-\zeta)/8$
$N_\xi{}^{10} = \eta\,(1-2\,\xi)\,(1-\eta)\,(1-\zeta^2)/4$
$N_\xi{}^{11} = -\eta\,(-2\,\xi)\,(1-\eta)\,(1-\zeta^2)/2$
$N_\xi{}^{12} = -\eta\,(1+2\,\xi)\,(1-\eta)\,(1-\zeta^2)/4$
$N_\xi{}^{13} = -(1-2\,\xi)\,(1-\eta^2)\,(1-\zeta^2)/2$
$N_\xi{}^{14} = (-2\,\xi)\,(1-\eta^2)\,(1-\zeta^2)$
$N_\xi{}^{15} = (1+2\,\xi)\,(1-\eta^2)\,(1-\zeta^2)/2$
$N_\xi{}^{16} = -\eta\,(1-2\,\xi)\,(1+\eta)\,(1-\zeta^2)/4$
$N_\xi{}^{17} = \eta\,(-2\,\xi)\,(1+\eta)\,(1-\zeta^2)/2$
$N_\xi{}^{18} = \eta\,(1+2\,\xi)\,(1+\eta)\,(1-\zeta^2)/4$
$N_\xi{}^{19} = \eta\,\zeta\,(1-2\,\xi)\,(1-\eta)\,(1+\zeta)/8$
$N_\xi{}^{20} = -\eta\,\zeta\,(-2\,\xi)\,(1-\eta)\,(1+\zeta)/4$
$N_\xi{}^{21} = -\eta\,\zeta\,(1+2\,\xi)\,(1-\eta)\,(1+\zeta)/8$
$N_\xi{}^{22} = -\zeta\,(1-2\,\xi)\,(1-\eta^2)\,(1+\zeta)/4$
$N_\xi{}^{23} = \zeta\,(-2\,\xi)\,(1-\eta^2)\,(1+\zeta)/2$
$N_\xi{}^{24} = \zeta\,(1+2\,\xi)\,(1-\eta^2)\,(1+\zeta)/4$
$N_\xi{}^{25} = -\eta\,\zeta\,(1-2\,\xi)\,(1+\eta)\,(1+\zeta)/8$
$N_\xi{}^{26} = \eta\,\zeta\,(-2\,\xi)\,(1+\eta)\,(1+\zeta)/4$
$N_\xi{}^{27} = \eta\,\zeta\,(1+2\,\xi)\,(1+\eta)\,(1+\zeta)/8$

Table A.2 (continued)

Derivatives w.r.t. η

$N_\eta{}^1 = -\xi\,\zeta\,(1-\xi)\,(1-2\,\eta)\,(1-\zeta)/8$
$N_\eta{}^2 = \zeta\,(1-\xi^2)\,(1-2\,\eta)\,(1-\zeta)/4$
$N_\eta{}^3 = \xi\,\zeta\,(1+\xi)\,(1-2\,\eta)\,(1-\zeta)/8$
$N_\eta{}^4 = \xi\,\zeta\,(1-\xi)\,(-2\,\eta)\,(1-\zeta)/4$
$N_\eta{}^5 = -\zeta\,(1-\xi^2)\,(-2\,\eta)\,(1-\zeta)/2$
$N_\eta{}^6 = -\xi\,\zeta\,(1+\xi)\,(-2\,\eta)\,(1-\zeta)/4$
$N_\eta{}^7 = \xi\,\zeta\,(1-\xi)\,(1+2\,\eta)\,(1-\zeta)/8$
$N_\eta{}^8 = -\zeta\,(1-\xi^2)\,(1+2\,\eta)\,(1-\zeta)/4$
$N_\eta{}^9 = -\xi\,\zeta\,(1+\xi)\,(1+2\,\eta)\,(1-\zeta)/8$
$N_\eta{}^{10} = \xi\,(1-\xi)\,(1-2\,\eta)\,(1-\zeta^2)/4$
$N_\eta{}^{11} = -(1-\xi^2)\,(1-2\,\eta)\,(1-\zeta^2)/2$
$N_\eta{}^{12} = -\xi\,(1+\xi)\,(1-2\,\eta)\,(1-\zeta^2)/4$
$N_\eta{}^{13} = -\xi\,(1-\xi)\,(-2\,\eta)\,(1-\zeta^2)/2$
$N_\eta{}^{14} = (1-\xi^2)\,(-2\,\eta)\,(1-\zeta^2)$
$N_\eta{}^{15} = \xi\,(1+\xi)\,(-2\,\eta)\,(1-\zeta^2)/2$
$N_\eta{}^{16} = -\xi\,(1-\xi)\,(1+2\,\eta)\,(1-\zeta^2)/4$
$N_\eta{}^{17} = (1-\xi^2)\,(1+2\,\eta)\,(1-\zeta^2)/2$
$N_\eta{}^{18} = \xi\,(1+\xi)\,(1+2\,\eta)\,(1-\zeta^2)/4$
$N_\eta{}^{19} = \xi\,\zeta\,(1-\xi)\,(1-2\,\eta)\,(1+\zeta)/8$
$N_\eta{}^{20} = -\zeta\,(1-\xi^2)\,(1-2\,\eta)\,(1+\zeta)/4$
$N_\eta{}^{21} = -\xi\,\zeta\,(1+\xi)\,(1-2\,\eta)\,(1+\zeta)/8$
$N_\eta{}^{22} = -\xi\,\zeta\,(1-\xi)\,(-2\,\eta)\,(1+\zeta)/4$
$N_\eta{}^{23} = \zeta\,(1-\xi^2)\,(-2\,\eta)\,(1+\zeta)/2$
$N_\eta{}^{24} = \xi\,\zeta\,(1+\xi)\,(-2\,\eta)\,(1+\zeta)/4$
$N_\eta{}^{25} = -\xi\,\zeta\,(1-\xi)\,(1+2\,\eta)\,(1+\zeta)/8$
$N_\eta{}^{26} = \zeta\,(1-\xi^2)\,(1+2\,\eta)\,(1+\zeta)/4$
$N_\eta{}^{27} = \xi\,\zeta\,(1+\xi)\,(1+2\,\eta)\,(1+\zeta)/8$

Table A.2 (continued)

Derivatives w.r.t. ζ

$N_\zeta^1 = -\xi\,\eta\,(1-\xi)\,(1-\eta)\,(1-2\,\zeta)/8$
$N_\zeta^2 = \eta\,(1-\xi^2)\,(1-\eta)\,(1-2\,\zeta)/4$
$N_\zeta^3 = \xi\,\eta\,(1+\xi)\,(1-\eta)\,(1-2\,\zeta)/8$
$N_\zeta^4 = \xi\,(1-\xi)\,(1-\eta^2)\,(1-2\,\zeta)/4$
$N_\zeta^5 = -(1-\xi^2)\,(1-\eta^2)\,(1-2\,\zeta)/2$
$N_\zeta^6 = -\xi\,(1+\xi)\,(1-\eta^2)\,(1-2\,\zeta)/4$
$N_\zeta^7 = \xi\,\eta\,(1-\xi)\,(1+\eta)\,(1-2\,\zeta)/8$
$N_\zeta^8 = -\eta\,(1-\xi^2)\,(1+\eta)\,(1-2\,\zeta)/4$
$N_\zeta^9 = -\xi\,\eta\,(1+\xi)\,(1+\eta)\,(1-2\,\zeta)/8$
$N_\zeta^{10} = \xi\,\eta\,(1-\xi)\,(1-\eta)\,(-2\,\zeta)/4$
$N_\zeta^{11} = -\eta\,(1-\xi^2)\,(1-\eta)\,(-2\,\zeta)/2$
$N_\zeta^{12} = -\xi\,\eta\,(1+\xi)\,(1-\eta)\,(-2\,\zeta)/4$
$N_\zeta^{13} = -\xi\,(1-\xi)\,(1-\eta^2)\,(-2\,\zeta)/2$
$N_\zeta^{14} = (1-\xi^2)\,(1-\eta^2)\,(-2\,\zeta)$
$N_\zeta^{15} = \xi\,(1+\xi)\,(1-\eta^2)\,(-2\,\zeta)/2$
$N_\zeta^{16} = -\xi\,\eta\,(1-\xi)\,(1+\eta)\,(-2\,\zeta)/4$
$N_\zeta^{17} = \eta\,(1-\xi^2)\,(1+\eta)\,(-2\,\zeta)/2$
$N_\zeta^{18} = \xi\,\eta\,(1+\xi)\,(1+\eta)\,(-2\,\zeta)/4$
$N_\zeta^{19} = \xi\,\eta\,(1-\xi)\,(1-\eta)\,(1+2\,\zeta)/8$
$N_\zeta^{20} = -\eta\,(1-\xi^2)\,(1-\eta)\,(1+2\,\zeta)/4$
$N_\zeta^{21} = -\xi\,\eta\,(1+\xi)\,(1-\eta)\,(1+2\,\zeta)/8$
$N_\zeta^{22} = -\xi\,(1-\xi)\,(1-\eta^2)\,(1+2\,\zeta)/4$
$N_\zeta^{23} = (1-\xi^2)\,(1-\eta^2)\,(1+2\,\zeta)/2$
$N_\zeta^{24} = \xi\,(1+\xi)\,(1-\eta^2)\,(1+2\,\zeta)/4$
$N_\zeta^{25} = -\xi\,\eta\,(1-\xi)\,(1+\eta)\,(1+2\,\zeta)/8$
$N_\zeta^{26} = \eta\,(1-\xi^2)\,(1+\eta)\,(1+2\,\zeta)/4$
$N_\zeta^{27} = \xi\,\eta\,(1+\xi)\,(1+\eta)\,(1+2\,\zeta)/8$

Linear basis functions

$Np^1 = (1-\xi)\,(1-\eta)\,(1-\zeta)/8$
$Np^3 = (1+\xi)\,(1-\eta)\,(1-\zeta)/8$
$Np^7 = (1-\xi)\,(1+\eta)\,(1-\zeta)/8$
$Np^9 = (1+\xi)\,(1+\eta)\,(1-\zeta)/8$
$Np^{19} = (1-\xi)\,(1-r_i)\,(1+\zeta)/8$
$Np^{21} = (1+\xi)\,(1-\eta)\,(1+\zeta)/8$
$Np^{25} = (1-\xi)\,(1+\eta)\,(1+\zeta)/8$
$Np^{27} = (1+\xi)\,(1+\eta)\,(1+\zeta)/8$

Table A.3 Jacobian Entries in u–v–w–p–h–T formulation of free surface flow

Preliminary definitions

$$u = \sum_i N^i u^i, \quad v = \sum_i N^i v^i, \quad w = \sum_i N^i w^i, \quad P = \sum_i N_p^i P^i, \quad T = \sum_i N^i T^i$$

$$x = \sum_i N^i x^i, \quad y = \sum_i N^i y^i, \quad z = \sum_i N^i z^i$$

$$u_\xi = \sum_i N_\xi^i u^i, \quad v_\xi = \sum_i N_\xi^i v^i, \quad w_\xi = \sum_i N_\xi^i w^i, \quad T_\xi = \sum_i N_\xi^i T^i$$

$$x_\xi = \sum_i N_\xi^i x^i, \quad y_\xi = \sum_i N_\xi^i y^i, \quad z_\xi = \sum_i N_\xi^i z^i$$

same w.r.t. η, ζ

$$|J| = x_\xi y_\eta z_\zeta + y_\xi z_\eta x_\zeta + z_\xi x_\eta y_\zeta - x_\zeta y_\eta z_\xi - y_\zeta z_\eta x_\xi - z_\zeta x_\eta y_\xi$$

$$A11 = y_\eta z_\zeta - y_\zeta z_\eta$$

$$A12 = -(x_\eta z_\zeta - x_\zeta z_\eta)$$

$$A13 = x_\eta y_\zeta - x_\zeta y_\eta$$

$$A21 = -(y_\xi z_\zeta - y_\zeta z_\xi)$$

$$A22 = x_\xi z_\zeta - x_\zeta z_\xi$$

$$A23 = -(x_\xi y_\zeta - x_\zeta y_\xi)$$

$$A31 = y_\xi z_\eta - y_\eta z_\xi$$

$$A32 = -(x_\xi z_\eta - x_\eta z_\xi)$$

$$A33 = x_\xi y_\eta - x_\eta y_\xi$$

Table A.3 (continued)

$$N^i_x = (N^i_\xi A11 + N^i_\eta A21 + N^i_\zeta A31)/|J|$$

$$N^i_y = (N^i_\xi A12 + N^i_\eta A22 + N^i_\zeta A32)/|J|$$

$$N^i_z = (N^i_\xi A13 + N^i_\eta A23 + N^i_\zeta A33)/|J|$$

$$u_x = \sum_i N^i_x u^i, \qquad v_x = \sum_i N^i_x v^i, \qquad w_x = \sum_i N^i_x w^i, \qquad T_x = \sum_i N^i_x T^i$$

same w.r.t. y , z

$$\mu = \mu_w(|\dot{\gamma}|)e(-\alpha T)$$

$$\frac{\partial \mu}{\partial T^i} = -\alpha \mu N^i$$

$$|\dot{\gamma}| = [2u_x^2 + 2v_y^2 + 2w_z^2 + (u_y + v_x)^2 + (u_z + w_x)^2 + (v_z + w_y)^2)^{1/2}$$

$$\frac{\partial \mu}{\partial u^j} = \frac{\partial \mu}{\partial |\dot{\gamma}|}[2u_x N^i_x + (u_y + v_x)N^i_y + (u_z + w_x)N^i_z]\frac{1}{|\dot{\gamma}|}$$

$$\frac{\partial \mu}{\partial v^j} = \frac{\partial \mu}{\partial |\dot{\gamma}|}[(u_y + v_x)N^i_x + 2v_y N^i_y + (v_z + w_y)N^i_z]\frac{1}{|\dot{\gamma}|}$$

$$\frac{\partial \mu}{\partial w^j} = \frac{\partial \mu}{\partial |\dot{\gamma}|}[(u_z + w_x)N^i_x + (v_z + w_y)N^i_y + 2w_z N^i_z]\frac{1}{|\dot{\gamma}|}$$

$$n_1 = y_\xi z_\zeta - y_\zeta z_\xi$$

$$n_2 = x_\zeta z_\xi - x_\xi z_\zeta$$

$$n_3 = x_\xi y_\zeta - x_\zeta y_\xi$$

where n_1, n_2, n_3 are the components of the outward normal vector to the free surface.

$$|J^*| = (n_1^2 + n_2^2 + n_3^2)^{1/2}$$

Table A.3 (continued)

x-Momentum Equation

$$R_x^i = \int_{-1}^{1}\int_{-1}^{1}\int_{-1}^{1} \{(-P+2\mu u_x)N_x^i + \mu(u_y+v_x)N_y^i + \mu(u_z+w_x)N_z^i\}|J|\,d\xi d\eta d\zeta$$

$$\frac{\partial R_x^i}{\partial u^j} = \int_{-1}^{1}\int_{-1}^{1}\int_{-1}^{1} \left\{\mu(2N_x^iN_x^j + N_y^iN_y^j + N_z^iN_z^j) + [2u_xN_x^i + (u_y+v_x)N_y^i + (u_z+w_x)N_z^i]\frac{\partial \mu}{\partial u^j}\right\}|J|\,d\xi d\eta d\zeta$$

$$\frac{\partial R_x^i}{\partial v^j} = \int_{-1}^{1}\int_{-1}^{1}\int_{-1}^{1} \left\{\mu N_y^iN_x^j + [2u_xN_x^i + (u_y+v_x)N_y^i + (u_z+w_x)N_z^i]\frac{\partial \mu}{\partial v^j}\right\}|J|\,d\xi d\eta d\zeta$$

$$\frac{\partial R_x^i}{\partial w^j} = \int_{-1}^{1}\int_{-1}^{1}\int_{-1}^{1} \left\{\mu N_z^iN_x^j + [2u_xN_x^i + (u_y+v_x)N_y^i + (u_z+w_x)N_z^i]\frac{\partial \mu}{\partial w^j}\right\}|J|\,d\xi d\eta d\zeta$$

$$\frac{\partial R_x^i}{\partial P^j} = \int_{-1}^{1}\int_{-1}^{1}\int_{-1}^{1} \{-N_x^iN_p^j\}|J|\,d\xi d\eta d\zeta$$

$$\frac{\partial R_x^i}{\partial T^j} = \int_{-1}^{1}\int_{-1}^{1}\int_{-1}^{1} \left\{[2u_xN_x^i + (u_y+v_x)N_y^i + (u_z+w_x)N_z^i]\frac{\partial \mu}{\partial T^j}\right\}|J|\,d\xi d\eta d\zeta$$

Table A.3 (continued)

y-Momentum Equation

$$R_y^i = \int_{-1}^{1}\int_{-1}^{1}\int_{-1}^{1} \{\mu(u_y + v_x)N_x^i + (-P + 2\mu v_y)N_y^i + \mu(v_z + w_y)N_z^i\}|J|\, d\xi d\eta d\zeta$$

$$\frac{\partial R_y^i}{\partial u^j} = \int_{-1}^{1}\int_{-1}^{1}\int_{-1}^{1} \left\{\mu N_x^i N_y^j + [(u_y + v_x)N_x^i + 2v_y N_y^i + (v_z + w_y)N_z^i]\frac{\partial \mu}{\partial u^j}\right\}|J|\, d\xi d\eta d\zeta$$

$$\frac{\partial R_y^i}{\partial v^j} = \int_{-1}^{1}\int_{-1}^{1}\int_{-1}^{1} \left\{\mu(N_x^i N_x^j + 2N_y^i N_y^j + N_z^i N_z^j) + [(u_y + v_x)N_x^i + 2v_y N_y^i + (v_z + w_y)N_z^i]\frac{\partial \mu}{\partial v^j}\right\}|J|\, d\xi d\eta d\zeta$$

$$\frac{\partial R_y^i}{\partial w^j} = \int_{-1}^{1}\int_{-1}^{1}\int_{-1}^{1} \left\{\mu N_z^i N_y^j + [(u_y + v_x)N_x^i + 2v_y N_y^i + (v_z + w_y)N_z^i]\frac{\partial \mu}{\partial w^j}\right\}|J|\, d\xi d\eta d\zeta$$

$$\frac{\partial R_y^i}{\partial P^j} = \int_{-1}^{1}\int_{-1}^{1}\int_{-1}^{1} \{-N_y^i N_p^j\}|J|\, d\xi d\eta d\zeta$$

$$\frac{\partial R_y^i}{\partial T^j} = \int_{-1}^{1}\int_{-1}^{1}\int_{-1}^{1} \left\{[(u_y + v_x)N_x^i + 2v_y N_y^i + (v_z + w_y)N_z^i]\frac{\partial \mu}{\partial T^j}\right\}|J|\, d\xi d\eta d\zeta$$

Table A.3 (continued)

z-Momentum Equation

$$R_z^i = \int_{-1}^{1}\int_{-1}^{1}\int_{-1}^{1} \{\mu(u_z + w_x)N_x^i + \mu(v_z + w_y)N_y^i + (-P + 2\mu w_z)N_z^i\}|J|\, d\xi d\eta d\zeta$$

$$\frac{\partial R_z^i}{\partial u^j} = \int_{-1}^{1}\int_{-1}^{1}\int_{-1}^{1} \left\{\mu N_y^i N_z^j + [(u_z + w_x)N_x^i + (v_z + w_y)N_y^i + 2w_z N_z^i]\frac{\partial \mu}{\partial u^j}\right\}|J|\, d\xi d\eta d\zeta$$

$$\frac{\partial R_z^i}{\partial v^j} = \int_{-1}^{1}\int_{-1}^{1}\int_{-1}^{1} \left\{\mu N_y^i N_z^j + [(u_z + w_x)N_x^i + (v_z + w_y)N_y^i + 2w_z N_z^i]\frac{\partial \mu}{\partial v^j}\right\}|J|\, d\xi d\eta d\zeta$$

$$\frac{\partial R_z^i}{\partial w^j} = \int_{-1}^{1}\int_{-1}^{1}\int_{-1}^{1} \left\{\mu(N_x^i N_x^j + N_y^i N_y^j + N_z^i N_z^j) + [(u_z + w_x)N_x^i + (v_z + w_y)N_y^i + 2w_z N_z^i]\frac{\partial \mu}{\partial w^j}\right\}|J|\, d\xi d\eta d\zeta$$

$$\frac{\partial R_z^i}{\partial P^j} = \int_{-1}^{1}\int_{-1}^{1}\int_{-1}^{1} \{-N_z^i N_p^j\}|J|\, d\xi d\eta d\zeta$$

$$\frac{\partial R_z^i}{\partial T^j} = \int_{-1}^{1}\int_{-1}^{1}\int_{-1}^{1} \left\{[(u_z + w_x)N_x^i + (v_z + w_y)N_y^i + 2w_z N_z^i]\frac{\partial \mu}{\partial T^j}\right\}|J|\, d\xi d\eta d\zeta$$

Table A.3 (continued)

Continuity Equation

$$R_c^i = \int_{-1}^{1}\int_{-1}^{1}\int_{-1}^{1} \{u_x + v_y + w_z\} N_p^i |J| \, d\xi d\eta d\zeta$$

$$\frac{\partial R_c^i}{\partial u^j} = \int_{-1}^{1}\int_{-1}^{1}\int_{-1}^{1} \{N_x^j\} N_p^i |J| \, d\xi d\eta d\zeta$$

$$\frac{\partial R_c^i}{\partial v^j} = \int_{-1}^{1}\int_{-1}^{1}\int_{-1}^{1} \{N_y^j\} N_p^i |J| \, d\xi d\eta d\zeta$$

$$\frac{\partial R_c^i}{\partial w^j} = \int_{-1}^{1}\int_{-1}^{1}\int_{-1}^{1} \{N_z^j\} N_p^i |J| \, d\xi d\eta d\zeta$$

Table A.3 (continued)

Energy Equation

$$R_T^i = \int_{-1}^{1}\int_{-1}^{1}\int_{-1}^{1}\Big\{Pe(u\,T_x + v\,T_y + w\,T_z) + (T_x N_x^i + T_y N_y^i + T_z N_z^i)$$

$$- 2Br\,\mu\,(u_x^2 + v_y^2 + w_z^2) - Br\,\mu[(u_y + v_x)^2 + (u_z + w_x)^2 + (v_z + w_y)^2]\Big\}$$

$$\cdot N^i |J|\,d\xi d\eta d\zeta - \int_{-1}^{1}\int_{-1}^{1} Nu(T+1)N^i |J^*|\,d\xi d\zeta,\quad \eta = 1$$

$$\frac{\partial R_T^i}{\partial u^j} = \int_{-1}^{1}\int_{-1}^{1}\int_{-1}^{1}\Big\{Pe\,N^j\,T_x - 4Br\,\mu\,u_x N_x^j - 2Br(u_x^2 + v_y^2 + w_z^2)\frac{\partial \mu}{\partial u^j}$$

$$- Br\,\mu\,[2(u_y + v_x)N_y^j + 2(u_z + w_x)N_z^j] - Br[(u_y + v_x)^2 + (u_z + w_x)^2$$

$$+ (v_z + w_y)^2]\frac{\partial \mu}{\partial u^j}\Big\} N^i |J|\,d\xi d\eta d\zeta$$

$$\frac{\partial R_T^i}{\partial v^j} = \int_{-1}^{1}\int_{-1}^{1}\int_{-1}^{1}\Big\{Pe\,N^j\,T_y - 4Br\,\mu\,v_y N_y^j - 2Br(u_x^2 + v_y^2 + w_z^2)\frac{\partial \mu}{\partial v^j}$$

$$- Br\,\mu[2(u_y + v_x)N_x^j + 2(v_z + w_y)N_z^j] - Br[(u_y + v_x)^2 + (u_z + w_x)^2$$

$$+ (v_z + w_y)^2]\Big\}\frac{\partial \mu}{\partial v^j} N^i |J|\,d\xi d\eta d\zeta$$

$$\frac{\partial R_T^i}{\partial w^j} = \int_{-1}^{1}\int_{-1}^{1}\int_{-1}^{1}\Big\{Pe\,N^j\,T_z - 4Br\,\mu\,w_z N_z^j - 2Br(u_x^2 + v_y^2 + w_z^2)\frac{\partial \mu}{\partial w^j}$$

$$- Br\,\mu[2(u_z + w_x)N_x^j + 2(v_z + w_y)N_y^j] - Br[(u_y + v_x)^2 + (u_z + w_x)^2$$

$$+ (v_z + w_y)^2]\Big\}\frac{\partial \mu}{\partial w^j} N^i |J|\,d\xi d\eta d\zeta$$

Table A.3 (continued)

$$\frac{\partial R_T^i}{\partial T^j} = \int_{-1}^{1}\int_{-1}^{1}\int_{-1}^{1}\left\{Pe(u\,N_x^j + v\,N_y^j + w\,N_z^j) + (N_x^i N_x^j + N_y^i N_y^j + N_z^i N_z^j)\right.$$

$$\left. - 2Br\,(u_x^2 + v_y^2 + w_z^2)\frac{\partial \mu}{\partial T^j} - Br[(u_y + v_x)^2 + (u_z + w_x)^2 + (v_z + w_y)^2]\frac{\partial \mu}{\partial T^j}\right\}$$

$$\cdot N^i |J|\, d\xi d\eta d\zeta - \int_{-1}^{1}\int_{-1}^{1} \{Nu\, N^j\} N^i |J^*|\, d\xi d\zeta, \qquad \eta = 1$$

Table A.3 (continued)

Kinematic Equation

$$R_k^i = \int_{-1}^{1}\int_{-1}^{1} \{n_1 u + n_2 v + n_3 w\}N^i \, d\xi d\zeta, \quad \eta = 1$$

where $n_1 = y_\xi z_\zeta - y_\zeta z_\xi$

$n_2 = x_\zeta z_\xi - x_\xi z_\zeta$

$n_3 = x_\xi y_\zeta - x_\zeta y_\xi$

$$\frac{\partial R_k^i}{\partial u^j} = \int_{-1}^{1}\int_{-1}^{1} \{n_1 N^j\}N^i \, d\xi d\zeta, \quad \eta = 1$$

$$\frac{\partial R_k^i}{\partial v^j} = \int_{-1}^{1}\int_{-1}^{1} \{n_2 N^j\}N^i \, d\xi d\zeta, \quad \eta = 1$$

$$\frac{\partial R_k^i}{\partial w^j} = \int_{-1}^{1}\int_{-1}^{1} \{n_3 N^j\}N^i \, d\xi d\zeta, \quad \eta = 1$$

Table A.3 (continued)

Free Surface Derivatives

$$DJDX^i = \frac{\partial |J|}{\partial x^i} = N^i_\xi y_\eta z_\zeta + y_\xi z_\eta N^i_\zeta + z_\xi N^i_\eta y_\zeta$$

$$- N^i_\zeta y_\eta z_\xi - y_\zeta z_\eta N^i_\xi - z_\zeta N^i_\eta y_\xi$$

$$DJDY^i = \frac{\partial |J|}{\partial y^i} = x_\xi N^i_\eta z_\zeta + N_\xi z_\eta x_\zeta + z_\xi x_\eta N^i_\zeta$$

$$- x_\zeta N^i_\eta z_\xi - N^i_\zeta z_\eta x_\xi - z_\zeta x_\eta N^i_\xi$$

$$DJDZ^i = \frac{\partial |J|}{\partial z^i} = x_\xi y_\eta N^i_\zeta + y_\xi N^i_\eta x_\zeta + N^i_\xi x_\eta y_\zeta$$

$$- x_\zeta y_\eta N^i_\xi - y_\zeta N^i_\eta x_\xi - N^i_\zeta x_\eta y_\xi$$

$$\frac{\partial |J|}{\partial h^i} = \sum_i \left[\frac{\partial |J|}{\partial x^i} \frac{\partial x^i}{\partial h^j} + \frac{\partial |J|}{\partial y^i} \frac{\partial y^i}{\partial h^j} + \frac{\partial |J|}{\partial z^i} \frac{\partial z^i}{\partial h^j} \right]$$

$$= \sum_i \left(DJDX^i \frac{\partial x^i}{\partial h^j} + DJDY^i \frac{\partial y^i}{\partial h^j} + DJDZ^i \frac{\partial z^i}{\partial h^j} \right)$$

$$\frac{\partial x_\xi}{\partial h^j} = \sum_i N^i_\xi \frac{\partial x^i}{\partial h^j}, \qquad \frac{\partial x_\eta}{\partial h^j} = \sum_i N^i_\eta \frac{\partial x^i}{\partial h^j}, \qquad \frac{\partial x_\zeta}{\partial h^j} = \sum_i N^i_\zeta \frac{\partial x^i}{\partial h^j},$$

$$\frac{\partial y_\xi}{\partial h^j} = \sum_i N^i_\xi \frac{\partial y^i}{\partial h^j}, \qquad \frac{\partial y_\eta}{\partial h^j} = \sum_i N^i_\eta \frac{\partial y^i}{\partial h^j}, \qquad \frac{\partial y_\zeta}{\partial h^j} = \sum_i N^i_\zeta \frac{\partial y^i}{\partial h^j},$$

$$\frac{\partial z_\xi}{\partial h^j} = \sum_i N^i_\xi \frac{\partial z^i}{\partial h^j}, \qquad \frac{\partial z_\eta}{\partial h^j} = \sum_i N^i_\eta \frac{\partial z^i}{\partial h^j}, \qquad \frac{\partial z_\zeta}{\partial h^j} = \sum_i N^i_\zeta \frac{\partial z^i}{\partial h^j},$$

Table A.3 (continued)

$$\frac{\partial A11}{\partial h^j} = z_\zeta \frac{\partial y_\eta}{\partial h^j} + y_\eta \frac{\partial z_\zeta}{\partial h^j} - z_\eta \frac{\partial y_\zeta}{\partial h^j} - y_\zeta \frac{\partial z_\eta}{\partial h^j}$$

$$\frac{\partial A12}{\partial h^j} = - z_\zeta \frac{\partial x_\eta}{\partial h^j} - x_\eta \frac{\partial z_\zeta}{\partial h^j} + z_\eta \frac{\partial x_\zeta}{\partial h^j} + x_\zeta \frac{\partial z_\eta}{\partial h^j}$$

$$\frac{\partial A13}{\partial h^j} = y_\zeta \frac{\partial x_\eta}{\partial h^j} + x_\eta \frac{\partial y_\zeta}{\partial h^j} - y_\eta \frac{\partial x_\zeta}{\partial h^j} - x_\zeta \frac{\partial y_\eta}{\partial h^j}$$

$$\frac{\partial A21}{\partial h^j} = -z_\zeta \frac{\partial y_\xi}{\partial h^j} - y_\xi \frac{\partial z_\zeta}{\partial h^j} + z_\xi \frac{\partial y_\zeta}{\partial h^j} + y_\zeta \frac{\partial z_\xi}{\partial h^j}$$

$$\frac{\partial A22}{\partial h^j} = z_\zeta \frac{\partial x_\xi}{\partial h^j} + x_\xi \frac{\partial z_\zeta}{\partial h^j} - z_\xi \frac{\partial x_\zeta}{\partial h^j} - x_\zeta \frac{\partial z_\xi}{\partial h^j}$$

$$\frac{\partial A23}{\partial h^j} = -y_\zeta \frac{\partial x_\xi}{\partial h^j} - x_\xi \frac{\partial y_\zeta}{\partial h^j} + y_\xi \frac{\partial x_\zeta}{\partial h^j} + x_\zeta \frac{\partial y_\xi}{\partial h^j}$$

$$\frac{\partial A31}{\partial h^j} = z_\eta \frac{\partial y_\xi}{\partial h^j} + y_\xi \frac{\partial z_\eta}{\partial h^j} - z_\xi \frac{\partial y_\eta}{\partial h^j} - y_\eta \frac{\partial z_\xi}{\partial h^j}$$

$$\frac{\partial A32}{\partial h^j} = -z_\eta \frac{\partial x_\xi}{\partial h^j} - x_\xi \frac{\partial z_\eta}{\partial h^j} + z_\xi \frac{\partial x_\eta}{\partial h^j} + x_\eta \frac{\partial z_\xi}{\partial h^j}$$

$$\frac{\partial A33}{\partial h^j} = y_\eta \frac{\partial x_\xi}{\partial h^j} + x_\xi \frac{\partial y_\eta}{\partial h^j} - y_\xi \frac{\partial x_\eta}{\partial h^j} - x_\eta \frac{\partial y_\xi}{\partial h^j}$$

Table A.3 (continued)

$$\frac{\partial\left(\frac{A11}{|J|}\right)}{\partial h^j} = \frac{|J|\frac{\partial A11}{\partial h^j} - A11\frac{\partial|J|}{\partial h^j}}{|J|^2}$$

$$\frac{\partial\left(\frac{A12}{|J|}\right)}{\partial h^j} = \frac{|J|\frac{\partial A12}{\partial h^j} - A12\frac{\partial|J|}{\partial h^j}}{|J|^2}$$

$$\frac{\partial\left(\frac{A13}{|J|}\right)}{\partial h^j} = \frac{|J|\frac{\partial A13}{\partial h^j} - A13\frac{\partial|J|}{\partial h^j}}{|J|^2}$$

$$\frac{\partial\left(\frac{A21}{|J|}\right)}{\partial h^j} = \frac{|J|\frac{\partial A21}{\partial h^j} - A21\frac{\partial|J|}{\partial h^j}}{|J|^2}$$

$$\frac{\partial\left(\frac{A22}{|J|}\right)}{\partial h^j} = \frac{|J|\frac{\partial A22}{\partial h^j} - A22\frac{\partial|J|}{\partial h^j}}{|J|^2}$$

$$\frac{\partial\left(\frac{A23}{|J|}\right)}{\partial h^j} = \frac{|J|\frac{\partial A23}{\partial h^j} - A23\frac{\partial|J|}{\partial h^j}}{|J|^2}$$

Table A.3 (continued)

$$\frac{\partial\left(\frac{A31}{|J|}\right)}{\partial h^j} = \frac{|J|\frac{\partial A31}{\partial h^j} - A31\frac{\partial|J|}{\partial h^j}}{|J|^2}$$

$$\frac{\partial\left(\frac{A32}{|J|}\right)}{\partial h^j} = \frac{|J|\frac{\partial A32}{\partial h^j} - A32\frac{\partial|J|}{\partial h^j}}{|J|^2}$$

$$\frac{\partial\left(\frac{A33}{|J|}\right)}{\partial h^j} = \frac{|J|\frac{\partial A33}{\partial h^j} - A33\frac{\partial|J|}{\partial h^j}}{|J|^2}$$

$$\frac{\partial u_x}{\partial h^j} = u_\xi \frac{\partial\left(\frac{A11}{|J|}\right)}{\partial h^j} + u_\eta \frac{\partial\left(\frac{A21}{|J|}\right)}{\partial h^j} + u_\zeta \frac{\partial\left(\frac{A31}{|J|}\right)}{\partial h^j}$$

$$\frac{\partial u_y}{\partial h^j} = u_\xi \frac{\partial\left(\frac{A12}{|J|}\right)}{\partial h^j} + u_\eta \frac{\partial\left(\frac{A22}{|J|}\right)}{\partial h^j} + u_\zeta \frac{\partial\left(\frac{A32}{|J|}\right)}{\partial h^j}$$

$$\frac{\partial u_z}{\partial h^j} = u_\xi \frac{\partial\left(\frac{A13}{|J|}\right)}{\partial h^j} + u_\eta \frac{\partial\left(\frac{A23}{|J|}\right)}{\partial h^j} + u_\zeta \frac{\partial\left(\frac{A33}{|J|}\right)}{\partial h^j}$$

$$\frac{\partial v_x}{\partial h^j} = v_\xi \frac{\partial\left(\frac{A11}{|J|}\right)}{\partial h^j} + v_\eta \frac{\partial\left(\frac{A21}{|J|}\right)}{\partial h^j} + v_\zeta \frac{\partial\left(\frac{A31}{|J|}\right)}{\partial h^j}$$

$$\frac{\partial v_y}{\partial h^j} = v_\xi \frac{\partial\left(\frac{A12}{|J|}\right)}{\partial h^j} + v_\eta \frac{\partial\left(\frac{A22}{|J|}\right)}{\partial h^j} + v_\zeta \frac{\partial\left(\frac{A32}{|J|}\right)}{\partial h^j}$$

$$\frac{\partial v_z}{\partial h^j} = v_\xi \frac{\partial\left(\frac{A13}{|J|}\right)}{\partial h^j} + v_\eta \frac{\partial\left(\frac{A23}{|J|}\right)}{\partial h^j} + v_\zeta \frac{\partial\left(\frac{A33}{|J|}\right)}{\partial h^j}$$

Table A.3 (continued)

$$\frac{\partial w_x}{\partial h^j} = w_\xi \frac{\partial\left(\frac{A11}{|J|}\right)}{\partial h^j} + w_\eta \frac{\partial\left(\frac{A21}{|J|}\right)}{\partial h^j} + w_\zeta \frac{\partial\left(\frac{A31}{|J|}\right)}{\partial h^j}$$

$$\frac{\partial w_y}{\partial h^j} = w_\xi \frac{\partial\left(\frac{A12}{|J|}\right)}{\partial h^j} + w_\eta \frac{\partial\left(\frac{A22}{|J|}\right)}{\partial h^j} + w_\zeta \frac{\partial\left(\frac{A32}{|J|}\right)}{\partial h^j}$$

$$\frac{\partial w_z}{\partial h^j} = w_\xi \frac{\partial\left(\frac{A13}{|J|}\right)}{\partial h^j} + w_\eta \frac{\partial\left(\frac{A23}{|J|}\right)}{\partial h^j} + w_\zeta \frac{\partial\left(\frac{A33}{|J|}\right)}{\partial h^j}$$

$$\frac{\partial T_x}{\partial h^j} = T_\xi \frac{\partial\left(\frac{A11}{|J|}\right)}{\partial h^j} + T_\eta \frac{\partial\left(\frac{A21}{|J|}\right)}{\partial h^j} + T_\zeta \frac{\partial\left(\frac{A31}{|J|}\right)}{\partial h^j}$$

$$\frac{\partial T_y}{\partial h^j} = T_\xi \frac{\partial\left(\frac{A12}{|J|}\right)}{\partial h^j} + T_\eta \frac{\partial\left(\frac{A22}{|J|}\right)}{\partial h^j} + T_\zeta \frac{\partial\left(\frac{A32}{|J|}\right)}{\partial h^j}$$

$$\frac{\partial T_z}{\partial h^j} = T_\xi \frac{\partial\left(\frac{A13}{|J|}\right)}{\partial h^j} + T_\eta \frac{\partial\left(\frac{A23}{|J|}\right)}{\partial h^j} + T_\zeta \frac{\partial\left(\frac{A33}{|J|}\right)}{\partial h^j}$$

$$\text{DNXJDH}^i = \frac{\partial(N_x^i |J|)}{\partial h^j} = N_\xi^i \frac{\partial A11}{\partial h^j} + N_\eta^i \frac{\partial A21}{\partial h^j} + N_\zeta^i \frac{\partial A31}{\partial h^j}$$

$$\text{DNYJDH}^i = \frac{\partial(N_y^i |J|)}{\partial h^j} = N_\xi^i \frac{\partial A12}{\partial h^j} + N_\eta^i \frac{\partial A22}{\partial h^j} + N_\zeta^i \frac{\partial A32}{\partial h^j}$$

$$\text{DNZJDH}^i = \frac{\partial(N_z^i |J|)}{\partial h^j} = N_\xi^i \frac{\partial A13}{\partial h^j} + N_\eta^i \frac{\partial A23}{\partial h^j} + N_\zeta^i \frac{\partial A33}{\partial h^j}$$

Table A.3 (continued)

For shear thinning viscosity

$$\frac{\partial \mu}{\partial h^j} = \frac{\partial \mu}{\partial |\gamma|} \frac{\partial |\gamma|}{\partial h^j}$$

$$\frac{\partial |\gamma|}{\partial h^j} = \left[2u_x \frac{\partial u_x}{\partial h^j} + 2v_y \frac{\partial v_y}{\partial h^j} + 2w_z \frac{\partial w_z}{\partial h^j} + (u_y + v_x)\left(\frac{\partial u_y}{\partial h^j} + \frac{\partial v_x}{\partial h^j} \right) \right.$$

$$\left. + (u_z + w_x)\left(\frac{\partial u_z}{\partial h^j} + \frac{\partial w_x}{\partial h^j} \right) + (v_z + w_y)\left(\frac{\partial v_z}{\partial h^j} + \frac{\partial w_y}{\partial h^j} \right) \right] \frac{1}{|\gamma|}$$

$$\frac{\partial n_1}{\partial h^j} = y_\xi \frac{\partial z_\zeta}{\partial h^j} + z_\zeta \frac{\partial y_\xi}{\partial h^j} - y_\zeta \frac{\partial z_\xi}{\partial h^j} - z_\xi \frac{\partial y_\zeta}{\partial h^j}$$

$$\frac{\partial n_2}{\partial h^j} = x_\zeta \frac{\partial z_\xi}{\partial h^j} + z_\xi \frac{\partial x_\zeta}{\partial h^j} - x_\xi \frac{\partial z_\zeta}{\partial h^j} - z_\zeta \frac{\partial x_\xi}{\partial h^j}$$

$$\frac{\partial n_3}{\partial h^j} = x_\xi \frac{\partial y_\zeta}{\partial h^j} + y_\zeta \frac{\partial x_\xi}{\partial h^j} - x_\zeta \frac{\partial y_\xi}{\partial h^j} - y_\xi \frac{\partial x_\zeta}{\partial h^j}$$

$$|J^*| = (n_1^2 + n_2^2 + n_3^2)^{1/2}$$

$$\frac{\partial |J^*|}{\partial h^j} = \left(n_1 \frac{\partial n_1}{\partial h^j} + n_2 \frac{\partial n_2}{\partial h^j} + n_3 \frac{\partial n_3}{\partial h^j} \right) \frac{1}{|J^*|}$$

Table A.3 (continued)

$$\frac{\partial R_x^i}{\partial h^j} = \int_{-1}^{1}\int_{-1}^{1}\int_{-1}^{1}\Big\{(-P+2\mu u_x)DNXJDH^j + \mu(u_y+v_x)DNYJDH^j$$

$$+ \mu(u_z+w_x)DNZJDH^j + \mu|J|\Big[2N_x^i\frac{\partial u_x}{\partial h^j} + N_y^i\Big(\frac{\partial u_y}{\partial h^j} + \frac{\partial v_x}{\partial h^j}\Big)$$

$$+ N_z^i\Big(\frac{\partial u_z}{\partial h^j} + \frac{\partial w_x}{\partial h^j}\Big)\Big] + |J|[2u_x N_x^i + (u_y+v_x)N_y^i + (u_z+w_x)N_z^i]\frac{\partial \mu}{\partial h^j}\Big\}d\xi d\eta d\zeta$$

$$\frac{\partial R_y^i}{\partial h^j} = \int_{-1}^{1}\int_{-1}^{1}\int_{-1}^{1}\Big\{\mu(u_y+v_x)DNXJDH^j + (-P+2\mu v_y)DNYJDH^j$$

$$+ \mu(v_z+w_y)DNZJDH^j + \mu|J|\Big[N_x^i\Big(\frac{\partial u_y}{\partial h^j} + \frac{\partial v_x}{\partial h^j}\Big) + 2N_y^i\frac{\partial v_y}{\partial h^j}$$

$$+ N_z^i\Big(\frac{\partial v_z}{\partial h^j} + \frac{\partial w_y}{\partial h^j}\Big)\Big] + |J|[(u_y+v_x)N_x^i + 2v_y N_y^i + (v_z+w_y)N_z^i]\frac{\partial \mu}{\partial h^j}\Big\}d\xi d\eta d\zeta$$

$$\frac{\partial R_z^i}{\partial h^j} = \int_{-1}^{1}\int_{-1}^{1}\int_{-1}^{1}\Big\{\mu(u_z+w_x)DNXJDH^j + \mu(v_z+w_y)DNYJDH^j$$

$$+ (-P+2\mu w_z)DNZJDH^j + \mu|J|\Big[N_x^i\Big(\frac{\partial u_z}{\partial h^j} + \frac{\partial w_x}{\partial h^j}\Big) + N_y^i\Big(\frac{\partial v_z}{\partial h^j} + \frac{\partial w_y}{\partial h^j}\Big)$$

$$+ 2N_z^i\frac{\partial w_z}{\partial h^j}\Big] + |J|[(u_z+w_x)N_x^i + (v_z+w_y)N_y^i + 2w_z N_z^i]\frac{\partial \mu}{\partial h^j}\Big\}d\xi d\eta d\zeta$$

Table A.3 (continued)

$$\frac{\partial R_c^i}{\partial h^j} = \int_{-1}^{1}\int_{-1}^{1}\int_{-1}^{1}\left\{(u_x+v_y+w_z)\frac{\partial|J|}{\partial h^j}+|J|\left[\frac{\partial u_x}{\partial h^j}+\frac{\partial v_y}{\partial h^j}+\frac{\partial w_z}{\partial h^j}\right]\right\}N_p^i\,d\xi d\eta d\zeta$$

$$\frac{\partial R_T}{\partial h^j} = \int_{-1}^{1}\int_{-1}^{1}\int_{-1}^{1}\left\{Pe\left[\left(u\frac{\partial T_x}{\partial h^j}+v\frac{\partial T_y}{\partial h^j}+w\frac{\partial T_z}{\partial h^j}\right)|J|\right.\right.$$

$$\left.+(uT_x+vT_y+wT_z)\frac{\partial|J|}{\partial h^j}\right]+|J|\left(\frac{\partial T_x}{\partial h^j}N_x^i+\frac{\partial T_y}{\partial h^j}N_y^i+\frac{\partial T_z}{\partial h^j}N_z^i\right)$$

$$+(DNXJDH^j T_x+DNYJDH^j T_y+DNZJDH^j T_z)$$

$$-2Br\,\mu|J|\left[2\left(u_x\frac{\partial u_x}{\partial h^j}+v_y\frac{\partial v_y}{\partial h^j}+w_z\frac{\partial w_z}{\partial h^j}\right)\right]$$

$$-2Br(u_x^2+v_y^2+w_z^2)\left(\mu\frac{\partial|J|}{\partial h^j}+|J|\frac{\partial\mu}{\partial h^j}\right)-Br\,\mu|J|\left[2(u_y+v_x)\left(\frac{\partial u_y}{\partial h^j}+\frac{\partial v_x}{\partial h^j}\right)\right.$$

$$\left.+2(u_z+w_x)\left(\frac{\partial u_z}{\partial h^j}+\frac{\partial w_x}{\partial h^j}\right)+2(v_z+w_y)\left(\frac{\partial v_z}{\partial h^j}+\frac{\partial w_y}{\partial h^j}\right)\right]$$

$$-Br[(u_y+v_x)^2+(u_z+w_x)^2+(v_z+w_y)^2]\left(\mu\frac{\partial|J|}{\partial h^j}+|J|\frac{\partial\mu}{\partial h^j}\right)N^i\,d\xi d\eta d\zeta$$

$$+\int_{-1}^{1}\int_{-1}^{1}\left\{Nu(T+1)N^i\frac{\partial|J^*|}{\partial h^j}\right\}d\xi d\zeta,\quad \eta=1$$

$$\frac{\partial R_k}{\partial h^j} = \int_{-1}^{1}\int_{-1}^{1}\left\{\frac{\partial n_1}{\partial h^j}u+\frac{\partial n_2}{\partial h^j}v+\frac{\partial n_3}{\partial h^j}w\right\}N^i\,d\xi d\zeta,\quad \eta=1$$

APPENDIX B

A FINITE ELEMENT CONVERGENCE STUDY FOR SHEAR THINNING FLOW PROBLEMS

INTRODUCTION

Finite element simulation of the steady-state Navier-Stokes equations for shear thinning fluids involves the solution of a large set of nonlinear equations. A nonlinear equation solving algorithm must be robust with respect to the degree of nonlinearity and starting point and be capable of handling very large equation sets if it is to be used in a large variety of physical situations. The rank order of algorithm efficiency may change depending on the specific problem and the "best" algorithm may be different depending upon the stage in the solution procedure in solving a particular problem. A strategy for solving the nonlinear equation sets may be necessary where different algorithms are used in sequence for the desirable properties that each may possess.

Nonlinearities arise from a number of different sources. For example, it is well known that high Reynolds number flows cause convergence problems due to the nonlinearity from the convective terms. Non-Newtonian problems have the stress tensor as a nonlinear function of the rate-of-strain tensor. Free boundary problems are very nonlinear when the free surface position coordinates are determined with the nodal velocities and pressures.

The difficulty of solving nonlinear fluid flow problems can often be related to a parameter intrinsic to the fluid/geometry system. For convective problems the degree of difficulty increases with the Reynolds number of the fluid. Shear thinning fluids described by a power law model,

$$\underline{\underline{\tau}} = -k\,[1/2\,\underline{\underline{\dot{\gamma}}}:\underline{\underline{\dot{\gamma}}}]^{(n-1)/2}\underline{\underline{\dot{\gamma}}} \qquad \text{(B.1)}$$

lead to increasingly nonlinear equations as n is decreased. The convergence of free boundary problems is sensitive to the curvature of the free surface and to the application of the boundary conditions at the contact lines between fluid and solid. The solution of very nonlinear equations requires an incremental approach. For convection dominated flow, the creeping flow case is used as a starting solution and the Reynolds number is incremented in a series of steps to the desired value. Similarly, in shear thinning fluids a series of problems with decreasing power law index are solved and for free boundary problems a series of interface shapes are examined until all the boundary conditions are satisfied. In polymer processing simulations it is common to find combinations of these nonlinearities in a single problem, for example the flow of a shear thinning polymer melt into a mold cavity.

For most polymer processing studies the non-Newtonian effects (viscoelasticity, shear thinning) are more significant than the convective effects because of the low Reynolds numbers involved. This appendix focuses on finite element equation convergence problems for shear thinning effects and is complementary to previous work (Gartling et al., 1977; Engelman et al., 1981; Engleman, 1982 and 1986).

When the Galerkin finite element method is applied to the fluid momentum equations, the resulting nonlinear equations are in the following form,

$$\underline{\underline{K}}(\underline{u})\underline{u} = \underline{F} \tag{B.2}$$

where $\underline{u}$ is a vector containing all the velocities and pressures at the finite element nodes. There are many solution procedures available but in this work four are compared: fixed point iteration (Picard iteration, PI), Newton- Raphson (NR), a quasi-Newton method by Broyden (BR), and the Dominant Eigenvalue Method - Kaniel-Stein version (DE). There has been considerable work done with the first three methods and the DE is proposed as an alternative. A comparative study of NR, PI and BR on convective and shear-thinning flow problems was also undertaken by Gartling (1977) and Engelman (1982).

We shall use the terminology that "problem" refers to the solution of the finite element equations at the parameter of interest (e.g. n = 0.25 for a shear thinning fluid), "subproblem" refers to the solution of the finite element equations at some intermediate value of the parameter (e.g. solve the equations for n = 0.5 to obtain a starting guess for n = 0.25), and "iterations" refer to the number of applications of a particular convergence scheme to obtain the solution for a subproblem.

Selection of a robust nonlinear equation solving technique involves two important issues. The radius of convergence is the difference between the initial trial vector for the unknowns and the true solution vector such that the equation set can be solved starting from the initial trial vector. For a given problem parameter value, it is desirable to have the radius of convergence to be as large as possible. The rate of convergence of the iterates should be maximized to minimize the number of iterations. Each of the iteration methods mentioned previously has its own strengths and weaknesses with regards to these two issues, which can conflict with each other as in a method that has a high rate of convergence but small radius of convergence.

PROBLEMS

The test problems are creeping flows (Re = 0) in the following standard geometries: square duct (Liu, 1983, 1985; Wheeler and Wissler, 1965), driven cavity (Olson and Tuann, 1979), and a 4:1 planar contraction.

The first problem considers the fully developed flow of an inelastic power law fluid in a square duct (Figure B.1a). The flow is assumed to be unidirectional and is governed by the Poisson equation with the no slip boundary conditions:

$$\frac{\partial}{\partial x}\left(\mu\frac{\partial w}{\partial x}\right) + \frac{\partial}{\partial y}\left(\mu\frac{\partial w}{\partial y}\right) = \frac{dP}{dz} \tag{B.3}$$

where

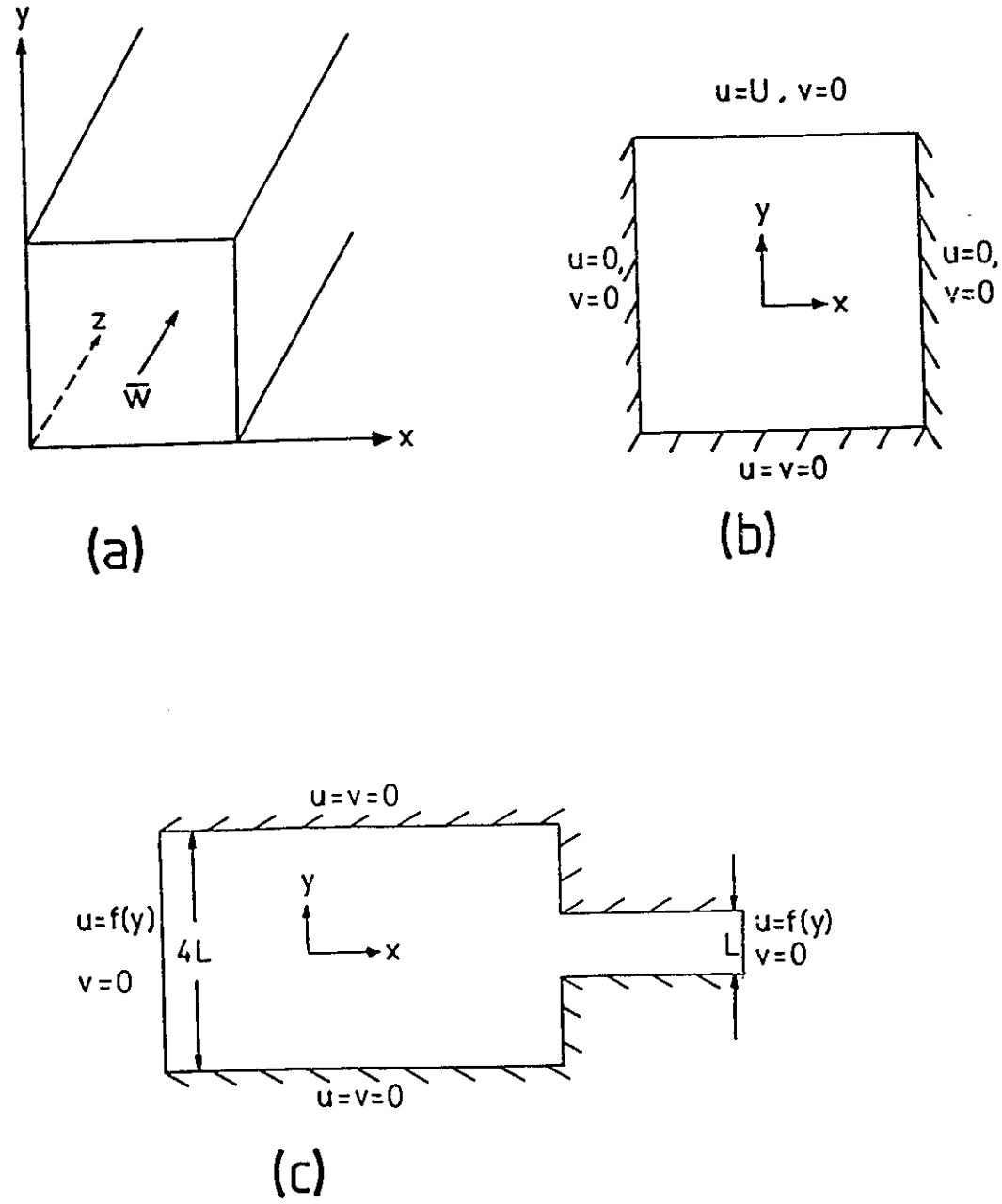

Figure B.1: Problem statement: a) Square Duct, b) Driven Cavity, c) 4:1 Contraction.

$$\mu = k\left[\left(\frac{\partial w}{\partial x}\right)^2 + \left(\frac{\partial w}{\partial y}\right)^2\right]^{\frac{n-1}{2}} \tag{B.4}$$

The second and third problems consider the flow of an inelastic power-law fluid inside a square cavity where one wall is moving with constant velocity (Figure B.1b) and in a 4:1 contraction (Figure B.1c), respectively. The governing equations are:

$$\frac{\partial}{\partial x}\left(2\mu\frac{\partial u}{\partial x}\right) + \frac{\partial}{\partial y}\left[\mu\left(\frac{\partial u}{\partial y} + \frac{\partial v}{\partial x}\right)\right] = \frac{\partial P}{\partial x} \tag{B.5a}$$

$$\frac{\partial}{\partial x}\left[\mu\left(\frac{\partial u}{\partial y} + \frac{\partial v}{\partial x}\right)\right] + \frac{\partial}{\partial y}\left(2\mu\frac{\partial v}{\partial y}\right) = \frac{\partial P}{\partial y} \tag{B.5b}$$

$$\frac{\partial u}{\partial x} + \frac{\partial v}{\partial y} = 0 \tag{B.5c}$$

where

$$\mu = k\left[2\left(\frac{\partial u}{\partial x}\right)^2 + 2\left(\frac{\partial v}{\partial y}\right)^2 + \left(\frac{\partial v}{\partial x} + \frac{\partial u}{\partial y}\right)^2\right]^{\frac{n-1}{2}} \tag{B.6}$$

The equations were discretized using a standard Galerkin finite element u-v-p formulation with triangular shaped elements which were C^0–P^2 for the nodal velocities and C^0–P^1 linear for the pressures (Huebner and Thornton, 1980).

The square duct problem mesh is shown in Figure B.2 (200 elements, 441 nodes or 361 variables). The driven cavity mesh for 200 elements is the same as that used for the square duct problem (861 variables) and the 72 element case is shown in Figure B.3 (169 nodes or 300 variables). The pressure contours are presented in Figure B.4 for the driven cavity problem with a power law index of 0.5 on the 200 element mesh with the appropriate velocity vector solution on Figure B.5. The 4:1 contraction problem mesh is shown in Figure B.6 and contains 220 elements (501 nodes or 966 variables). The pressure contours and velocity vectors are shown in Figures B.7 and B.8 for a power law index of 0.5.

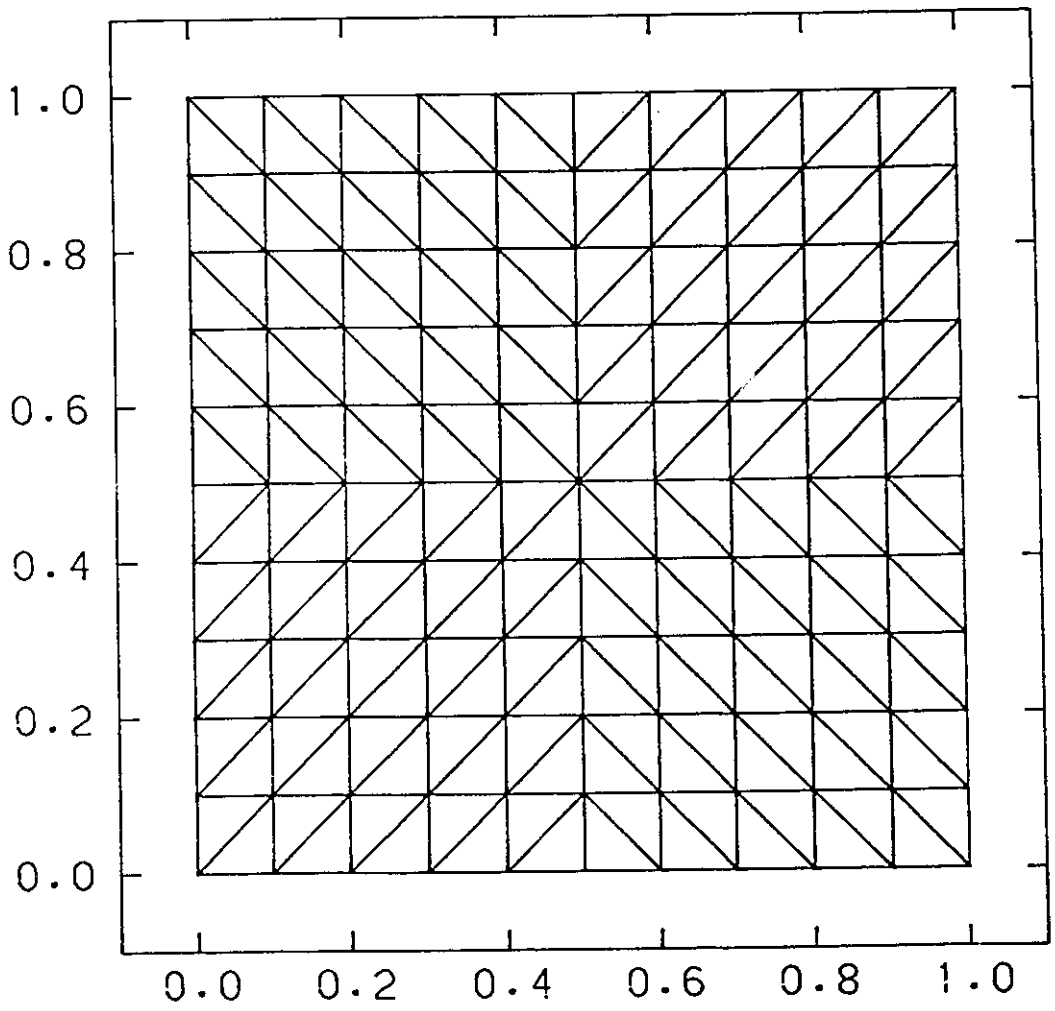

Figure B.2: Finite element grid, square duct and driven cavity problem, 200 elements.

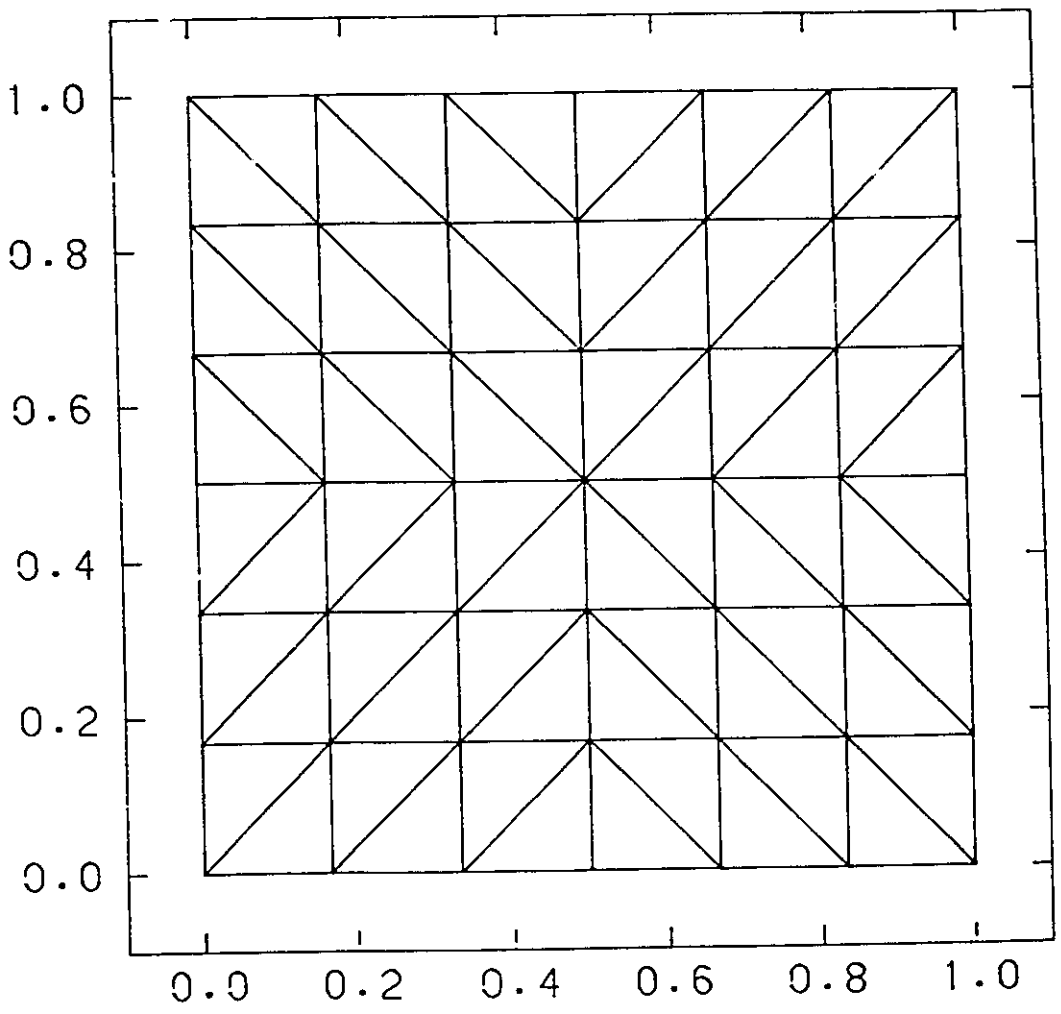

Figure B.3: Finite element grid, driven cavity problem, 72 elements.

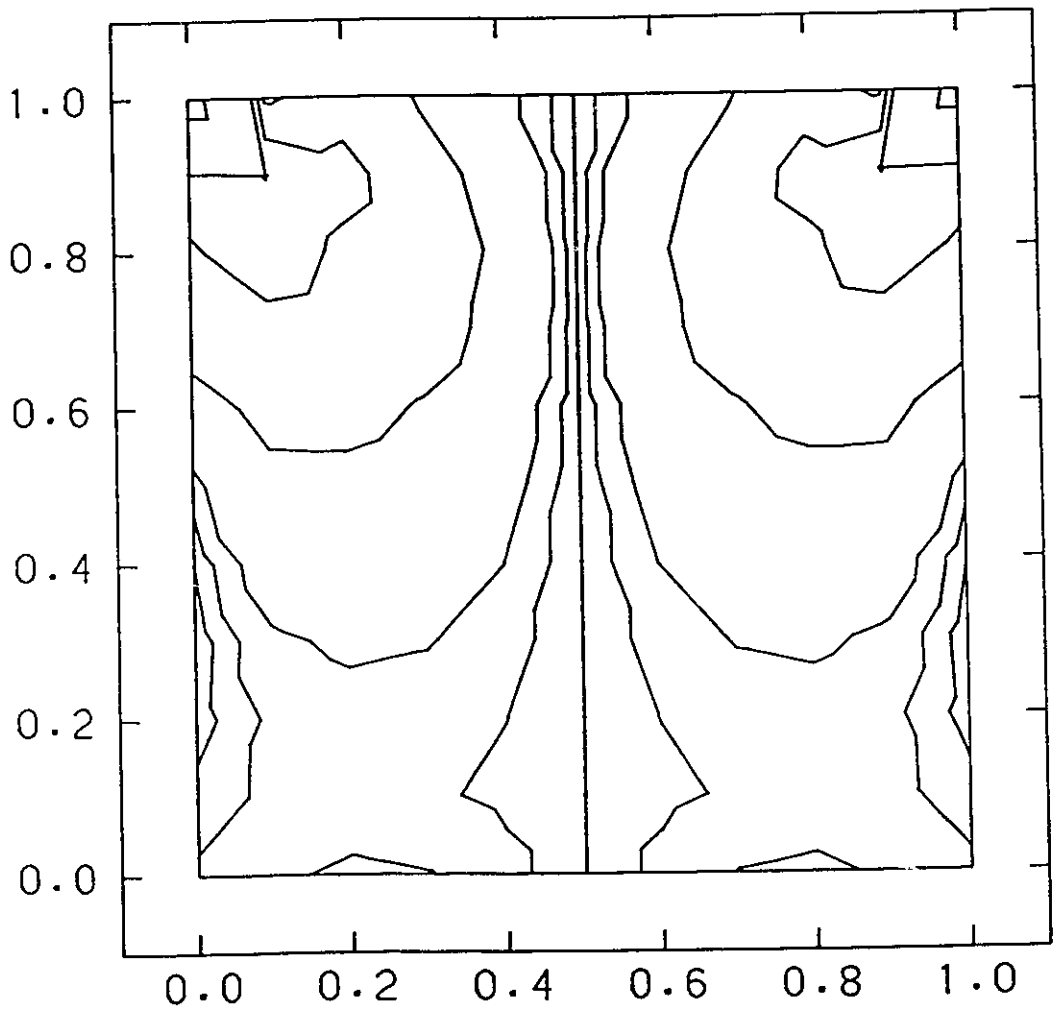

Figure B.4: Pressure contours, driven cavity problem, 200 element grid. Power-law index 0.5.

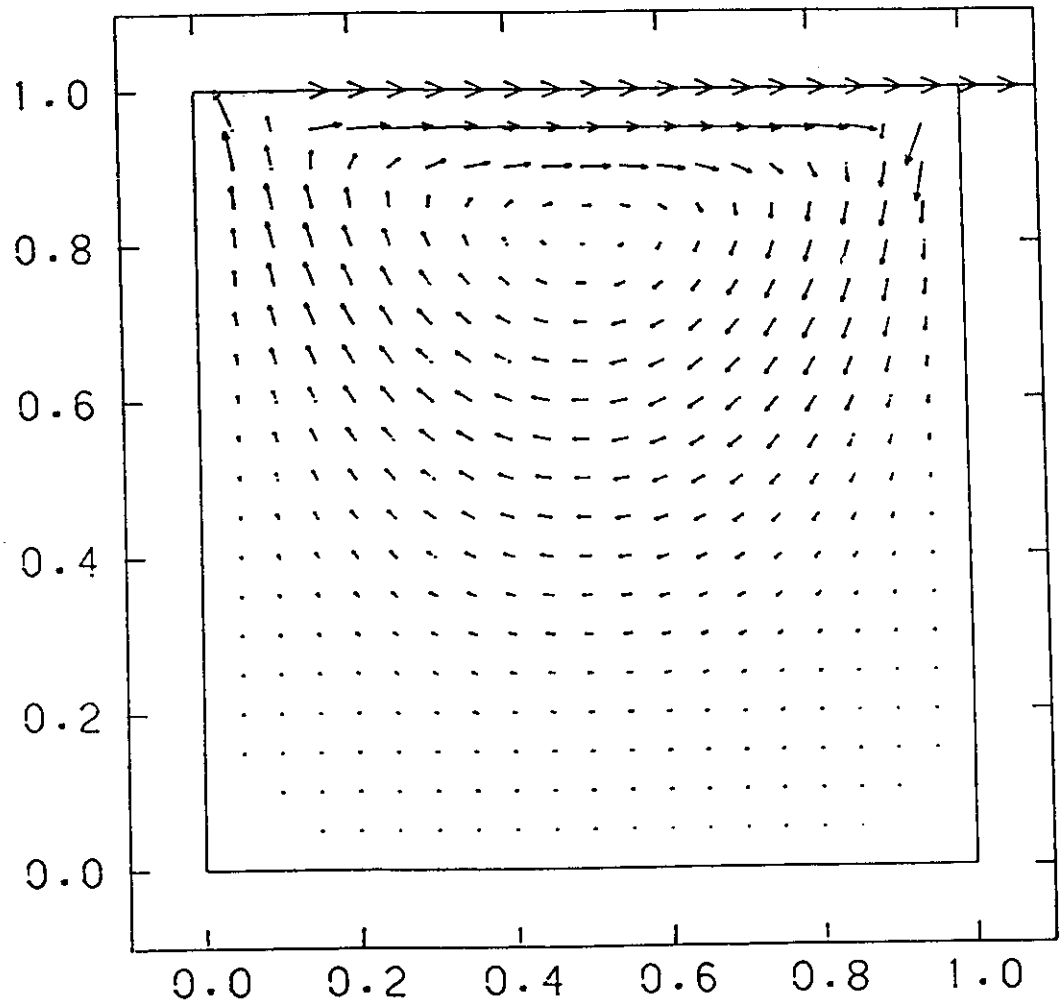

Figure B.5: Velocity vectors, driven cavity problem, 200 element grid. Power-law index 0.5.

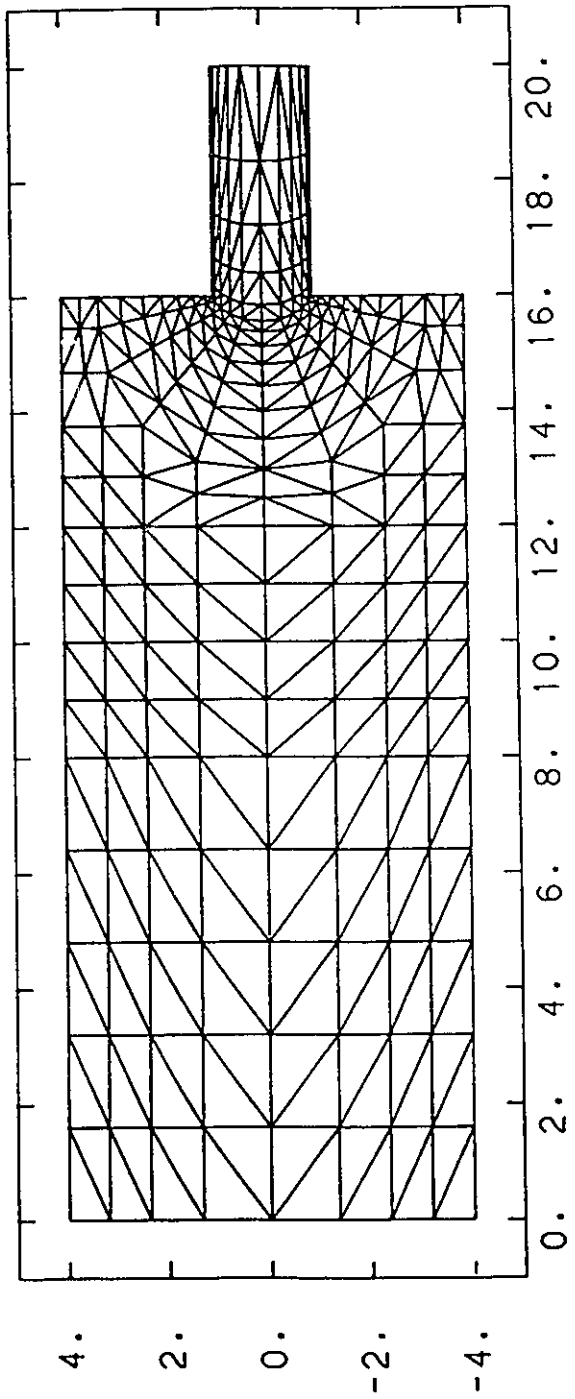

Figure B.6: Finite element grid, 4:1 contraction problem.

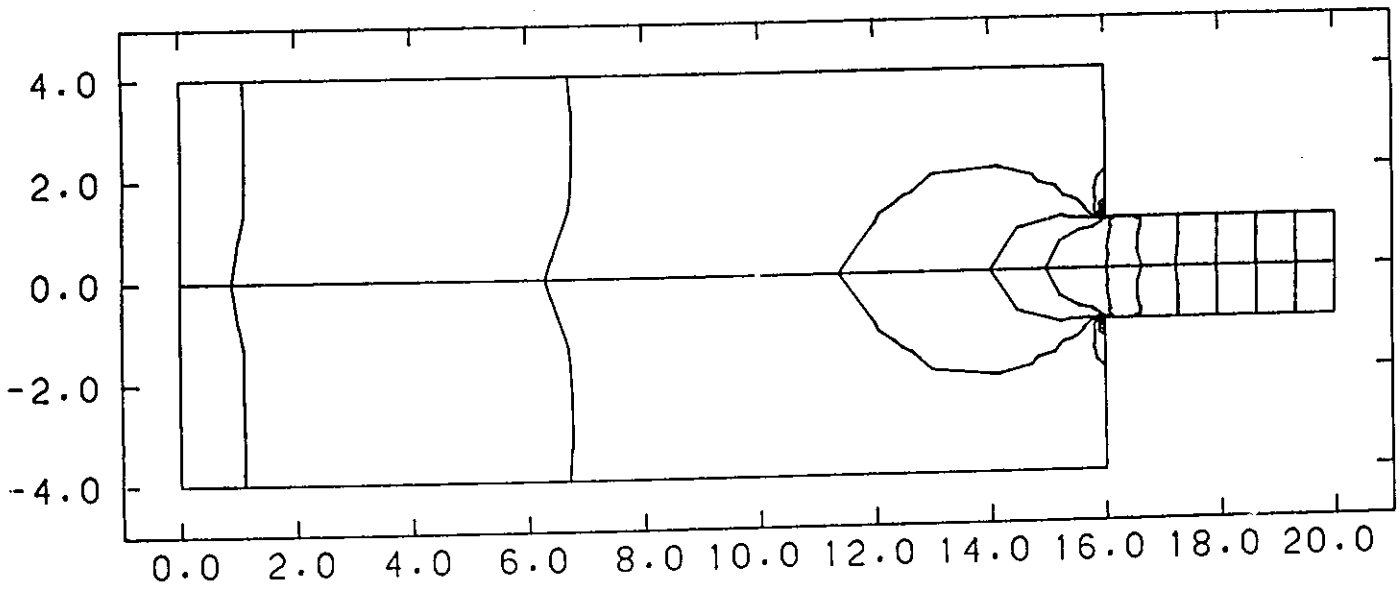

Figure B.7: Pressure contours, 4:1 contraction problem.
Power-law index 0.5.

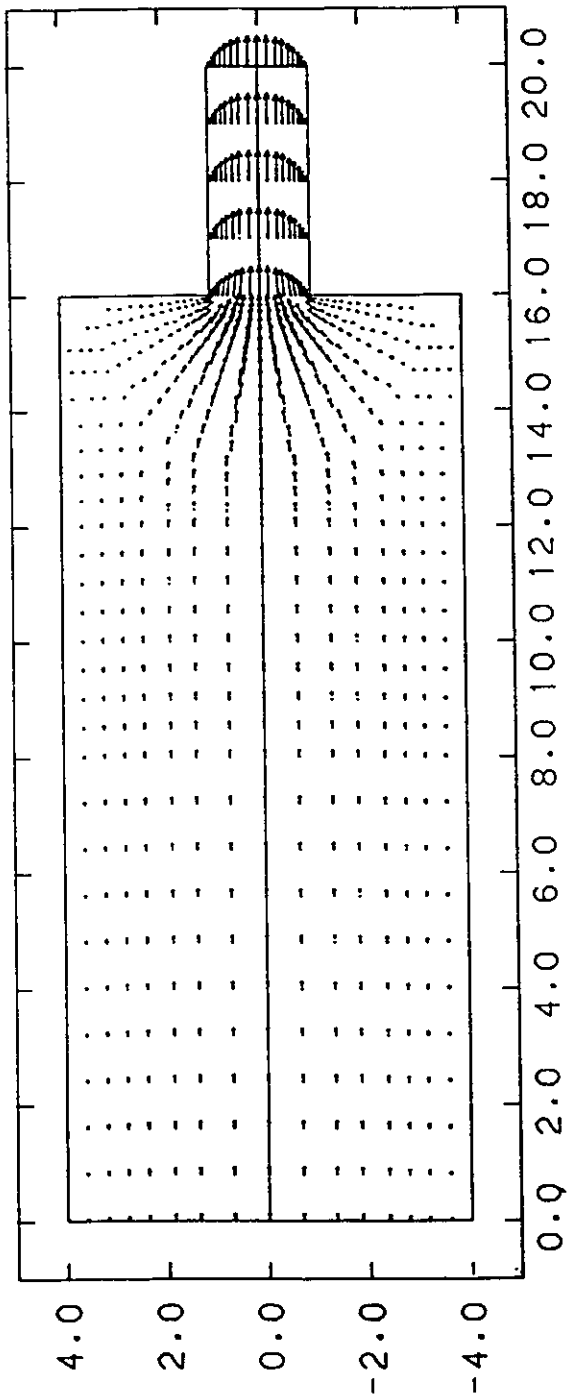

Figure B.8: Velocity vectors 4:1 contraction problem.
Power-law index 0.5.

ALGORITHMS

Picard Iteration

Picard or fixed point iteration is the simplest scheme to implement and is written as:

$$\underline{\underline{K}}(\underline{u}^i)\,\underline{u}^{i+1} = \underline{F} \tag{B.7}$$

The nonlinear coefficient matrix terms are evaluated using the values of $\underline{u}$ from the previous iteration and the entire equation set is solved again to determine the new vector quantities. The method's convergence rate is asymptotically linear (slow) but it converges for a relatively large parameter range and is not very sensitive to the initial vector $\underline{u}^0$.

Sometimes the basic scheme is modified by the addition of a weighting factor for the previous iteration solution:

$$\underline{\underline{K}}(\underline{u}^i)\underline{u}^* = \underline{F} \tag{B.8}$$

$$\underline{u}^{i+1} = \alpha\,\underline{u}^i + (1-\alpha)\underline{u}^* \tag{B.9}$$

The factor α varies between 0 and 1, with $\alpha = 0$ being the standard direct substitution case.

Newton-Raphson

We solve the following equation set:

$$\underline{R}(\underline{u}) = \underline{\underline{K}}(\underline{u})\,\underline{u} - \underline{F} = 0 \tag{B.10}$$

Using a first order Taylor series expansion around a nominal point and assuming a relatively small change in $\underline{u}$ from iteration i to iteration i+1:

$$\underline{\underline{J}}(\underline{u}^i)\,\Delta\underline{u} = -\underline{R}(\underline{u}^i) \tag{B.11}$$

where

$$\underline{\underline{J}}(\underline{u}^i) = \frac{\partial \underline{\underline{R}}}{\partial \underline{u}}\Big|\underline{u}^i \tag{B.12}$$

$$\underline{u}^{i+1} = \underline{u}^i + \beta\Delta\underline{u} \tag{B.13}$$

and β can be used to modify the step length with a line search, to minimize the sum of the residuals along a given search direction, if necessary.

The Newton-Raphson method has a quadratic asymptotic rate of convergence. However, the radius of convergence is quite small, i.e. one must start near the solution for very nonlinear problems. Generally, the initial vector is the solution of a linear version of the problem and a parameter is incremented in a series of subproblems to approach the solution of interest. This initialization strategy is sometimes called incremental loading or zero-order continuation. The superior convergence properties of the method insure that for "good" choices of the parameter increments the subproblems will be solved cost effectively. It is not possible at the present time to predict the values of the parameters for the least number of subproblem solutions. It is possible that many subproblems must be solved leading to longer total computation times than expected.

An automatic extension of a parameter incrementation strategy is to use a first order continuation method (or homotopy method) which uses the Jacobian from the solution to a given value of the parameter to predict the next parameter value to be used (Kheshgi et al., 1983). We have not pursued first order continuation method/Newton-Raphson combination approaches in this work.

Another alternative is the modification of the step length with a line search. The procedure increases the radius of convergence considerably (Engelman, 1982) but may still lead to long computation times if many line searches are performed.

The Jacobian for Newton-Raphson iterations was calculated using analytical derivatives of the finite element equations for all the examples in this work, and the variation in effective viscosity with velocity was included. Finite difference approximations to the derivatives could be used but would add another complication in comparing different nonlinear equation solving schemes. The accuracy of the finite derivative approximation directly affects

the rate of convergence of the Newton-Raphson method and a whole study would be needed for the effect of the perturbation selected in the numerical differencing.

Quasi-Newton Methods

The major objection to the Newton-Raphson method is the necessity of recalculating Jacobians and decomposing the linearized set of equations at every iteration. A quasi-Newton procedure (variable metric method) generalizes the Newton-Raphson method (Engelman et al., 1981) to:

$$\underline{u}^{i+1} = \underline{u}^{i} - s^{i}\underline{\underline{H}}^{i}\underline{R}^{i} \tag{B.14}$$

$\underline{R}^{i}$ is the residual evaluated at $\underline{u}^{i}$, $\underline{\underline{H}}^{i}$ is an approximation to the inverse of the Jacobian matrix and s^{i} is analogous to β of the Newton-Raphson method as a line search variable to force descent in the residual sum. The Jacobian inverse approximation is updated at each iteration:

$$\underline{\underline{H}}^{i+1} = \underline{\underline{H}}^{i} + \Delta\underline{\underline{H}}^{i} \tag{B.15}$$

The inverse form of the rank one update given by Broyden's (Broyden, 1965; Dennis and More, 1977; White, 1985) method is,

$$\underline{\underline{H}}^{i+1} = \underline{\underline{H}}^{i} + (\Delta\underline{u}^{i} - \underline{\underline{H}}^{i}\Delta\underline{R}^{i})(\Delta\underline{u}^{iT}\underline{\underline{H}}^{i})/(\Delta\underline{u}^{iT}\underline{\underline{H}}^{i}\Delta\underline{R}^{i}) \tag{B.16}$$

Note that the Jacobian inverse approximation is a full matrix. The method should be implemented to preserve sparsity and not use the full Jacobian matrix approximation as presented in the above equations.

Update vectors are stored and used to modify an initial approximation to the Jacobian inverse matrix.

The specific Broyden algorithm implemented is that of Engelman et al. (1981) and Engleman (1982) which calculates the updated $\underline{\underline{H}}^{i}$ from the original Jacobian inverse $\underline{\underline{H}}^{0}$ at each iterative cycle. A Broyden algorithm to solve $\underline{R}(\underline{u}) = \underline{\underline{K}}(\underline{u})\underline{u} - \underline{F} = \underline{0}$ is as follows:

1. Given $\underline{u}^0$, $\underline{\underline{J}}^0$ (Jacobian matrix after one NR or an approximation to the Jacobian after one PI iteration)

   set i = 0

   compute $\underline{R}^0 = \underline{R}(\underline{u}^0)$

   $\underline{\underline{J}}^0 \underline{d}^0 = \underline{R}^0$, $\underline{d}^0$ is the initial search direction.

   Estimate s^0 with a line search if necessary

   update $\underline{u}^1 = \underline{u}^0 - s^0 \underline{d}^0$

2. Set i to i+1

   compute $\underline{R}^i = \underline{R}(\underline{u}^i)$

   $\underline{\underline{J}}^0 \underline{q}^i = \underline{R}^i$

   if i = 1 go to 4

3. For j = 1, . . . , i–1

   compute $\underline{q}^{j+1} = \underline{q}^j + p^j (\underline{\delta}^j - \underline{r}^j) \underline{\delta}^j \underline{q}^j$

4. Compute and store

   $\underline{r}^i = \underline{q}^i - \underline{d}^{i-1}$

   $\underline{\delta}^i = \underline{u}^i - \underline{u}^{i-1} = -s^{i-1} \underline{d}^{i-1}$

   $p^i = 1/\underline{\delta}^{iT} \underline{r}^i$

   compute $\underline{d}^i = \underline{q}^i + p^i(\underline{\delta}^i - \underline{r}^i)\underline{\delta}^{iT} \underline{q}^i$, the new search direction,

   estimate s^i, with a line search if necessary

   update $\underline{u}^{i+1} = \underline{u}^i - s^i \underline{d}^i$

5. If norm of residuals is less than tolerance and norm of the error is less than tolerance,

   then stop

   else if $i < i_{max}$ go to 2

   else stop

In the implementation of the method, the LU factors of the linear equation decomposition that were found in step 1 are used as the initial Jacobian inverse. Then, if Broyden's method is interchanged with Newton-Raphson, the LU factors provide the inverse of an exact Jacobian, whereas if Broyden's method is interchanged with Picard, the LU factors provide the inverse of an approximate "Jacobian". Step 2 uses the LU factors and so involves only a back-substitution which is relatively inexpensive. An alternative would be to use an initial Jacobian found by using $\underline{u}^0$ and the analytical derivatives of $\underline{R}^0$.

While the algorithm uses all the updating vectors previously calculated, in general only a fixed number of updating vectors may be used. At the limit of stored update vectors one would restart the algorithm with the Jacobian inverse available at that time. Another alternative is to remove the oldest update vector and continue with the same fixed number of update vectors using the original estimate for the matrix. We investigate both alternatives. The former requires more computer time for matrix factorization while the latter option has slower convergence. The specific line search algorithm implemented was that of Matthies and Strang (1979). Line searches are not performed unless (Matthies and Strang, 1979)

$$|G| > \text{stol} * |G0|$$

where

$$G = \underline{d}^T \underline{R}(\underline{u}-\underline{d}) ,$$

$$G0 = \underline{d}^T \underline{R}(u)$$

and

$$\text{stol} = 0.5 , \text{the tolerance}$$

Dominant Eigenvalue Method

The dominant eigenvalue method (Orbach and Crowe, 1971; Crowe and Nishio, 1975; Kaniel and Stein, 1974) takes into account interaction between variables in determining

a weighted combination of previous iteration solutions to predict the solution of the iteration sequence. The basis of the method is to assume that the iterations approximately follow a linear matrix difference equation and computes the apparent solution by using estimates of the dominant eigenvalues.

The basic idea is to do a number of Picard iterations on the equation set, building up an iteration history, and then to accelerate the iteration process by predicting the apparent solution from the previous iterations. The predicted solution, after $\underline{u}^{i+1}$ is calculated, is given by

$$\underline{u}^{iP} = \sum_j \mu_j \underline{u}^{i-j+1} / \sum_j \mu_j \tag{B.17}$$

where $j = 0, \ldots,$ and is the number of dominant eigenvalues. The coefficients μ_j are determined by minimizing the following expression with respect to the coefficients

$$\min \| \sum_j \mu_j \Delta \underline{u}^{i-j} \| \tag{B.18}$$

and $1 \leq v \leq i \leq m$ and m is the number of equations. Solving the overdetermined set of equations,

$$\sum_j \mu_j b_{jk} = 0 \quad k = 1, 2, \ldots, v \tag{B.19}$$

with (Kaniel-Stein, 1974)

$$\sum_j \mu_j = 1 \tag{B.20a}$$

or (Crowe and Nishio, 1975)

$$\mu_o = 1 \tag{B.20b}$$

$$b_{jk} = <\Delta \underline{u}^{i-j}, \Delta \underline{u}^{i-k}> \tag{B.21}$$

provides the coefficients.

The number of dominant eigenvalues is problem dependent, but we found that for the problems presented in this work, only one was needed, i.e. we weighted the i+1 and i iterations. More coefficients may be used, but we found only marginal improvement in com-

putation time. The criterion for taking a promotion step is to promote when estimates of the apparent solution on iteration i, $\underline{u}^{iP}$, do not change more than a prescribed amount in the norm compared to the next prediction, $\underline{u}^{i+1P}$. Promoting too frequently leads to numerical instability. The method is stabilized by taking a promotion step no more than every ν iterations. For the simple one dominant eigenvalue case according to Kaniel and Stein (1974),

$$\underline{u}^{P} = \underline{u}^{i} + \mu_0 (\underline{u}^{i+1} - \underline{u}^{i}) \tag{B.22}$$

$$\mu_0 = -b_{11}/(b_{01} - b_{11}) \tag{B.23a}$$

$$\mu_1 = b_{01}/(b_{01} - b_{11}) \tag{B.23b}$$

or according to Crowe and Nishio (1975):

$$\underline{u}^{P} = \underline{u}^{i} + (\underline{u}^{i+1} - \underline{u}^{i})/(1 + \mu_1) \tag{B.24}$$

$$\mu_1 = -b_{01}/b_{11} \tag{B.25}$$

Discussion

The deficiencies of each of the methods can probably be overcome by combining methods for different purposes. For example, Picard iteration has a large radius of convergence while Newton-Raphson has a fast rate of convergence so a strategy could be to start with Picard and switch to Newton- Raphson.

Iterative solutions to nonlinear equations require a criterion to end the iteration cycles. The criteria must not only signal an acceptable solution that is within specified tolerances, but also warn of divergence. There is always a trade-off between accuracy and computer time since high accuracy demands many more iterations. Relative error criteria are preferred to absolute error criteria because of differences in scale in the nodal variables.

Two standard termination criteria are that the relative change in the solution vector be less than a preset error:

$$\|\Delta \underline{u}^{i}\| \leq \varepsilon \|\underline{u}^{i}\| \tag{B.26}$$

and that the value of the residual sum be less than a preset error:

$$\|\underline{R}(\underline{u}^i)\| \leq \varepsilon \tag{B.27}$$

For all matrix factorizations we used an unsymmetric band solver using LU decomposition from the LINPACK library (DGBFA and DGBSL). The finite element mesh was generated and automatically renumbered for minimum band width using standard mesh techniques. A frontal method or a skyline method (Hasbani and Engelman, 1979) for solving the finite element equations may be used, but in this work a generally available equation solver was chosen (Dongarra et al., 1979).

RESULTS

For all runs performed, the Newtonian problem was solved first to obtain an initial solution and then a Picard or Newton-Raphson iteration is performed with the power law index set to the first subproblem. Then either Picard, Newton-Raphson, Broyden or DE was performed with or without line search. The single iteration needed to obtain the Newtonian (linear) solution is not included in the iteration count for the nonlinear problem. The convergence criterion used was that the norm of the residuals be less than 10^{-6}. All runs were performed on a VAX 8600 computer in double precision.

In cases using the Broyden method, one Picard or Newton-Raphson iteration is performed after every 4 Broyden iterations except where noted. This strategy proved to stabilize the procedure leading to convergence even for very nonlinear cases (power-law index $n = 0.2$).

Table B.1 shows that for the square duct problem, all the methods converged for $n = 0.5$ and Broyden's method was fastest in total computer time. The solution is very regular. DE-1 signifies that only one dominant eigenvalue was assumed. In the case of $n = 0.3$, the NR method would not converge from the Newtonian case while it converges with

the use of line searches. The cost of NR with line searches is equal to that of the DE method. Note that in the case where the Broyden algorithm uses an approximate Jacobian (from a Picard iteration), the solution proceeds without difficulty, whereas in the case where an exact Jacobian (from a Newton-Raphson iteration) is used, convergence was achieved with some difficulty. The method needed an excessive number of line searches resulting in a high cost. The superior properties of the Picard iteration with respect to the radius of convergence seem to stabilize Broyden's algorithm.

TABLE B.1 Square Duct

	Method	Total Iterations	No. of Line searches	CPU time(s)
n = 0.5				
	Newton-Raphson	6	2	69
	Picard	16	–	123
	DE-1	10	–	83
	BR-P	15	11	49
	BR-N	8	11	44
n = 0.3				
	Newton-Raphson	13	26	147
	Picard	31	–	187
	DE-1	19	–	148
	BR-P	20	29	72
	BR-N	31	85	165

Table B.2 shows the results for the driven cavity problem with 72 elements. For n = 0.5 Broyden's method is very fast relative to the other methods. At n = 0.3 the Picard is quite slow, and Newton-Raphson cannot converge from the Newtonian solution unless line searches or continuation are performed. What is significant is that the DE works for every case at a cost approximately half that of the Picard and comparable to that of Newton-Raphson in the very nonlinear case of n = 0.2. Broyden's method with an approximate Jacobian is able to converge with the lowest cost even when no line searches are performed.

TABLE B.2 Driven Cavity 72 elements

	Method	Total Iterations	No. of Line searches	CPU time(s)
n = 0.5				
	Newton-Raphson	7	2	105
	Picard	21	—	184
	DE-1	13	—	119
	DE-3	14	—	130
	BR-P	14	4	55
	BR-N	10	9	89
n = 0.3				
	Newton-Raphson	9	8	134
	Newton-Raphson*	18	—	244
	Picard	49	—	417
	DE-1	24	—	210
	BR-P	23	—	73
	BR-P	25	24	99
	BR-N	16	28	152
n = 0.2				
	Newton-Raphson	20	39	296
	DE-1	35	—	305
	BR-P	49	—	137

* Newton-Raphson method without line search required a series of subproblems of n = 1, n = 0.5, n = 0.35, n = 0.3 for convergence and the time is total of all CPU times. One Picard iteration was performed before switching to Newton-Raphson in all subproblems.

However, NR required the implementation of line searches or continuation and Broyden's method required some strategy to obtain a solution (which was not obvious) while the DE required no extra steps at all. When the 200 element case is compared in Table B.3 it is seen that for n = 0.5 and n = 0.3 DE requires half the cost of Picard while Broyden's method is again the fastest, but when the exact Jacobian is used in the case of n = 0.3, the algorithm would not converge. In the case of n = 0.5, Broyden's method with approximate Jacobian did not require any line searches while in the 72 element case, it required 4 line searches. The significant result is that for the case of n = 0.2, the DE method is faster than the NR which required line searches to converge.

TABLE B.3 Driven Cavity 200 elements

	Method	Total Iterations	No. of Line searches	CPU time(s)
n = 0.5				
	Newton-Raphson	8	1	682
	Picard	18	—	1221
	DE-1	11	—	775
	DE-3	13	—	958
	BR-P	14	0	313
	BR-N	11	8	452
n = 0.3				
	Newton-Raphson	13	15	1087
	Picard	34	—	2254
	DE-1	20	—	1367
	BR-P	30	—	558
	BR-P	23	28	549
	BR-N	Divergence		
n = 0.2				
	Newton-Raphson	26	49	2165
	DE-1	29	—	1986

Table B.4 shows the results for the 4:1 contraction problem, which was the most difficult problem of the group, mainly because of the variety of flow regimes in the solution. For n = 0.5, Newton-Raphson with line searches and Broyden with exact Jacobian are surprisingly time-consuming, while DE and Broyden with approximate Jacobian have no difficulties. However, in the n = 0.3 case, Broyden method with line searches and exact Jacobian would not converge, while the case with approximate Jacobian had convergence difficulties leading to high computation times. Note that the Broyden with approximate Jacobian /n = 0.5 case did not have any difficulty in the square duct or the driven cavity, and this is an example of how methods can fail depending on the specific fluid/geometry problem. DE converged without any special steps for both n = 0.5 and n = 0.3 cases from the

Newtonian solution and what is more significant is that in the case of n = 0.3, DE was the fastest surpassed only by Broyden without line searches.

TABLE B.4 4:1 Contraction

	Method	Total Iterations	No. of Line searches	CPU time(s)
n = 0.5				
	Newton-Raphson	10	10	411
	Picard	21	—	457
	DE-1	12	—	276
	DE-3	14	—	312
	BR-P	17	3	183
	BR-N	16	24	431
n = 0.3				
	Newton-Raphson	13	16	516
	Picard	38	—	798
	DE-1	18	—	398
	BR-P	23	—	230
	BR-P	33	52	414
	BR-N	Divergence		

The results in the cases where line searches were performed are in general agreement with those of Engelman (1982) for the Picard, Broyden and Newton-Raphson methods.

Figure B.9 shows a plot of the norm of the residuals versus the iteration number for the 200 element driven cavity, and Figure B.10 for the 4:1 contraction. In both plots, NR converges very rapidly, Picard very slowly, and the other methods are somewhere in between. The tables also point out the fact that even though NR has few iterations, the iterations are expensive because they entail a Jacobian evaluation and a matrix factorization. The cost of the algorithms increases when excessive line searches are performed. In tables B.1-B.4 the number of line searches shown is the number of function evaluations within the line search subroutine.

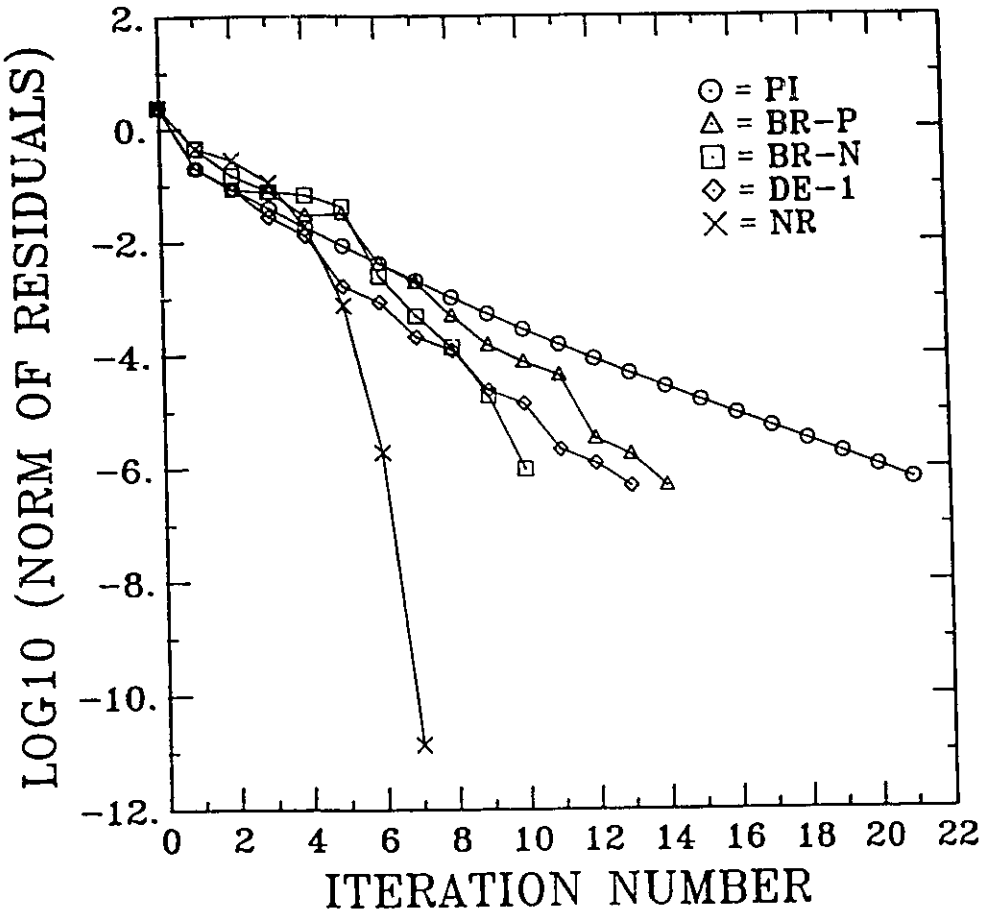

Figure B.9: Logarithm of the norm of residuals vs. iteration number. Driven cavity problem, 72 elements. Power-law index 0.5.

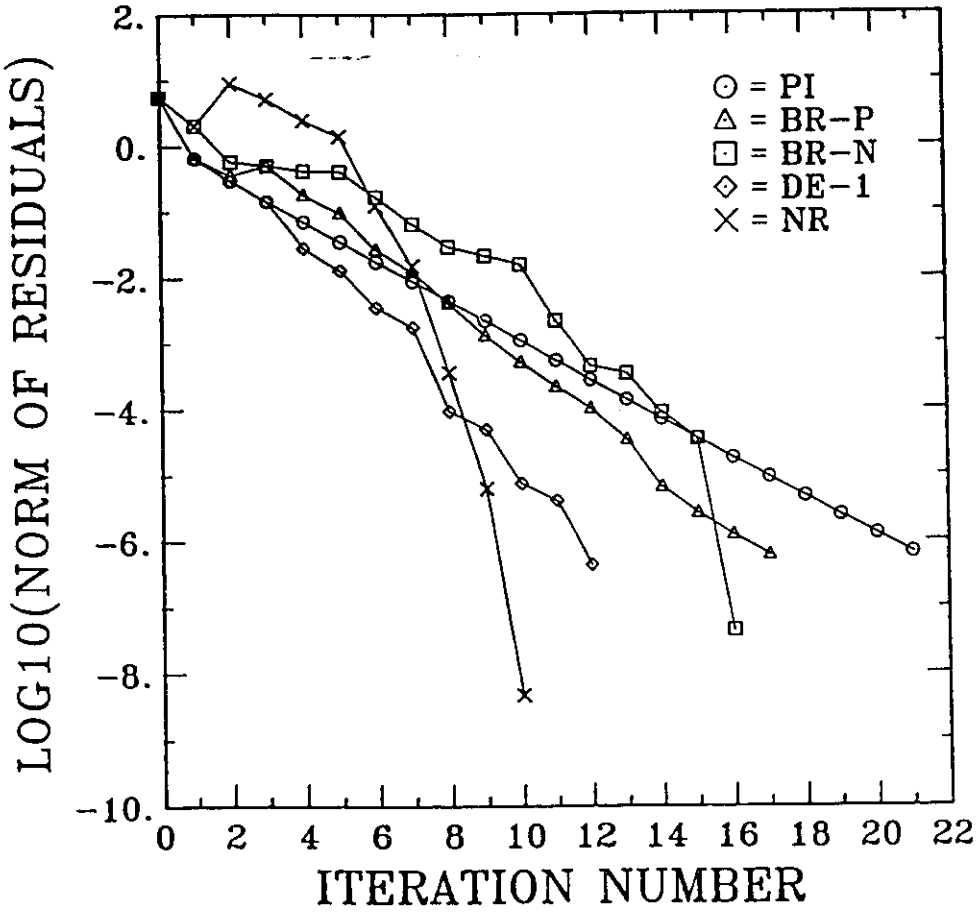

Figure B.10: Logarithm of the norm of residuals vs. iteration number. 4:1 contraction problem. Power-law index 0.5.

SUMMARY

Broyden's method is the least expensive solution method, computationally, but does not converge for strongly nonlinear problems.

One solution is to reform the Jacobian matrix after a prescribed number of Broyden iterations. The use of an approximate initial Jacobian (Picard) seems to increase the radius of convergence of the method more than the use of an exact initial Jabobian (Newton-Raphson) which seems to have a better rate of convergence. Line searches did not always help the convergence of the algorithm. The Newton-Raphson method for strongly nonlinear problems requires line searches or continuation to converge. The cost in some cases becomes excessive. The Dominant Eigenvalue method appears to be robust and converged in all cases examined without any additional steps required. In very nonlinear cases, the Dominant Eigenvalue proved faster than the Newton-Raphson method. Dominant Eigenvalue is very simple to implement and provides an alternative for users who want to keep a Picard iteration as the basic iteration scheme.

APPENDIX C

FORTRAN CODE VECTORIZATION AND I/O OPTIMIZATION

The 3-D finite element analysis is difficult because it requires the simultaneous solution of large systems of equations. Typically systems of 10,000 to 30,000 unknowns were encountered in the 3-D finite element studies in this thesis, characterized by large frontwidths or bandwidths due to the 3-D geometry. The memory requirements are high and the coefficients during the frontal matrix decomposition procedure have to be stored on disk. Even then, about 1 million words of core memory are required for the most difficult cases. Due to the presence of long vectors, the 3-D analysis is very well suited for vector processing machines.

In this Appendix, some indicative examples of enhanced performance on the CRAY X-MP 2/4 will be presented. Higher speeds on the CRAY resulted from manually inducing vectorization by reprogramming or restructuring parts of the initial finite element code and also optimization of the I/O operations to the Solid State Disk (SSD) that is attached to the CRAY at the University of Toronto.

FORTRAN CODE VECTORIZATION

Vector processing machines (super-computers) can yield very favorable performances even if the source code is not manually vectorized because of the automatic partial vectorization that the system's compiler (OCLSC, 1986) supports. Table C.1 compares the CPU times that typical test cases required on the VAX-8600 and the CRAY. It can be seen that the CRAY was already 38.6 times faster than the VAX-8600 when no manual vectorization or I/O optimization was done.

Table C.1

Comparison of program performance on a VAX-8600 and a CRAY X-MP 2/4

Number of Unknowns	VAX 8600 (CPU s)	CRAY X-MP 2/4 (CPU s)	Ratio (VAX/CRAY)
401	52.88	1.03	51.1
1851	1854	48.*	38.6
1851	1854	11.03	168.1
3165	3722**	15.9	234.1

* CRAY before vectorization

** VAX-8650

The CRAY system supports a number of utilities that help monitoring the time that is spent within each subroutine or part of each subroutine of the code and the program performance. The FLOWTRACE, SPY, PERFMON and LOOPMARK utilities were used (OCLSC, 1986).

The FLOWTRACE enables the user to see the amount of time spent in each routine of a program.

The SPY utility is a tool that allows the programmer to time much smaller sections of a program. SPY is based on a statistical sampling of a register (P-register) that contains the address in memory of the instruction the program is currently executing. When the program is executed under SPY, the operating system will interrupt the program every 500 micro seconds and look at the value in the P-register. SPY will already have set up a table with a series of counters. There will be one counter for each 4 word span where the P-address might be. Each time the program is interrupted and the P-address pertaining to that address will be incremented by one. SPY can then report the number of times a counter has been addressed. The report also contains the CPU time and the percentage of the total CPU time spent at that

address, and the same information is given at the subroutine level. This way, one can identify parts of the program or whole subroutines that spent an appreciable amount of the CPU time and focus one's efforts in reducing the CPU time requirements in that area.

The LOOPMARK is a CFT control statement keyword parameter and when specified it draws brackets to delimit DO-loops in the source code listing. For each delimited loop, LOOPMARK uses a symbol to indicate which innermost loops vectorized and which did not. Also messages explaining why loops did not vectorize are issued.

Finally, the PERFMON utility monitors the performance of the programm with respect to various parameters. Here the number of Million Floating Point Operations per Second (MFLOPS) is indicated.

With the help of the described tools, the areas where the program did not vectorize were identified. Basic guidelines for enhancing vectorization (OCLSC, 1986) were followed and combined with I/O operations optimization, yielded significant reduction of the total CPU time requirement as can be seen in Table C.1. Vectorization of the program and I/O optimization reduced the CPU time spent between the initial and the vectorized program on the CRAY by a factor of 4.36, resulting in a performance that requires 168 times less CPU time compared to the VAX-8600 to solve the same problem.

The relative performance on the CRAY increases with the number of unknowns because of the longer vectors involved. It can be seen that when a system of 3165 unknowns is solved, the performance ratio increases to 234 (compared against a VAX-8650).

Rates as high as 57.37 MFLOPS were reached for the test case containing 1851 unknowns.

For the specific implementation of the 3-D finite element equations, the CPU time spent in the frontal solver (Taylor and Hughes, 1981) is the most significant fraction, ranging from 60% to 90% of the total CPU time depending on the problem size. This signifies the need

for development of more efficient, vectorizable solvers that would reduce significantly the cost of the 3-D analysis and increase its potential dramatically.

I/O OPERATIONS OPTIMIZATION

When extensive use of scratch space is needed during the execution of the program to reduce core memory requirements, the issue of optimizing the I/O traffic to the disk becomes very important. Unformatted, synchronous or asynchronous, blocked or unblocked I/O can be used with varying effectiveness.

Table C.2 shows the performance of different I/O schemes that were used for the 1851 unknowns case of Table C.1. Asynchronous unformatted I/O Operations seem to result in the lowest CPU time requirement.

Table C.2

Comparison of I/O schemes (CRAY X/MP 2/4).

I/O Scheme	instruction (OCLSC, 1986)	CPU time (s)
Asynchronous	(BUFFER IN-BUFFER OUT)	11.03
Random Access Asynchronous datasets	(WRITEMS-READMS)	14.32
Word-Addressable, Synchronous Random Access Datasets	(PUTWA-GETWA)	11.5
Word-Addressable, Asynchronous Random Access Datasets	(APUTWA-AGETWA)	11.83